Institut für
Chemische und Thermische
Verfahrenstechnik
ICTV

David Appelhaus

On the Fluid Dynamics in Wiped Film Evaporators during Evaporation

ICTV – Schriftenreihe Band 56
Hrsg. Stephan Scholl und Wolfgang Augustin

Technische
Universität
Braunschweig

Bibliografische Information der Deutschen Nationalbibliothek
Die Deutsche Nationalbibliothek verzeichnet diese Publikation in der Deutschen Nationalbibliografie; detaillierte bibliografische Daten sind im Internet über http://dnb.dnb.de abrufbar.
1. Aufl. – Göttingen: Cuvillier, 2026
Zugl.: (TU) Braunschweig, Univ., Diss., 2025

Herausgeber:
Stephan Scholl, Wolfgang Augustin
ICTV – Institut für Chemische und Thermische Verfahrenstechnik
Langer Kamp 7
38106 Braunschweig
Telefon + 49 (0)531 391 2781
Telefax + 49 (0)531 391 2792
ictv@tu-braunschweig.de
www.ictv.tu-bs.de

CUVILLIER VERLAG GmbH, Göttingen 2026
Nonnenstieg 8, 37075 Göttingen
Telefon: 0551-54724-0
Telefax: 0551-54724-21
www.cuvillier.de

Diese Publikation wurde durch Mittel aus dem Publikationsfonds NiedersachsenOPEN unterstützt, der von zukunft.niedersachsen finanziert wird.

1. Auflage, 2026
Gedruckt auf umweltfreundlichem, säurefreiem Papier aus nachhaltiger Forstwirtschaft.

ISSN 1860-1316
eISSN 3053-8300
ISBN 978-3-68952-373-2
eISBN 978-3-68952-374-9
ORCID https://orcid.org/0000-0001-6260-7148
DOI https://doi.org/10.61061/ISBN_9783689523732

On the Fluid Dynamics in Wiped Film Evaporators during Evaporation

Von der Fakultät für Maschinenbau

der Technischen Universität Braunschweig

zur Erlangung der Würde

eines Doktor-Ingenieurs (Dr.-Ing.)

genehmigte Dissertation

kumulative Arbeit

von:	David Appelhaus
geboren in:	Dortmund

eingereicht am:	09.07.2025
mündliche Prüfung am:	22.09.2025

Vorsitz:	Jun.-Prof. Dr. Michael Heere
Gutachter:	Prof. Dr.-Ing. Stephan Scholl
Gutachter:	Prof. Dr.-Ing. Thomas Grützner

2026

Preface

„There's something that doesn't make sense.
Let's go and poke it with a stick."
– The Eleventh Doctor, *Amy's Choice* (Author: Steven Moffat)

This dissertation was written during my doctoral studies from 2020 to 2025 at the Institute for Chemical and Thermal Process Engineering at TU Braunschweig, under the supervision of Prof. Dr.-Ing. Stephan Scholl. During my time at the institute, I had the opportunity to explore how mechanical agitation, heat transfer, and fluid dynamics interact in a wiped film evaporator. The results of this work, along with a contribution to a better understanding of wiped film evaporators, are presented in this thesis.

I am especially grateful to Prof. Dr.-Ing. Stephan Scholl for supervising this work, for many valuable ideas and discussions, and for giving me the freedom to try things out, make mistakes, and learn along the way. That kind of trust and support made a big difference.

Thanks also to Prof. Dr.-Ing. Thomas Grützner for taking on the role of second reviewer, and to Jun.-Prof. Dr. Michael Heere for chairing the examination committee.

There are many people I would like to thank who made this journey possible. First of all, my group leader Katharina Jasch, who guided me throughout these five years with many helpful discussions.

To all of my colleagues, thank you for your helpful advice, coffee breaks, and good conversations. A special thanks goes to my office colleagues Lukas, Natalie, Martin, and Anna, who made work much more fun.

I also want to thank all of the students who supported me with their theses, project work, or as student assistants, whether by helping set up experiments, carrying out investigations, or analyzing the results. Your contributions greatly influenced the outcome of this thesis.

Finally, I would like to thank my family, my friends and especially Sophia. Your support, patience, and encouragement meant a lot, especially during times when things got difficult or deadlines were getting too close. I could not have done this without you.

David Appelhaus
Braunschweig, 2025

Contents

Kurzfassung

Dünnschichtverdampfer (DSV) werden in der chemischen Industrie zur schonenden thermischen Trennung viskoser und temperaturempfindlicher Gemische eingesetzt, etwa bei der Rückgewinnung von Lösungsmitteln oder in der Lebensmittel- und Pharmaindustrie. Dabei wird das zu verdampfende Fluid durch ein rotierendes Wischersystem als dünner Film auf einer beheizten Wand verteilt. Die komplexen Wechselwirkungen zwischen der mechanischen Einflussnahme durch das Wischersystem, der resultierenden Fluiddynamik und dem Wärmeübergang sind bislang allerdings nur unzureichend verstanden und in der wissenschaftlichen Literatur kaum ganzheitlich betrachtet worden.
Im Rahmen dieser Dissertation werden daher diese Wechselwirkungen experimentell und modellbasiert systematisch analysiert. Zu diesem Zweck wurde ein DSV mit Rollenwischersystem unter Verwendung der Reinstoffe Diethylenglykol, Decan-1-ol und Isopropanol experimentell untersucht. Darüber hinaus wurden binäre Gemische aus Diethylenglykol mit Decan-1-ol, Glycerin und Isopropanol hinsichtlich ihrer thermophysikalischen Eigenschaften charakterisiert, um Modellstoffsysteme für weiterführende Studien zur Trennleistung von DSV zu etablieren. Brechungsindex, Dichte, Viskosität und Oberflächenspannung der Reinstoffe und Gemische wurden im Temperaturbereich von 20 °C bis zu 130 °C experimentell bestimmt. Die Exzessgrößen der binären Systeme wurden mittels Redlich-Kister-Gleichungen beschrieben.
Zur Charakterisierung der Fluiddynamik wurden Verweilzeitverteilungen unter adiabaten sowie unter Verdampfungsbedingungen mittels eines Farbstofftracers gemessen. Die Ergebnisse zeigen, dass insbesondere Viskosität und Dichte einen signifikanten Einfluss auf die Verweilzeitverteilung haben, während die Oberflächenspannung für einen geschlossenen Flüssigkeitsfilms eine untergeordnete Rolle spielt. Hochgeschwindigkeitsaufnahmen während des Betriebs belegen, dass Filmaufriss und Entnetzung zu einem deutlichen Anstieg der mittleren Verweilzeit führen können. Dieser Effekt verstärkt sich mit zunehmender Wandüberhitzung, insbesondere bei niedriger Umfangsbelastung bzw. hohen Eindampfverhältnissen.
Ergänzend zu den experimentellen Untersuchungen wurde ein modulares, mechanistisches Modell in Modelica entwickelt. Der DSV wird dabei in vertikale Segmente unterteilt, in denen Wärmeübertragung, Verdampfung und die resultierende Fluiddynamik berechnet werden. Das prädiktive Modell, das ausschließlich auf Basis betrieblicher und geometrischer Größen parametrisiert wird, liefert Schätzwerte für lokale Strömungsverhältnisse, Wärmeübergangskoeffizienten und Verweilzeiten. Die Validierung anhand experimenteller Daten ergab eine gute Übereinstimmung für die mittlere Verweilzeit und den Wärmeübergang. Abweichungen konnten überwiegend auf idealisierte Modellannahmen sowie auf nicht berücksichtigte dynamische Entnetzungseffekte zurückgeführt werden.
Der kombinierte experimentelle und modellbasierte Ansatz dieser Arbeit erlaubt eine detaillierte Analyse des Zusammenspiels von Wischersystem, Fluideigenschaften, Wärmeübertragung und Verweilzeit im DSV. Die Ergebnisse dieser Arbeit leisten nicht nur einen Beitrag zum vertieften Verständnis von DSV, sondern bilden auch eine belastbare Grundlage für die weitere Entwicklung prädiktiver Modelle sowie die zielgerichtete Prozessoptimierung bei der Aufarbeitung temperaturempfindlicher Komponenten.

Abstract

Wiped film evaporators (WFE) are employed in the chemical industry for the gentle thermal separation of viscous and temperature-sensitive mixtures, for example in solvent recovery or in food and pharmaceutical processing. In such systems, the liquid feed is mechanically distributed as a thin film on a heated surface by means of a rotating wiper system. The resulting fluid dynamics and heat transfer are strongly influenced by this mechanical action. However, the coupled interaction between film formation, fluid properties, and thermal transport phenomena remains insufficiently understood and has rarely been analyzed in a holistic manner in the scientific literature.

This dissertation systematically investigates these interactions using both experimental and model-based approaches. To this end, a WFE equipped with roller wipers was operated using diethylene glycol, 1-decanol, and isopropanol as pure components. In addition, binary mixtures of diethylene glycol with 1-decanol, glycerol, and isopropanol were characterized with respect to their thermophysical properties to establish a set of robust model fluids for future studies on separation performance. The refractive index, density, viscosity and surface tension were measured in the temperature range from 20 up to 130 °C. Excess properties were described using the Redlich-Kister equations.

The fluid dynamics was characterized by measuring residence time distributions (RTD) under both adiabatic and evaporation conditions. The results show that viscosity and density significantly affect RTD, whereas surface tension is of minor relevance in the regime of a stable liquid film. High-speed imaging revealed that film rupture and dewetting can lead to a significant increase in mean residence time. This effect is intensified under increased wall superheat, particularly at low peripheral loads or high evaporation ratios.

To complement the experimental investigations, a modular mechanistic model was developed in Modelica. The model discretizes the WFE into vertical segments and simulates local flow behavior, heat transfer, and evaporation dynamics. Parameterization is based solely on operational and geometric data, enabling predictive simulations of RTD and heat transfer. The validation against experimental data showed good agreement for mean residence time and heat transfer. Deviations were primarily attributed to simplifying model assumptions and the omission of transient dewetting effects.

This dissertation presents a combined experimental and modeling approach that captures the complex interactions between the wiper system, fluid properties, heat transfer, and residence time in WFE. The results contribute to a deeper understanding of WFE and provide a solid foundation for the development of predictive models and the targeted optimization of separation processes involving heat-sensitive components.

List of Tables

List of Figures

List of Symbols

Latin symbols

Symbol	Explanation	Unit
A	Antoine parameter	–
A	heat transfer surface area	m^2
A	pressure drop across the gap zone	$\mathrm{Pa\ m}^{-1}$
$a_1 \dots a_6$	empirical constants	–
B	Antoine parameter	K
B_1	film parameter	m
B_2	film parameter	m^{-1}
B_3	film parameter	m
b	roller diameter	m
b_g	diameter of guide rod	m
b_o	outer diameter of roller wiper	m
b_i	inner diameter of roller wiper	m
C	Antoine parameter	K
$C_{1,2}$	integration constant	–
C_a	integration constant	–
C_b	integration constant	–
C_c	integration constant	$\mathrm{m}^3\,\mathrm{s}^{-1}$
C_d	discharge coefficient	–
c	concentration	$\mathrm{mol\ m}^{-3}$
c_P	isobaric heat capacity	$\mathrm{J\ kg}^{-1}\ \mathrm{K}^{-1}$
D	inner diameter of evaporator	m
D_{diff}	diffusion coefficient	$\mathrm{m}^2\ \mathrm{s}^-1$
d_e	equivalent diameter	m
d_r	inner diameter of apparatus	m
d_o	outer diameter	m
d_∞	diameter of apparatus	m
dz	length of a height element	m
$E(t)$	exit function	s^{-1}
F_N	force normal to the rod	N
F_R	force tangential to the rod	N
F_{cen}	centrifugal force	N

Symbol	Explanation	Unit
$F(t)$	dimensionless residence time response function	-
f	correction factor	–
f	wiping frequency	s^{-1}
f_{wavy}	correction factor for waviness	–
f_{η}	correction factor for influence of viscosity	–
g	standard acceleration of gravity	m s^{-2}
h	heat transfer coefficient	W m^{-2} K^{-1}
h_{prod}	heat transfer coeff.| product side	W m^{-2} K^{-1}
$h_{\mathrm{L,utility}}$	local heat transfer coeff.| utility side	W m^{-2} K^{-1}
h_B	height of bow wave	m
j	elements in y-direction in the film	–
k	proportionality factor	–
K_1	coefficient for axial velocity	–
$\mathcal{L}$	characteristic length, free film	m
$L_{B,w}$	length of bow wave	m
L_{WFE}	wiped length of the WFE	m
m_B	mass of the bow wave	kg
$\dot{m}$	mass flow	kg s^{-1}
$\dot{m}_F$	feed mass flow	kg s^{-1}
$\dot{m}_{\mathrm{axial}}$	axial mass flow	kg s^{-1}
$\dot{m}_{\mathrm{dead}}$	dead-volume mass flow	kg s^{-1}
$\dot{m}_{\mathrm{tan}}$	tangential mass flow	kg s^{-1}
N	number of CSTR	–
N_B	number of wiper elements	–
n	wiper frequency	s^{-1}
n_{CSTR}	CSTR layers per height element	–
n_D	refractive index	-
n_x	segments in radial direction	–
n_y	segments in the film	–
n_z	segments along the height	–
P	parachor	m^3 $kg^{0.25}$ $s^{-0.5}$ mol^{-1}
p	pressure	Pa
$\dot{p}$	tangential momentum flow	kg m s^{-2}
$\dot{Q}$	heat flow	W
$\dot{q}$	heat flux	W m^{-2}
R	heat transfer resistance	K W^{-1}
R	radius	m

Symbol	Explanation	Unit
r	radius coordinate	m
r_δ	free inner radius	m
s	gap width	m
s	experimental standard deviation	-
T	temperature	K
T_c	critical temperature	K
T_p	temperature, product side	K
T_s	temperature, utility side	K
t	time	s
t_{sc}	time between wiper passes	s
U	voltage	V
U	overall heat transfer coefficient	W m^{-2} K^{-1}
u	absolute uncertainty	-
u_M	uncertainty of the corresponding sensor	-
u_s	uncertainty of the measurement	-
$\dot{V}$	volume flow	m^3 s^{-1}
V_{H}	hold-up volume	m^3
V_{m}	molar volume	m^3 mol^{-1}
v_{ax}	axial flow velocity	m s^{-1}
v_k	peripheral velocity of the roll	m s^{-1}
v_S	axial flow velocity	m s^{-1}
v_r	peripheral velocity	m s^{-1}
w	wiper speed	m s^{-1}
w_V	vapor velocity	m s^{-1}
x, y, z	coordinates	m

Greek symbols

Symbol	Explanation	Unit
α	thermal diffusivity	m^2 s^{-1}
β_{Dead}	dead volume factor	–
Δh_v	heat of evaporation	J kg^{-1}
Δ_{min}	minimal dimensionless film thickness	-
ΔT	temperature difference	K
ΔU	voltage drop	V
δ	film thickness	m
δ_0	initial film thickness	m
δ^*	dimensionless film thickness	–
δ_{film}	equivalent film thickness	m
ζ	correction term	-

Symbol	Explanation	Unit
η	viscosity	Pa s
η_L	viscosity of liquid	Pa s
η_V	viscosity of vapor	Pa s
Θ	contact angle	°
Θ	dimensionless residence time	-
ϑ	temperature	°C
Γ	peripheral load	$m^3\ m^{-1}\ s^{-1}$
Γ_F	feed peripheral load	$m^3\ m^{-1}\ s^{-1}$
Γ_S	sump peripheral load	$m^3\ m^{-1}\ s^{-1}$
Γ_x	local peripheral load	$L\ m^{-1}\ s^{-1}$
γ	surface tension	$N\ m^{-1}$
λ	thermal conductivity	$W\ m^{-1}\ K^{-1}$
λ	wavelength	m
λ_L	thermal conductivity of liquid	$W\ m^{-1}\ K^{-1}$
λ_W	thermal conductivity of apparatus wall	$W\ m^{-1}\ K^{-1}$
μ_t	first moment of RTD	s
ν	kinematic viscosity	$m^2\ s^{-1}$
ρ	density	$kg\ m^{-3}$
ρ_L	density of liquid	$kg\ m^{-3}$
ρ_V	density of vapor	$kg\ m^{-3}$
σ_t	standard deviation of RTD	s
$\overline{\tau}$	mean residence time	s
τ_δ	tangential shear stress	$N\ m^{\ 2}$
τ_δ^*	dimensionless shear stress	–
τ_r	shear stress	$N\ m^{-2}$
Φ	angular coordinate	rad
Φ_m	molar fraction	$mol\ mol^{-1}$
φ	correction factor	-
ω	peripheral velocity	$m\ s^{-1}$
ξ	evaporation ratio	$kg_D\ kg_F^{-1}$

Dimensionless numbers

Number	Explanation	Definition
Eu	Euler number	$h_B \cdot d_r^{-1}$
Fr	Froude number	$\Gamma^2 \cdot \delta_{\text{film}}^{-3} \cdot g^{-1}$
Ka	Kapitza number	$g \cdot \eta^4 \cdot \gamma^{-3} \cdot \rho^{-1}$

Number	Explanation	Definition
Nu	Nusselt number	$h_P \cdot \mathcal{L} \cdot \lambda^{-1}$
$\mathrm{Nu}_{\mathrm{L},x,l}$	local laminar Nusselt number	$h_{\mathrm{L},x,l} \cdot \mathcal{L} \cdot \lambda_L^{-1}$
$\mathrm{Nu}_{\mathrm{L},x,t}$	local turbulent Nusselt number	$h_{\mathrm{L},x,t} \cdot \mathcal{L} \cdot \lambda_L^{-1}$
$\mathrm{Nu}_{\mathrm{F},x}$	local Nusselt number	$h_{\mathrm{L},x} \cdot \mathcal{L} \cdot \lambda_L^{-1}$
Pr	Prandtl number	$\eta \cdot c_P \cdot \lambda^{-1}$
Re_{F}	film Reynolds number	$\Gamma \cdot \eta^{-1}$
$\mathrm{Re}_{\mathrm{L},x}$	local film Reynolds number	$\Gamma_x \cdot \eta^{-1}$
Re_V	vapor Reynolds number	$\overline{w}_V \cdot 2 \cdot r_\delta \cdot \nu_V^{-1}$
Re_{R}	rotational Reynolds number	$d^2 \cdot n \cdot \rho \cdot \eta^{-1}$
$\mathrm{We}_{\mathrm{film}}$	film Weber number	$\rho \cdot \Gamma^2 \cdot \delta_{\mathrm{film}}^{-1} \cdot \gamma^{-1}$

List of Abbreviations

Abbreviation	Meaning
CSTR	Continuous Stirred Tank Reactor
DEG	Diethylene Glycol
FFE	Falling Film Evaporator
GC	Gas Chromatography
IPA	Isopropyl Alcohol
KF	Karl-Fischer
LED	Light Emitting Diode
PTFE	Polytetrafluoroethylene
RTD	Residence Time Distribution
WFE	Wiped Film Evaporator

1. Introduction

Global efforts to defossilize industrial production are transforming the chemical and process industry, shifting the focus to sustainable, resource-efficient, and environmentally friendly processes [1, 2]. At the same time, the demand for high quality products is increasing. These parallel developments call for highly flexible processes and innovative apparatus technologies [3]. Thermal separation processes play a crucial role in purifying products and recovering valuable components such as solvents, significantly influencing ecological and economic evaluations due to their high energy demands and their impact on the quality of the final product [4]. However, many conventional thermal separation methods are unsuitable for complex fluids, e.g., polymer solutions, with high viscosity, thermal instability, or tendencies toward fouling and scaling. In such systems, excessive thermal stress can cause decomposition or unwanted side reactions such as polymerization or degradation, thereby reducing product quality [5, 6]. To minimize thermal damage, operation at reduced pressures and narrow residence time distributions (RTDs) with low mean residence times are advantageous.

In this context, wiped film evaporators (WFEs) are an established type of apparatus that allows high heat transfer rates and low residence times with narrow RTDs [7]. Within a WFE, a rotating wiper system, consisting of rotor blades or flexible wipers, continuously redistributes a liquid film along the heated inner surface of the cylindrical evaporator body. This intensifies heat and mass transfer, preventing film stagnation and allowing the processing of even highly viscous or particle-containing fluids [8]. These features enable the recovery of valuable components from complex mixtures like industrial waste streams and the purification of heat-sensitive products such as pharmaceuticals [9, 10, 11, 12]. Beyond conventional separations, WFEs also offer promising perspectives for integrated processes such as continuous reactive distillation [13]. Consequently, WFEs can contribute to cost reductions and decrease the carbon footprint of chemical processes [14].

Reliable design and operation of WFEs require detailed knowledge of the flow phenomena within the liquid phase and their interaction with heat and mass transfer [15]. Previous investigations have focused on fluid dynamics [16, 17, 18], heat transfer behavior [19, 20, 21], or the impact of wiper geometry [17, 18, 22]. However, the results are mostly system-specific, lack scalability, and insufficiently consider the coupling of mechanical agitation, heat transfer and fluid dynamics. The large number of variables, including thermophysical properties, specific wiper designs, and operating parameters, further amplify the complexity of WFEs. Therefore, a thorough understanding of the interactions within WFEs is still limited. This leads to costly pilot experiments, oversized equipment, and hinders the use of WFEs for integrated processes. Consequently, the full potential of WFEs remains underutilized.

This work addresses this knowledge gap by investigating the morphology and flow behavior of the liquid under evaporation conditions in WFEs. Particular attention is placed on understanding how heat transfer influences fluid dynamics and the RTD, with the aim of optimizing process performance. The research focuses on a WFE equipped with roller wipers, combining experimental investigations with a mechanistic modeling approach to improve the general understanding of the system. The methodical framework is illustrated in Figure 1.1, which outlines the research objective, the use of the experimental data alongside the complementary modeling approach, and the outcome of this

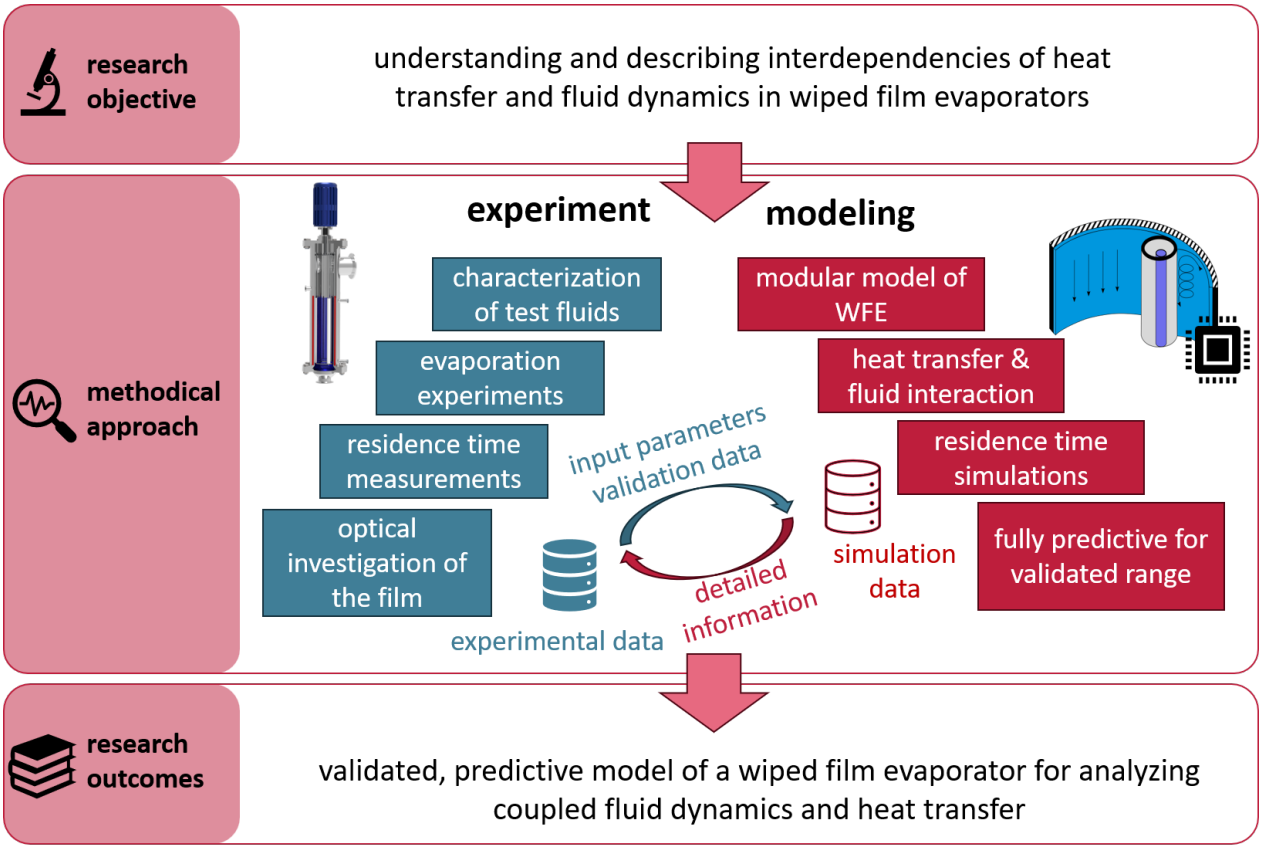

Figure 1.1.: Research objective, methodical approach and research outcomes of this dissertation.

research, resulting in improved knowledge and understanding of WFE.

To contextualize this study within the current state of research and highlight existing research gaps, key findings and correlations from the literature are critically reviewed and discussed in chapter 2.

For experimental characterization, RTDs during evaporation were measured in a laboratory-scale, steam-heated WFE made of stainless steel. The experimental procedure and the applied methodology are described in detail in chapter 3. These experimental data serve as the basis for the parameterization and validation of a modular model of the WFE. To ensure consistency and comparability, four reference fluids (diethylene glycol, isopropyl alcohol, decan-1-ol, and glycerol) were selected based on specific criteria, such as viscosity range, availability, and toxicity. The pure substances and their binary mixtures were subsequently analyzed with respect to their relevant thermophysical properties. The results of the reference system study, previously published in J. Chem. Eng. Data, 69, pp. 2927–2948, 10.1021/acs.jced.4c00152 are reprinted in chapter 4.

Diethylene glycol was selected as the primary reference system for comprehensive analysis during WFE operation. Alongside process data and RTD measurements, high-speed videos of the inner evaporator wall were recorded to capture film flow patterns and instabilities. The video data were evaluated in conjunction with experimental measurements in order to understand the effect of evaporation on fluid dynamics. These experimental results are reprinted in section 5.1 and were published in Chem. Eng. Res. Des. 218, pp. 341–349, 10.1016/j.cherd.2025.04.036.

The measured heat transfer coefficients are compared with established correlations in section 5.2, in which the influence of the operational parameters is estimated. For a more detailed assessment of

the influence of temporary or permanent dewetting phenomena on heat transfer and residence time distribution, height-resolved image series are analyzed in section 5.3 and compared with experimental findings.
The experiments were complemented by comprehensive modeling of the entire apparatus, incorporating both heat transfer and fluid dynamics. To better understand the coupling of these processes, a detailed and modular model of the WFE was developed using Modelica. Initially, a fluid dynamic model was developed and calibrated to experimentally determined RTDs. This model included the gap width between the wiper and the inner wall as well as an empirical dead volume factor as fitting parameters. The model structure of the fluid dynamic model and the results of the simulations are presented in chapter 6, in which section 6.2 is an updated reprint of Chem. Eng. Res. Des. 161, pp. 115–124, 10.1016/j.cherd.2020.07.001.
The model was subsequently expanded to integrate heat transfer, resulting in a fully predictive model by reducing the degree of freedom of the WFE system. The simulation results are compared with the experimental data during evaporation, providing insight into the interactions of fluid dynamics and heat transfer processes. The segmental model structure taking into account heat transfer and its simulation results is shown and discussed in chapter 7 in wich section 7.1 is reprinted from a publication of Sep. Purif. Technol. 371, pp. 132840, 10.1016/j.seppur.2025.132840.
This combined approach enables a detailed evaluation of how evaporation influences fluid dynamics in WFE. Potential dewetting phenomena arising from film destabilization, decreased volume flow, or gas-liquid interactions can be assessed. In addition, the influence of important operating parameters such as rotational speed or superheat can be systematically analyzed and compared with experimental observations during evaporation. This not only improves the fundamental understanding of coupled thermal–hydrodynamic processes in WFEs, but also allows for targeted validation and future refinement of the developed model.
This thesis lays the groundwork for more effective design and operation of WFEs by combining experimental insights and a adaptable modeling framework. These advancements not only improve the economic and environmental performance of existing processes, but also open up new applications of WFEs.
The results of this work were produced as part of the “Industrielle Gemeinschaftsforschung” (IGF) research project “Recovery of valuable materials using wiped film evaporation” funded by the “Bundesministerium für Wirtschaft und Klimaschutz” (BMWK) (funding code: 01IF22220N1).
This dissertation is structured as a cumulative thesis. Parts of the work have already been published in peer-reviewed journals. The respective sections are clearly stated, and any changes from the original publications are indicated.

2. Theoretical Background

This chapter provides an overview of typical applications and the design of wiped film evaporators (WFEs), outlines the main factors that influence their performance, and discusses challenges associated with their operation. The current state of knowledge with regard to the flow and heat transfer behavior of WFEs is presented, including a comparative assessment of different investigations. Finally, the scope and objectives of this work in the context of the state–of–the–art are outlined.

2.1. Design and Use of Wiped Film Evaporators in Industrial Thermal Separation

Evaporation is a unit operation in which a fluid is (partially) transferred to the gas phase by transferring heat to a liquid at boiling temperature. It is used to concentrate liquid solutions as well as to separate homogeneous mixtures, in which the phase equilibrium leads to a composition difference between the gas and liquid phase. Despite the simplicity of the operation itself, a variety of different evaporator designs are used to ensure a high heat transfer coefficient and low investment. Low-cost options such as forced-circulation and thermosyphon reboilers are commonly used for various fluid systems but can harm products through thermal stress and are unsuitable for highly viscous fluids. An evaporator type providing high heat transfer coefficients yet having very low pressure losses is the falling film evaporator (FFE). In this apparatus, a free-falling film is formed along the surface of a heated wall. Although FFEs exhibit high heat transfer rates, their operation is often limited by film instability and dewetting effects caused by surface tension forces [27]. To overcome this limitation, WFEs can be used in which moving wiper systems redistribute the liquid film periodically.

2.1.1. Working Principle of Wiped Film Evaporators and Common Use Cases

WFEs operate on a working principle similar to that of FFEs. The design and operation mechanism of the WFEs are presented in Figure 2.1 and have been used for more than 75 years [28, 29]. The liquid feed is typically preheated to reach the boiling temperature of the mixture and distributed by a liquid distributor. The liquid is then continuously spread along the wall using a wiper system. The wall may be heated using electricity, a heating medium such as thermal oil or steam [7]. The vapor condenses in an external condenser. The sump is drained either by the wiper system or by gravity. Due to the wiper, the film is continuously renewed, allowing the processing of highly viscous fluids as well as film thicknesses that would cause film rupturing in FFEs [30]. The distribution of the liquid on the wall increases the turbulence and the heat transfer coefficient on the product side, while at the same time reducing the mean residence time of highly viscous fluids [6, 31]. Therefore, in the literature, residence times of less than 60 s are typically reported [32].
Due to the large free cross section, very small pressure losses can be realized along the height, allowing low process pressures down to 1 mbar and consequently reduced process temperatures, which ultimately minimize thermal stress on the fluids [33, 34]. WFEs can therefore be used in a variety of challenging process tasks. The most common uses cover the evaporation and purification

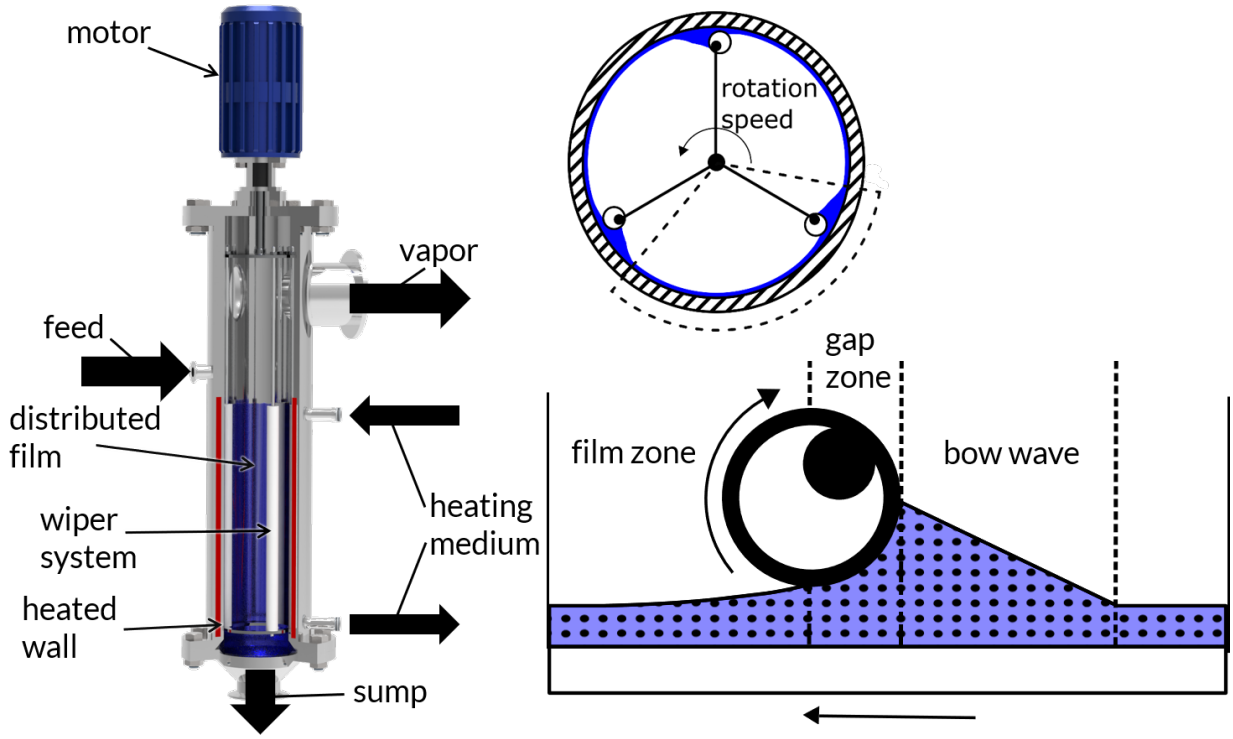

Figure 2.1.: Working principle of a wiped film evaporator, with the wiper system ensuring uniform film distribution. This leads to the formation of a bow wave zone in front of the wiper, a gap zone under the wiper and a free-falling film region.

of thermosensitive fluids, the recovery of solvents from highly viscous or foaming media, and the concentration of food [21]. WFEs have also gained attention for their use as a reactor in reactive distillation, because of their ability to achieve almost isothermal temperature profiles with very short residence times [13, 35, 36, 37]. Due to their numerous benefits compared to other types of evaporators, WFEs are utilized in various industries, such as pharmaceuticals, chemicals, and food processing, usually as one of the last refining steps [21].

If WFEs cannot achieve the necessary operating pressure, short-path evaporators can be used, which follow a similar working principle. As in the WFE, there is a mechanical wiper system that distributes the liquid on a heated wall, but the condenser in the short path evaporator is located inside [38]. This allows the pressure in short-path evaporators to be reduced down to $p_{\mathrm{abs}} = 10^{-3}\ \mathrm{mbar}$ [34]. At such low pressures, molecular distillation occurs, which means that the fluid evaporates without any signs of boiling [39]. However, short-path evaporators follow the same physical principles as WFEs in terms of influencing variables, heat transfer, and fluid dynamics, as described in the following.

2.1.2. Factors Affecting Process Performance

The operation of WFEs depends on the geometric dimensions and design of the apparatus itself, its material and wiper system used, the processed mixtures and their thermophysical properties, as well as the operational parameters that influence both heat transfer and fluid dynamics in WFEs [31]. An overview of the main influencing variables is shown in Table 2.1 [40]. Understanding the interactions between geometric and operational parameters, as well as the thermophysical properties

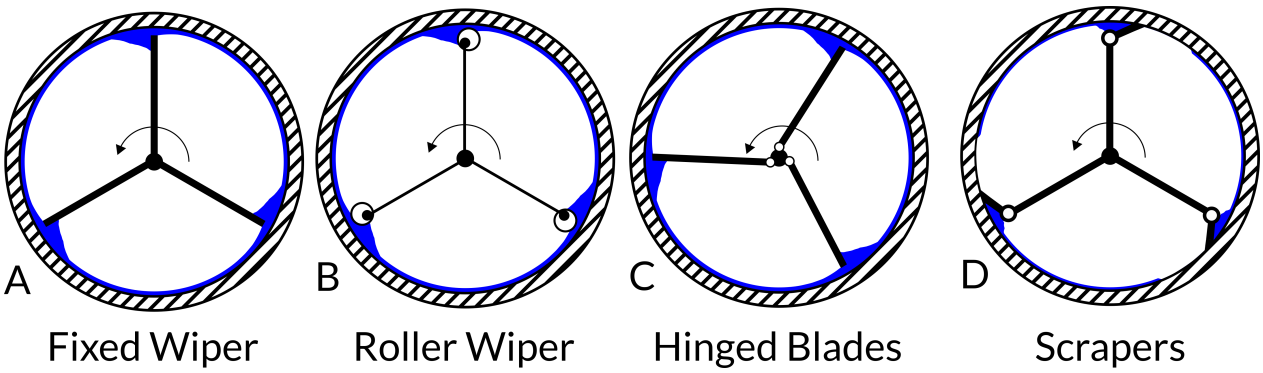

Figure 2.2.: Overview of different wiper types commonly applied in wiped film evaporators (adapted from [40]).

of the fluids, is essential to predict the operational behavior of WFEs. These interactions influence heat transfer, wettability, and fluid dynamics. Although there have been numerous comprehensive studies on these parameters, the multitude of influencing factors makes it challenging to transfer the research findings to other applications without restrictions [39, 41, 42]. The influence of the most relevant input parameters is explained in detail in the following section.

2.1.2.1. Equipment Specific Parameters

As equipment specific parameters the wiper design, the number of wiper elements, the geometry of the inner and outer shell as well as general specifications such as the sealing material or the liquid distributor can be defined. The geometric dimensions directly interact with the operational parameters, such as the wiping frequency or the surface peripheral load. Therefore, they also define the maximum and minimum throughput. The diameter of the device, its length, the thickness, as well as the material (glass/metal) of the wall, and its thermal conductivity influence the heat and mass transfer [43, 44]. The wiper system, that is directly in contact with the liquid film, has a significant impact on the fluid dynamics that forms and can be selected individually depending on the application. Figure 2.2 provides an overview of different common wiper types. Generally, a distinction can be made between wipers with a fixed wall distance, with a movable wiper system, and those with a very small wall distance (the so-called scrapers) [17]. With fixed wiper systems (Figure 2.2 A) - also known as Sambay type - the gap width is fixed. Those wipers can transmit high shear rates and induce turbulence in the medium [45, 46]. This design is therefore often chosen for systems that tend to

Table 2.1.: Geometrical, thermophysical and operational parameters influencing the operation of WFEs (adapted from [40]).

equipment specific	**fluid properties**	**operational**
wiper design	viscosity	wiper speed
equipment geometry	density	temperature utility
wall material	vapor pressure	peripheral load
design utility side	surface tension	process pressure
seals	temperature sensitivity	feed temperature
liquid distributors	phase equilibria	
	fouling, foaming, etc.	

foul or for highly viscous fluids up to 2000 Pa·s such as polymer solutions, as the gap width remains independent of the viscosity [16]. Fixed wipers can lead to an increase in the mean thickness of the film and residence time due to the deceleration of the liquid on the wiper and an overall increase in hold-up volume compared to FFEs [32]. This effect persists even if the equivalent film thickness of the falling film is less than the gap width between the wiper element and the wall. As surface waves can reach amplitudes of two to six times the average film thickness, the wiper can still induce a pronounced bow wave under these conditions [32, 47]. However, at high evaporation ratios, the bow wave may be significantly diminished as a result of the decreased liquid volume. This can result in film thicknesses well below the wiper gap, thereby leaving the wiper system without any effect [48]. As an alternative, movable wiper elements or hinged blades can be used (Figure 2.2 B + C). Here, the wiper elements are pressed onto the wall of the apparatus by means of centrifugal forces or elastic springs [49, 50]. The wiper gap is created as a result of a balance of fluid dynamic and centrifugal forces, which ensures continuous wetting of the apparatus wall [50, 51]. Thus, thin films up to 0.6 mm are formed, and even suspensions or mixtures in which salts can precipitate can be processed [33].

Scraper systems (Figure 2.2 D) can be used for very viscous substances or substance systems with a strong fouling tendency [30]. Next to the wiper type itself, the wiper geometry, the number of wiper elements, and their arrangement can influence the operating behavior [52].

Although usually WFEs are constructed in a tubular shape, special forms include conical design and horizontal layout. In a conical evaporator design (design Sako), the width of the gap can be set precisely by adjusting the height and the risk of film rupturing is reduced [53, 54]. Although it is more difficult to manufacture, it allows for the evaporation of the liquid while maintaining a minimum peripheral load. Additional components such as retaining rings showed a significant increase in the mean liquid hold-up, which ensures wetting and greatly increases the mean residence time of the fluid [32]. A horizontal layout is mostly used for drying processes, ensuring the transport of the liquid by choosing a wiper system that directs the flow towards the evaporator exit. More complex designs are commonly implemented on an industrial scale. For example, a segmented heating jacket supports precise temperature control [55]. Furthermore, a height-dependent wiper system can be used to vary the wiper frequency in different segments [56], which improves the flexibility of the process.

2.1.2.2. Fluid Properties

The fluid properties are mostly predefined by the mixture to be purified. The fluid dynamics and heat transfer are influenced by the viscosity η, density ρ, surface tension γ, diffusion coefficient D_{diff}, thermal conductivity λ, the boiling temperature T_b and phase equilibria that occur.

In WFEs, fluids ranging from aqueous solutions to polymer melts, with viscosities of up to 2000 Pa·s, are processed [16, 57, 58]. Highly viscous fluids often exhibit non-Newtonian behavior in terms of shear rate- and time-dependent properties [16]. Due to the wide range of viscosities and fluid types processed in WFEs, the resulting flow morphologies can vary significantly (see subsection 2.2.1) [6, 59]. For fluids with high viscosities, laminar flow regimes may occur, leading to reduced heat and mass transfer as well as increased mean residence time [6, 39, 60, 61].

The transport properties of thermal conductivity λ and diffusion coefficient D_{diff} play a crucial role

in heat and mass transfer, especially for highly viscous fluids. Based on penetration theory, which is explained in more detail in subsection 2.2.2, it can be assumed that periodical mixing of the film and the bow wave lead to transient, diffusive heat and mass transfer within the film [62, 63], which depends on the transport properties of the fluid.

The gravimetric flow as well as the impulse transport within the liquid film is influenced by the density of the liquid. An increase in fluid density tends to increase the heat transfer coefficient and the mass flows that occur, reducing the mean residence time in the apparatus [22, 64].

Surface and interfacial phenomena occur in the apparatus due to evaporation from thin layers. This can lead to rupturing of the film, especially under evaporation conditions and at lower peripheral loads [65]. In order to properly understand these phenomena, it is essential not only to evaluate the surface tension but also to include the dynamic contact angle, given its important role in dynamic dewetting phenomena [66, 67]. The underlying mechanisms of the formation of thin films, their stability and the influence of evaporation are discussed in more detail in subsection 2.2.3. The local boiling temperature results from the phase equilibria of the individual components of the system and their vapor pressures. This can lead to a significant change in the fluid temperature and thus the temperature-dependent fluid properties along the evaporator height, particularly in the case of wide-boiling mixtures [68].

2.1.2.3. Operational Parameters

The variables that can be controlled to influence the process are typically the operational parameters. They allow the flexible adaption of one WFE to different processes. The boiling temperature can be set via the process pressure. Besides the process pressure, the feed mass flow $\dot{m}_F$ significantly determines which flow velocities and liquid hold-ups occur in the evaporator. To achieve a better comparability of the results of different authors, it is often beneficial to use the peripheral load Γ instead of the mass flow $\dot{m}$, which may be calculated according to Equation 2.1.

$$\Gamma = \frac{\dot{m}}{\rho \cdot \pi \cdot d_r} = \frac{\dot{V}}{\pi \cdot d_r} \tag{2.1}$$

While mass flow and operating pressure are also varied in other devices, the wiper speed is an additional, WFE-specific process variable. As shown in section 2.2, the wiper speed influences both heat transfer and residence time, whereby no further change in heat transfer and fluid dynamics can be expected above a process-specific wiper speed [19, 69]. In particular, during scale-up, the motor frequency n is less important than the wiper speed w and the wiper frequency f_{wiper}, which result from Equation 2.2.

$$f_{\mathrm{wiper}} = n \cdot N_B = \frac{w}{\pi \cdot d_r} \cdot N_B \tag{2.2}$$

Assuming an almost constant heat transfer coefficient, the heat flow can be adjusted via the superheat ΔT (see Equation 2.3). The superheat is adjusted by changing the temperature of the utility side T_{util}. During evaporation, the process temperature T_p is equal to the boiling temperature of the liquid.

$$\Delta T = T_{\mathrm{util}} - T_p \tag{2.3}$$

In cases involving mixtures, high evaporation ratios, or feeds below the boiling temperature, it is crucial to consider the temperature change along the height of the evaporator. This can be achieved by calculating an appropriate mean superheat or conducting a segmental simulation [68].

2.2. Heat Transfer Characteristics and Flow Behavior in Wiped Film Evaporators

The different influencing parameters described in subsection 2.1.2 impact heat transfer and fluid dynamics. In order to better understand the dependencies of the operating behavior on these variables, the current state of knowledge on the most important influencing parameters is summarized below. Fluid dynamics is initially discussed in subsection 2.2.1, followed by a presentation of various mechanistic and empirical methods to describe heat transfer in subsection 2.2.2. Finally, subsection 2.2.3 briefly summarizes the current state of knowledge on the stability of thin films under adiabatic and evaporation conditions.

2.2.1. Flow Regimes and Their Effect on Fluid Dynamics

The fluid dynamics of liquid and gas flows in WFEs is critically important to characterize the flow behavior within these devices. Local velocity distributions provide information about the type of flow (laminar/turbulent) and the RTD. Indicating the mixing efficiency between different areas, these factors are fundamental for further considerations of mass and heat transport. An understanding of liquid distributions during operation is also essential for the transferability of processes and the optimization of a WFE as an apparatus.

2.2.1.1. Fluid Dynamics without Evaporation

The flow in the vertical WFE is influenced by both gravity and the wiper movement, resulting in the overall spiral downward fluid movement shown in Figure 2.3 [70]. In the feed area of the liquid, the wiper elements engage in the film and accumulate the liquid forming a bow wave in front of the wiper [44]. The accumulation of the liquid results in a rotational flow in the bow wave, which is usually turbulent, but can also be laminar for high values of the viscosity and low rotor speed [16, 60]. At high wiper speeds, secondary vortices can be induced in the bow wave [52]. The resulting convective mixing processes increase heat and mass transfer [70].
For a more precise analysis, the flow is usually divided into the three zones bow wave, gap zone and film zone as shown in Figure 2.4, which are described separately [25, 71, 72].

2.2.1.1.1. Bow Wave As the liquid builds up in front of the wiper, a bow wave forms in which convective mixing is increased due to increased turbulence. The shape of the bow wave varies between wedge-shaped and circular geometries depending on the set operating conditions [52]. A vortex forms in the bow wave, which induces a secondary vortex with increasing Reynolds numbers [44, 73, 74, 75]. The resulting vortices increase the mass transfer between the bow wave and the film [45]. The higher turbulence also increases heat transfer significantly [76]. However, with low Reynolds

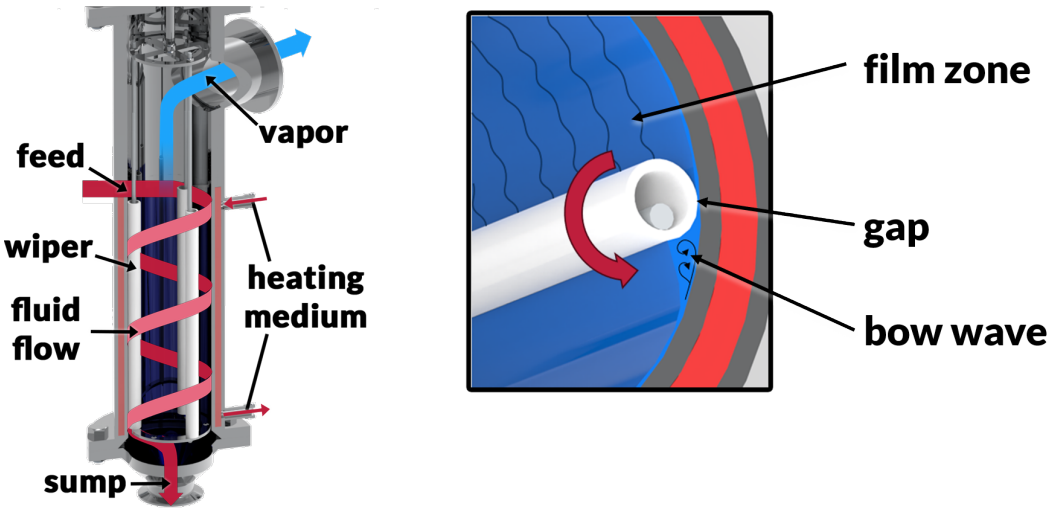

Figure 2.3.: Concept of the flow in the WFE with the additional turbulence in the bow wave and film induced by the wiper.

numbers and laminar flow conditions, only a small mass transfer between the film and the bow wave can be observed [18, 60]. As a result, the liquid in the bow wave bypasses the film with minimal interaction between the zones [50, 60]. This is reflected in bimodal RTDs and pronounced tailing effects [13, 51, 77]. Typically, a turbulent flow is aimed for, as this enables narrower RTDs and higher heat and mass transfer rates. However, the transition point and the actual flow morphology are mostly unknown and systematic studies on this have not yet been carried out. The impact of potential dewetting effects on the RTD is also unclear, causing uncertainty in predicting residence time and heat transfer.

For the laminar case, the axial velocity v_{ax} can be calculated as a function of the density ρ, the viscosity η, the bow wave height h_B and the gap width s following Equation 2.4 [15].

$$v_{\mathrm{ax}} = \frac{K_1 \rho g}{\eta}(h_B + s)^2 \tag{2.4}$$

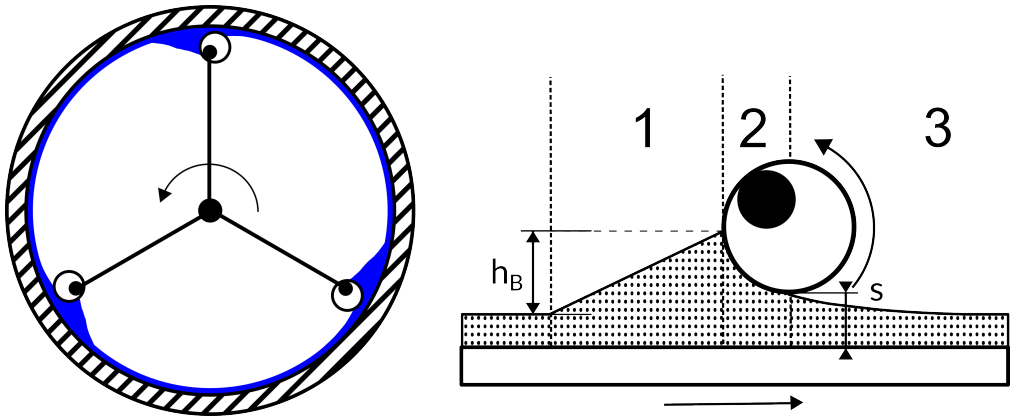

Figure 2.4.: Division of the film into the characteristic regions: (1) bow wave of the height h_B, (2) gap with gap width s and (3) film zone [25].

Equation 2.4 is similar to that of a free-falling film. However, the proportionality constant K_1 depends on the geometry of the bow wave and can be assumed to be 0.0703 for the case of an isosceles triangular profile [15]. For many practically relevant cases, the film thickness in the bow wave is much greater than the film thickness ($h_B \gg s$) and therefore $v_{\mathrm{ax}} \propto h_B^2$ [16]. Although the axial velocity in the bow wave is usually significantly higher than in the film, the convective, periodic mixing of this area with the other areas must also be taken into account for the integral fluid dynamics.

2.2.1.1.2. Gap Zone Due to the small dimensions and high speeds of the wiper elements, large shear forces occur in the gap [64]. In a highly viscous system, the resulting energy dissipation can make a significant contribution to the energy balance. At the same time, due to the non-slip conditions on the wall and wiper, the axial mass flow in the gap is significantly reduced [52]. In the radial direction, the flow profile consists of a Couette flow and a pressure-driven flow due to the hydrostatic pressure of the bow wave. The resulting flow profile in the gap determines the tangential mass flow and the behavior of the subsequent film zone [52, 76].
Determining the flow of the gap zone experimentally is difficult due to its small dimensions, which require the use of indirect measurements [17]. An indicator of the degree of turbulence is the wiper-induced kinetic energy. The gap region is where most of the energy is dissipated and turbulence generally characterizes the flow profile [76]. This assumption was confirmed by computational fluid dynamics (CFD) simulations [45, 78]. However, most models assume laminar flow, leading to a Couette flow in the gap, which may not accurately represent the actual turbulent or transitional behavior observed [15, 60, 71]. Furthermore, the mechanisms of energy dissipation with moving wipers and the effects of the induced turbulence on heat transfer remain unclear.

2.2.1.1.3. Film Zone In the film zone, a gravity-driven acceleration of the liquid takes place in the axial direction [52]. At the same time, the wiper-induced tangential flow is gradually dissipated by internal fluid friction, leading to vortex formation and local turbulences within the film. The vortex trail shortens for higher viscosities [71, 74]. The resulting falling film is usually laminar due to its small dimensions [52, 64].
Although the axial volume flow in the film is small compared to the bow wave, the liquid volume in the film regularly represents above 70% of the total liquid volume [16, 25]. Therefore, the thickness of the film is the crucial parameter for quantifying hold-up within the apparatus, though determining it experimentally requires considerable effort [17]. As an alternative to a direct measurement in the WFE, McKelvey and Sharps [79] applied liquid to the outer surface of a rotating cylinder and distributed the liquid on the outside with a stationary wiper. They were able to show that the film behind the wiper rapidly loses thickness. The minimum practical film thickness can also be estimated for highly viscous fluids and fixed blade wipers with half the gap width [52, 60].

2.2.1.1.4. Residence Time The different zones individually contribute to fluid dynamics and thus influence all variables that depend on them, such as the heat transfer coefficient and the RTD. The latter is particularly relevant when the thermal load on the fluids to be processed is critical. A number of studies have therefore dealt with its modeling. For a simple estimation of the mean residence time, the mean film thickness can be calculated on the foundation of correlation equations. The hold-up

volume and the mean residence time can then be estimated on this basis [16]. Axial dispersion models allow for the calculation of RTDs, provided that axial dispersion is either known or can be estimated from experiments [80]. Using stirred tank cascade models, Zeboudj et al. and Cvengros et al. were able to reproduce experimentally determined RTDs well [77, 81]. In particular, stirred tank cascades offer the possibility of a segmental approach, in which the change in thermophysical properties due to concentration changes can also be modeled [25]. Describing a WFE using interconnected CSTR creates an accurate, simple, and fast residence time model. However, these models lack transferability to other types of wiper, as both the configuration of stirred tank cascades and the axial dispersion coefficient must be adapted to experimental data. A predictive alternative could be CFD simulations, which have already been successfully used to simulate the flow field, residence time and the heat transfer coefficients, but must also be reconfigured for each new geometry [45, 64, 78, 82, 83, 84]. In addition, previous CFD simulations are subject to limitations with regard to dewetting, heat transfer, and the influence of gravity [45, 82].

2.2.1.2. Fluid Dynamics with Evaporation

The mechanically agitated flow created in the WFE increases the heat and mass transfer in the liquid film. Evaporation induces additional convective effects, which may promote film rupture and dewetting phenomena in the WFE. As a result, there is an interaction between the mechanically induced flow and evaporation, which in practice complicates the accurate prediction of heat and mass transfer and important fluid dynamic parameters such as residence time [17, 32, 40].
Although the impact of wetting conditions on heat transfer has been extensively documented, the influence of heat transfer on wetting behavior is not sufficiently explored in the literature [65, 69, 85]. Existing models for heat transfer, such as the penetration theory presented in paragraph 5.1.3.3.1, take into account convective mixing and the influence of the wiper speed, but do not fully consider the effect of thermophysical properties [63]. In viscous fluids, this leads to overestimated heat transfer coefficients and the need for correction factors [64]. CFD simulations that take into account the influence of fluid dynamics on heat transfer primarily focused on fixed wiper systems or scraped film evaporators [45, 86]. Movable wiper systems, possible dewetting processes, and the influence of heat transfer on film stability have not yet been considered in detail.
Furthermore, as discussed in subsection 2.2.3, local wall overheating and, in multicomponent systems, concentration gradients can destabilize the liquid film and promote partial rupture or film dewetting. Fluid dynamics form the basis for heat and mass transfer and thus directly impact evaporator performance. Therefore, to fully understand WFEs, it is important to investigate these interactions.

2.2.2. Heat and Mass Transfer in Mechanically Agitated Film Flows

Heat and mass transfer in WFEs have been extensively studied through both experimental and numerical approaches [15, 17, 19, 43, 69, 87].
For approximate calculations of the heat transfer, application-specific classifications for heat transfer coefficients according to Figure 2.5 can be used [88, 89]. For a detailed design, the integral heat transfer coefficient can be calculated according to Equation 2.5, considering thermal resistances on

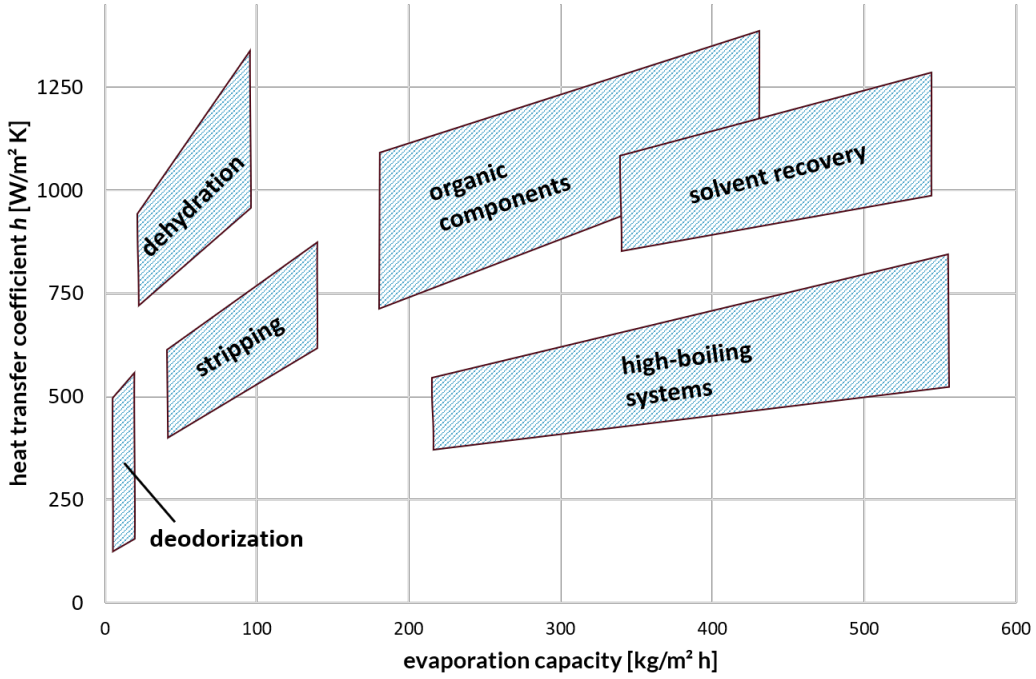

Figure 2.5.: Mean heat transfer coefficients in dependence of the application (redrawn according to [88]).

both the utility and product side as well as within the equipment wall for a pipe geometry.

$$h = \left(\frac{1}{h_{\text{utility}}} + \frac{d_o}{2 \cdot \lambda_w} \cdot \ln\left(\frac{d_o}{d_i}\right) + \frac{1}{h_{\text{prod}}} \cdot \frac{d_o}{d_i} \right)^{-1} \tag{2.5}$$

While reliable correlations and data are available for h_{utility} and λ_w, the heat transfer coefficient on the product side h_{prod} of WFEs is subject to considerable uncertainties, due to the variety of different wiper systems and apparatus geometries as well as the difficulty to precisely measure film thicknesses within the WFE. However, several theoretical, semiempirical and empirical models and equations have been proposed to calculate the product-side heat transfer coefficient [17]. Most of those approaches have been derived for pure components. Therefore, considerable uncertainties may arise from the estimation of thermophysical properties and the definition of the mean superheat, especially in systems with high boiling components and high evaporation ratios [68].

Based on experimental data, empirical equations have been established to describe the heat transfer coefficient. In line with common practice in process engineering, these models typically employ dimensionless numbers to generalize the governing physical principles, as shown in Equation 2.6:

$$\text{Nu} = \frac{h \cdot d_e}{\lambda} = f(\text{Re}_F, \text{Re}_R, \text{Fr}, N_B, d_r/L) \tag{2.6}$$

The Nusselt number Nu is defined as a function of the film Reynolds number Re_F, the rotational Reynolds number Re_R, the Froude number Fr, the number of wiper elements N_B and the ratio of the rotor diameter d_r to the effective length of the wiped zone L. The dependence on the wiper frequency n was determined to be in the range $\text{Nu} \propto n^{0.27} \ldots n^{0.43}$ [20, 62, 90, 91]. However, there is an optimal speed above which a further improvement in heat transfer is not expected [20].

These correlations are typically derived under apparatus-specific flow conditions. Since the complex interaction between fluid dynamics and heat transfer, most importantly local turbulence, film thickness, and flow velocity, is often neglected or unknown, the transfer- and scalability of these models remain limited [17]. Therefore, the validity of these models is highly dependent on the specific system under investigation, particularly with respect to wiper geometry, viscosity, and peripheral load [63]. Ensuring a minimum peripheral load is crucial, as insufficient liquid coverage substantially reduces actual heat transfer performance [65, 92].
Another critical challenge lies in the selection of an appropriate characteristic length scale d_e. Initially, models employed the internal diameter of the apparatus as the reference length [43]. This was later shown to be physically inappropriate due to its minor influence on the dominant transport processes [91]. While the actual film thickness would represent a more meaningful physical parameter, it is rarely available in practice. Therefore, approximations such as the equivalent film thickness of a FFE or the apparent mean film thickness derived from the hold-up volume have been suggested instead [91]. However, this approach may not be suitable for scraped wiper systems, in which the use of the bow wave height as characteristic length is suggested instead [91].
For a theoretical and physically sound approach, two different mechanisms for two-phase heat transfer have been proposed:

1. Surface boiling under moderate heat flux, in which evaporation takes place primarily at the liquid-vapor interface [91].

2. Nucleate boiling under high heat flux and low film velocities, characterized by nucleating vapor bubbles, localized overheating (hot spots), and turbulent mixing, all of which can significantly enhance the heat transfer coefficient [19].

Both mechanisms assume that the main heat transfer occurs within the liquid film. Surface boiling is generally predominant under standard operating conditions [62]. However, local dry-out phenomena can arise at elevated superheating and high evaporation ratios, particularly when the residual film becomes too thin to sustain liquid coverage [65].
For the assumption that only surface boiling occurs Kirschbaum and Dieter as well as Lustenader *et al.* assume a model in which heat transfer is governed by stationary heat conduction through the liquid film [62, 93]. In this case, the heat transfer coefficient on the product side can be expressed as:

$$h_{\mathrm{prod}} = \frac{\lambda_l}{\delta_{\mathrm{film}}} \tag{2.7}$$

Equation 2.7 requires knowledge of the local film thickness δ_{film}, which is governed by the balance of viscous, inertial, and centrifugal forces acting within the WFE.
To address this issue, analogies to lubrication theory were employed. This resulted in the semi-empirical correlation in Equation 2.8, where the film thickness is not needed explicitly [94].

$$h_{\mathrm{prod}} = K_1 \cdot \left(\frac{n_r \cdot d_i}{\eta_l} \right)^{\frac{1}{3}} \cdot \lambda_l \tag{2.8}$$

Based on experimental data and practical applications, the dimensionless coefficient K_1 typically ranges between 250 and 500 [56, 62, 88, 94]. In this context, it is important to note that the

parameters of Equation 2.8 must have the following units: n_r in min^{-1}, d_i in mm, η_l in $\mathrm{Pa \cdot s}$, and λ_l in $\mathrm{W/(m \cdot K)}$.

Alternatively, a transient liquid film model can be assumed, drawing on analogies to mass transfer as formulated by Danckwerts [95]. Here, heat transfer is described using penetration theory [63, 96, 97].

In penetration theory, it is assumed that heat conduction takes place within a laminar sublayer that is periodically mixed with the bulk liquid [63]. Assuming a short mixing time in relation to heat transport, the transient one-dimensional heat conduction problem is governed by Fourier's law and the heat diffusion equation:

$$\dot{q} = -\lambda \frac{\partial T}{\partial y} \tag{2.9}$$

$$\frac{\partial T}{\partial t} = \alpha \cdot \frac{\partial^2 T}{\partial x^2} \tag{2.10}$$

with boundary conditions $T(y = 0) = T_\mathrm{W}$ and $T(y \to \infty) = T_\mathrm{B}$. This leads to the dimensionless solution:

$$\frac{T - T_W}{T_B - T_W} = \frac{2}{\sqrt{\pi}} \int_0^{y/(2\sqrt{\alpha t})} \exp(-y^2)\, dy \tag{2.11}$$

$$\dot{q} = -\lambda \frac{\partial T}{\partial y}\bigg|_{y=0} = (T_B - T_W) \left(\frac{\lambda \cdot \rho \cdot c_p}{\pi \cdot t} \right)^{0.5} \tag{2.12}$$

Accordingly, the heat transfer coefficient based on penetration theory is expressed as:

$$h = \frac{2}{\sqrt{\pi}} \left(\frac{\lambda \cdot \rho \cdot c_p}{t_\mathrm{sc}} \right)^{0.5} \tag{2.13}$$

Here, the contact time t_sc between successive wiping events is defined as:

$$t_\mathrm{sc} = \frac{1}{n \cdot N_B} \tag{2.14}$$

If the Nusselt number is defined with the rotor diameter as the characteristic length, Equation 2.13 can also be formulated as stated in Equation 2.15 [98].

$$\mathrm{Nu} = \frac{2}{\sqrt{\pi}} \cdot \left(\frac{d_i^2 \cdot n \cdot N_B \cdot \rho \cdot c_p}{\lambda} \right)^{0.5} = \frac{2}{\sqrt{\pi}} \cdot (\mathrm{Re}_R \cdot \mathrm{Pr} \cdot N_B)^{0.5} \tag{2.15}$$

At high viscosities, the assumptions of ideal film renewal become invalid due to surpressed convection within the bow wave. Introducing a correction factor can account for non-ideal mixing in the bow wave, which reduces heat transfer [99]. Different correction terms were proposed for this. It was proposed that Equation 2.13 be multiplied by a correction factor of $1/f$, chosen according to Equation 2.16 [20].

$$f = 3.5 + \frac{\mathrm{Pr}}{500} \tag{2.16}$$

It should be noted that the constant offset of 3.5 limits the applicability of the model to higher

Prandtl numbers. Alternatively, it was suggested to multiply Equation 2.15 by an empirical correction multiplier φ [100]. Beyond a system-specific critical rotational Reynolds number, a generally applicable correlation described by Equation 2.17 was established [98].

$$\varphi = 2 \cdot \mathrm{Pr}^{-0.25} \tag{2.17}$$

2.2.2.1. Coupling of Mass and Heat Transfer

In several studies, heat and mass transfer have been modeled simultaneously to assess the enhancement induced by mechanical agitation [39, 87]. Mass transfer in WFEs is inherently linked to local fluid dynamics [39] and can limit separation efficiency [101]. However, the impact of fluid dynamics on mass transfer remains insufficiently explored and is not yet completely understood. Studies on mass transport often seek to indirectly measure heat transfer coefficients [44, 102, 103]. In principle, penetration theory used for heat transfer can also be applied to describe mass transfer under analogous assumption [58, 104]. Alternatively, empirical approaches based on enhancement factors relative to FFEs may be used [39].

One widely discussed effect related to mass transport is the presence of internal rectification processes in WFEs. Most experimental studies under technically relevant conditions did not observe significant rectification effects [21, 42]. However, a partial rectification effect has been shown to occur, especially in low vapor flows, which occurs when small amounts of solvent are removed [105]. Under these conditions, the separation effect can be increased by partially returning the distillate to the feed stream [94].

The models presented for heat and mass transfer are based on the assumption of a stable liquid film, which is essential for the performance of WFE. Although penetration theory may remain applicable under conditions of partial film rupture (assuming the film is rapidly renewed), experimental research indicates that inadequate peripheral loads result in a notable decrease in heat transfer efficiency [40]. Therefore, understanding both stabilizing and destabilizing mechanisms, as well as the kinetics of film rupture, is essential to interpret fluid dynamic behavior. These aspects are discussed in detail in subsection 2.2.3.

2.2.3. Stability of Thin Liquid Films and Dynamics of Film Rupture

As shown in subsection 2.2.1 and subsection 2.2.2, the main improvement of WFEs compared to FFEs is that the thin film generated by the wiper system and the induced turbulence reduces the residence time for highly viscous fluid systems and increases the heat and mass transfer, which reduces the thermal stress. However, as in FFEs, film stability is important for the operation of WFEs.

Since the stability of thin films on heated and unheated surfaces is relevant for many other applications, e.g. in coating processes or absorption columns, this area is a well-studied field of research, with comprehensive reviews having been produced by Oron *et al.* as well as Craster and Matar [67, 106]. In the gravity-driven flow in the WFE and FFE, the density ρ and the dynamic viscosity η are relevant for fluid dynamics and film stability [15].

The minimum peripheral load $\Gamma_{\mathrm{F,min}}$ can therefore be derived from the relevant thermophysical properties and the contact angle Θ, whereby correlations such as Equation 2.18 are suggested [107,

108]. The static contact angle of a liquid results from the equilibrium of surface forces according to Young [109].

$$\Gamma_{\mathrm{F,min}} = 1.69 \cdot \left(\frac{\eta_L \cdot \rho_L}{g} \right)^{1/5} \cdot \left(\gamma_L \cdot (1 - \cos(\Theta)) \right)^{3/5} \tag{2.18}$$

The liquid film loses stability as a result of low viscosity, surface tension, or density, as indicated in Equation 2.18 [110]. The film thickness and the peripheral load can be converted to each other using the correlations found by Nusselt for a laminar falling film [111]. This results in a minimum film thickness δ_{min} or a dimensionless minimum film thickness $\Delta_{\mathrm{min}} = \left(\delta_{\mathrm{min}} \left(\rho_L^3 g^2 / 15 \nu_L^2 \sigma_{LV} \right)^{0.2} \right)$, which can be calculated with empirical equations like the one found by El-Genk and Saber (see Equation 2.19) for the case of flat, unheated plates [112]. Equation 2.19 also applies when surface curvature is negligible, as in typical FFEs and WFEs.

$$\Delta_{\mathrm{min}} = \left(1 - \cos\left(\Theta \right) \right)^{0.22} \tag{2.19}$$

In WFEs, mechanical spreading can reduce the film to less than the critical thickness Δ_{min}, making it thermodynamically unstable yet kinetically stabilized. Even minor disturbances can trigger dewetting phenomena, such as local rupture, wave formation, and the development of liquid ridges, commonly referred to as long-wave instabilities [113, 114].

Wave crests in falling films can reach 2 to 5 times the mean laminar film thickness. In WFEs, such wave structures may locally exceed the gap width between wiper and wall, even when the mean film thickness is below that threshold [47]. This interaction can increase the residence time and liquid hold-up compared to FFEs [32].

Additional destabilizing mechanisms arise during evaporation. Temperature and concentration gradients cause surface tension variations, leading to Marangoni convection, which can promote film rupture [115, 116, 117, 118]. During evaporation and high superheat, bubble nucleation may further destabilize the film and accelerate dry-out phenomena [119, 120]. The disintegration of the film eventually results in the creation of dry spots on the surface of the evaporator [121]. Dewetted regions not only decrease heat transfer in FFEs and WFEs, but also contribute to mechanical wear of the wiper components used [31, 122].

Jahnke *et al.* identified critical sump peripheral loads below which film rupture becomes increasingly likely [31]. Partial dewetting considerably reduces the area-averaged heat transfer coefficient [31, 53, 123]. Although minimum liquid loads required to maintain a continuous film under boiling conditions have been investigated for specific apparatus geometries and moderate load conditions [123], the transient dynamics of film rupture and subsequent renewal processes remain poorly understood. The impact of temporary dewetting events on heat transfer and flow behavior is therefore still uncertain.

In FFEs and coating processes, absolute thermodynamic film stability is usually considered the crucial parameter for wetting. In contrast to FFEs, dewetting in WFEs is often temporary, as the mechanical action of the wiper redistributes liquid on the surface, resulting in a periodic tearing and renewal of the film. Unheated film has already been shown to be stabilized by increasing the wiper speed, demonstrating the importance of dynamic film behavior in WFEs [124]. However, even a temporary film rupture can locally increase wall temperature, potentially accelerating subsequent dewetting.

Assuming a dynamic dewetting regime, the duration of film rupture events can vary by several orders

of magnitude depending on the thermophysical properties of the liquid [125, 126, 127, 128]. This introduces considerable complexity into the prediction of the behavior of heat and mass transfer under operating conditions, which requires further consideration.

2.3. Challenges and Uncertainties of Wiped Film Evaporators during Design and Operation

WFEs and technically similar short-path evaporators have a wide range of applications in the field of temperature-sensitive and viscous fluidic systems. However, their broader application is limited by high investment and significant uncertainties in both design and operation [34, 129].
These higher investment and operational costs arise from the complex design and moving parts, particularly the wiper system, and the challenges associated with scale-up. The latter result from complex interdependencies between thermophysical properties, design, and operating conditions [70]. Experimental and numerical investigations have been conducted to understand the dependencies, but are restricted to specific operating conditions and geometries [9, 17, 122]. Although empirical correlations can capture general trends, experimental validation and pilot-scale studies remain indispensable for reliable process design [39, 87, 130].
In addition to the previously mentioned research deficits, there are significant knowledge gaps in the area of dewetting processes in WFEs. While the mean film thickness in unheated WFEs with fixed wipers is well-studied [52], and thin film stability in FFEs is extensively researched [47, 131], the behavior and stability of thin films in heated WFEs remain unexplored. The thermodynamic effects and operational consequences of dewetting, especially its adverse effect on heat transfer, are conceptually recognized [31]. Due to the high complexity, direct experimental investigations of dynamic dewetting in WFEs have not yet been realized [65, 122]. Since many of the existing studies on WFEs date back to the 1950s to 1970s, the use of modern measurement methods such as high-speed cameras to characterize the fluid dynamics seems promising.
CFD simulations also face challenges in this domain, primarily due to the high dimensionality and the moving boundary conditions imposed by the wiper geometry as well as possible film rupturing. As a result, there is currently no comprehensive and validated modeling framework that enables a reliable transfer of findings from laboratory-scale studies to industrial processes. Scale-up tests are still required to determine operational feasibility [70]. Developing coupled heat transfer and fluid dynamic models, ideally extendable to include mass transfer phenomena, would significantly improve the transferability of process knowledge and allow further optimization of WFEs.

2.4. Scope and Objectives of the Present Work

The current state of research provides a solid foundation for wiped film evaporation, but still lacks transferable models for predictive design and operation of WFEs. In particular, novel fluid systems still rely heavily on scale-up experiments [70]. Although there are promising approaches for modeling fluid dynamics and heat transfer, a holistic framework that captures all relevant physical interactions under realistic process conditions is still lacking.

A central limitation lies in the insufficient coupling of evaporation and flow phenomena. Although theoretical studies suggest strong interdependencies, systematic experimental investigations and integrated modeling approaches remain underdeveloped. The absence of validated model fluids and limited research on dynamic wiper systems, such as roller wipers, hinders comparative studies and model development.
The present work addresses these gaps by first identifying and characterizing appropriate model fluids. Based on these, systematic residence time measurements are conducted by varying the evaporation ratio. High-speed imaging with high spatial resolution is employed to detect local dewetting phenomena, which are correlated with thermal loading and the corresponding RTDs. Calculating dimensionless residence times enables assessment of the scalability and transferability of the observed phenomena to other devices and operating conditions.
In addition, a modular and segmented simulation model is developed to close the current modeling gap. Based on the segmental approach of Jahnke, the model is developed to allow for predictive calculation of both fluid dynamics and heat transfer with a reduced number of empirical parameters [40]. The modeling workflow is structured in two stages:

1. A non-evaporation base model is calibrated using measured RTDs.

2. The effects of evaporation are incorporated into a predictive model. This encompasses variations in the peripheral load along the height, changes in thermophysical properties, and gas-liquid interactions.

Overall, this work aims to improve the fundamental understanding of coupled heat and mass transfer in WFEs and to establish a predictive modeling framework. This is expected to significantly advance both the scientific basis and the practical design of efficient WFE processes.

3. Methodological Approach

The methodological approach during the experiments is described in this section. The experimental setup, including plant design and operation, RTD measurements, and optical investigations, is described first. Subsequently, data evaluation, data extraction, and the calculation of experimental uncertainties are explained. Further descriptions regarding the determination of the fluid properties as well as the conduction of the experiments are provided in the methods sections of the corresponding reprinted papers.
The raw data from the experiments and residence time measurements were systematically processed using a data management system developed in Python. A detailed description of the models developed for the miniplant investigated is provided in chapter 6 and chapter 7.

3.1. Experimental Setup and Operation of the Miniplant with a Wiped Film Evaporator

A miniplant with an integrated WFE was used for the experimental investigations. A similar experimental setup was the system used by Jahnke [40], which was expanded to include additional measurement and control technology as part of this research. The process flow diagrams are shown in Figure 3.1 for the process side and in Figure 3.2 for the utility side. A photographic representation of the actual plant setup with marked heat exchanger E1 - E4, a close-up of the WFE (2), and the roller wiper system used is shown in Figure 3.3. The characteristic dimensions of the evaporator inner surface correspond to 0.256 m $\times$ 0.08 m (L $\times$ D). The evaporator (type RF6, UIC GmbH, Alzenau Hörstein) is made of stainless steel (1.4571) with a shell thickness of 5 mm and a gap in the heating section of 8 mm. The roller wiper illustrated in Figure 3.3 was used for all experiments considered in this work. The wiper basket (stainless steel 1.4571) comprises three strands of roller wipers made of glass fiber-reinforced PTFE.
The main process variables were recorded and controlled using the sensors and actuators specified below. The wiper speed was measured via the frequency sensor SIRC112 and controlled using a frequency converter. The feed was dosed through the pump P1, while the mass and volume flow was recorded via the Coriolis flow meter FDIC117. The process pressure was adjusted using the vacuum pump P4 and regulating the leak rate with needle valve V12 upstream of the pump. The evaporated portion of the fluid was condensed in the heat exchanger E3 and then collected in tank T2. Residual vapors are condensed in the heat exchanger E4 cooled with liquid nitrogen and subsequently discharged. The fill level in T2 was continuously monitored using the sensors LIC125 and LIC119 and was maintained constant through the pump speed control P2. The flow of the product remaining in the sump was also recorded in a collecting tank and controlled through the sensors LIC124 and LIC118 and pump P3.
Two oval wheel flow meters (FI122 and FI120) were used to determine the flow of the distillate and the sump. In addition, the mass flow was checked by weighing using scales W108 and W110 in order to check the measurements for consistency.

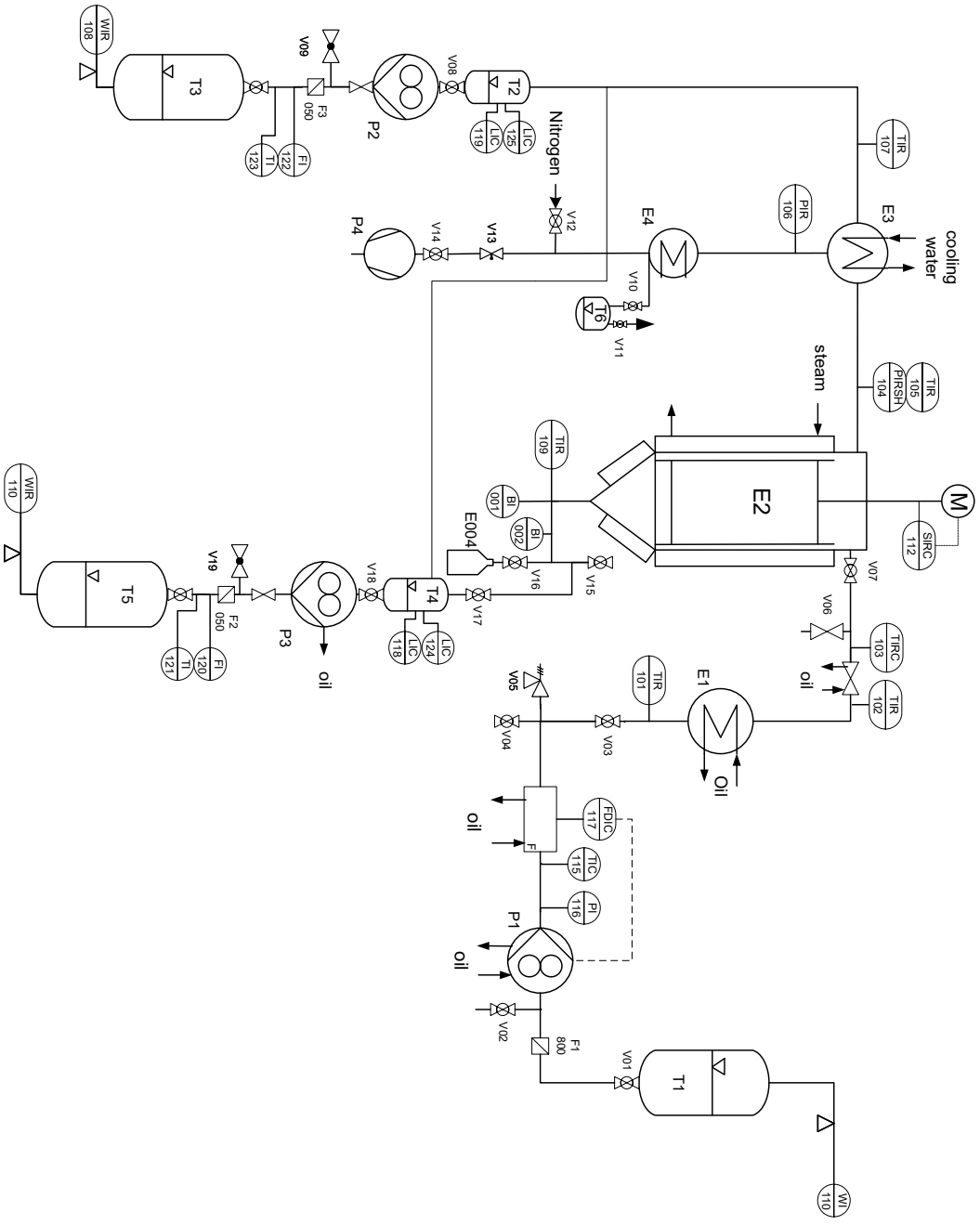

Figure 3.1.: Simplified flow diagram of the process side.

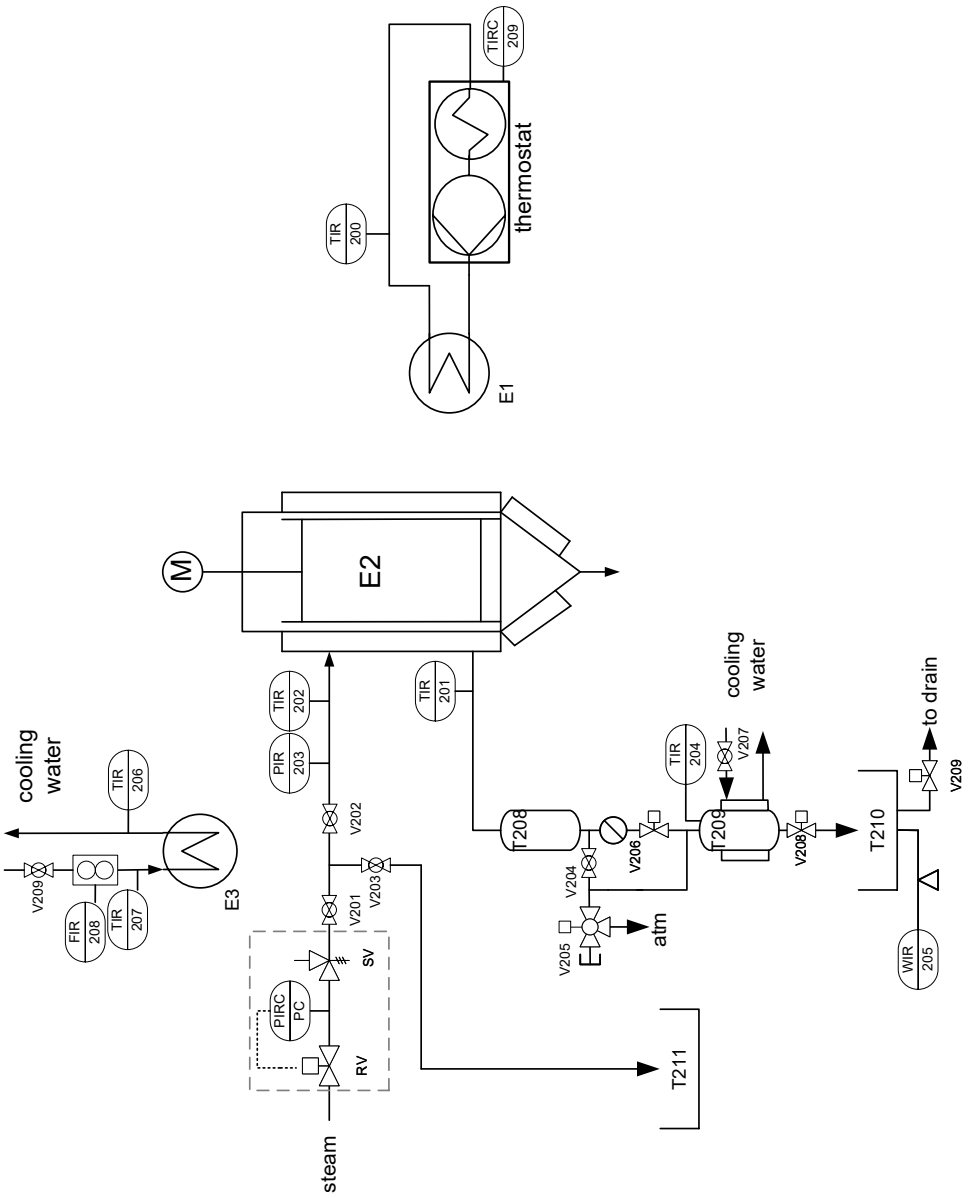

Figure 3.2.: Simplified flow diagram of the utility side.

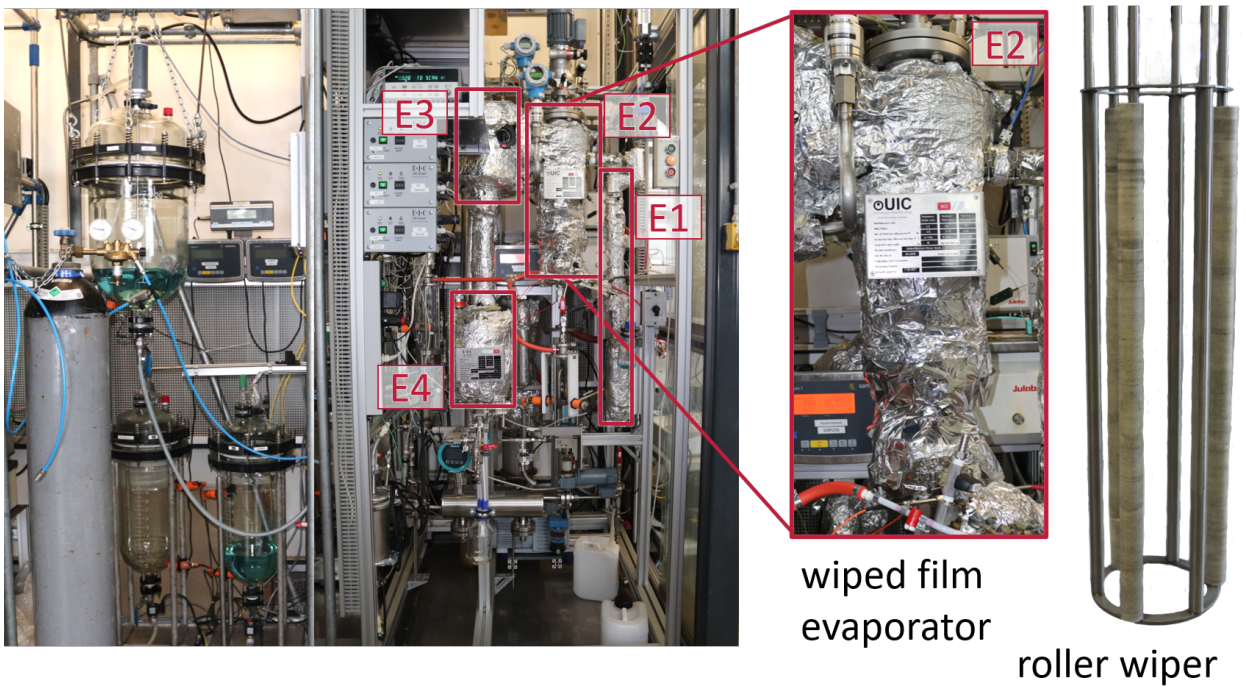

Figure 3.3.: Photo of the used miniplant with main components and roller wiper system used.

The temperature was measured using calibrated type T thermocouples. The high-speed camera BI001 was used to monitor the process during operation under vacuum conditions. This was connected to a borescope, which was inserted into the evaporator chamber via a compression fitting.

Thermal energy for E2 was provided by supplying heating steam from a central network. The steam pressure could be adjusted via a controlled proportional valves ensuring constant pressures from 0.2 bar(g) up to 6 bar(g), which corresponded to a temperature range of around 105 °C to 150 °C. Periodical and time-controlled draining of the condensate from T208 to T210 enabled a mass and energy balance on the utility side. In addition, the feed could be preheated to the calculated boiling temperature via a separate oil thermostat and heat exchanger E1.

Data acquisition and process control were implemented in a LabVIEW environment. For safety purposes, the responsibility of dry-running protection for the pumps was delegated to a separate, logic module. A stationary test procedure was defined as having been achieved if all temperatures and mass flows were constant over a period of at least ten minutes. Under steady-state conditions, measurement data were collected with a sampling frequency of approximately 0.5 Hz. The mean values and standard deviations of all sensors were computed from the raw measurements to evaluate the experimental results. The condensate mass flow was calculated using the scale measurements, determining the mass of condensate collected between two drainage cycles. The mean condensate mass flow was calculated as the collected condensate mass divided by the duration of the drainage cycle.

In addition to the system process data, residence time data was recorded in parallel to the experiments, which is described in more detail in subsection 3.1.1.

3.1.1. Residence Time Measurements

The miniplant was expanded to record residence times quantitatively. The inclusion of a optical sensor enabled the continuous and precise detection of a tracer, allowing to track the temporal behavior of fluid flows within the system.
The tracer used was brilliant blue FCF dye (Merck), which is characterized by its high water solubility and good photometric detectability with an absorption maximum at 630 nm. A light emitting diode (LED) with an emission maximum at 630 nm (type LED630-03, Roithner LaserTechnik) was used for light generation.
The measuring cell at the output of the system consists of two opposing optical probes (see Figure A.1 in the Appendix). One probe is used to emit light via a fiber optic connection to the LED, while the second probe transmits the light transmitted through the liquid to a photodiode (type SPD17-0F, Roithner LaserTechnik). The photodiode has a maximum sensitivity at 620 nm and is therefore suitable for detecting the brilliant blue.
To ensure that liquid is permanently present at the measuring point, the measuring cell was installed in a siphon. This ensures complete wetting of the optical paths, but at the same time increases the dead space volume of the system by up to 50 ml. This additional dead space was taken into account when modeling the residence time and must also be considered when evaluating the experimental data.
The linearity of the detection signal as a function of tracer concentration was checked and confirmed experimentally in advance, enabling a quantitative evaluation of the measurement results[1]. The diagrams for the linearity of the different fluid systems are in the Appendix (see Figure A.2, Figure A.3 and Figure A.4).
The electrical signal generated by the photodiode is normalized via an amplifier board and converted in the voltage range of 0 to 4 V. The signals are digitally recorded at a sampling rate of 20 Hz, which ensures a sufficiently high temporal resolution to display the residence time curves.
The residence time distribution (RTD) was characterized by the exit age function $E(t)$, based on the concentration profile of the tracer Brilliant Blue FCF at the outlet [95]. To determine the RTD, optical absorption measurements were employed to monitor the tracer concentration over time. The recorded voltage drop $\Delta U(t)$ was assumed to be linearly proportional to the tracer concentration, according to the Beer-Lambert law. Therefore, the residence time density function for each experiment was calculated as shown in Equation 3.1.

$$E(t) = \frac{\Delta U(t)}{\sum_0^n (\Delta U(t) \Delta t)} \tag{3.1}$$

The voltage signal was automatically processed as follows:

1. Outliers are removed based on an offset of typically 1 V.
2. The original signal is smoothed using a moving average of 30 data points.
3. Sudden voltage changes within a signal due to gas bubbles are removed from the data.

[1] The evaluation and calibration of the measurement technology for RTD measurements was carried out as part of a student thesis by Claus [132].

4. The start time of the injection is used as the start time of the residence time measurement.

5. The residence time density signal is calculated from the smoothed signal using Equation 3.1

6. The end time is modified to exclude data points occurring beyond three times t_{90}, where $F(t_{90}) = 0.9$.

The RTD was normalized so that the following condition is met:

$$\lim_{t\to\infty} F(t) = \int_0^\infty E(t)\,dt = 1 \tag{3.2}$$

Each experiment involved triplicates measurements of the experimental residence time, used to calculate a mean residence time density function with standard deviation for each data point. From the averaged RTD, the mean residence time $\overline{\tau}$ (1st moment, Equation 3.3) and the standard deviation (root of variance σ_t^2 / 2nd moment, Equation 3.4) were calculated, where the associated uncertainties were determined by error propagation. The processing of the experimental raw data of the residence time measurement and the calculation of the RTD is illustrated in the Appendix in Figure A.5.

$$\overline{\tau} = \mu_t = \frac{\int_0^\infty t \cdot E(t)\,dt}{\int_0^\infty E(t)\,dt} = \int_0^1 t\,dF \approx \frac{\sum_{t_0}^{t_{\text{end}}} t_i \cdot E_i(t)\,\Delta t}{\sum_{t_0}^{t_{\text{end}}} E_i(t)\,\Delta t} \tag{3.3}$$

$$\sigma_t^2 = \frac{\int_0^\infty (t-\overline{\tau})^2 \cdot E(t)\,dt}{\int_0^\infty E(t)\,dt} = \int_0^1 (t-\overline{\tau})^2\,dF \approx \frac{\sum_{t_0}^{t_{\text{end}}} (t_i-\overline{\tau})^2 \cdot E_i(t)\,\Delta t}{\sum_{t_0}^{t_{\text{end}}} E_i(t)\,\Delta t} \tag{3.4}$$

To better understand the influence of different process parameters on the flow behavior and to examine whether the flow profile relevant to the measured RTDs exhibits a shift, dimensionless RTDs were calculated. A shift in the regions relevant to fluid dynamics is expected to result in a visible shift in the dimensionless RTD, regardless of the actual fluid load. The dimensionless residence time density function $E(t/\overline{\tau})$ and the dimensionless residence time Θ were calculated according to Equation 3.5 and Equation 3.6.

$$E(t/\overline{\tau}) = E(t) \cdot \overline{\tau} \tag{3.5}$$

$$\Theta = t/\overline{\tau} \tag{3.6}$$

3.1.2. Image-Based Analysis of Liquid Film Behavior

A camera system was installed to qualitatively analyze the liquid distribution and to identify possible inhomogeneities in the liquid film. A schematic drawing of the installed system is provided in Figure 3.4. It allows direct visual observation of the inner surface during operation and provides valuable information on the distribution and dynamics of the liquid phase within the evaporator.
Visual inspection was carried out using a borescope from Leitner Industrial Endoscopy GmbH & Co. KG. The borescope has a 90° viewing direction and an image aperture angle of 55°, allowing a wide field of view to be captured inside the evaporator. A 300 W xenon light source with variably adjustable intensity was used to illuminate the observation area. The light source is coupled to the borescope using a liquid light guide, ensuring bright, uniform illumination of the inner evaporator. However,

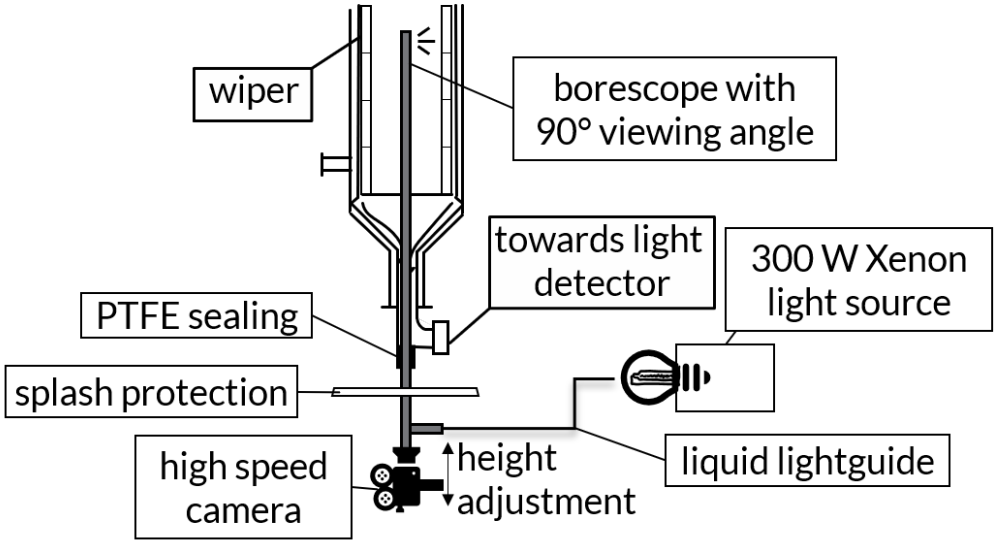

Figure 3.4.: Schematic drawing of the system for recording high-speed images.

because of the central light source in combination with the reflective stainless steel surface, some light reflection and uneven lighting are unavoidable.
A high-speed camera of the type Phantom High Speed, Miro C210 was connected with the borescope to record the image data. The images were taken at a frame rate of 2400 fps and an exposure time of 0.2 ms with a resolution of 640 $\times$ 480 px. Based on a wiper speed of 500 rpm and an exposure time of 0.2 ms, this results in a maximum local measurement blur of 0.4 mm. This high temporal and spatial resolution enabled the detailed observation of transient phenomena within the liquid film, such as wave formations, local accumulations, or film instabilities under real operating conditions.

3.1.3. Calculation of Experimental Heat Transfer Coefficients

The product-side heat transfer coefficient, denoted as h_{prod}, was essential for modeling the thermal performance of the evaporator. Therefore, selected literature correlations, as described in subsection 2.2.2, were implemented and validated against experimentally derived heat transfer coefficients based on the measured heat flow.
The heat flow to the product, $\dot{Q}_{\mathrm{prod}}$, was determined using an enthalpy balance:

$$\dot{Q}_{\mathrm{prod}} = \dot{m}_{\mathrm{distillate}} \cdot (c_{p,\mathrm{distillate}} \cdot T_{\mathrm{vapor}} + \Delta h_v) + \dot{m}_{\mathrm{sump}} \cdot c_{p,\mathrm{sump}} \cdot T_{\mathrm{sump}} - \dot{m}_{\mathrm{feed}} \cdot c_{p,\mathrm{feed}} \cdot T_{\mathrm{feed}} \quad (3.7)$$

This balance includes sensible heat contributions from the all streams, as well as the latent heat of vaporization Δh_v in the distillate stream. To validate Equation 3.7 and assess heat losses, a comparison between the experimentally determined heat flows from the heating side and the utility side was carried out in subsection 3.2.1.
The integral product-side heat transfer coefficient was then computed according to Equation 3.8.

$$h = \frac{\dot{Q}_{\mathrm{prod}}}{A \cdot \Delta T} \quad (3.8)$$

A represents the wiped heat transfer area, while ΔT is the temperature difference between the

heating steam and the product film. The temperature on the product side was assumed to correspond to the boiling temperature T_b of the fluid, calculated using the Antoine equation (Equation 5.7) with parameters from Table 5.1 in subsubsection 7.1.2.3). The saturation temperature T_s on the utility side was derived from the applied steam pressure using the IAPWS Industrial Formulation 1997 [133].

For the utility side, the average heat transfer coefficient h_{steam} was estimated using the VDI Heat Atlas methodology for condensation in vertical falling films [134]. Therefore, the Nusselt number is calculated in order to determine, the heating-side heat transfer coefficient as:

$$h_{\mathrm{steam}} = \frac{\mathrm{Nu}_F \cdot \lambda_l}{\mathcal{L}} \tag{3.9}$$

where λ_l is the thermal conductivity of the condensed liquid.

The characteristic film length $\mathcal{L}$ was calculated as:

$$\mathcal{L} = \left(\frac{\nu_{\mathrm{liq}}^2}{g} \right)^{1/3} \tag{3.10}$$

where ν_{liq} is the kinematic viscosity of the boiling liquid, and g is gravitational acceleration.

The Reynolds number Re_l is defined with the experimentally measured condensate mass flow rate $\dot{m}_{\mathrm{steam}}$, dynamic viscosity η_l, and outer diameter of the evaporator d_o:

$$\mathrm{Re}_l = \frac{\dot{m}_{\mathrm{steam}}}{\pi \cdot d_o \cdot \eta_l} \tag{3.11}$$

The mean Nusselt number for the laminar regime was calculated using Equation 3.12 and for the turbulent regime using Equation 3.13.

$$\mathrm{Nu}_{F,\mathrm{laminar}} = 0.925 \left(\frac{1 - \frac{\rho_{\mathrm{steam}}}{\rho_{\mathrm{liq}}}}{\mathrm{Re}_l} \right)^{1/3} \tag{3.12}$$

$$\mathrm{Nu}_{F,\mathrm{turbulent}} = \frac{0.020 \cdot \mathrm{Re}_l^{7/24} \cdot \mathrm{Pr}_l^{1/3}}{1 + 20.52 \cdot \mathrm{Re}_l^{-3/8} \cdot \mathrm{Pr}_l^{-1/6}} \tag{3.13}$$

Pr_l is the Prandtl number of the boiling liquid.

The improvement of heat transfer due to a wavy film surface was considered by Equation 3.14.

$$f_{\mathrm{wavy}} = \begin{cases} 1 & \text{for } \mathrm{Re}_l < 1 \\ Re_l^{0.04} & \text{for } \mathrm{Re}_l \geq 1 \end{cases} \tag{3.14}$$

The overall Nusselt number was then obtained by combining the laminar and turbulent contributions using Equation 3.15, where the viscosity correction factor f_η was set to 1, assuming negligible variation between wall and bulk liquid viscosities.

$$\mathrm{Nu}_F = \sqrt[1.2]{(f_{\mathrm{wavy}} \cdot \mathrm{Nu}_{F,\mathrm{laminar}})^{1.2} + (\mathrm{Nu}_{F,\mathrm{turbulent}})^{1.2}} \cdot f_\eta \tag{3.15}$$

3.2. Experimental System Characterization and Evaluation of Uncertainties

The reliability of the results is assessed by evaluating the mass and energy balances and considering the experimental uncertainties.

3.2.1. Mass and Energy Balance Characterization

For the evaluation of data consistency, the mass and energy balances were calculated both for the values based on the measurements of the scales and based on the measurements of the mass and volume flow meters. A maximum deviation of 5% was found for the mass balance and a deviation of $\pm$0.2 kW for the heat flow, assuming a static power loss of 1.034 kW on the heating steam side. The corresponding figures can be found in the Appendix (see Figure A.6 and Figure A.7).
Based on the results, the enthalpy balance on the process side was used to evaluate the amount of heat transferred. For the mass flows, the measured values of the oval gear meters (FI120 and FI122) were used, whereby the mass flows were determined based on the density correlation in chapter 4 and the temperature measured next to the flow meters.
This procedure allowed for estimating the product-side heat transfer coefficient, though significant uncertainties arise mainly from the inaccuracy in measuring the mass flow rates of the sump, distillate, and condensate streams. In addition, heat losses may further contribute to deviations. These factors significantly increase uncertainty in the calculated values of h_{prod}, which is discussed in section 5.2
The determination of uncertainties in general is discussed in more detail in the following subsection 3.2.2.

3.2.2. Determination of Experimental Uncertainties

The combined uncertainty $u(y)$ of each measured quantity was determined by combining the sensor uncertainty $u_M(y)$ (absolute or relative) with the statistical measurement uncertainty $u_s(y)$ using the root-sum-square (RSS) method, as expressed in Equation 3.16:

$$u(y) = \sqrt{u_M^2(y) + u_s^2(y)} \tag{3.16}$$

For temperature sensors, an calibration series from 20 °C to 200 °C was conducted using a reference thermometer (PT100, accuracy $\pm$0.01 K) to validate and confirm the specified measurement accuracy of $\pm$0.1 K. The uncertainties for other sensors were derived from manufacturer specifications and are summarized in Table 3.1.
The statistical measurement uncertainty $u_s(y)$ was estimated based on the respective standard deviations for each sensor explained in section 3.1.
For the mass flow measurements of distillate and sump, the statistical measurement uncertainty was estimated differently, based on the volume difference between level sensors T2 and T4 (approximately 100 mL, based on geometry) and the duration of the corresponding experiment Δt_{exp}, according to the following equation:

$$\dot{V}_{\mathrm{uncertainty}} = \frac{V_{\mathrm{up}} - V_{\mathrm{down}}}{\Delta t_{\mathrm{exp}}} \tag{3.17}$$

Table 3.1.: Relative and absolute uncertainties of the used sensors at the corresponding measurement points.

Sensor	Unit	Uncertainty	Sensor	Unit	Uncertainty
TIR101	K	0.1	PIRSH104	bar	0.05%
TIRC103	K	0.1	F117	kg/h	0.5%
TIR105	K	0.1	D117	kg/m³	0.5%
TIR107	K	0.1	FI120	l/min	1.0%
TIR109	K	0.1	FI122	l/min	1.0%
TI121	K	0.1	PIR203	bar	0.5%
TI123	K	0.1	WIR108	kg	0.00008
TIR200	K	0.1	WI109	kg	0.00008
TIR201	K	0.1	WIR110	kg	0.002
TIR202	K	0.1	SIRC112	rpm	0.1
TIR206	K	0.1	WIR205	kg	0.00008
TIR207	K	0.1	FIR208	l/h	0.1
TIRC209	K	0.1			

Here, V_{up} and V_{down} denote the upper and lower sensor readings.
The uncertainties of derived quantities, such as heat flows, wiper speed, and heat transfer coefficients, were calculated using error propagation, utilizing the Python *Uncertainties* package [135].
The determination of the uncertainty of the thermophysical properties of the fluid systems used is described in detail in chapter 4.

4. Characterization of the Used Model Fluids

For the experiments and simulations carried out, it was essential to use reliable model fluids with precisely characterized fluid properties to ensure the validity and reproducibility of the results. Furthermore, mixtures are of particular interest for future investigations of the separation performance of WFEs. Therefore, binary mixtures of diethylene glycol with decan-1-ol, glycerol, and isopropyl alcohol are characterized in addition to pure components to establish a basis for future studies.

The following chapter represents an updated version of the publication: D. Appelhaus, F. Claus, S. Knoblauch, K. Jasch, and S. Scholl. “Density, Viscosity, Refractive Index, and Surface Tension of Binary Mixtures of 3-oxa-1,5-Pentanediol with 2-Propanol, 1,2,3-Propanetriol, and 1-Decanol from 283.15 to 403.15 K as Reference Systems for Evaporation Experiments”. In: *J. Chem. Eng. Data* 69.9 (2024), pp. 2927–2948.

While updating, editorial changes were made. The data point stated in the text as a deviating data point in Figure 4.8 was corrected from $x_2 = 0.5\,\mathrm{mol/mol}$ to $x_2 = 0.417\,\mathrm{mol/mol}$. Figure 4.6 changed from linear to logarithmic scale for viscosity to better differentiate data points.

Abstract

Thermophysical properties of potential reference systems for the characterization of evaporators, especially wiped film evaporators, are presented. Therefore, the binary mixtures of diethylene glycol (IUPAC: 3-oxa-1,5-pentanediol) with decan-1-ol, glycerol (IUPAC: 1,2,3-propanetriol) and isopropyl alcohol (IUPAC: 2-propanol) were considered. The refractive index at 293.15 K (589 nm) was measured using a refractrometer. The density was measured in a temperature range from 283.15 K to 403.15 K depending on the boiling temperature of the fluids using an oscillating U-tube. The dynamic viscosity was determined in a temperature range from 283.15 K to 403.15 K depending on the boiling temperature of the fluids using a kinematic viscometer based on a modified Couette measuring principle (Stabinger viscometer). The surface tension was measured in a temperature range from 293.15 K to 363.15 K using the pendant drop method. The temperature dependence of the density, viscosity and surface tension of the pure components was described using standard literature models. The excess properties excess refractive index, excess molar volume, $\Delta \ln (\eta/\mathrm{mPa \cdot s})^E$ and excess parachor were modelled using a temperature dependent Redlich-Kister approach.

4.1. Introduction

Thermal separation processes are widely used in the chemical industry for separation, isolation and purification of products. However, they are also energy-intensive and involve a high thermal load on the products. Besides overall process conditions, such as pressure, temperature, pH, the latter is dominated by product exposure to local wall temperatures as well as residence time distribution. The development and optimization of gentle evaporators is therefore a subject of current research. Wiped film evaporators (WFE) are particularly suitable for such applications [8]. In this apparatus, the product to be evaporated is distributed as a thin liquid film on the inner surface of the evaporator by a rotating wiper system. The residence time can thus be better adjusted and the thermal load is reduced [22]. At the same time, these apparatuses allow high heat transfer coefficients and the evaporation of highly viscous substances [93, 136]. A disadvantage, however, is that WFE have many degrees of freedom in design and operation. Theoretical knowledge is limited, standardized design methods hardly exist in practice, thus requiring pilot plant experiments for reliable sizing of production scale equipment [7, 70]. To improve the comparability of experimental studies, it seems advisable to define one or more reference substance systems. For multistage distillation columns these are narrow-boiling mixtures with as little interaction as possible, such as chlorobenzene/ethylbenzene (CB/EB) or cyclohexane/n-heptane (C6/C7) [137]. For WFE, however, these reference systems cannot be transferred, since the physical properties lie outside the usual range of application. Instead, very different test systems have been applied in experimental investigations to date. In most cases, pure substances were used [31, 87, 123]. When mixtures were investigated, they were usually very low-viscosity substances and the evaporators were operated at ambient pressure [21, 138]. Therefore, it seems necessary to define model substance systems for the investigation of real operating behavior, which can reflect different physical properties and are thus suitable for the comparison of different apparatus designs. In this paper three substance systems are proposed and characterized, which cover the usual operating range better and are suitable for comparative measurements. In advance, requirements for the system were determined so that it can be used as widely as possible. The defined requirements were in accordance with Bradtmöller and Scholl [139]:

1. increased viscosity at process conditions while remaining pumpable at room temperature
2. low toxicity
3. liquid at room temperature
4. evaporation temperature in vacuum below condensing temperature of steam at 6 bar
5. condensation temperature above 303 K at typical process conditions allowing the use of cooling water at 293 K
6. low chemical aggressiveness
7. narrow-boiling and wide-boiling mixtures
8. low cost
9. little to no tendency to decomposition, fouling or foaming, easy to clean

Based on the specifications above, three test systems were selected depending on the investigated use case. The characterized systems are binary mixtures of diethylene glycol (DEG) as the base component and with glycerol, decan-1-ol and isopropyl alcohol (IPA) as the second component. The chemicals are widely available at relatively low costs and do not present any specific health, safety and environment issues. For the proposed pure substances, measured data exist for the investigated physical properties surface tension [140, 141, 142], refractive index [141, 143, 144, 145, 146], density [144, 146, 147, 148, 149] and viscosity [146, 147, 148, 149], but no measurements exist for the respective mixtures, except for the mixture of DEG and isopropyl alcohol [150].

For the investigations in the WFE, the range of typical evaporation conditions between 293.15 K and 393.15 K is particularly relevant.

4.2. Experimental Methods

4.2.1. Investigated Fluids

The chemicals used were diethylene glycol (DEG), glycerol, decan-1-ol and isopropyl alcohol (IPA). The manufacturer data as well as IUPAC names, CAS registry numbers, molecular weights and purity according to the certificates of analysis are stated in Table 4.1. The chemical structures of the investigated fluids are shown in Figure 4.1. For the preparation of the test series, 13 mixtures were used for each of the binary systems DEG+decan-1-ol, DEG+IPA and DEG+glycerol. Equidistant mole fractions were chosen for the mixing ratios. The mixtures were prepared at 100 g each on a Sartorius LC G6220D balance with a combined standard uncertainty of 0.02 g. The uncertainty of the sample weight and the purity of the pure substances results in a maximum standard uncertainty of $u(x) = 0.0013$ with regard to the mole fraction and a maximum standard uncertainty with regard to the molality $b_i = n_i/m$ of $u(b) = 0.032$ mol/kg. For an evaluation of the long-term stability of the samples, one part was stored at room temperature, one part at 277 K and one part at 252 K for the sample with an equimolar ratio and a reference value for the density was determined at intervals of 1 week, 1 month and 6 months.

Table 4.1.: Used chemicals with their chemical identifiers, manufacturers and purities as stated by manufacturers.

IUPAC Name	3-oxa-1,5-pentanediol	1-decanol	2-propanol	1,2,3-propanetriol
Alternative Name	diethylene glycol	decan-1-ol	isopropyl alcohol	glycerol
Abbreviation	DEG	decan-1-ol	IPA	glycerol
CAS registry number	111-46-6	112-30-1	67-63-0	56-81-5
manufacturer	Carl Roth	Merck	Carl Roth	Sigma-Aldrich
purity (GC)	99.9%	99.5%	99.98%	99.8%
water content/ (kg_{water}/kg_{total}) (KF)	0.0005	n.a.	0.0001	0.0001
molar mass/(kg/kmol)	106.12	158.28	60.096	92.09
critical temperature T_c/K	753 [151]	690 [152]	509 [152]	850 [153]

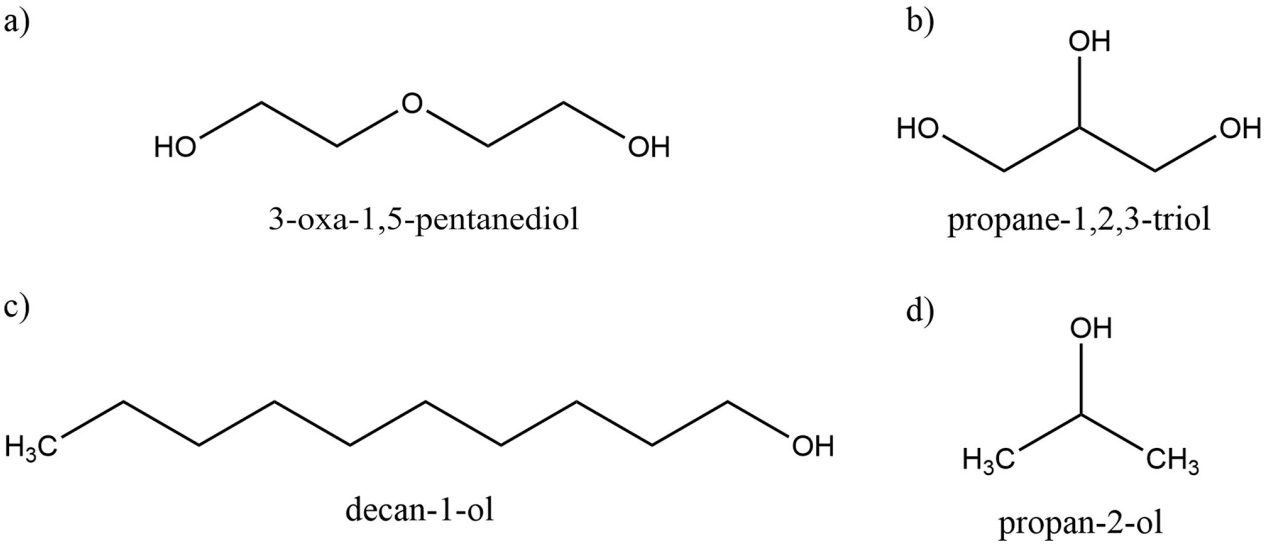

Figure 4.1.: Chemical structures of the used chemicals a) diethylene glycol b) glycerol c) decan-1-ol and d) isopropyl alcohol.

4.2.2. Refractive Index Measurements

For the measurements of the refractive index an Abbemat 500 (Anton Paar) was used. The measurements were conducted at 293.15 K at a wavelength of $\lambda = 589$ nm using water as a reference substance. The uncertainty provided in the technical specifications of the refractive index meter was checked using purified water. For each measured value, three individual measurements were carried out. The mean values as well as the standard deviations were calculated. The uncertainty in the temperature measurement is 0.03 K. The standard uncertainty of the refractive index due to the instrument specification is 0.00002. For the uncertainty due to mixture contamination, it was assumed that the refractive index of trace elements differ from the main component by an absolute value of 0.04. This results in a standard uncertainty of u(n_D) = 0.0002 for decan-1-ol due to its lower purity and of u(n_D) = 0.00008 for the other components.

4.2.3. Density Measurements

The Anton Paar DMA 4100 M density meter was used for the density measurements up to 363 K. For the density above 363 K the Anton Paar SVM 3001 was used up to 403 K. Densities were measured with an increasing temperature ramp from 293 K to 363 K at 5 K intervals and from 363 K to 403 K at 10 K intervals. The mixtures with IPA were measured in the range from 283 K to 343 K with an interval of 5 K. For each measured value, three individual measurements were carried out. Purified water and dry air were used to calibrate the density meter. The uncertainty in the temperature measurement is 0.02 K. The standard uncertainty in the determination of the density due to the instrument specification is 0.00005 g/cm^3. For the standard uncertainty due to mixture contamination, it was estimated that the trace elements differ from the main component by 0.2 g/cm^3. This results in a combined standard uncertainty of u(ρ) = 1 kg/m^3 for decan-1-ol and of u(ρ) = 0.4 kg/m^3 for the other components.

4.2.4. Viscosity Measurements

The Anton Paar SVM 3001 Stabinger viscosimeter was applied for the viscosity measurements. Viscosity was measured in the range from 293 K to 403 K with increasing temperature. Deviating from this, the mixtures with IPA and DEG were measured in the range from 283 K to 343 K. For each measured value, three individual, randomized measurements were carried out. A viscosity standard (Sigma Aldrich, S6, η_{cal} = 7.442 mPa s (25°C)) was used to calibrate the viscosimeter at 293.15 K, 333.15 K and 373.15 K . The maximum deviation was 0.2% of the referenced value and is within the specifications provided by the manufacturer. The uncertainty in the temperature measurement is 0.03 K. The uncertainty in the determination of the viscosity due to the instrument specification is $\mathrm{u}_r(\eta)$ = 0.0035 of the measured value. For the uncertainty due to mixture contamination, it was estimated that the trace elements differ in viscosity from the main component by 50%. This results in an uncertainty of $\mathrm{u}_r(\eta)$ = 0.0035. Contributions to the uncertainty were added in quadrature resulting in a combined standard uncertainty of $\mathrm{u}_r(\eta)$ = 0.006 resp. 0.6% for the viscosity.

4.2.5. Measurements of Surface Tension

A Krüss Droplet Shape Analyzer DSA100E was used for the surface tension measurements. For density, the measured values of the density measurements were used. As a measurement method, the pendant drop method was evaluated using the integrated Young-Laplace's equation by optical measurements and edge detection. The measurement accuracy of the DSA100E was checked prior usage using purified water. The surface tension was determined in the range from 293 K to 363 K. Deviating from this, the temperature range from 283 K to 343 K was considered for the mixtures with IPA. The individual measurements for each temperature step were randomized. At least 5 multiple measurements were carried out for each measuring point. The uncertainty in the temperature measurement is 0.2 K. The uncertainty in the determination of the surface tension due to the instrument specification was 0.01 mN/m. For the uncertainty due to mixture contamination, it was estimated that the trace elements differ in surface tension from the main component by 50%. This results in an uncertainty of $\mathrm{u}_r(\gamma)$ = 0.25% for decan-1-ol and of $\mathrm{u}_r(\gamma)$ = 0.15% for the other components. Furthermore, by comparing the deviation between measurement points and the experimental data with literature [154], the uncertainty due to the measurement method was estimated to $\mathrm{u}(\gamma)$ = 1 mN/m. The resulting combined standard uncertainty is $\mathrm{u}_r(\gamma)$ = 2.97% for decan-1-ol or $\mathrm{u}_r(\gamma)$ = 2.87% for the other components.

4.2.6. Evaluation of the Measurements

For the evaluation, the molar density and the molar volume were calculated from the data using the molar masses of the individual substance systems as stated in Table 4.1. For the pure components, the temperature dependence of the investigated quantities was calculated and for this purpose the parameters of the following equations were adapted to the experimental data using the Python function scypi.curvefit [155].

4.2.6.1. Refractive Index

The refractive index n_D of the mixture with the molar volume fraction $\Phi_i = xV_{m,i}/V_m^{id}$ of the component i and the excess refractive index n_D^E was calculated according to Equation 4.1[156]:

$$n_D = \sum_i \Phi_i \cdot n_{D,i} + n_D^E \tag{4.1}$$

4.2.6.2. Density

The temperature dependence of the density was calculated using Racket Equation (Equation 4.2)[157]:

$$\frac{\rho}{\mathrm{kg/m^3}} = \frac{A}{B^{1+\left(1-\frac{T/K}{C}\right)^D}} \tag{4.2}$$

The molar volume was calculated from the experimentally determined values according to [157]:

$$v_m = \frac{M}{\rho} \tag{4.3}$$

The molar volume of the mixture may be calculated according to:

$$v_m = \sum_i x_i \cdot v_{m,i} + v^E \tag{4.4}$$

4.2.6.3. Viscosity

Equation 4.5 is used for the temperature dependence of the viscosity [157].

$$\ln\left(\frac{\eta}{\mathrm{mPa \cdot s}}\right) = A + \frac{B}{T/\mathrm{K}} + C\,(T/\mathrm{K}) + D\,(T/\mathrm{K})^2 \tag{4.5}$$

For the mixture the viscosity is calculated with [157]:

$$\ln\left(\frac{\eta}{\mathrm{mPa \cdot s}}\right) = \sum_i x_i \cdot \ln\left(\frac{\eta_i}{\mathrm{mPa \cdot s}}\right) + \ln\left(\frac{\eta}{\mathrm{mPa \cdot s}}\right)^E \tag{4.6}$$

4.2.6.4. Surface Tension

Equation 4.7 is used for the temperature dependence of the surface tension [157]:

$$\frac{\gamma}{\mathrm{mN/m}} = A \cdot (1 - T_r)^B \tag{4.7}$$

The reduced temperature T_r is calculated using the critical temperature T_c as stated in Table 4.1:

$$T_r = \frac{T}{T_c} \tag{4.8}$$

For the calculation of the mixture surface tension the parachor P is used [157, 158]:

$$P = \left(\frac{\widetilde{\rho}}{\text{mol/cm}^3}\right)^{-1} \cdot \left(\frac{\gamma}{\text{mN/m}}\right)^{1/4} \tag{4.9}$$

$$P_m = \sum_i \sum_j x_i \cdot x_j \cdot \frac{P_i + P_j}{2} + P^E \tag{4.10}$$

For the calculated excess quantities, the temperature-dependent Redlich-Kister parameters A_k were fitted to the measured quantities as follows [159]:

$$Y^E = x_1 x_2 \cdot \sum_{k=0}^{2} A_k \cdot (x_1 - x_2)^k \tag{4.11}$$

$$A_k = \sum_{i=0}^{2} a_{k,i} \cdot T^i \tag{4.12}$$

The considered excess properties are n_D^E, v^E, $\ln(\frac{\eta}{\text{mPa·s}})^E$ and P^E. To model the temperature dependence of the excess properties correctly the parameters of Equation 4.12 were fitted to the experimental data. The equations thus obtained for the excess quantities as well as the final substance data were plotted. The accuracy of the estimated excess properties were evaluated by means of a residual plots.
To specify the combined standard uncertainties of the measured values y given below, the uncertainties of the measurement methods u_M used and the experimentally determined variances s^2 according to Equation 4.13 are combined with each other [160].

$$u^2(y) = u_M^2(y) + s^2(y) \tag{4.13}$$

4.3. Results and Discussion

4.3.1. Experimental Results of the Pure Components

The experimental results with the compined standard uncertainties using Equation 4.13 for the refractive index, density, viscosity and surface tension for the pure were summarized and compared with experimental values reported in the literature in Table 4.2 - Table 4.5.

Table 4.2.: Refractive index n_D, density ρ, viscosity η and surface tension γ of diethylene glycol at 101 kPa compared with data from literature (standard uncertainty in brackets).

T/K [a]	n_D		ρ/(kg/m^3)		η/(mPa · s)		γ/(mN/m)	
	exp.	lit.	exp.	lit.	exp.	lit.	exp.	lit.
283.15			1123.5 (0.41)					
288.15			1119.9 (0.41)					
293.15	1.44692 (0.00016)	1.4475 [143]	1116.6 (0.41)		35.75 (0.21)	36.52 [147]	43.22 (1.08)	45.55 [154]

[a]: Standard uncertainty of temperature measurement: $u(T)_{n_D} = 0.03$ K, $u(T)_\rho = 0.02$ K, $u(T)_\eta = 0.03$ K, $u(T)_\gamma = 0.2$ K

Table 4.2.: Refractive index n_D, density ρ, viscosity η and surface tension γ of diethylene glycol at 101 kPa compared with data from literature (standard uncertainty in brackets). (continued)

T/K [a]	n_D		ρ/(kg/m^3)		η/(mPa · s)		γ/(mN/m)	
	exp.	lit.	exp.	lit.	exp.	lit.	exp.	lit.
		1.4472 [161]		1118.4 [162]				48.5 [161]
298.15			1113.07 (0.4)	1.1124 [150]				
				1.11704 [147]				
303.15			1109.5 (0.41)	1109.8 [150]	22.33 (0.14)	22.76 [147]	42.39 (1.12)	44.8 [154]
				1114.02 [147]		21.87 [150]		
308.15			1105.9 (0.41)	1105.6 [150]				
				1.11099 [147]				
313.15			1102.3 (0.41)	1102.3 [150]	14.82 (0.09)	15.16 [147]	41.04 (1.07)	
				1107.84 [147]		14.81 [150]		
						15.1 [163]		
318.15			1098.7 (0.41)	1104.62 [147]				
323.15			1095.0 (0.41)	1101.33 [147]	10.35 (0.07)	10.54 [147]	40.03 (1.07)	
				1094.2 [164]				
328.15			1091.4 (0.41)	1097.98 [147]				
333.15			1087.7 (0.41)	1094.55 [147]	7.53 (0.05)	7.61 [147]	39.36 (1.06)	
						7.64 [163]		
338.15			1084.0 (0.41)	1091.05 [147]				
343.15			1080.3 (0.41)	1.087.48 [147]	5.68 (0.04)	5.68 [147]	38.84 (1.07)	
348.15			1076.6 (0.41)	1083.85 [147]				
				1075.4 [164]				
353.15			1072.8 (0.41)	1080.14 [147]	4.41 (0.03)	4.36 [147]	38.12 (1.06)	
					4.41 [163]			
358.15			1069.0 (0.41)	1076.36 [147]				
363.15			1065.2 (0.41)	1072.51 [147]	3.51 (0.02)	3.44 [147]	36.93 (1.06)	
373.15			1057.49 (0.4)	1.068.6 [147]	2.86 (0.02)	2.78 [147]		
				1056.2 [164]		2.73 [163]		
383.15			1049.74 (0.41)	1060.55 [147]	2.37 (0.02)	2.28 [147]		
393.15			1041.88 (0.42)	1052.23 [147]	2.0 (0.02)	1.91 [147]		

[a]: Standard uncertainty of temperature measurement: $u(T)_{n_D} = 0.03$ K, $u(T)_\rho = 0.02$ K, $u(T)_\eta = 0.03$ K, $u(T)_\gamma = 0.2$ K

Table 4.2.: Refractive index n_D, density ρ, viscosity η and surface tension γ of diethylene glycol at 101 kPa compared with data from literature (standard uncertainty in brackets). (continued)

T/K [a]	n_D		ρ/(kg/m^3)		η/(mPa · s)		γ/(mN/m)	
	exp.	lit.	exp.	lit.	exp.	lit.	exp.	lit.
403.15			1033.92 (0.43)	1043.62 [147]	1.71 (0.01)	1.63 [147]		

[a]: Standard uncertainty of temperature measurement: $u(T)_{n_D} = 0.03$ K, $u(T)_\rho = 0.02$ K, $u(T)_\eta = 0.03$ K, $u(T)_\gamma = 0.2$ K

Table 4.3.: Refractive index n_D, density ρ, viscosity η and surface tension γ of decan-1-ol at 101 kPa compared with data from literature (standard uncertainty in brackets).

T/K [a]	n_D		ρ/(kg/m^3)		η/(mPa · s)		γ/(mN/m)	
	exp.	lit.	exp.	lit.	exp.	lit.	exp.	lit.
293.15	1.437119 (0.00023)	1.4367 [144]	829.8 (1.0)	829.5 [144]	14.36 (0.09)		27.17 (1.13)	
		1.4372 [161]		829.7 [165]				
		1.43694 [166]		829.73 [167]				
298.15			826.4 (1.0)	826.3 [144] 826.5 [165]		11.09 [149]		28.35 [168]
303.15			823.0 (1.0)	823 [144]	9.75 (0.06)	9.2 [169]	26.47 (1.07)	26.64 [142]
				822.94 [167]		9.716 [170]		27.29 [168]
308.15			819.6 (1.0)	819.4 [144] 819.46 [165]		7.632 [149]		
313.15			816.17 (1.0)	816.1 [144]	6.84 (0.04)	6.47 [169]	25.53 (1.08)	25.89 [142]
				816.06 [167]		6.82 [170]		25.17 [168]
318.15			812.67 (1.0)	812.6 [144]		5.375 [149]		
				812.58 [165]				
323.15			809.17 (1.0)		4.95 (0.03)	4.69 [169]	24.87 (1.07)	25.1 [142]
				809.17 [167]				
328.15			805.67 (1.0)		3.928 [149]			
333.15			802.13 (1.0)		3.68 (0.02)	3.52 [169]	24.42 (1.06)	24.35 [142]
				802.07 [167]				
338.15			798.57 (1.0)		2.964 [149]			
343.15			794.97 (1.0)		2.81 (0.02)	2.7 [169]	23.11 (1.07)	23.6 [142]
348.15			791.33 (1.0)		2.399 [149]			
353.15			787.63 (1.0)		2.19 (0.02)		22.28 (1.06)	
358.15			783.93 (1.0)					

[a]: Standard uncertainty of temperature measurement: $u(T)_{n_D} = 0.03$ K, $u(T)_\rho = 0.02$ K, $u(T)_\eta = 0.03$ K, $u(T)_\gamma = 0.2$ K

Table 4.3.: Refractive index n_D, density ρ, viscosity η and surface tension γ of decan-1-ol at 101 kPa compared with data from literature (standard uncertainty in brackets). (continued)

T/K [a]	n_D		ρ/(kg/m^3)		η/(mPa · s)		γ/(mN/m)	
	exp.	lit.	exp.	lit.	exp.	lit.	exp.	lit.
363.15			780.17 (1.0)		1.74 (0.01)		21.77 (1.06)	
373.15			772.44 (1.0)		1.41 (0.01)			
383.15			764.7 (1.0)		1.16 (0.01)			
393.15			756.8 (1.0)		0.96 (0.01)			
403.15			748.79 (1.0)		0.8 (0.01)			

[a]: Standard uncertainty of temperature measurement: $u(T)_{n_D} = 0.03$ K, $u(T)_\rho = 0.02$ K, $u(T)_\eta = 0.03$ K, $u(T)_\gamma = 0.2$ K

Table 4.4.: Refractive index n_D, density ρ, viscosity η and surface tension γ of isopropyl alcohol at 101 kPa compared with data from literature (standard uncertainty in brackets).

T/K [a]	n_D		ρ/(kg/m^3)		η/(mPa · s)		γ/(mN/m)	
	exp.	lit.	exp.	lit.	exp.	lit.	exp.	lit.
283.15			795.13 (0.5)		3.31 (0.02)		21.23 (1.03)	
288.15			791.03 (0.5)	780.69				
293.15	1.37741 (0.0008)		786.83 (0.5)	785.28 [148] 781.18 [141]	2.41 (0.01)	2.382 [148] 2.386 [171]	20.4 (1.03)	20.48 [141]
298.15			782.6 (0.48)	780.69 [148] 780.93 [174]		2.070 [172]		20.85 [173]
303.15			778.3 (0.48)	776.15 [148] 776.75 [174] 777.12 [172]	1.78 (0.01)	1.743 [148] 1.763 [171] 1.785 [172]	19.62 (1.03)	19.75 [141]
308.15			773.9 (0.48)	772.88 [172]		1.550 [173] 1.546 [172]		20.05 [173]
313.15			769.47 (0.47)	766.34 [148] 768.79 [172]	1.34 (0.01)	1.288 [148] 1.325 [171] 1.325 [172]	19.19 (1.03)	19.08 [141]
318.15			764.9 (0.48)	763.61 [141] 763.97 [172]		1.176 [171] 1.176 [172]		19.35 [173]
323.15			760.2 (0.48)	755.66 [148] 759.68 [172]	1.03 (0.01)	1.002 [148] 1.033 [172]	18.67 (1.03)	

[a]: Standard uncertainty of temperature measurement: $u(T)_{n_D} = 0.03$ K, $u(T)_\rho = 0.02$ K, $u(T)_\eta = 0.03$ K, $u(T)_\gamma = 0.2$ K

[†]: Value is considered an outlier.

Table 4.4.: Refractive index n_D, density ρ, viscosity η and surface tension γ of isopropyl alcohol at 101 kPa compared with data from literature (standard uncertainty in brackets). (continued)

T/K [a]	n_D		ρ/(kg/m^3)		η/(mPa · s)		γ/(mN/m)	
	exp.	lit.	exp.	lit.	exp.	lit.	exp.	lit.
328.15			755.47 (0.47)	754.84 [141]				
				754.89 [172]		0.914 [172]		
333.15			750.57 (0.47)	745.51 [148]	0.80 (0.01)	0.789 [148]	18.26 (1.03)	
				750.41 [172]		0.811 [172]		
338.15			745.57 (0.47)					
343.15			740.4 (0.48)	735.02 [148]	0.75 (0.01)[†]	0.626 [148]	17.75 (1.04)	

[a]: Standard uncertainty of temperature measurement: $u(T)_{n_D} = 0.03$ K, $u(T)_\rho = 0.02$ K, $u(T)_\eta = 0.03$ K, $u(T)_\gamma = 0.2$ K

[†]: Value is considered an outlier.

Table 4.5.: Refractive index n_D, density ρ, viscosity η and surface tension γ of glycerol at 101 kPa compared with data from literature (standard uncertainty in brackets).

T/K [a]	n_D		ρ/(kg/m^3)		η/(mPa · s)		γ/(mN/m)	
	exp.	lit.	exp.	lit.	exp.	lit.	exp.	lit.
293.15	1.47436 (0.00008)	1.47399 [175]	1260.77 (0.4)	1261.025 [146]	1423.47 (15.71)	1412 [176]	62.51 (1.11)	64 [177]
		1.47301 [146]		1264.40 [178]				63.4 [179]
298.15			1257.7 (0.4)	1257.8 [180]				62.5 [181]
				1257.943 [146]				
303.15			1254.5 (0.4)	1254.7 [180]	605.62 (4.78)	628.9 [180]	60.96 (1.18)	60.94 [177]
			1257.91 [178]			600.83 [146]		62.8 [179]
						612 [176]		
308.15			1251.4 (0.4)	1252.2 [180]				
				1254.83 [146]				
				1251.66 [178]				
313.15			1248.3 (0.4)	1249.4 [180]	285.66 (1.98)	295.9 [180]	60.12 (1.11)	58.92 [177]
						284 [176]		62.2 [179]
318.15			1245.17 (0.4)	1245.8 [180]				
323.15			1241.9 (0.4)	1242.3 [180]	147.77 (0.96)	151.2 [180]	58.86 (1.10)	57.68 [177]
				1242.11 [178]		142 [176]		61.6 [179]
328.15			1238.7 (0.4)	1239.3 [180]				

[a]: Standard uncertainty of temperature measurement: $u(T)_{n_D} = 0.03$ K, $u(T)_\rho = 0.02$ K, $u(T)_\eta = 0.03$ K, $u(T)_\gamma = 0.2$ K

Table 4.5.: Refractive index n_D, density ρ, viscosity η and surface tension γ of glycerol at 101 kPa compared with data from literature (standard uncertainty in brackets). (continued)

T/K [a]	n_D		ρ/(kg/m^3)		η/(mPa · s)		γ/(mN/m)	
	exp.	lit.	exp.	lit.	exp.	lit.	exp.	lit.
333.15			1235.4 (0.4)	1236.1 [180] 1235.71 [178]	82.83 (0.53)	84.8 [180] 81.3 [176]	57.94 (1.09)	
338.15			1232.1 (0.4)	1232.8 [180]				
343.15			1228.8 (0.4)		49.76 (0.31)	50.6 [176]	57.06 (1.09)	
348.15			1225.43 (0.4)	1225.79 [178]				
353.15			1222.07 (0.4)		31.74 (0.20)	31.9 [176]	55.71 (1.10)	59.8 [179]
358.15			1218.63 (0.4)					
363.15			1215.2 (0.4)		21.3 (0.14)	21.3 [176]	54.5 (1.10)	
373.15			1207.75 (0.52)		14.95 (0.08)	14.8 [176]		
383.15			1200.81 (0.51)		10.91 (0.10)			
393.15			1193.78 (0.51)		8.25 (0.08)			
403.15			1186.65 (0.5)		6.42 (0.04)			

[a]: Standard uncertainty of temperature measurement: $u(T)_{n_D} = 0.03$ K, $u(T)_\rho = 0.02$ K, $u(T)_\eta = 0.03$ K, $u(T)_\gamma = 0.2$ K

In general, the measured values are close to values reported in literature, so that the measurement methods used can be considered suitable. Very small standard deviations noted in parentheses indicate high repeatability of the data and support reliability of the obtained values. The comparative measurements of density and refractive index after a time interval of 1 week, 1 month and 6 months resulted mostly in measurements within the standard deviation. Only for the sample with IPA a slight change in the mixture composition was detected, so that here storage at 279 K is recommended if mixtures with IPA are to be stored for longer. The temperature dependence of the analyzed variables density, viscosity and surface tension is explained in more detail below.

4.3.1.1. Density

The dependence of the measured density values for the the studied systems as given in Table 4.2 - Table 4.5 is graphically illustrated in Figure 4.2. For the estimation of the density values as a function of temperature the parameters of Equation 4.2 were adjusted to fit the experimental values. The values of the determined parameters are summarized in Table 4.6 and the estimated values are compared with the experimental values for the different material systems in Figure 4.2.

Overall, very good agreement was achieved between the calculated and experimental values, which is reflected by the low deviation between experimental and estimated values as well as in very high values for the coefficient of determination with $R^2 \geq 0.9999$ in Table 4.6.

Table 4.6.: Parameters of Equation 4.2 for the calculation of the density of DEG, decan-1-ol, IPA and glycerol in dependence of the temperature.

	$A/(\mathrm{kg/m^3})$	$B/1$	C/K	$D/1$	R^2
DEG	0.64861	0.022353	827.59	0.092474	0.99999
decan-1-ol	1.4198	0.037782	678.26	0.10054	0.99999
IPA	400.87	0.63945	405.00	0.52593	0.99999
glycerol	783.35	0.74328	510.01	0.58965	0.99992

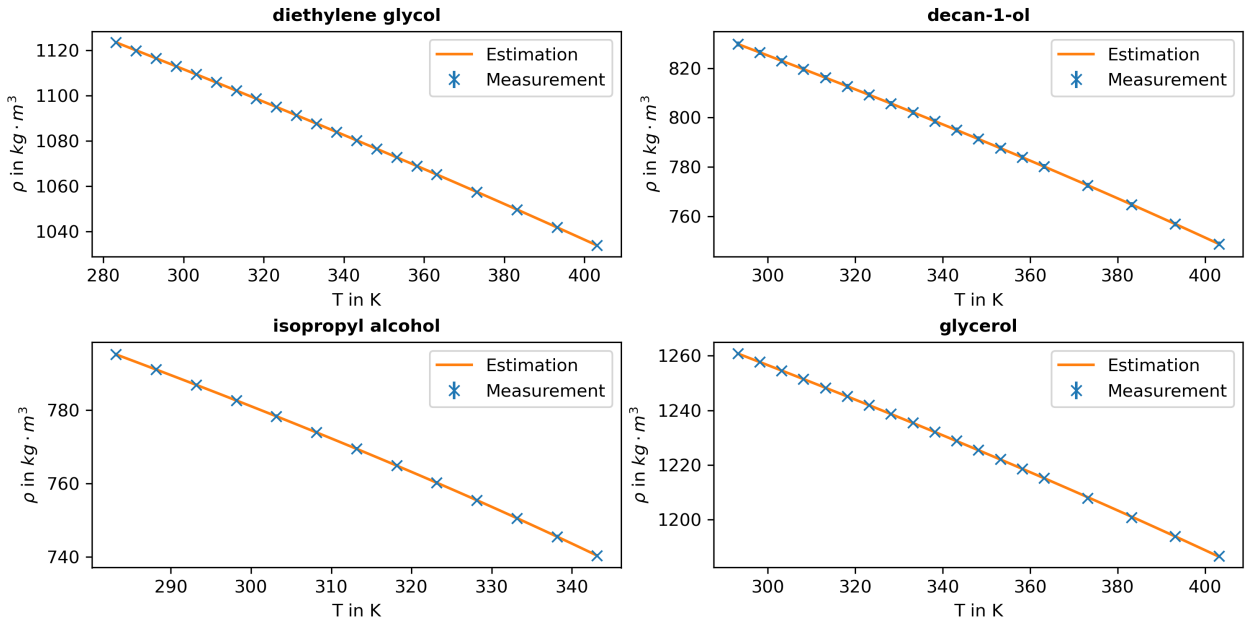

Figure 4.2.: Measured and calculated density of DEG, decan-1-ol, IPA and glycerol in dependence of the temperature.

4.3.1.2. Viscosity

The values for the experimentally determined viscosity for the different components can be found in Table 4.2 - Table 4.5. The parameters of Equation 4.5 to estimate the temperature dependence were adjusted using the experimental data and the determined parameters are presented in Table 4.7. The values calculated with these parameters are compared with the experimental data in Figure 4.3. High regression coefficients of $R^2 \geq 0.999$ were achieved and the temperature dependence can be described well using the determined parameters in combination with Equation 4.5.

Table 4.7.: Parameters of Equation 4.5 for the calculation of the viscosity of DEG, decan-1-ol, IPA and glycerol in dependence of the temperature.

	$A/1$	B/K	$C/\mathrm{K^{-1}}$	$D/\mathrm{K^{-2}}$	R^2
DEG	$-7.858 \cdot 10^1$	$1.229 \cdot 10^4$	$1.816 \cdot 10^{-1}$	$-1.512 \cdot 10^{-4}$	0.9999
decan-1-ol	$-3.073 \cdot 10^1$	$6.115 \cdot 10^3$	$5.527 \cdot 10^{-2}$	$-4.267 \cdot 10^{-5}$	0.9999
IPA	$3.971 \cdot 10^2$	$-3.868 \cdot 10^4$	-1.323	$1.4375 \cdot 10^{-3}$	0.9991
glycerol	$-1.1402 \cdot 10^2$	$1.942 \cdot 10^4$	$2.404 \cdot 10^{-1}$	$-1.799 \cdot 10^{-4}$	0.9999

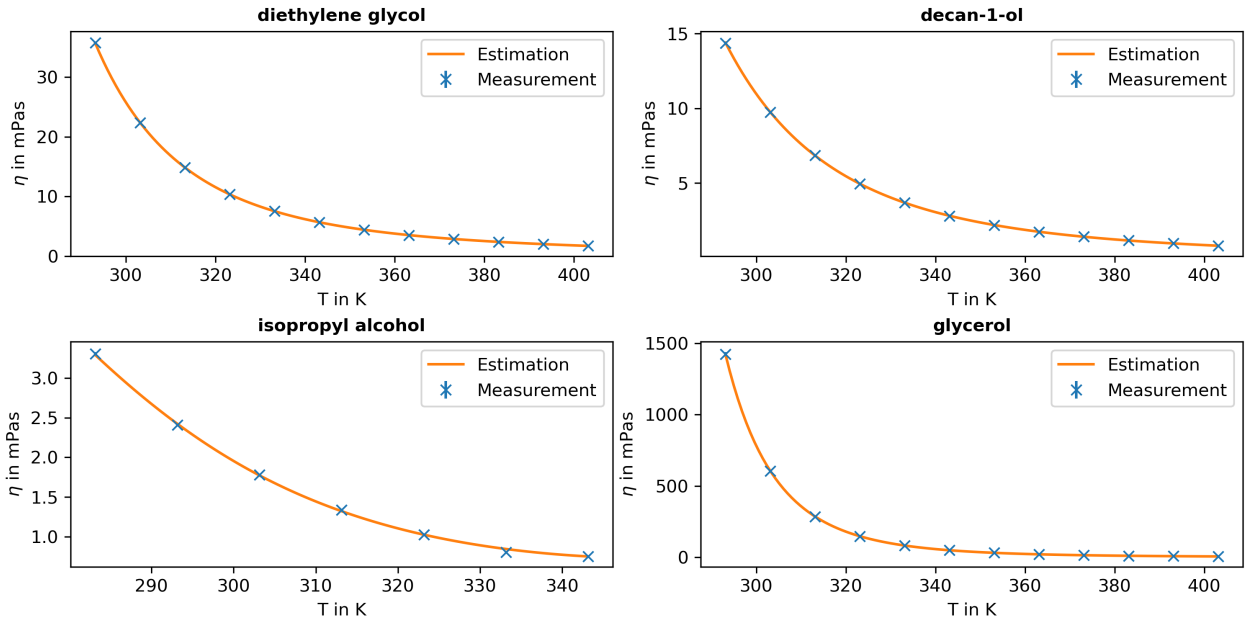

Figure 4.3.: Measured and calculated viscosity of DEG, decan-1-ol, IPA and glycerol in dependence of the temperature.

4.3.1.3. Surface Tension

The values of the measured surface tension of the pure components are also displayed in Table 4.2 - Table 4.5. To calculate the surface tension as a function of temperature, the parameters of Equation 4.7 were fitted to the experimental data. The parameters determined and the coefficient of determination resulting from the fit are summarized in Table 4.8. It can be seen that the values for the resulting coefficients of determination with $R^2 \geq 0.978$ are still quite high, but also clearly lower than for the density and viscosity. The larger deviations can also be seen in Figure 4.4, in which the experimental data of the surface tension are compared with the calculated values. There is a significantly greater experimental scatter of the measured values, which leads to increased deviations from the calculated values and therefore a smaller coefficient of determination.

Table 4.8.: Parameters of Equation 4.7 for the calculation of the surface tension of DEG, decan-1-ol, IPA and glycerol in dependence of the temperature.

	$A/(\mathrm{mN/m})$	$B/1$	R^2
DEG	63.80	0.8206	0.985
decan-1-ol	52.02	1.1623	0.991
IPA	36.67	0.6766	0.978
glycerol	94.16	0.9748	0.996

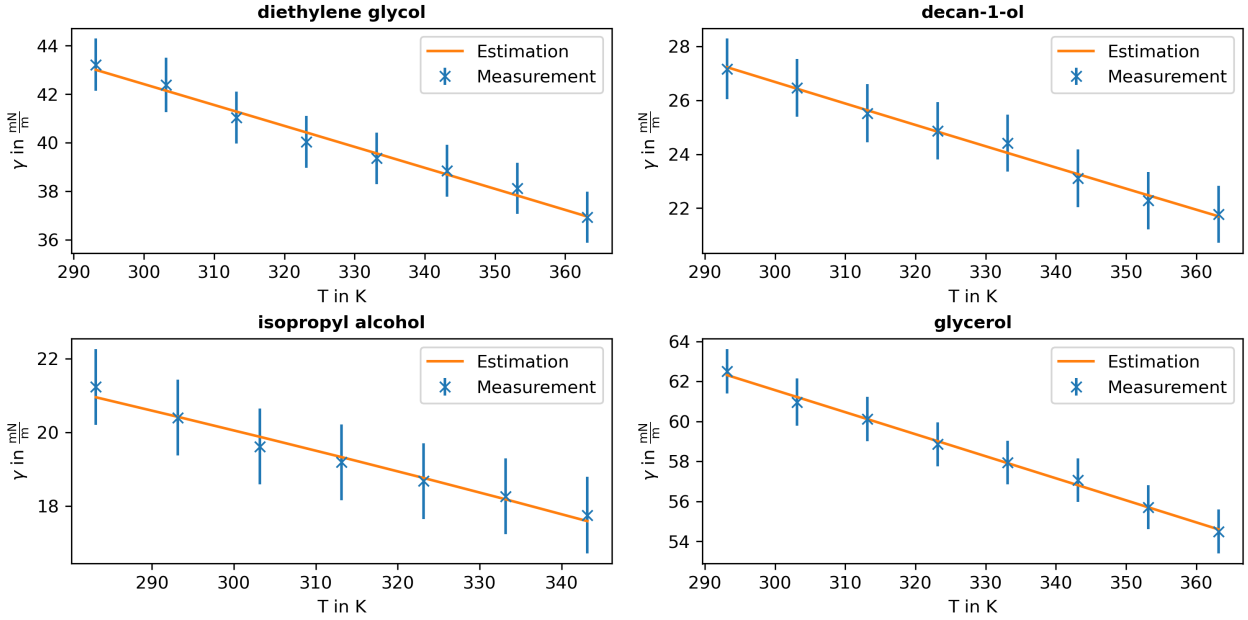

Figure 4.4.: Measured and calculated surface tension of DEG, decan-1-ol, IPA and glycerol in dependence of the temperature.

4.3.2. Experimental Data of Binary Mixtures

4.3.2.1. Density

The densities of all investigated systems depending on composition and temperature are listed in Table 4.9 and illustrated in Figure 4.5. The estimated values were determined using the procedure described in subsection 4.3.3.

Table 4.9.: Density of all studied systems at the investigated temperatures at 101 kPa (standard uncertainty in brackets).

T/K [a]	x_1 [b]	ρ/(kg· m^{-3})	x_1 [b]	ρ/(kg· m^{-3})	x_1 [b]	ρ/(kg· m^{-3})
diethylene glycol (1) - decan-1-ol (2)						
293.15	0.0835	841.47 (1.04)	0.417	901.93 (1.0)	0.7501	998.47 (1.02)
	0.1672	854.3 (1.01)	0.5002	921.77 (1.0)	0.8333	1031.37 (1.0)
	0.2511	868.4 (1.01)	0.5836	944.07 (1.0)	0.9165	1070.4 (1.0)
	0.3333	884.27 (1.02)	0.6666	969.5 (1.04)		
298.15	0.0835	838.13 (1.03)	0.417	898.47 (1.0)	0.7501	994.93 (1.03)
	0.1672	850.9 (1.01)	0.5002	918.3 (1.0)	0.8333	1027.83 (1.0)
	0.2511	864.97 (1.02)	0.5836	940.57 (1.0)	0.9165	1066.83 (1.0)
	0.3333	880.83 (1.03)	0.6666	965.97 (1.03)		
303.15	0.0835	834.67 (1.04)	0.417	895.0 (1.0)	0.7501	991.37 (1.02)
	0.1672	847.5 (1.01)	0.5002	914.77 (1.0)	0.8333	1024.27 (1.0)
	0.2511	861.5 (1.01)	0.5836	936.97 (1.0)	0.9165	1063.27 (1.0)
	0.3333	877.37 (1.02)	0.6666	962.4 (1.04)		
308.15	0.0835	831.23 (1.03)	0.417	891.5 (1.0)	0.7501	987.77 (1.02)
	0.1672	844.0 (1.01)	0.5002	911.23 (1.0)	0.8333	1020.67 (1.0)
	0.2511	858.07 (1.02)	0.5836	933.47 (1.0)	0.9165	1059.7 (1.0)
	0.3333	873.87 (1.02)	0.6666	958.87 (1.03)		
313.15	0.0835	827.83 (1.03)	0.417	887.97 (1.0)	0.7501	984.2 (1.01)
	0.1672	840.6 (1.01)	0.5002	907.7 (1.0)	0.8333	1017.07 (1.0)

[a]: Standard uncertainty of temperature measurement: $u(T) = 0.02$ K

[b]: Standard uncertainty of mole fraction: $u(x) = 0.0013$

[†]: Value is an outlier.

Table 4.9.: Density of all studied systems at the investigated temperatures at 101 kPa (standard uncertainty in brackets). (continued)

T/K [a]	x_1 [b]	ρ/(kg· m^{-3})	x_1 [b]	ρ/(kg· m^{-3})	x_1 [b]	ρ/(kg· m^{-3})
	0.2511	854.6 (1.01)	0.5836	929.87 (1.0)	0.9165	1056.1 (1.0)
	0.3333	870.37 (1.02)	0.6666	955.27 (1.03)		
318.15	0.0835	824.33 (1.03)	0.417	884.43 (1.0)	0.7501	980.6 (1.01)
	0.1672	837.1 (1.01)	0.5002	904.13 (1.0)	0.8333	1013.47 (1.0)
	0.2511	851.1 (1.01)	0.5836	926.33 (1.01)	0.9165	1052.5 (1.0)
	0.3333	866.87 (1.02)	0.6666	951.67 (1.03)		
323.15	0.0835	820.83 (1.03)	0.417	880.93 (1.0)	0.7501	976.93 (1.01)
	0.1672	833.6 (1.01)	0.5002	900.6 (1.0)	0.8333	1009.83 (1.0)
	0.2511	847.6 (1.01)	0.5836	922.77 (1.0)	0.9165	1048.83 (1.0)
	0.3333	863.3 (1.01)	0.6666	948.07 (1.03)		
328.15	0.0835	817.33 (1.03)	0.417	877.33 (1.0)	0.7501	973.3 (1.01)
	0.1672	830.1 (1.01)	0.5002	897.0 (1.0)	0.8333	1006.17 (1.0)
	0.2511	844.03 (1.01)	0.5836	919.1 (1.0)	0.9165	1045.2 (1.0)
	0.3333	859.77 (1.02)	0.6666	944.4 (1.02)		
333.15	0.0835	813.8 (1.01)	0.417	873.73 (1.0)	0.7501	969.63 (1.01)
	0.1672	826.5 (1.01)	0.5002	893.37 (1.0)	0.8333	1002.47 (1.0)
	0.2511	840.5 (1.01)	0.5836	915.47 (1.0)	0.9165	1041.53 (1.0)
	0.3333	856.2 (1.01)	0.6666	940.77 (1.03)		
338.15	0.0835	810.2 (1.01)	0.417	870.13 (1.0)	0.7501	965.93 (1.01)
	0.1672	822.93 (1.01)	0.5002	889.73 (1.0)	0.8333	998.83 (1.0)
	0.2511	836.9 (1.01)	0.5836	911.87 (1.0)	0.9165	1037.83 (1.0)
	0.3333	852.6 (1.01)	0.6666	937.07 (1.03)		
343.15	0.0835	806.6 (1.01)	0.417	866.43 (1.0)	0.7501	962.23 (1.01)
	0.1672	819.3 (1.01)	0.5002	886.03 (1.0)	0.8333	995.07 (1.0)
	0.2511	833.27 (1.01)	0.5836	908.17 (1.0)	0.9165	1034.13 (1.0)
	0.3333	848.93 (1.01)	0.6666	933.37 (1.03)		
348.15	0.0835	802.9 (1.01)	0.417	862.73 (1.0)	0.7501	958.5 (1.01)
	0.1672	815.67 (1.01)	0.5002	882.33 (1.0)	0.8333	991.37 (1.0)
	0.2511	829.6 (1.01)	0.5836	904.47 (1.0)	0.9165	1030.43 (1.0)
	0.3333	845.3 (1.01)	0.6666	929.67 (1.03)		
353.15	0.0835	799.3 (1.01)	0.417	859.03 (1.0)	0.7501	954.73 (1.01)
	0.1672	811.97 (1.01)	0.5002	878.63 (1.0)	0.8333	987.57 (1.0)
	0.2511	825.9 (1.01)	0.5836	900.67 (1.0)	0.9165	1026.63 (1.0)
	0.3333	841.6 (1.01)	0.6666	925.9 (1.02)		
358.15	0.0835	795.57 (1.01)	0.417	855.33 (1.0)	0.7501	950.93 (1.01)
	0.1672	808.27 (1.01)	0.5002	874.9 (1.0)	0.8333	983.77 (1.0)
	0.2511	822.17 (1.01)	0.5836	896.93 (1.0)	0.9165	1022.83 (1.0)
	0.3333	837.83 (1.01)	0.6666	922.1 (1.02)		
363.15	0.0835	791.8 (1.01)	0.417	851.53 (1.0)	0.7501	947.1 (1.01)
	0.1672	804.53 (1.01)	0.5002	871.1 (1.0)	0.8333	979.97 (1.0)
	0.2511	818.43 (1.01)	0.5836	893.13 (1.0)	0.9165	1019.03 (1.0)
	0.3333	834.07 (1.01)	0.6666	918.3 (1.02)		
373.15	0.0835	788.1 (3.71)[†]	0.417	843.72 (1.0)	0.7501	939.09 (1.0)
	0.1672	796.72 (1.0)	0.5002	863.22 (1.0)	0.8333	972.03 (1.0)
	0.2511	810.61 (1.0)	0.5836	885.18 (1.0)	0.9165	1011.2 (1.0)
	0.3333	826.22 (1.0)	0.6666	910.24 (1.01)		
383.15	0.0835	776.43 (1.01)	0.417	835.96 (1.0)	0.7501	931.32 (1.0)
	0.1672	789.01 (1.0)	0.5002	855.44 (1.0)	0.8333	964.24 (1.0)
	0.2511	802.88 (1.0)	0.5836	877.41 (1.01)	0.9165	1003.44 (1.0)
	0.3333	818.46 (1.0)	0.6666	902.38 (1.0)		
393.15	0.0835	768.38 (1.0)	0.417	828.06 (1.0)	0.7501	923.37 (1.0)
	0.1672	781.13 (1.0)	0.5002	847.53 (1.0)	0.8333	956.32 (1.0)
	0.2511	795.06 (1.01)	0.5836	869.45 (1.0)	0.9165	995.6 (1.0)

[a]: Standard uncertainty of temperature measurement: $u(T) = 0.02$ K

[b]: Standard uncertainty of mole fraction: $u(x) = 0.0013$

[†]: Value is an outlier.

Table 4.9.: Density of all studied systems at the investigated temperatures at 101 kPa (standard uncertainty in brackets). (continued)

T/K [a]	x_1 [b]	ρ/(kg· m^{-3})	x_1 [b]	ρ/(kg· m^{-3})	x_1 [b]	ρ/(kg· m^{-3})
	0.3333	810.54 (1.0)	0.6666	894.43 (1.0)		
403.15	0.0835	760.33 (1.0)	0.417	820.0 (1.0)	0.7501	915.32 (1.0)
	0.1672	773.05 (1.0)	0.5002	839.43 (1.0)	0.8333	948.31 (1.0)
	0.2511	786.93 (1.0)	0.5836	861.41 (1.0)	0.9165	987.58 (1.0)
	0.3333	802.54 (1.0)	0.6666	886.4 (1.0)		
diethylene glycol (1) - isopropyl alcohol (2)						
283.15	0.0834	828.4 (0.4)	0.4166	954.05 (0.41)	0.7573	1059.85 (0.41)
	0.1667	862.1 (0.4)	0.5	981.7 (0.4)	0.8333	1080.65 (0.41)
	0.25	894.1 (0.4)	0.5834	1008.45 (0.41)	0.9164	1102.7 (0.4)
	0.3334	924.55 (0.45)	0.6665	1033.8 (0.4)		
288.15	0.0834	824.4 (0.4)	0.4166	950.2 (0.4)	0.7573	1056.2 (0.4)
	0.1667	858.1 (0.4)	0.5	977.95 (0.41)	0.8333	1077.0 (0.4)
	0.25	890.2 (0.4)	0.5834	1004.7 (0.4)	0.9164	1099.1 (0.4)
	0.3334	920.75 (0.45)	0.6665	1030.1 (0.4)		
293.15	0.0834	820.3 (0.4)	0.4166	946.4 (0.4)	0.7573	1052.55 (0.41)
	0.1667	854.1 (0.4)	0.5	974.2 (0.4)	0.8333	1073.4 (0.4)
	0.25	886.2 (0.4)	0.5834	1000.95 (0.41)	0.9164	1095.5 (0.4)
	0.3334	916.85 (0.45)	0.6665	1026.4 (0.4)		
298.15	0.0834	816.2 (0.4)	0.4166	942.55 (0.41)	0.7573	1048.9 (0.4)
	0.1667	850.1 (0.4)	0.5	970.4 (0.4)	0.8333	1069.8 (0.4)
	0.25	882.2 (0.4)	0.5834	997.2 (0.4)	0.9164	1091.9 (0.4)
	0.3334	912.95 (0.45)	0.6665	1022.7 (0.4)		
303.15	0.0834	812.0 (0.4)	0.4166	938.65 (0.41)	0.7573	1045.2 (0.4)
	0.1667	846.0 (0.4)	0.5	966.55 (0.41)	0.8333	1066.1 (0.4)
	0.25	878.2 (0.4)	0.5834	993.45 (0.41)	0.9164	1088.3 (0.4)
	0.3334	908.95 (0.45)	0.6665	1019.0 (0.4)		
308.15	0.0834	807.8 (0.4)	0.4166	934.75 (0.41)	0.7573	1041.5 (0.4)
	0.1667	841.8 (0.4)	0.5	962.7 (0.4)	0.8333	1062.5 (0.4)
	0.25	874.2 (0.4)	0.5834	989.65 (0.41)	0.9164	1084.7 (0.4)
	0.3334	905.05 (0.45)	0.6665	1015.25 (0.41)		
313.15	0.0834	803.5 (0.4)	0.4166	930.8 (0.4)	0.7573	1037.8 (0.4)
	0.1667	837.7 (0.4)	0.5	958.8 (0.4)	0.8333	1058.8 (0.4)
	0.25	870.1 (0.4)	0.5834	985.85 (0.41)	0.9164	1081.1 (0.4)
	0.3334	901.0 (0.49)	0.6665	1011.5 (0.4)		
318.15	0.0834	799.1 (0.4)	0.4166	926.85 (0.41)	0.7573	1034.05 (0.41)
	0.1667	833.4 (0.4)	0.5	954.95 (0.41)	0.8333	1055.1 (0.4)
	0.25	865.9 (0.4)	0.5834	982.0 (0.4)	0.9164	1077.4 (0.4)
	0.3334	896.95 (0.45)	0.6665	1007.7 (0.4)		
323.15	0.0834	794.65 (0.41)	0.4166	922.8 (0.4)	0.7573	1030.3 (0.4)
	0.1667	829.1 (0.4)	0.5	951.0 (0.4)	0.8333	1051.4 (0.4)
	0.25	861.7 (0.4)	0.5834	978.15 (0.41)	0.9164	1073.75 (0.41)
	0.3334	892.85 (0.45)	0.6665	1003.9 (0.4)		
328.15	0.0834	790.1 (0.4)	0.4166	918.75 (0.41)	0.7573	1026.5 (0.4)
	0.1667	824.7 (0.4)	0.5	947.0 (0.4)	0.8333	1047.7 (0.4)
	0.25	857.5 (0.4)	0.5834	974.25 (0.41)	0.9164	1070.1 (0.4)
	0.3334	888.7 (0.49)	0.6665	1000.05 (0.41)		
333.15	0.0834	785.45 (0.41)	0.4166	914.65 (0.41)	0.7573	1022.7 (0.4)
	0.1667	820.2 (0.4)	0.5	943.0 (0.4)	0.8333	1043.9 (0.4)
	0.25	853.1 (0.4)	0.5834	970.3 (0.4)	0.9164	1066.35 (0.41)
	0.3334	884.45 (0.45)	0.6665	996.2 (0.4)		
338.15	0.0834	780.7 (0.4)	0.4166	910.5 (0.4)	0.7573	1018.9 (0.4)
	0.1667	815.7 (0.4)	0.5	939.0 (0.4)	0.8333	1040.2 (0.4)
	0.25	848.7 (0.4)	0.5834	966.35 (0.41)	0.9164	1062.6 (0.4)

[a]: Standard uncertainty of temperature measurement: $u(T) = 0.02$ K

[b]: Standard uncertainty of mole fraction: $u(x) = 0.0013$

[†]: Value is an outlier.

Table 4.9.: Density of all studied systems at the investigated temperatures at 101 kPa (standard uncertainty in brackets). (continued)

T/K [a]	x_1 [b]	ρ/(kg· m^{-3})	x_1 [b]	ρ/(kg· m^{-3})	x_1 [b]	ρ/(kg· m^{-3})
	0.3334	880.25 (0.45)	0.6665	992.3 (0.4)		
343.15	0.0834	775.8 (0.4)	0.4166	906.3 (0.4)	0.7573	1015.0 (0.4)
	0.1667	811.0 (0.4)	0.5	934.85 (0.41)	0.8333	1036.3 (0.4)
	0.25	844.3 (0.4)	0.5834	962.3 (0.4)	0.9164	1058.9 (0.4)
diethylene glycol (1) - glycerol (2)						
293.15	0.0833	1246.6 (0.4)	0.4167	1194.3 (0.4)	0.7497	1148.1 (0.4)
	0.1666	1232.8 (0.4)	0.5	1182.2 (0.4)	0.8333	1137.3 (0.4)
	0.2487	1219.7 (0.4)	0.5833	1170.5 (0.4)	0.9165	1126.8 (0.4)
	0.3332	1206.8 (0.4)	0.6665	1159.1 (0.4)		
298.15	0.0833	1243.4 (0.4)	0.4167	1191.0 (0.4)	0.7497	1144.57 (0.4)
	0.1666	1229.7 (0.4)	0.5	1178.8 (0.4)	0.8333	1133.73 (0.4)
	0.2487	1216.5 (0.4)	0.5833	1167.0 (0.4)	0.9165	1123.3 (0.4)
	0.3332	1203.5 (0.4)	0.6665	1155.6 (0.4)		
303.15	0.0833	1240.3 (0.4)	0.4167	1187.6 (0.4)	0.7497	1141.0 (0.4)
	0.1666	1226.5 (0.4)	0.5	1175.4 (0.4)	0.8333	1130.2 (0.4)
	0.2487	1213.2 (0.4)	0.5833	1163.5 (0.4)	0.9165	1119.7 (0.4)
	0.3332	1200.2 (0.4)	0.6665	1152.1 (0.4)		
308.15	0.0833	1237.1 (0.4)	0.4167	1184.2 (0.4)	0.7497	1137.5 (0.4)
	0.1666	1223.2 (0.4)	0.5	1171.9 (0.4)	0.8333	1126.6 (0.4)
	0.2487	1209.9 (0.4)	0.5833	1160.03 (0.4)	0.9165	1116.2 (0.4)
	0.3332	1196.8 (0.4)	0.6665	1148.6 (0.4)		
313.15	0.0833	1233.9 (0.4)	0.4167	1180.7 (0.4)	0.7497	1133.9 (0.4)
	0.1666	1220.0 (0.4)	0.5	1168.4 (0.4)	0.8333	1123.1 (0.4)
	0.2487	1206.6 (0.4)	0.5833	1156.5 (0.4)	0.9165	1112.6 (0.4)
	0.3332	1193.4 (0.4)	0.6665	1145.0 (0.4)		
318.15	0.0833	1230.7 (0.4)	0.4167	1177.3 (0.4)	0.7497	1130.3 (0.4)
	0.1666	1216.7 (0.4)	0.5	1165.0 (0.4)	0.8333	1119.5 (0.4)
	0.2487	1203.2 (0.4)	0.5833	1153.0 (0.4)	0.9165	1109.0 (0.4)
	0.3332	1190.0 (0.4)	0.6665	1141.5 (0.4)		
323.15	0.0833	1227.4 (0.4)	0.4167	1173.8 (0.4)	0.7497	1126.77 (0.4)
	0.1666	1213.3 (0.4)	0.5	1161.5 (0.4)	0.8333	1115.9 (0.4)
	0.2487	1199.8 (0.4)	0.5833	1149.5 (0.4)	0.9165	1105.3 (0.4)
	0.3332	1186.6 (0.4)	0.6665	1137.9 (0.4)		
328.15	0.0833	1224.1 (0.4)	0.4167	1170.3 (0.4)	0.7497	1123.1 (0.4)
	0.1666	1210.0 (0.4)	0.5	1157.9 (0.4)	0.8333	1112.2 (0.4)
	0.2487	1196.4 (0.4)	0.5833	1145.9 (0.4)	0.9165	1101.7 (0.4)
	0.3332	1183.1 (0.4)	0.6665	1134.3 (0.4)		
333.15	0.0833	1220.8 (0.4)	0.4167	1166.8 (0.4)	0.7497	1119.5 (0.4)
	0.1666	1206.6 (0.4)	0.5	1154.4 (0.4)	0.8333	1108.6 (0.4)
	0.2487	1193.0 (0.4)	0.5833	1142.37 (0.4)	0.9165	1098.0 (0.4)
	0.3332	1179.7 (0.4)	0.6665	1130.7 (0.4)		
338.15	0.0833	1217.4 (0.4)	0.4167	1163.3 (0.4)	0.7497	1115.9 (0.4)
	0.1666	1203.2 (0.4)	0.5	1150.8 (0.4)	0.8333	1104.9 (0.4)
	0.2487	1189.5 (0.4)	0.5833	1138.8 (0.4)	0.9165	1094.37 (0.4)
	0.3332	1176.2 (0.4)	0.6665	1127.1 (0.4)		
343.15	0.0833	1214.0 (0.4)	0.4167	1159.7 (0.4)	0.7497	1112.2 (0.4)
	0.1666	1199.7 (0.4)	0.5	1147.2 (0.4)	0.8333	1101.2 (0.4)
	0.2487	1186.1 (0.4)	0.5833	1135.1 (0.4)	0.9165	1090.67 (0.4)
	0.3332	1172.6 (0.4)	0.6665	1123.5 (0.4)		
348.15	0.0833	1210.6 (0.4)	0.4167	1156.1 (0.4)	0.7497	1108.5 (0.4)
	0.1666	1196.3 (0.4)	0.5	1143.6 (0.4)	0.8333	1097.5 (0.4)
	0.2487	1182.6 (0.4)	0.5833	1131.5 (0.4)	0.9165	1086.9 (0.4)
	0.3332	1169.1 (0.4)	0.6665	1119.8 (0.4)		

[a]: Standard uncertainty of temperature measurement: $u(T) = 0.02$ K

[b]: Standard uncertainty of mole fraction: $u(x) = 0.0013$

[†]: Value is an outlier.

Table 4.9.: Density of all studied systems at the investigated temperatures at 101 kPa (standard uncertainty in brackets). (continued)

T/K [a]	x_1 [b]	ρ/(kg· m^{-3})	x_1 [b]	ρ/(kg· m^{-3})	x_1 [b]	ρ/(kg· m^{-3})
353.15	0.0833	1207.2 (0.4)	0.4167	1152.5 (0.4)	0.7497	1104.8 (0.4)
	0.1666	1192.8 (0.4)	0.5	1140.0 (0.4)	0.8333	1093.8 (0.4)
	0.2487	1179.0 (0.4)	0.5833	1127.8 (0.4)	0.9165	1083.2 (0.4)
	0.3332	1165.5 (0.4)	0.6665	1116.1 (0.4)		
358.15	0.0833	1203.7 (0.4)	0.4167	1148.9 (0.4)	0.7497	1101.0 (0.4)
	0.1666	1189.3 (0.4)	0.5	1136.3 (0.4)	0.8333	1090.0 (0.4)
	0.2487	1175.5 (0.4)	0.5833	1124.1 (0.4)	0.9165	1079.4 (0.4)
	0.3332	1161.9 (0.4)	0.6665	1112.33 (0.4)		
363.15	0.0833	1200.2 (0.4)	0.4167	1145.2 (0.4)	0.7497	1097.2 (0.4)
	0.1666	1185.7 (0.4)	0.5	1132.6 (0.4)	0.8333	1086.2 (0.4)
	0.2487	1171.9 (0.4)	0.5833	1120.4 (0.4)	0.9165	1075.6 (0.4)
	0.3332	1158.3 (0.4)	0.6665	1108.6 (0.4)		
373.15	0.0833	1192.96 (0.42)	0.4167	1137.51 (0.42)	0.7497	1089.39 (0.41)
	0.1666	1178.66 (0.41)	0.5	1124.73 (0.45)	0.8333	1078.35 (0.4)
	0.2487	1164.13 (0.44)	0.5833	1112.71 (0.41)	0.9165	1067.6 (0.42)
	0.3332	1150.62 (0.54)	0.6665	1100.76 (0.41)		
383.15	0.0833	1185.96 (0.43)	0.4167	1130.1 (0.42)	0.7497	1081.77 (0.41)
	0.1666	1171.5 (0.41)	0.5	1117.26 (0.45)	0.8333	1070.68 (0.4)
	0.2487	1156.88 (0.43)	0.5833	1105.2 (0.42)	0.9165	1059.9 (0.42)
	0.3332	1143.32 (0.5)	0.6665	1093.18 (0.41)		
393.15	0.0833	1178.7 (0.42)	0.4167	1122.59 (0.42)	0.7497	1074.03 (0.41)
	0.1666	1164.23 (0.4)	0.5	1109.69 (0.45)	0.8333	1062.98 (0.4)
	0.2487	1149.53 (0.43)	0.5833	1097.57 (0.41)	0.9165	1052.14 (0.43)
	0.3332	1135.93 (0.46)	0.6665	1085.51 (0.41)		
403.15	0.0833	1171.44 (0.42)	0.4167	1115.0 (0.42)	0.7497	1066.29 (0.42)
	0.1666	1156.91 (0.4)	0.5	1102.05 (0.46)	0.8333	1055.06 (0.41)
	0.2487	1142.1 (0.44)	0.5833	1089.87 (0.42)	0.9165	1044.22 (0.42)
	0.3332	1128.47 (0.43)	0.6665	1077.79 (0.41)		

a: Standard uncertainty of temperature measurement: $u(T) = 0.02$ K

b: Standard uncertainty of mole fraction: $u(x) = 0.0013$

†: Value is an outlier.

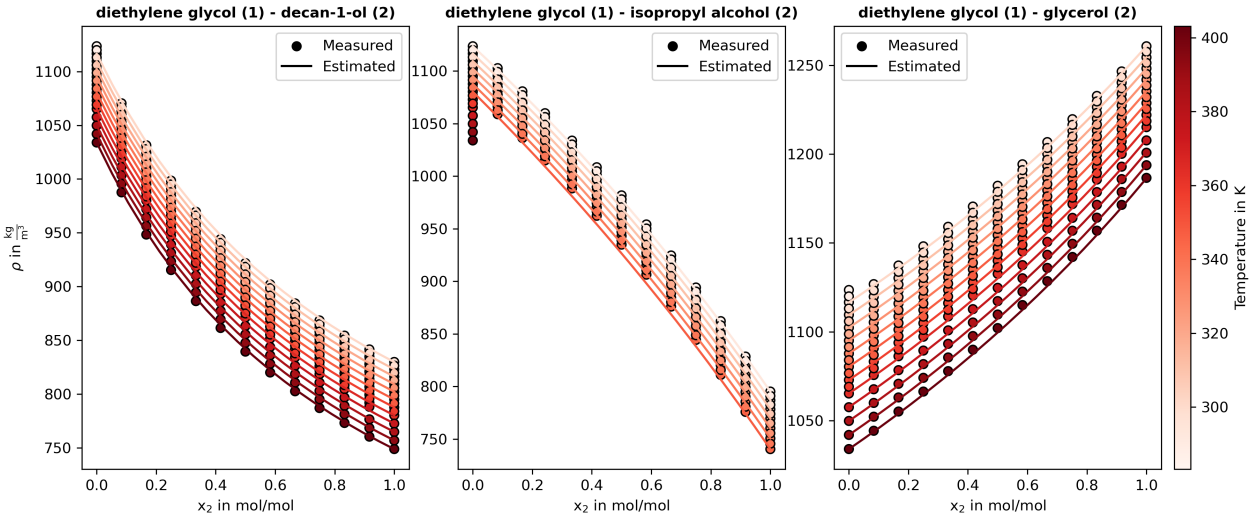

Figure 4.5.: Measured values and estimated density values for the studied systems and temperatures.

4.3.2.2. Viscosity

The measured values of the viscosity depending on the mixture composition as well as the temperature for the investigated systems are listed in Table 4.10 and illustrated in Figure 4.6. The estimated values were calculated using the method described in subsection 4.3.3.

Table 4.10.: Viscosity of all studied systems at the investigated temperatures at 101 kPa (standard uncertainty in brackets).

T/K[a]	x_1[b]	η/(mPa · s)	x_1	η/(mPa · s)	x_1[b]	η/(mPa · s)
diethylene glycol (1) - decan-1-ol (2)						
293.15	0.0835	14.76 (0.09)	0.417	18.13 (0.11)	0.7501	26.36 (0.16)
	0.1672	15.21 (0.11)	0.5002	19.72 (0.15)	0.8333	28.85 (0.21)
	0.2511	15.98 (0.12)	0.5836	21.69 (0.14)	0.9165	31.43 (0.22)
	0.3333	16.97 (0.11)	0.6666	23.81 (0.2)		
303.15	0.0835	10.06 (0.06)	0.417	12.26 (0.07)	0.7501	17.08 (0.1)
	0.1672	10.41 (0.06)	0.5002	13.21 (0.08)	0.8333	18.53 (0.12)
	0.2511	10.9 (0.07)	0.5836	14.36 (0.09)	0.9165	19.98 (0.13)
	0.3333	11.51 (0.07)	0.6666	15.62 (0.11)		
313.15	0.0835	7.09 (0.04)	0.417	8.59 (0.05)	0.7501	11.63 (0.07)
	0.1672	7.35 (0.04)	0.5002	9.2 (0.06)	0.8333	12.52 (0.08)
	0.2511	7.68 (0.05)	0.5836	9.92 (0.06)	0.9165	13.41 (0.08)
	0.3333	8.09 (0.05)	0.6666	10.72 (0.07)		
323.15	0.0835	5.15 (0.03)	0.417	6.22 (0.04)	0.7501	8.25 (0.05)
	0.1672	5.35 (0.03)	0.5002	6.64 (0.04)	0.8333	8.84 (0.05)
	0.2511	5.59 (0.03)	0.5836	7.12 (0.04)	0.9165	9.43 (0.06)
	0.3333	5.88 (0.04)	0.6666	7.66 (0.05)		
333.15	0.0835	3.85 (0.02)	0.417	4.64 (0.03)	0.7501	6.07 (0.04)
	0.1672	4.0 (0.02)	0.5002	4.94 (0.03)	0.8333	6.48 (0.04)
	0.2511	4.18 (0.03)	0.5836	5.28 (0.03)	0.9165	6.9 (0.04)
	0.3333	4.39 (0.03)	0.6666	5.66 (0.04)		
343.15	0.0835	2.94 (0.02)	0.417	3.55 (0.02)	0.7501	4.61 (0.03)
	0.1672	3.06 (0.02)	0.5002	3.77 (0.02)	0.8333	4.91 (0.03)
	0.2511	3.2 (0.02)	0.5836	4.03 (0.02)	0.9165	5.22 (0.03)
	0.3333	3.36 (0.02)	0.6666	4.3 (0.03)		
353.15	0.0835	2.3 (0.01)	0.417	2.78 (0.02)	0.7501	3.59 (0.02)

[a]: Standard uncertainty of temperature measurement: $u(T) = 0.03$ K

[b]: Standard uncertainty of mole fraction: $u(x) = 0.0013$

Table 4.10.: Viscosity of all studied systems at the investigated temperatures at 101 kPa (standard uncertainty in brackets). (continued)

T/K[a]	x_1[b]	η/(mPa · s)	x_1[b]	η/(mPa · s)	x_1[b]	η/(mPa · s)
	0.1672	2.39 (0.01)	0.5002	2.95 (0.02)	0.8333	3.81 (0.02)
	0.2511	2.51 (0.02)	0.5836	3.15 (0.02)	0.9165	4.06 (0.02)
	0.3333	2.63 (0.02)	0.6666	3.35 (0.02)		
363.15	0.0835	1.84 (0.01)	0.417	2.22 (0.01)	0.7501	2.86 (0.02)
	0.1672	1.91 (0.01)	0.5002	2.36 (0.01)	0.8333	3.04 (0.02)
	0.2511	2.0 (0.01)	0.5836	2.51 (0.02)	0.9165	3.24 (0.02)
	0.3333	2.1 (0.01)	0.6666	2.67 (0.02)		
373.15	0.0835	1.49 (0.01)	0.417	1.81 (0.01)	0.7501	2.32 (0.01)
	0.1672	1.55 (0.01)	0.5002	1.92 (0.01)	0.8333	2.47 (0.02)
	0.2511	1.63 (0.01)	0.5836	2.04 (0.01)	0.9165	2.64 (0.02)
	0.3333	1.71 (0.01)	0.6666	2.17 (0.01)		
383.15	0.0835	1.23 (0.01)	0.417	1.49 (0.01)	0.7501	1.92 (0.01)
	0.1672	1.28 (0.01)	0.5002	1.58 (0.01)	0.8333	2.04 (0.01)
	0.2511	1.34 (0.01)	0.5836	1.69 (0.01)	0.9165	2.19 (0.01)
	0.3333	1.41 (0.01)	0.6666	1.79 (0.01)		
393.15	0.0835	1.03 (0.01)	0.417	1.24 (0.01)	0.7501	1.61 (0.01)
	0.1672	1.06 (0.01)	0.5002	1.32 (0.01)	0.8333	1.71 (0.01)
	0.2511	1.12 (0.01)	0.5836	1.41 (0.01)	0.9165	1.84 (0.01)
	0.3333	1.18 (0.01)	0.6666	1.5 (0.01)		
403.15	0.0835	0.87 (0.01)	0.417	1.05 (0.01)	0.7501	1.36 (0.01)
	0.1672	0.89 (0.01)	0.5002	1.12 (0.01)	0.8333	1.45 (0.01)
	0.2511	0.94 (0.01)	0.5836	1.19 (0.01)	0.9165	1.57 (0.01)
	0.3333	0.99 (0.01)	0.6666	1.27 (0.01)		
diethylene glycol (1) - isopropyl alcohol (2)						
283.15	0.0834	4.24 (0.03)	0.4166	12.06 (0.07)	0.7573	32.1 (0.2)
	0.1667	5.48 (0.03)	0.5	15.54 (0.11)	0.8333	40.28 (0.26)
	0.25	7.12 (0.04)	0.5834	19.93 (0.12)	0.9164	50.07 (0.37)
	0.3334	9.26 (0.06)	0.6665	25.38 (0.15)		
293.15	0.0834	3.09 (0.02)	0.4166	8.25 (0.05)	0.7573	19.96 (0.12)
	0.1667	3.97 (0.02)	0.5	10.39 (0.07)	0.8333	24.42 (0.15)
	0.25	5.08 (0.03)	0.5834	13.02 (0.08)	0.9164	29.68 (0.19)
	0.3334	6.49 (0.04)	0.6665	16.18 (0.1)		
303.15	0.0834	2.29 (0.01)	0.4166	5.85 (0.04)	0.7573	13.16 (0.08)
	0.1667	2.93 (0.02)	0.5	7.25 (0.04)	0.8333	15.8 (0.1)
	0.25	3.72 (0.02)	0.5834	8.91 (0.05)	0.9164	18.85 (0.11)
	0.3334	4.69 (0.03)	0.6665	10.88 (0.07)		
313.15	0.0834	1.73 (0.01)	0.4166	4.29 (0.03)	0.7573	9.12 (0.05)
	0.1667	2.21 (0.01)	0.5	5.24 (0.03)	0.8333	10.78 (0.06)
	0.25	2.79 (0.02)	0.5834	6.36 (0.04)	0.9164	12.69 (0.08)
	0.3334	3.48 (0.02)	0.6665	7.65 (0.05)		
323.15	0.0834	1.33 (0.01)	0.4166	3.23 (0.02)	0.7573	6.58 (0.04)
	0.1667	1.7 (0.01)	0.5	3.91 (0.02)	0.8333	7.69 (0.05)
	0.25	2.14 (0.01)	0.5834	4.7 (0.03)	0.9164	8.95 (0.05)
	0.3334	2.65 (0.02)	0.6665	5.58 (0.03)		
333.15	0.0834	1.05 (0.01)	0.4166	2.5 (0.02)	0.7573	4.92 (0.03)
	0.1667	1.33 (0.01)	0.5	3.0 (0.02)	0.8333	5.7 (0.03)
	0.25	1.67 (0.01)	0.5834	3.57 (0.02)	0.9164	6.57 (0.04)
	0.3334	2.06 (0.01)	0.6665	4.21 (0.03)		
343.15	0.0834	0.82 (0.01)	0.4166	1.97 (0.01)	0.7573	3.79 (0.02)
	0.1667	1.06 (0.01)	0.5	2.35 (0.01)	0.8333	4.35 (0.03)
	0.25	1.33 (0.01)	0.5834	2.78 (0.02)	0.9164	4.99 (0.03)
	0.3334	1.63 (0.01)	0.6665	3.26 (0.02)		
diethylene glycol (1) - glycerol (2)						
293.15	0.0833	970.9 (7.85)	0.4167	236.04 (1.42)	0.7497	73.85 (0.48)

[a]: Standard uncertainty of temperature measurement: $u(T) = 0.03$ K

[b]: Standard uncertainty of mole fraction: $u(x) = 0.0013$

Table 4.10.: Viscosity of all studied systems at the investigated temperatures at 101 kPa (standard uncertainty in brackets). (continued)

T/K[a]	x_1[b]	η/(mPa · s)	x_1[b]	η/(mPa · s)	x_1[b]	η/(mPa · s)
	0.1666	676.12 (5.86)	0.5	174.35 (1.41)	0.8333	56.75 (0.36)
	0.2487	468.63 (3.94)	0.5833	128.2 (0.8)	0.9165	44.64 (0.32)
	0.3332	334.0 (2.48)	0.6665	95.91 (1.01)		
303.15	0.0833	428.01 (2.7)	0.4167	120.32 (0.81)	0.7497	42.52 (0.26)
	0.1666	309.31 (2.09)	0.5	91.44 (0.68)	0.8333	33.7 (0.2)
	0.2487	222.27 (1.58)	0.5833	69.74 (0.42)	0.9165	27.24 (0.17)
	0.3332	163.9 (1.11)	0.6665	53.75 (0.56)		
313.15	0.0833	208.68 (1.26)	0.4167	66.71 (0.48)	0.7497	26.3 (0.16)
	0.1666	155.7 (0.95)	0.5	52.12 (0.37)	0.8333	21.4 (0.13)
	0.2487	115.66 (0.79)	0.5833	40.98 (0.25)	0.9165	17.7 (0.11)
	0.3332	87.96 (0.57)	0.6665	32.44 (0.33)		
323.15	0.0833	111.2 (0.67)	0.4167	39.84 (0.29)	0.7497	17.28 (0.1)
	0.1666	85.36 (0.51)	0.5	31.91 (0.22)	0.8333	14.38 (0.09)
	0.2487	65.3 (0.43)	0.5833	25.74 (0.16)	0.9165	12.13 (0.08)
	0.3332	51.05 (0.32)	0.6665	20.86 (0.21)		
333.15	0.0833	64.0 (0.39)	0.4167	25.34 (0.18)	0.7497	11.94 (0.07)
	0.1666	50.38 (0.3)	0.5	20.75 (0.14)	0.8333	10.12 (0.06)
	0.2487	39.55 (0.26)	0.5833	17.1 (0.1)	0.9165	8.69 (0.05)
	0.3332	31.68 (0.2)	0.6665	14.15 (0.13)		
343.15	0.0833	39.37 (0.24)	0.4167	17.0 (0.12)	0.7497	8.61 (0.06)
	0.1666	31.66 (0.19)	0.5	14.19 (0.09)	0.8333	7.42 (0.05)
	0.2487	25.43 (0.17)	0.5833	11.92 (0.07)	0.9165	6.46 (0.04)
	0.3332	20.81 (0.13)	0.6665	10.04 (0.09)		
353.15	0.0833	25.64 (0.16)	0.4167	11.94 (0.08)	0.7497	6.43 (0.05)
	0.1666	21.0 (0.13)	0.5	10.13 (0.07)	0.8333	5.63 (0.04)
	0.2487	17.21 (0.11)	0.5833	8.65 (0.05)	0.9165	4.96 (0.03)
	0.3332	14.34 (0.09)	0.6665	7.4 (0.06)		
363.15	0.0833	17.53 (0.11)	0.4167	8.71 (0.06)	0.7497	4.96 (0.04)
	0.1666	14.58 (0.09)	0.5	7.5 (0.05)	0.8333	4.39 (0.03)
	0.2487	12.16 (0.09)	0.5833	6.5 (0.04)	0.9165	3.91 (0.02)
	0.3332	10.31 (0.07)	0.6665	5.64 (0.05)		
373.15	0.0833	12.5 (0.09)	0.4167	6.59 (0.04)	0.7497	3.93 (0.03)
	0.1666	10.54 (0.06)	0.5	5.75 (0.04)	0.8333	3.51 (0.02)
	0.2487	8.93 (0.07)	0.5833	5.03 (0.03)	0.9165	3.16 (0.02)
	0.3332	7.68 (0.05)	0.6665	4.42 (0.03)		
383.15	0.0833	9.26 (0.07)	0.4167	5.13 (0.03)	0.7497	3.18 (0.02)
	0.1666	7.9 (0.05)	0.5	4.52 (0.03)	0.8333	2.87 (0.02)
	0.2487	6.79 (0.05)	0.5833	4.0 (0.02)	0.9165	2.6 (0.02)
	0.3332	5.9 (0.04)	0.6665	3.55 (0.03)		
393.15	0.0833	7.08 (0.05)	0.4167	4.1 (0.03)	0.7497	2.63 (0.02)
	0.1666	6.12 (0.04)	0.5	3.65 (0.03)	0.8333	2.39 (0.02)
	0.2487	5.31 (0.04)	0.5833	3.25 (0.02)	0.9165	2.18 (0.01)
	0.3332	4.67 (0.03)	0.6665	2.91 (0.02)		
403.15	0.0833	5.58 (0.04)	0.4167	3.35 (0.02)	0.7497	2.21 (0.02)
	0.1666	4.86 (0.03)	0.5	3.0 (0.02)	0.8333	2.02 (0.01)
	0.2487	4.26 (0.03)	0.5833	2.7 (0.02)	0.9165	1.85 (0.01)
	0.3332	3.78 (0.03)	0.6665	2.43 (0.02)		

[a]: Standard uncertainty of temperature measurement: $u(T) = 0.03$ K

[b]: Standard uncertainty of mole fraction: $u(x) = 0.0013$

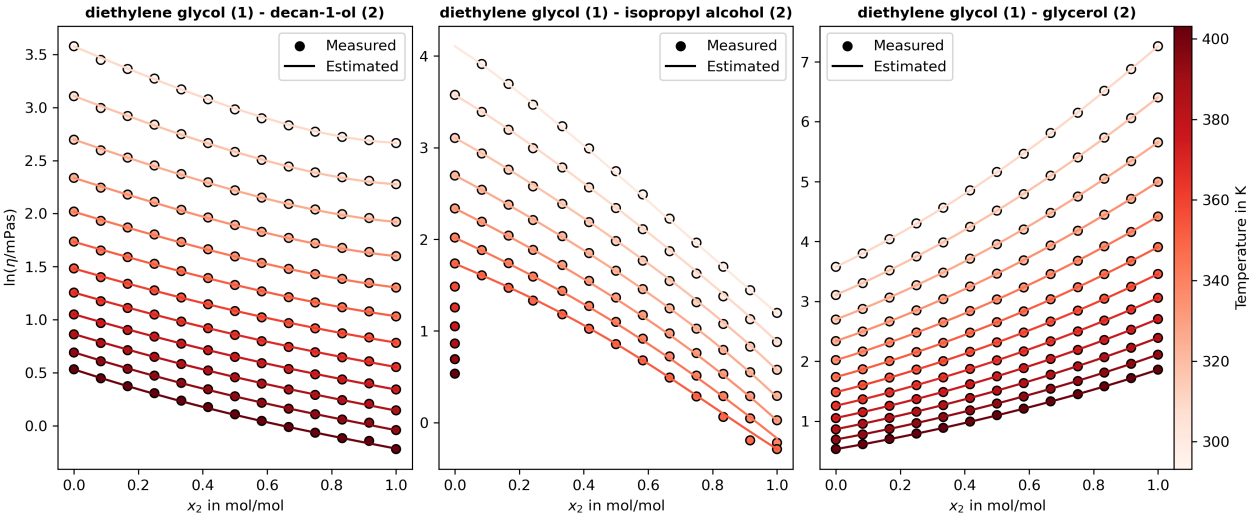

Figure 4.6.: Measured values and estimated logarithmic viscosity values for the studied systems and temperatures.

4.3.2.3. Surface Tension

The measured surface tension of the binary mixtures can be found in Table 4.11. The experimental values are also displayed in Figure 4.7 compared to the estimated data, which were determined according subsection 4.3.3.

Table 4.11.: Surface Tension of all studied systems at the investigated temperatures at 101 kPa (standard uncertainty in brackets).

T/K[a]	x_1[b]	γ/(mN/m)	x_1[b]	γ/(mN/m)	x_1[b]	γ/(mN/m)
diethylene glycol (1) - decan-1-ol (2)						
293.15	0.0835	26.92 (1.07)	0.417	27.21 (1.09)	0.7501	27.63 (1.18)
	0.1672	26.81 (1.07)	0.5002	27.51 (1.08)	0.8333	28.0 (1.11)
	0.2511	27.22 (1.07)	0.5836	27.81 (1.09)	0.9165	28.86 (1.08)
	0.3333	27.46 (1.07)	0.6666	27.58 (1.08)		
303.15	0.0835	27.39 (1.07)	0.417	28.03 (1.07)	0.7501	28.01 (1.07)
	0.1672	27.48 (1.07)	0.5002	27.71 (1.08)	0.8333	29.12 (1.08)
	0.2511	27.37 (1.07)	0.5836	28.46 (1.08)	0.9165	29.77 (1.09)
	0.3333	27.41 (1.09)	0.6666	28.12 (1.07)		
313.15	0.0835	26.06 (1.07)	0.417	26.81 (1.07)	0.7501	27.45 (1.07)
	0.1672	26.4 (1.07)	0.5002	26.99 (1.07)	0.8333	27.92 (1.07)
	0.2511	26.04 (1.07)	0.5836	26.83 (1.07)	0.9165	28.57 (1.07)
	0.3333	26.34 (1.07)	0.6666	26.96 (1.07)		
323.15	0.0835	23.95 (1.17)	0.417	26.5 (1.08)	0.7501	26.29 (1.07)
	0.1672	25.15 (1.07)	0.5002	26.0 (1.07)	0.8333	26.8 (1.07)
	0.2511	25.97 (1.08)	0.5836	26.94 (1.07)	0.9165	27.85 (1.07)
	0.3333	25.99 (1.09)	0.6666	27.03 (1.07)		
333.15	0.0835	23.78 (1.08)	0.417	25.52 (1.07)	0.7501	26.4 (1.07)
	0.1672	24.44 (1.06)	0.5002	25.71 (1.07)	0.8333	26.88 (1.07)
	0.2511	25.04 (1.07)	0.5836	26.21 (1.07)	0.9165	28.14 (1.07)
	0.3333	25.01 (1.07)	0.6666	26.28 (1.07)		
343.15	0.0835	24.31 (1.06)	0.417	25.33 (1.07)	0.7501	26.56 (1.07)
	0.1672	23.92 (1.06)	0.5002	25.17 (1.07)	0.8333	26.75 (1.07)
	0.2511	24.4 (1.06)	0.5836	25.31 (1.07)	0.9165	27.87 (1.07)
	0.3333	24.46 (1.06)	0.6666	25.37 (1.07)		

[a]: Standard uncertainty of temperature measurement: $u(T) = 0.2$ K

[b]: Standard uncertainty of mole fraction: $u(x) = 0.0013$

Table 4.11.: Surface Tension of all studied systems at the investigated temperatures at 101 kPa (standard uncertainty in brackets). (continued)

T/K[a]	x_1[b]	γ/(mN/m)	x_1[b]	γ/(mN/m)	x_1[b]	γ/(mN/m)
353.15	0.0835	22.91 (1.12)	0.417	24.85 (1.07)	0.7501	26.51 (1.07)
	0.1672	22.79 (1.08)	0.5002	24.99 (1.07)	0.8333	27.26 (1.07)
	0.2511	24.57 (1.11)	0.5836	25.76 (1.07)	0.9165	28.64 (1.08)
	0.3333	24.73 (1.06)	0.6666	26.01 (1.07)		
363.15	0.0835	20.88 (1.06)	0.417	23.25 (1.07)	0.7501	24.94 (1.07)
	0.1672	21.17 (1.06)	0.5002	23.67 (1.06)	0.8333	25.17 (1.09)
	0.2511	22.84 (1.26)	0.5836	23.83 (1.07)	0.9165	27.15 (1.07)
	0.3333	22.35 (1.12)	0.6666	24.31 (1.07)		
diethylene glycol (1) - isopropyl alcohol (2)						
283.15	0.0834	22.12 (1.04)	0.4166	25.59 (1.04)	0.7573	32.6 (1.05)
	0.1667	22.86 (1.04)	0.5	27.16 (1.04)	0.8333	35.01 (1.06)
	0.25	24.06 (1.04)	0.5834	28.58 (1.05)	0.9164	38.46 (1.06)
	0.3334	24.82 (1.04)	0.6665	30.14 (1.05)		
293.15	0.0834	21.61 (1.04)	0.4166	25.64 (1.04)	0.7573	31.72 (1.06)
	0.1667	22.52 (1.04)	0.5	26.13 (1.04)	0.8333	34.55 (1.06)
	0.25	23.59 (1.04)	0.5834	28.08 (1.05)	0.9164	38.05 (1.06)
	0.3334	24.32 (1.04)	0.6665	29.89 (1.05)		
303.15	0.0834	20.6 (1.03)	0.4166	24.25 (1.04)	0.7573	31.65 (1.05)
	0.1667	21.5 (1.03)	0.5	26.78 (1.04)	0.8333	34.26 (1.06)
	0.25	22.44 (1.04)	0.5834	27.35 (1.05)	0.9164	37.92 (1.07)
	0.3334	23.85 (1.04)	0.6665	28.88 (1.05)		
313.15	0.0834	20.21 (1.03)	0.4166	25.13 (1.04)	0.7573	31.41 (1.09)
	0.1667	21.24 (1.04)	0.5	26.5 (1.05)	0.8333	34.42 (1.07)
	0.25	22.78 (1.04)	0.5834	27.62 (1.05)	0.9164	37.53 (1.06)
	0.3334	23.56 (1.04)	0.6665	29.16 (1.08)		
323.15	0.0834	19.83 (1.04)	0.4166	24.2 (1.04)	0.7573	31.29 (1.05)
	0.1667	20.85 (1.03)	0.5	25.54 (1.05)	0.8333	34.11 (1.06)
	0.25	22.15 (1.04)	0.5834	27.14 (1.05)	0.9164	36.64 (1.06)
	0.3334	23.07 (1.04)	0.6665	29.13 (1.05)		
333.15	0.0834	19.26 (1.03)	0.4166	23.06 (1.04)	0.7573	30.47 (1.07)
	0.1667	19.52 (1.04)	0.5	24.76 (1.04)	0.8333	32.53 (1.06)
	0.25	20.57 (1.03)	0.5834	25.83 (1.05)	0.9164	37.3 (1.06)
	0.3334	22.15 (1.04)	0.6665	28.37 (1.09)		
343.15	0.0834	18.13 (1.04)	0.4166	23.36 (1.09)	0.7573	30.26 (1.07)
	0.1667	18.97 (1.04)	0.5	24.06 (1.05)	0.8333	32.7 (1.15)
	0.25	20.32 (1.08)	0.5834	24.85 (1.18)	0.9164	36.4 (1.08)
	0.3334	21.98 (1.12)	0.6665	27.57 (1.16)		
diethylene glycol (1) - glycerol (2)						
293.15	0.0833	56.62 (1.09)	0.4167	49.17 (1.09)	0.7497	46.02 (1.07)
	0.1666	54.68 (1.09)	0.5	48.41 (1.08)	0.8333	44.76 (1.07)
	0.2487	51.9 (1.08)	0.5833	47.36 (1.08)	0.9165	44.5 (1.07)
	0.3332	51.1 (1.08)	0.6665	46.44 (1.08)		
303.15	0.0833	54.31 (1.09)	0.4167	49.12 (1.08)	0.7497	45.29 (1.07)
	0.1666	52.23 (1.08)	0.5	48.29 (1.09)	0.8333	42.63 (1.07)
	0.2487	51.51 (1.08)	0.5833	46.66 (1.08)	0.9165	43.84 (1.07)
	0.3332	49.87 (1.08)	0.6665	46.45 (1.07)		
313.15	0.0833	55.63 (1.09)	0.4167	47.13 (1.08)	0.7497	43.12 (1.07)
	0.1666	51.83 (1.08)	0.5	45.61 (1.07)	0.8333	42.69 (1.07)
	0.2487	50.79 (1.08)	0.5833	44.88 (1.07)	0.9165	42.11 (1.07)
	0.3332	48.62 (1.08)	0.6665	43.86 (1.07)		
323.15	0.0833	53.61 (1.09)	0.4167	47.37 (1.08)	0.7497	43.04 (1.07)
	0.1666	51.52 (1.08)	0.5	45.65 (1.07)	0.8333	41.92 (1.07)
	0.2487	49.43 (1.08)	0.5833	44.37 (1.07)	0.9165	42.25 (1.07)

[a]: Standard uncertainty of temperature measurement: $u(T) = 0.2$ K

[b]: Standard uncertainty of mole fraction: $u(x) = 0.0013$

Table 4.11.: Surface Tension of all studied systems at the investigated temperatures at 101 kPa (standard uncertainty in brackets). (continued)

T/K[a]	x_1[b]	γ/(mN/m)	x_1[b]	γ/(mN/m)	x_1[b]	γ/(mN/m)
	0.3332	48.08 (1.08)	0.6665	43.56 (1.07)		
333.15	0.0833	54.48 (1.09)	0.4167	45.74 (1.07)	0.7497	41.97 (1.07)
	0.1666	50.75 (1.08)	0.5	44.71 (1.07)	0.8333	41.11 (1.07)
	0.2487	49.39 (1.08)	0.5833	44.0 (1.07)	0.9165	40.87 (1.07)
	0.3332	46.97 (1.08)	0.6665	42.99 (1.07)		
343.15	0.0833	52.8 (1.08)	0.4167	46.21 (1.08)	0.7497	41.89 (1.07)
	0.1666	50.73 (1.08)	0.5	44.81 (1.07)	0.8333	40.72 (1.07)
	0.2487	48.68 (1.08)	0.5833	43.67 (1.07)	0.9165	40.45 (1.07)
	0.3332	46.46 (1.08)	0.6665	42.54 (1.07)		
353.15	0.0833	51.44 (1.08)	0.4167	43.69 (1.07)	0.7497	39.97 (1.06)
	0.1666	48.48 (1.08)	0.5	42.41 (1.07)	0.8333	39.54 (1.06)
	0.2487	46.23 (1.08)	0.5833	42.0 (1.07)	0.9165	38.29 (1.06)
	0.3332	44.57 (1.07)	0.6665	40.09 (1.06)		
363.15	0.0833	50.25 (1.08)	0.4167	42.93 (1.07)	0.7497	38.77 (1.06)
	0.1666	48.01 (1.08)	0.5	42.11 (1.07)	0.8333	38.08 (1.06)
	0.2487	45.67 (1.07)	0.5833	40.96 (1.07)	0.9165	38.24 (1.06)
	0.3332	43.7 (1.07)	0.6665	39.57 (1.06)		

[a]: Standard uncertainty of temperature measurement: $u(T) = 0.2$ K
[b]: Standard uncertainty of mole fraction: $u(x) = 0.0013$

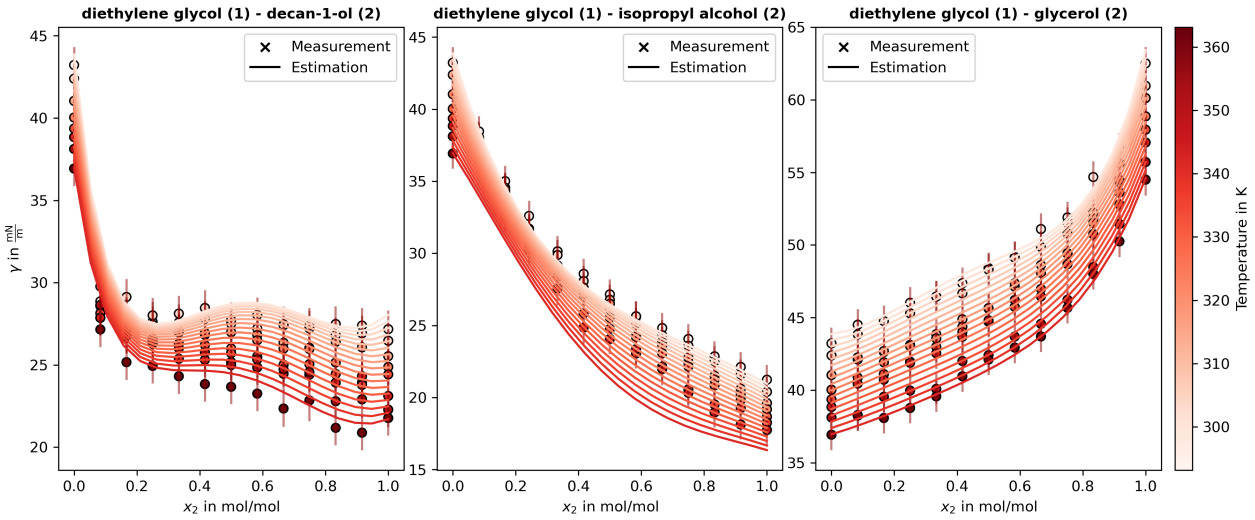

Figure 4.7.: Measured values and estimated surface tension values for the studied systems and temperatures.

4.3.3. Estimation of Excess Properties

4.3.3.1. Refractive Index

The measured values of the refractive index at 293.15 K of all studied systems with the respective calculated standard uncertainties are listed Table 4.12 and are presented graphically in Figure 4.8. Applying Equation 4.1 the excess refractive indices of the measured values were determined, which are listed in Table A.1 in section A.3 in the Appendix and are also shown in Figure 4.8 (Plots A to C).

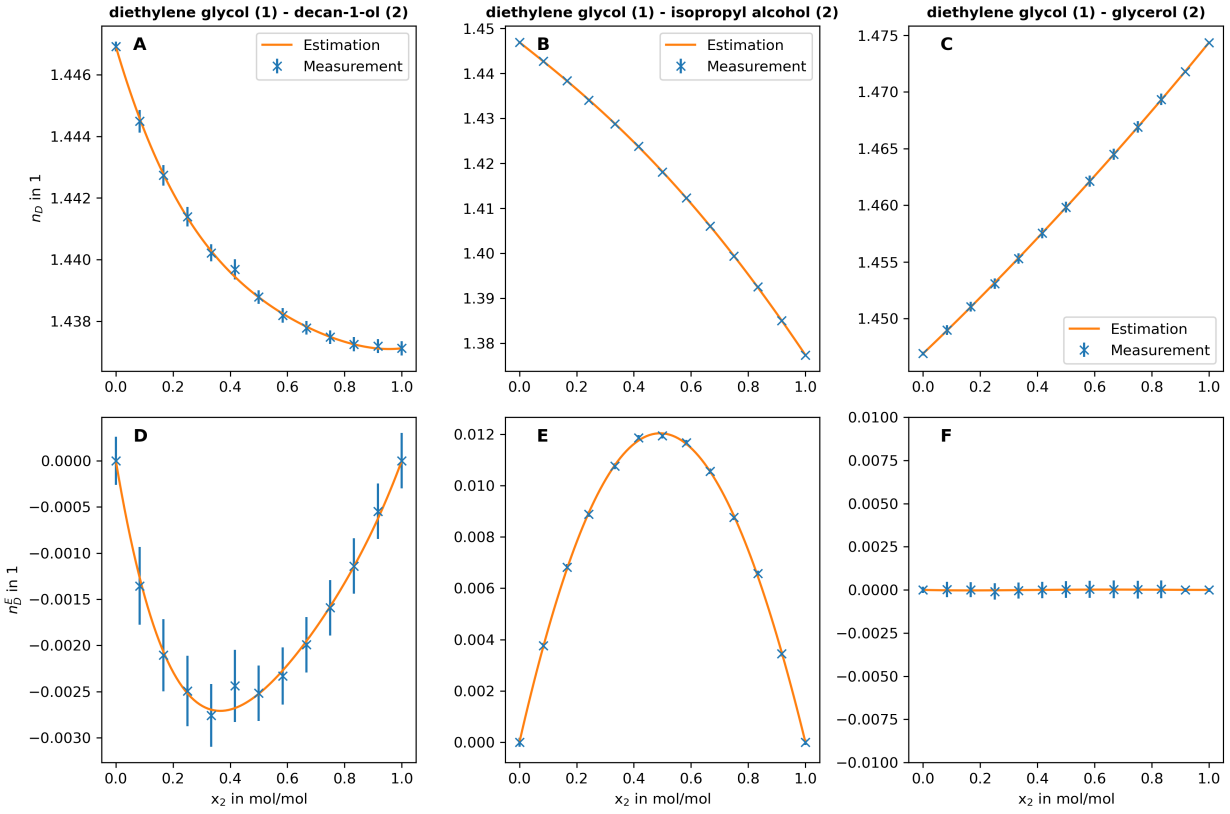

Figure 4.8.: Measured and calculated refractive index (A to C) and the estimated and calculated excess refractive index (D to F) of DEG-decan-1-ol, DEG-IPA and DEG-glycerol in molar fraction.

In order to estimate the excess values, the Redlich-Kister parameters of Equation 4.11 were fitted to the experimental data. The determined parameters as well as the coefficients of determination for the studied systems are listed in Table 4.13 and the results of the estimated refractive indices with them are shown in Figure 4.8 (Plots D to F) for comparison.
In general, good agreement between experiment and model can be seen. For decan-1-ol, there is a slight deviation at $x_2 = 0.417$, which can be attributed to experimental deviations. For the DEG-glycerol system nearly ideal behavior is observed, which leads to absolute values of the excess refractive index close to zero and therefore a low coefficient of determination. Usage of Redlich-Kister is neither necessary nor recommended in this case. For the other binary substance systems, the excess size can be determined accurately with the help of the given parameters with a coefficient of determination $R^2 \geq 0.992$.

Table 4.12.: Refractive index of all studied systems at T = 293.15 K[a] and 101 kPa.

x_1[b]	n_D	x_1[b]	n_D	x_1[b]	n_D
diethylene glycol (1) - decan-1-ol (2)					
0.0835	1.43719 (0.00023)	0.417	1.43819 (0.00024)	0.7501	1.44139 (0.00032)
0.1672	1.43725 (0.00023)	0.5002	1.43878 (0.00022)	0.8333	1.44274 (0.00033)
0.2511	1.43748 (0.00022)	0.5836	1.43968 (0.00033)	0.9165	1.44449 (0.00037)
0.3333	1.43778 (0.00022)	0.6666	1.44022 (0.00028)		
diethylene glycol (1) - isopropyl alcohol (2)					
0.0834	1.38504 (0.00008)	0.4166	1.41236 (0.00008)	0.7573	1.43408 (0.00008)
0.1667	1.39257 (0.00008)	0.5	1.41808 (0.00008)	0.8333	1.43837 (0.00009)
0.25	1.3994 (0.00008)	0.5834	1.4238 (0.00008)	0.9164	1.44271 (0.00009)
0.3334	1.40608 (0.00008))	0.6665	1.42881 (0.00009)		
diethylene glycol (1) - glycerol (2)					
0.0833	1.47181 (0.00008)	0.4167	1.46214 (0.00049)	0.7497	1.45309 (0.00046)
0.1666	1.46934 (0.00051)	0.5	1.45983 (0.00048)	0.8333	1.45106 (0.00042)
0.2487	1.46691 (0.0005)	0.5833	1.45755 (0.00047)	0.9165	1.44899 (0.00043)
0.3332	1.46449 (0.0005)	0.6665	1.45531 (0.00046)		

[a]: Standard uncertainty of temperature measurement: $u(T) = 0.03$ K

[b]: Standard uncertainty of mole fraction: $u(x) = 0.0013$

Table 4.13.: Redlich-Kister parameters of Equation 4.11 to calculate the excess refractive index for diethylene glycol with decan-1-ol, isopropyl alcohol and glycerol.

system	$A_0/1$	$A_1/1$	$A_2/1$	R^2
DEG (1) - decan-1-ol (2)	-0.010158	-0.0049314	-0.0029233	0.992
DEG (1) - isopropyl alcohol (2)	0.048467	0.0017233	-0.0032204	0.999
DEG (1) - glycerol (2)	0.00004406	-0.00019252	-0.00028293	0.311

4.3.3.2. Density

The excess volume for the studied systems was calculated according to Equation 4.4, listed in Table A.2 in section A.3 in the Appendix and illustrated in Figure 4.9 (A - C).

To compare the experimental results of the DEG-isopropyl alcohol system, the experimental excess volumes V^E and excess logarithmic viscosities $\ln(\eta/\text{mPa} \cdot s)^E$ as well as the experimental data from Almasi were compared in Figure 4.10 [150].

The absolute values determined in this work for the excess quantities are of a similar order of magnitude to those of Almasi. In addition, the excess volumes are constantly negative both in Almasi and in this work. However, it should be noted that while the excess volume decreases with increasing temperature in this work, it increases with increasing temperature in Almasi. The investigated temperature range in Almasi is smaller than in this work and a cause for the different dependencies cannot be conclusively clarified, but could be due to impurities in the investigated material systems. The material systems used in this work have a higher purity than the systems investigated by Almasi [150].

To estimate the excess volume as a function of composition and temperature the Redlich-Kister parameters were fitted using Equation 4.11 and thereafter the temperature-dependent Redlich-Kister

parameters of Equation 4.12 were adjusted and summarized in Table 4.14. The plots of the resulting Redlich-Kister parameters are depicted as a solid line in Figure 4.9 (D-F). In the comparison, the Redlich-Kister parameters are shown as individual points. To evaluate the quality of the regression, the resulting residual plots are also presented in Figure 4.9 (G to I).

Overall, it can be seen that the resulting excess volumes can be approximated well resulting in reasonable temperature-dependent Redlich-Kister parameters. Here, too, an approximately ideal behavior was observed for the DEG-glycerol system. The highest deviations for all systems were observed in the peripheral areas of the experimental space investigated. This can be explained by the fact that inaccuracies in the equations used are superimposed by measurement errors, which is particularly evident in the case of DEG-glycerol as the absolute values of the excess volume are low.

The mixtures under consideration are well suited as reference systems, since the differences in density allow an accurate and simple determination of the mixture composition and, on the other hand, the density of the test system under investigation can be adjusted over a wide range.

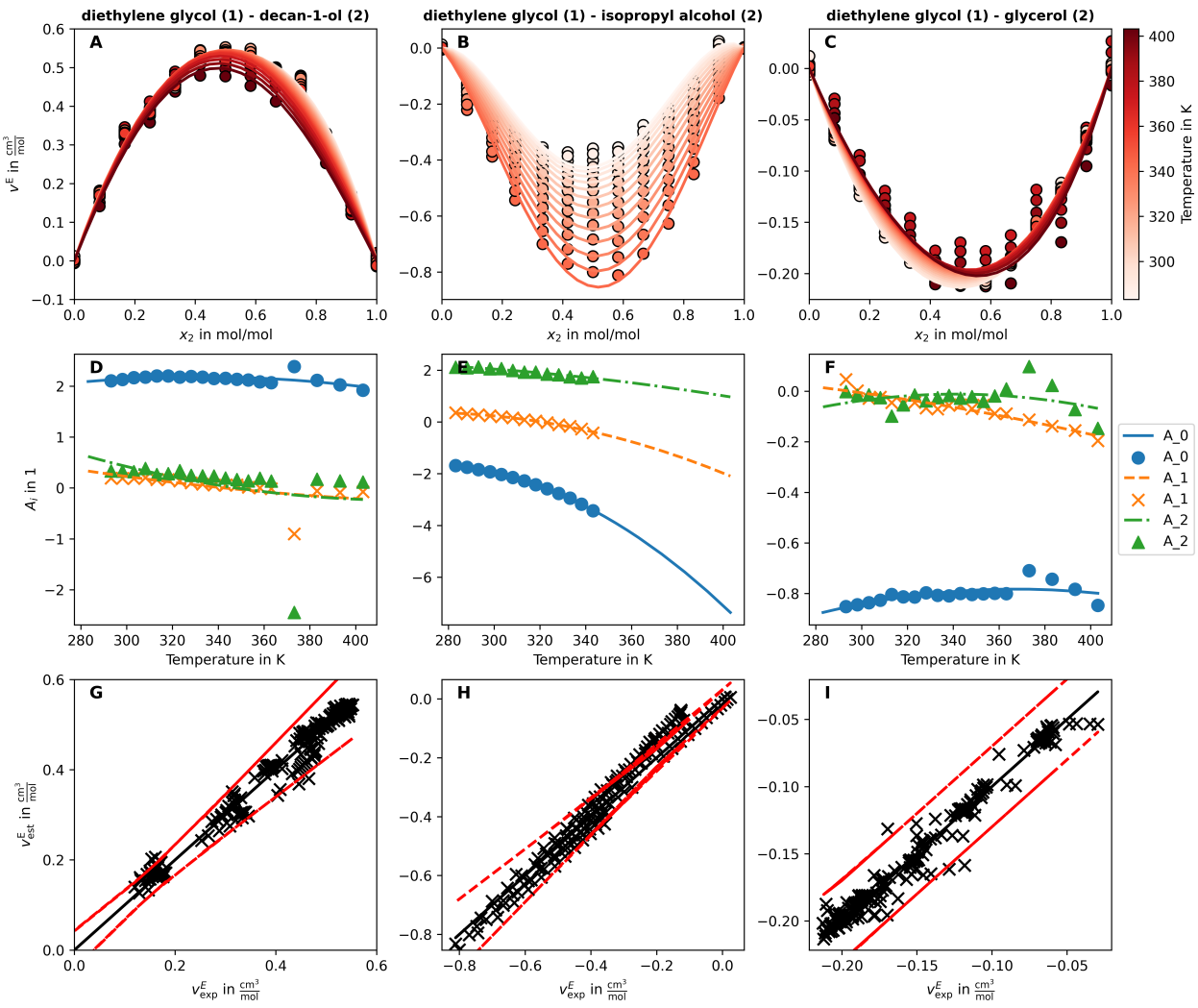

Figure 4.9.: Measured and calculated excess values for the molar volumes (plots A to C), the temperature dependence of the Redlich-Kister-parameters (plots D to F) and the resulting residual plots with 20% relative deviation (red lines) (plots G to I).

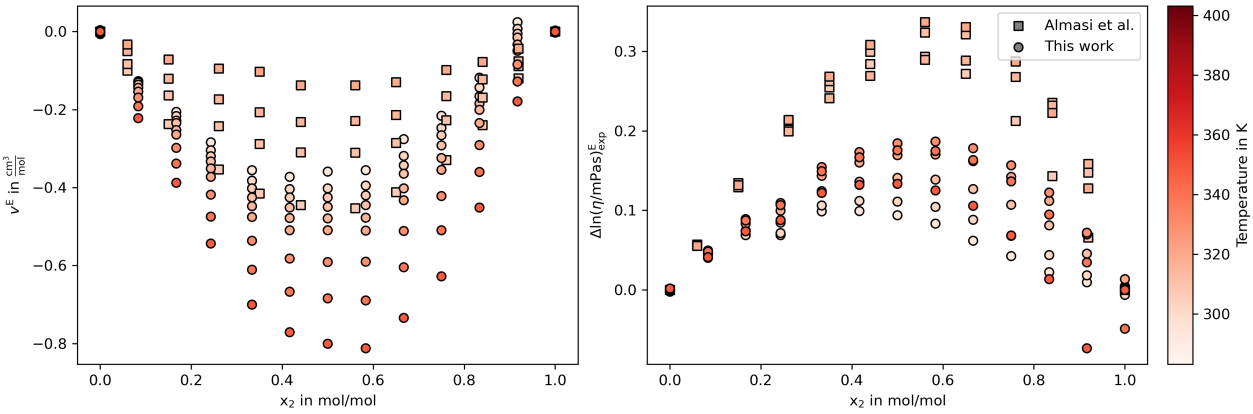

Figure 4.10.: Comparison of the experimental results on excess volume (left) and excess logarithmic viscosity (right) of Almasi with the experimental results of this work [150].

Table 4.14.: Parameters of Equation 4.12 for the calculation of the Redlich-Kister parameter and the excess molar volume of diethylene glycol with decan-1-ol, isopropyl alcohol and glycerol in dependence of the temperature.

	DEG (1) - decan-1-ol (2)	DEG (1) - IPA (2)	DEG (1) - glycerol (2)
$a_{0,0}$	-1.678885	-24.039977	-2.639537
$a_{0,1}$	0.023912	0.167550	0.010062
$a_{0,2}$	-0.000037	-0.000313	-0.000014
$a_{1,0}$	4.424483	-9.547713	-1.447589
$a_{1,1}$	-0.020582	0.073538	0.009743
$a_{1,2}$	0.000022	-0.000136	-0.000017
$a_{2,0}$	9.883131	0.547120	-12.196540
$a_{2,1}$	-0.049012	0.016640	0.074345
$a_{2,2}$	0.000058	-0.000039	-0.000113

4.3.3.3. Viscosity

The excess property $\ln(\eta)^E$ was calculated for the analyzed systems according to Equation 4.6 and listed in Table A.3 in section A.3 in the Appendix. The values for $\ln(\eta)^E$ are shown in Figure 4.11 (A - C). For the DEG - isopropyl alcohol system, the experimentally determined values for the excess property $\ln(\eta/\text{mPa}\cdot s)^E$ of this work are compared with the results of Almasi in Figure 4.10. Here, the absolute values determined by Almasi for $\ln(\eta/\text{mPa}\cdot s)^E$ are slightly higher, but the value range and the temperature dependence are similar. Overall, the deviations are greater than the uncertainties stated in this work and in the work of Almasi, although Almasi did not take into account the uncertainty due to possible contamination, which may be a possible cause of the deviations [150].
To estimate the excess property $\ln(\eta)^E$ as a function of composition and temperature, the Redlich-Kister parameters were calculated using Equation 4.11 and then the temperature-dependent Redlich-Kister parameters from Equation 4.12 were adjusted and presented in Table 4.15. Figure 4.11 (D-F) shows the curves of the determined Redlich-Kister parameters as a function of temperature and the fitted Redlich-Kister parameters. The resulting residuals are shown in Figure 4.11 (G to I).
It can be stated that the excess property $\ln(\eta)^E$ can be approximated well with the determined temperature-dependent Redlich-Kister parameters. However, for the DEG/decan-1-ol system a systematic deviation is observed for the sample with a mole fraction of $x_2 = 0.9165$, which is also

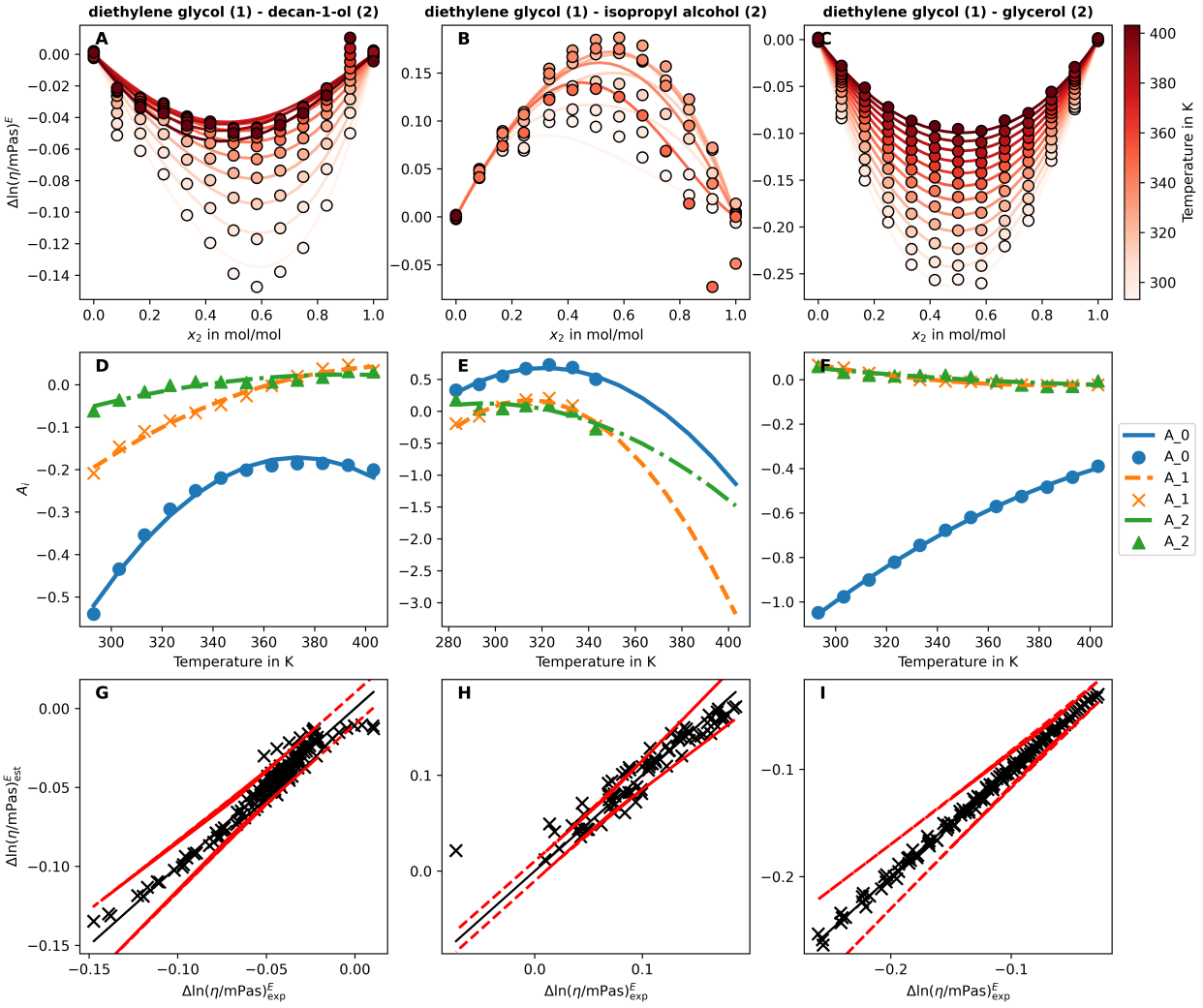

Figure 4.11.: Measured and calculated excess values for the viscosity (plots A to C), the temperature dependence of the Redlich-Kister-parameters (plots D to F) and the resulting residual plots with 20% relative deviation (red lines) (plots G to I).

recognizable in the parity plot. This is most likely due to a slight deviation between the actual and the weighed mole fraction. For the systems studied viscosities between 2 and 10 mPa · s can be expected for evaporation conditions at 393 K in the WFE. Although these values are below the viscosity values of highly viscous systems such as polymer melts, the systems have significantly higher values compared to aqueous systems and are therefore suitable for the evaluation of wiping systems such as roller wipers, which are preferred for medium-viscosity systems. If test systems with higher viscosities during evaporation are required other systems should be considered, whereby increased equipment costs are to be expected due to more powerful pumps and trace heating systems.

Table 4.15.: Parameters of Equation 4.12 for the calculation of the Redlich-Kister parameters and the excess logarithmic viscosity $\ln(\eta)^E$ of diethylene glycol with decan-1-ol, isopropyl alcohol and glycerol in dependence of the temperature.

	DEG (1) - decan-1-ol (2)	DEG (1) - IPA (2)	DEG (1) - glycerol (2)
$a_{0,0}$	-7.646263	-22.081900	-5.344620
$a_{0,1}$	0.039939	0.140664	0.020943
$a_{0,2}$	-0.000053	-0.000217	-0.000021
$a_{1,0}$	-3.097792	-32.818845	1.526731
$a_{1,1}$	0.015513	0.209331	-0.007935
$a_{1,2}$	-0.000019	-0.000332	0.000010
$a_{2,0}$	-0.826729	-11.335548	1.265861
$a_{2,1}$	0.004032	0.076844	-0.006635
$a_{2,2}$	-0.000005	-0.000129	0.000009

4.3.3.4. Surface Tension

To calculate the surface tension of the investigated mixtures, the parachor was calculated from the experimental data according to Equation 4.9 and then the excess parachor ΔP^E was determined using Equation 4.10. The values for the calculated experimental excess parachor of each temperature and composition are plotted in Figure 4.12 (Plots A to C) and also listed in Table A.4 in section A.3 in the Appendix. For each of the temperatures considered, the Redlich-Kister parameters were first adjusted to the calculated values of P^E according to Equation 4.11 and then the temperature-dependent curve was fitted by adjusting the parameters of Equation 4.12. The adjusted values for the Redlich-Kister parameters for the investigated temperatures as well as the plot of the temperature-dependent values are shown in Figure 4.12 (plots D to F) and summarized in Table 4.16. To assess the quality of the regression, the resulting residual plots are illustrated in subplots G to I of Figure 4.12.

The excess parachor could be approximated well for the DEG-IPA and DEG-glycerol systems. For DEG-glycerol, lower excess values were determined, which indicates a more ideal behavior. The system DEG-decan-1-ol had the highest absolute values for the excess parachor and the largest absolute deviations in the residual plot. As can be seen in Figure 4.7 the actual surface tension of the binary mixture can not be estimated well using the parachor in combination with the Redlich-Kister approach. This is most likely due to a surfactant character for this system. The surfactant character can be

Table 4.16.: Parameters of Equation 4.12 for the calculation of the Redlich-Kister parameters and the excess parachor of diethylene glycol with decan-1-ol, isopropyl alcohol and glycerol in dependence of the temperature.

	DEG (1) - decan-1-ol (2)	DEG (1) - IPA (2)	DEG (1) - glycerol (2)
$a_{0,0}$	-569.007611	-407.821292	-78.033374
$a_{0,1}$	3.109129	2.327793	0.440802
$a_{0,2}$	-0.004422	-0.003605	-0.000729
$a_{1,0}$	-768.496445	64.887649	-168.055654
$a_{1,1}$	5.453405	-0.069232	0.823932
$a_{1,2}$	-0.008815	-0.000288	-0.001072
$a_{2,0}$	-1141.113779	211.196450	-488.420975
$a_{2,1}$	6.343658	-1.608074	2.886531
$a_{2,2}$	-0.009631	0.002999	-0.004307

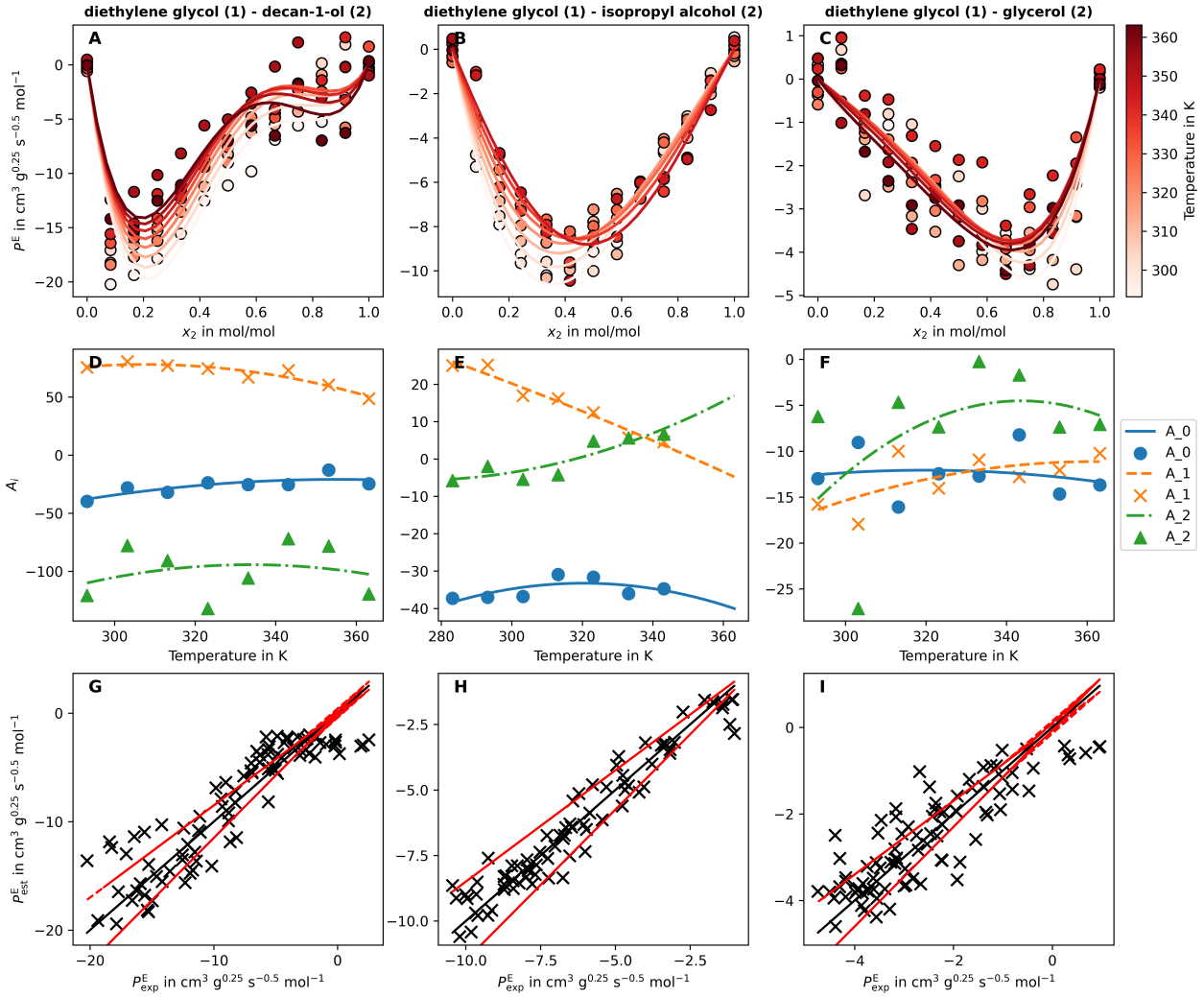

Figure 4.12.: Measured and calculated excess values for the parachor (plots A to C), the temperature dependence of the Redlich-Kister-parameters (plots D to F) and the resulting residual plots with 20% relative deviation (red lines) (plots G to I).

explained by the molecular structure presented in Figure 4.1, which shows that decan-1-ol has a long non-polar region and a polar OH group on one side. The surface tension for this system depended only slightly on the concentration of decan-1-ol over the entire concentration range investigated and essentially corresponded to the surface tension of pure decan-1-ol at the corresponding temperature. The method presented therefore only suitable to a limited extent to calculate the surface tension of the DEG-decan-1-ol system and it might be more advantageous to use the surface tension of pure decan-1-ol. However, the use of this system for evaporation experiments in WFE can be advantageous, as the surface tension of the overall system is practically unaffected by the concentration changes that occur as a result of evaporation.

4.4. Conclusions

For the studied systems, thermophysical properties for density, refractive index viscosity and surface tension up to 403.15 K were measured, whereby the values for the pure substances correspond well

with data from the literature. In order to model the experimentally determined excess values, the Redlich-Kister equation was used and the parameters for calculating the Redlich-Kister parameters as a function of temperature were calculated. Overall, the results appear reasonable and fit within the current state of knowledge.
With the studied systems, density, surface tension and viscosity can be varied independently of each other, making them suitable as possible test systems for the characterization of wiped film evaporators, especially with movable wiper elements. Since the number of experimental degrees of freedom in the investigation of WFE are high compared to other systems, the thermophysical properties of the used fluids should change in a defined manner during evaporation. Here, the diethylene glycol-decan-1-ol system appears to be particularly suitable for the universal characterization of heat transfer and fluid dynamics, as the surface tension is almost independent of the concentration of decan-1-ol, which eliminates one degree of freedom. Diethylene glycol-glycerol can be used if higher viscosities are desired, which is particularly useful with regard to other wiper systems and comparison with typical applications in the high-viscosity range. The diethylene glycol-isopropyl alcohol system can be used to investigate how efficiently volatile substances can be removed from a high-boiling component, which is a typical application in the purification of thermally sensitive product streams with volatile solvent content. The different systems can therefore be selected depending on the specific application and provide a good basis for the application-specific characterization of wiped film evaporators.

Notes

The authors declare no competing financial interest.

Acknowledgments

We gratefully acknowledge that this project was supported by Federal Ministry for Economic Affairs and Climate Action on the basis of a decision of the German Bundestag. This research was conducted as part of a project of the Industrielle Gemeinschaftsforschung (IGF) with the project number 01IF22220N.

5. Experimental Results of Fluid Dynamics during Evaporation

To characterize the fluid dynamics during evaporation, experiments were conducted on the WFE introduced in section 3.1, which was equipped with a roller wiper system. This chapter presents the results of these investigations, including RTDs, the achieved product-side heat transfer coefficients compared to established calculation equations, and the change in fluid dynamics along the evaporator length.

5.1. Evaporation Effects on Residence Time in Wiped Film Evaporators with Roller Wipers

The following section 5.1 represents an updated version of the publication: D. Appelhaus, K. Jasch, H. Meyer, and S. Scholl. “Evaporation Effects on Residence Time in Wiped Film Evaporators with Roller Wipers”. In: *Chem. Eng. Res. Des.* 218 (2025), pp. 341–349. While updating only editorial changes were made.
Reprinted with permission from D. Appelhaus, K. Jasch, H. Meyer, and S. Scholl. “Evaporation Effects on Residence Time in Wiped Film Evaporators with Roller Wipers”. In: *Chem. Eng. Res. Des.* 218 (2025), pp. 341–349.
The supplementary material is available online at https://doi.org/10.1016/j.cherd.2025.04.036.

Abstract

The influence of evaporation on the residence time distribution in a wiped film evaporator (WFE) with movable roller wipers and different solvents was investigated. Up to moderate evaporation ratios the measured residence time distributions showed self-similiar behavior. The fluid properties, namely the viscosity, and the density, influence the fluid dynamics in WFE, as a gravity-driven, falling film occurs. Although the peripheral load is the most important parameter for the residence time distribution, the wiper speed and the evaporation ratio also affect the residence time noticeably. Especially for high evaporation ratios associated with high temperature differences the liquid film tends to become instable, leading to significantly increased mean residence time. The associated film rupture was observed visually taking high-speed recordings of the inner evaporator surface during evaporation.

5.1.1. Introduction

The separation of volatile components from heat sensitive, highly viscous, or solid loaded fluid streams is a very challenging task in the process industry and cannot be done with the majority of common evaporator types, as they would either be damaged themselves or would degrade the products.
For these challenging processes, the wiped film evaporator (WFE) is commonly applied in the chemical, pharmaceutical, and food industries [70]. WFE can operate under reduced pressures and temperatures

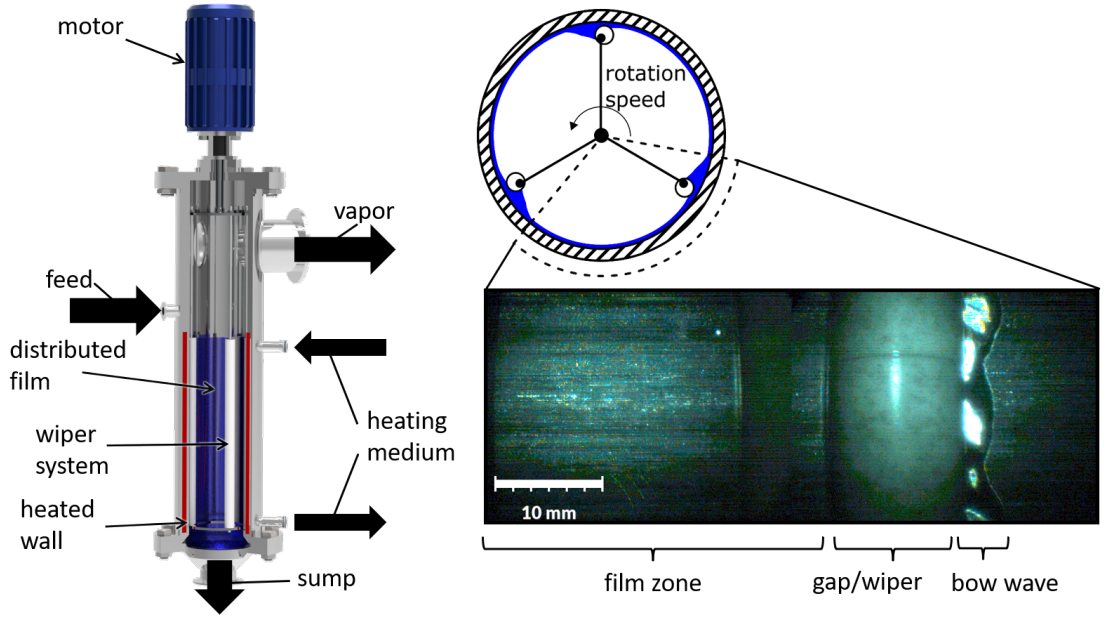

Figure 5.1.: Working principle of a wiped film evaporator. The liquid feed enters at the top and flows down by gravity while being heated by a heating medium and continuously distributed by a wiper system. The wiping motion creates a film zone behind the wiper and a bow wave in front of the wiper along the inner wall of the apparatus.

with very short residence times and a low fouling tendency [8].

The working principle of a WFE is shown in Figure 5.1. The constant distribution of the liquid significantly enhances the rate of mass and heat transfer while minimizing the thermal degradation of the product [39, 87]. As heat supply steam, thermal oil or electrical heating may be used [31]. The large free cross-section allows operation at very low operating pressures down to 1 mbar.

Due to these advantages compared to other types of evaporators, WFEs are widely applied for the evaporation of solvents from heat-sensitive materials [10, 130]. They also have great potential when it comes to reactive distillation processes, which have been the subject of several recent studies [37, 182].

However, additional degrees of freedom due to the wiper elements, their operation, and interaction with the distributed liquid flow lead to numerous uncertainties during operation, which require expensive pilot-scale experiments and large safety margins. Heat transfer and fluid dynamics in WFE depend on the thermophysical properties (e.g. viscosity, surface tension, thermal conductivity and density) of the fluids used as well as the equipment (e.g. wiper type, geometry, number of wipers) and operational (e.g. rotational speed, volumetric flow) parameters [31]. In order to adequately describe WFE, it is essential to gain a comprehensive understanding of the interactions between heat transfer and fluid dynamics.

Previous studies on fluid dynamics have generally been focused on fixed wiper geometries or pure components. Schweizer and Widmer showed that laminar flow conditions exist in high- and medium-viscosity systems and that mean residence times of fixed wiper elements can be predicted well, provided that suitable equations for calculating the bow wave height are available [6].

Cvengroš *et al.* were able to show that, depending on the peripheral load and wiper speed, there can be a change in the residence time distribution (RTD) as a result of liquid ripples [81]. This is

consistent with investigations in which the residence time distribution was modeled using a diffusive model taking into account the axial Peclét number [80].
Jasch *et al.* have found experimentally that the residence time behavior for roller wipers is mainly affected by the peripheral load and that the wiper frequency does not change the residence time distribution substantially [22]. Cvengroš *et al.* 2000 and Cvengroš *et al.* 2001 found that, although peripheral load effects agree with Jasch *et al.* wiper speed significantly alters residence time distributions in systems like comb wipers [50, 51]. Furthermore, studies with blade wipers indicate, that the mean residence time can increase with the wiper speed for a fixed gap width and also compared to a laminar falling film [6, 32]. This increase is also due to an overall increase of the liquid hold-up compared to falling film evaporators [32].
The differences in the several studies can be attributed to the fact that the gap between the wiper and the fluid significantly influences the resulting film while the structured wiper systems investigated by Cvengroš *et al.* [50] and Cvengroš *et al.* [51] affect the flow profile drastically. However, for roller wipers, as the gap width and wiper speed are correlated, the reduction of the gap width compensates for the higher deceleration of the axial flow, which is supported by simulations of roller wipers [25].
The stability of the liquid film is another important factor for fluid dynamics. Although wiped film evaporators can operate below the critical thickness of falling film evaporators, insufficient wetting can still cause critical operating conditions [31]. Surface forces destabilize the liquid film, leading to partial dewetting, which can create local hotspots and reduce heat transfer [31, 121]. Particular consideration must be given to the dynamics of the rupturing mechanism, as the liquid film is repeatedly renewed by the wiper as long as the liquid is available, which leads to dynamic wetting and rupturing processes [125, 126].
However, published studies do not consider the influence of evaporation on fluid dynamics systematically, so there is little knowledge about the effects that occur during actual operation. The simultaneous consideration of heat transfer, residence time, and film stability has not been studied, although it is crucial to evaluate the thermal stress on processed fluids [32].
The RTD together with the maximum product temperatures are the primary parameters that affect the thermal stress to the product while being evaporated, thus directly influencing the product quality and yield. The present work addresses this gap in knowledge, investigating the residence time distributions with varied peripheral loads, different solvents and wiper frequencies with and without evaporation. The interpretation of the experimental RTD measurements is supported by high-speed images of the wiping process during evaporation.

5.1.2. Experimental Setup

5.1.2.1. Plant Configuration

For the experiments, a stainless steel evaporator (UIC GmbH) was used with dimensions of 0.09 x 0.005 x 0.256 m (OD x WT x L) and a resulting heat transfer surface of 0.0643 m^2. The wiping system consisted of three roller wiping elements that were evenly distributed around the circumference. The roller wipers were made of polytetrafluoroethylene (PTFE) and the rolls had an outer diameter of 12 mm.
The evaporator was embedded in a miniplant, which was set up according to the flow sheet presented

in the Supplementary (Figure S2), available online. The feed flow was measured using the Coriolis flow meter FDIC117, controlled by pump P1 and preheated to evaporation temperature using the oil heated heat exchanger E1. By entering the WFE the liquid feed was distributed along the circumference. The rotational frequency of the wiper was regulated by SIRC112 and a frequency inverter. The pressure in the WFE was set by the vacuum pump P3 and reduced from ambient pressure to process pressure by an orifice immediately upstream of the evaporator E2. The product vapor stream was condensed in heat exchanger E3 and then collected in tank T2. The sump flow was collected in tank T4. The liquid levels in T2 and T4 are regulated at a constant filling level between two conductive sensors. Volume flows were measured using oval gear flow meters FI120 and FI122 and corrected by the temperature measured by TI121 and TI123. All temperature sensors in the miniplant were copper-constantan thermocouples (Type T). The thermocouples, each with a 1 mm diameter, were positioned at the center of the tubes. They were calibrated against a PT100 resistance thermometer and demonstrated a measurement accuracy of 0.1 K within the temperature range of 20 to 150 °C.
In the WFE condensing steam was used as the heating medium on the shell side. The steam pressure was controlled to adjust the temperature of the utility side. The mass flow of the condensed steam was measured periodically every two minutes using a scale on the utility side. Under steady-state conditions, the steam condensation rate remained unchanged. However, a direct comparison between the heat balance on the product side and that on the utility side indicated persistent heat losses ranging from 1.0 to 1.5 kW.
For each experiment, the mean values of the sensor measurements with the according standard deviations were calculated. Assuming normal distributed values, the standard uncertainty associated with the results was calculated. For further derived values, the uncertainties were calculated by error propagation.
The heat flux was quantified through an enthalpy balance on the product side, considering the in- and outlet temperature, heat of evaporation, as well as the in- and out-coming mass flows.

5.1.2.2. Experimental Methods

To characterize the fluid dynamics, RTD measurements with an optical tracer were performed and optical images using a high-speed camera of the liquid film were taken. Measurements were performed according to Figure 5.2. Parallel high-speed recordings allowed for optical observation of the liquid film. Brilliant blue FCF (Merck, purity $\geq$ 97%) was used as a tracer to measure the residence time. Approximately 500 µL of a tracer solution of 0.3 g / L of brilliant blue in the studied fluid system was pulse-induced within 500 µs using an automated syringe in the feed. At the outlet, a measuring cell was installed. The measuring cell itself consists of two optical probes, which are positioned opposite each other at a distance of 5 mm and connected by two fiber optic cables to a LED (LED630-03, Roithner LaserTechnik) with a wavelength maximum of 630 nm and a photodiode (SPD17-0F, Roithner LaserTechnik) for detection with a sensitivity maximum of 620 nm. The photodiode is connected to an amplifier board, which amplifies the photocurrent in the voltage range of 0 to 4 V. The voltage signal was recorded with a measuring frequency of 20 Hz.
A high-speed camera (Phantom High Speed, Miro C210) was used for the optical examinations. Optical accessibility during operation was provided by a borescope (Leitner Industrial Endoscopy

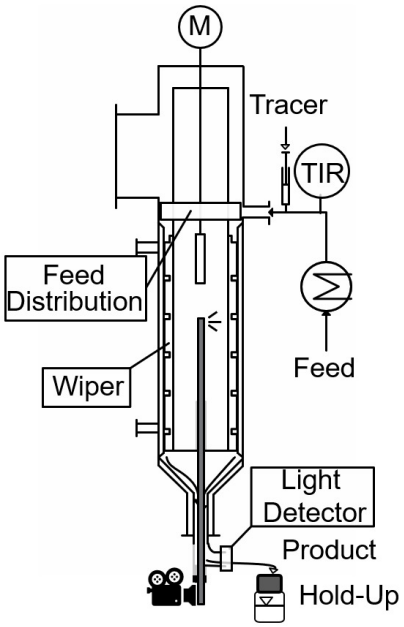

Figure 5.2.: WFE with tracer injection and detection position.

GmbH & Co. KG). The borescope shaft had a viewing direction of 90° with an image aperture angle of 55°. The illumination was provided by a 300 W xenon light source with variable light intensity control and transmission through a liquid light guide. The images during operation were taken with 2400 fps and an exposure time of 200 µs.

5.1.2.3. Investigated Operation Range

In order to systematically investigate the operating behavior of WFE the main influencing parameters were varied. For a given geometry, the operating behavior can be controlled by adjusting the wiper speed w, the feed preheating T_F, the superheat ΔT, the operating pressure p_p, the resulting evaporation temperature T_p and the liquid peripheral load Γ [31]. The latter describes the volume flow $\dot{V}$ related to the inner circumference πD (Equation 5.1) [17, 81]:

$$\Gamma = \frac{\dot{V}}{\pi D} \tag{5.1}$$

For the experiments diethylene glycol (Carl Roth, purity $\geq$ 99% (GC)) and decan-1-ol (Merck, purity $\geq$ 99% (GC)) were selected as test fluids with an evaporation temperature of 90 to 140 °C at typical pressures of 5 - 20 mbar based on the criteria formulated by Appelhaus *et al.* [23]. To further quantify the influence of pressure and consider a highly volatile system, isopropyl alcohol at 1000 mbar was chosen. The relevant thermophysical properties density, surface tension, and viscosity of the components were measured by Appelhaus *et al.* and corresponding equations were developed to estimate the properties as a function of temperature [23].

To evaluate the influence of the thermophysical properties on the fluid dynamics, the equivalent film thickness δ_{film} of a falling film was calculated based on the peripheral load and the fluid properties

according to Equation 5.2 provided by Nusselt for the laminar falling film [111, 134].

$$\delta_{\text{film}} = \left(\frac{3 \cdot \eta^2}{\rho^2 \cdot g}\right)^{1/3} \cdot (\text{Re}_{\text{film}})^{1/3} \tag{5.2}$$

The characteristic length of the dimensionless numbers was set to $L = \delta_{\text{film}}$, which simplifies Equation 5.2 to Equation 5.3.

$$\delta_{\text{film}} = \left(\frac{3 \cdot \eta \cdot \Gamma}{\rho \cdot g}\right)^{1/3} \tag{5.3}$$

Since both the heat transfer coefficient and the mass flow rate can vary in the experiments, the evaporation ratio ξ was selected as the ratio between the mass flow rate of the distillate $\dot{m}_D$ and the mass flow rate of the feed $\dot{m}_F$ in order to evaluate the evaporator utilization:

$$\xi = \frac{\dot{m}_D}{\dot{m}_F} \tag{5.4}$$

The transferred heat flows $\dot{Q}$ and the observable heat flux $\dot{q}$ are directly coupled with the evaporation ratio for a liquid-boiling feed:

$$\dot{q} = \frac{\dot{Q}}{A} = h \cdot \Delta T \approx \frac{\dot{m}_D \cdot \Delta h_v}{A} = \frac{\xi \cdot \dot{m}_F \cdot \Delta h_v}{A} \tag{5.5}$$

For the experimental results, therefore, the proportionality $\dot{q} \propto \xi$ is valid for $\dot{m}_F = const.$.

Table 5.1.: Used Antoine parameters of diethylene glycol, isopropyl alcohol and decan-1-ol.

component	A	B	C	pressure range [mbar]
diethylene glycol (fitted to [143])	7.9508	3994.831	0	10.6…978
isopropyl alcohol [183]	4.8610	1357.427	-75.815	330…1333
decan-1-ol [184]	4.53321	1742.392	-115.236	12.4…350

In order to evaluate the effect of evaporation, it is necessary to vary the transferred heat. Assuming a constant overall heat transfer coefficient, the temperature difference between the utility side and the product side is essential for the transferred heat flow. For pure components and constant pressure levels at the product and utility side, it can be assumed that both sides are isothermal. The temperature difference can therefore be calculated according to Equation 5.6.

$$\Delta T = T_s - T_p \tag{5.6}$$

The utility side temperature T_s was calculated using IAPWS97 equations for water and steam properties [133]. The temperature on the product side is calculated using the Antoine equation (Equation 5.7) with the coefficients given in Table 5.1.

$$\log_{10} p = A - \frac{B}{C + T} \tag{5.7}$$

5.1.2.4. Residence Time Distribution Measurements

The experimentally determined voltage values of the absorption measurement cell are used to calculate the residence time distribution at the bottom draw. Therefore, the general form of Equation 5.8 was applied to calculate the Exit-Function $E(t)$ [95]:

$$E\left(t\right) \;=\; \frac{c\left(t\right)}{\int_0^\infty c\left(t\right) dt} \tag{5.8}$$

Assuming applicability of the Beer-Bouguer-Lambert extinction law, the photocurrent and, therefore, the measured drop in voltage ΔU are proportional to the actual concentration of the tracer. This assumption was validated using calibration experiments on both a UV/vis spectrometer and also on the system itself and is fulfilled for the concentrations used. The concentration of tracer molecules can therefore be rewritten to Equation 5.9, whereby the proportionality factor k depends on the temperature, the initial concentration and the gap width:

$$c\left(t\right) = k \cdot \left(U_0 - U\left(t\right)\right) \tag{5.9}$$

This allows the residence time distribution to be determined directly from the voltage drop $\Delta U = U_0 - U\left(t\right)$. Discretisation then results in Equation 5.10.

$$E(t) = \Delta U(t) / \sum_{i=1}^{n} (\Delta U(t) \Delta t) \tag{5.10}$$

Nonetheless, the use of Equation 5.10 is confined to situations involving minor concentration variations and presumes that all tracer molecules can exit the apparatus within a finite period. These conditions might not apply under very high evaporation ratios, which could result in tracer precipitation. However, this scenario was not analyzed in this research.

For the evaluation of the results from the residence time experiments, the data are smoothed using a median filter with a filter width of 20 data points. The measurement signal is corrected by a linear baseline and the residence time distribution is calculated from the corrected voltage difference. The residence time distribution was shifted so that no negative values occurred and the integral of the RTD fulfilled Equation 5.11.

$$\lim_{t \to \infty} F(t) = \int_0^\infty E(t) dt = 1 \tag{5.11}$$

At least three different duplicate measurements of the residence time distribution per experimental data point were performed. For each data point, the mean value and the associated standard deviation were calculated.

5.1.3. Results and Discussion

The effect of peripheral load, temperature difference, and fluid type on residence time distributions were measured and analyzed.

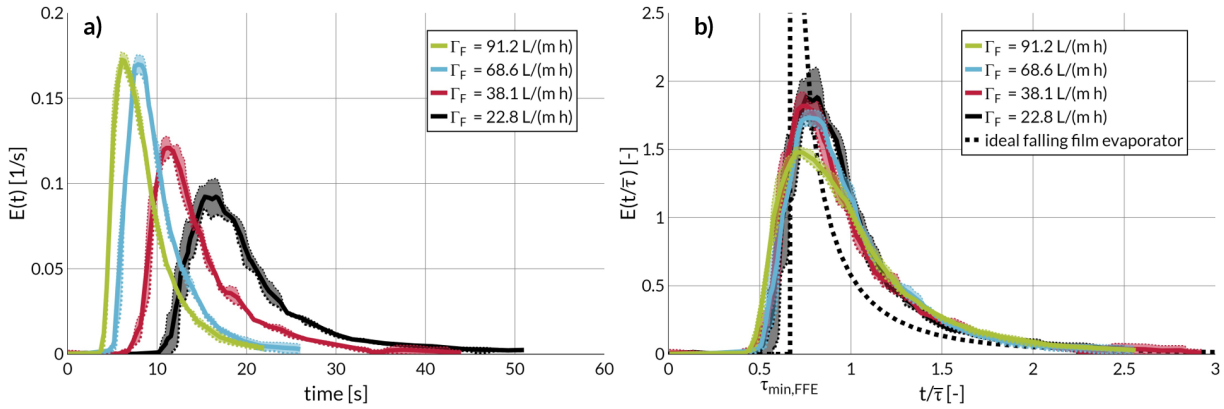

Figure 5.3.: Residence time distribution curves for different peripheral loads without evaporation in a) dimensional representation and b) normalized representation for diethylene glycol at 8 mbar and a wiper speed of 1.05 m/s.

5.1.3.1. Effect of Peripheral Load

The peripheral load is the main factor influencing the residence time distribution, as it defines the liquid volumes as well as the mass flows within the apparatus [22]. The effect of increasing peripheral load for diethylene glycol without evaporation is shown in Figure 5.3 a). The residence time distributions become broader and shift towards higher mean residence time for a decreasing peripheral load. The general distribution can be characterized by a defined lag-time until the first tracer elements reach the evaporator outlet followed by a steep increase once the minimal residence time is reached and a prolonged tailing after the RTD reaches its maximum. The shape of the residence time distributions measured is very common for WFE and can be explained by the periodic mixing of fluid in a bow wave in front of the wiper with a much slower liquid film adhered to the apparatus wall, which acts as a liquid reservoir.

When the resulting residence time distributions are normalized with their respective mean residence time $\overline{\tau}$ (Figure 5.3 b)), it can be seen that although the mean residence time varies with a different peripheral load, the residence time distribution is self-similar and the normalized curves overlap vastly for different process conditions. For typical process conditions, the minimum residence time is approximately 1/3 $\overline{\tau}$, the maximum peak is at 2/3 $\overline{\tau}$, and the ninth decile is reached after 2.5 $\overline{\tau}$ to 3 $\overline{\tau}$. For further reference, the normalized RTD behavior of an ideal falling film evaporator (FFE) is also shown in Figure 5.3 b). The RTD of the falling film evaporator was calculated by assuming a laminar falling film of constant thickness δ_{film} on a flat wall according to Equation 5.12 [185].

$$E_{FFE}(t/\overline{\tau}) = \begin{cases} 0 & \text{for } t/\overline{\tau} < 2/3 \\ \frac{\overline{\tau}^3}{3t^3}\left(1 - \frac{2\overline{\tau}}{3t}\right)^{-1/2} & \text{for } t/\overline{\tau} \geq 2/3 \end{cases} \tag{5.12}$$

Comparing the RTD of an ideal laminar falling film with that measured in the WFE shows that while both the falling film evaporator and WFE have RTD peaks at 2/3 $\overline{\tau}$, the WFE exhibits a shorter minimum residence time and a more significant tailing. The similarity between the two devices originates from their closely related fluid dynamics, as falling films are present in both. However, the

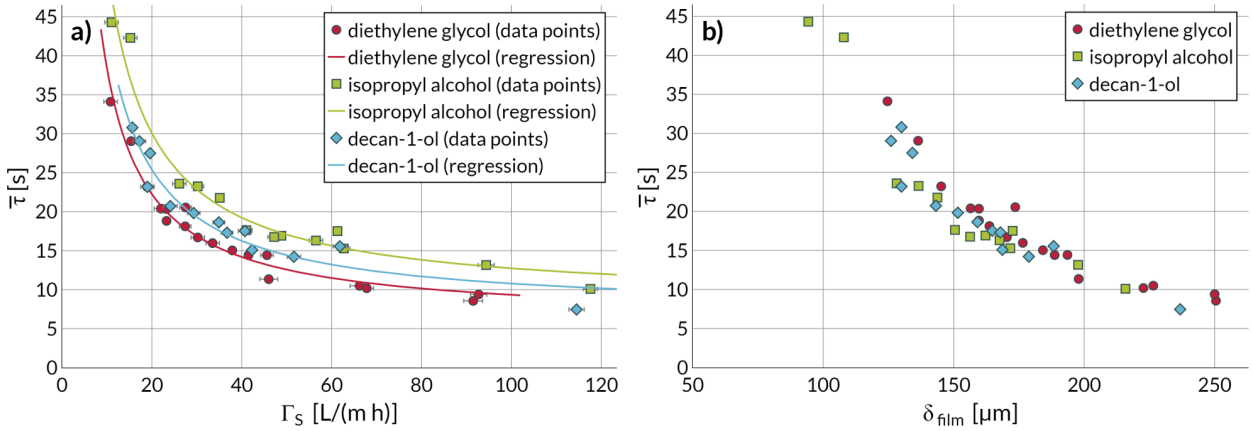

Figure 5.4.: Dependence of the mean residence time for diethylene glycol, isopropyl alcohol and decan-1-ol as a function of a) the mean peripheral load and b) the equivalent film thickness of a falling film.

differences can be explained from variations in flow morphology, particularly the characteristic zones illustrated in Figure 5.1, where only the film zone is present in falling film evaporators. The reduced minimum residence time is attributed to the significant impact of the bow wave on the residence time. Although in both the falling film evaporator and the WFE, the axial flow is solely gravity driven, the fluid volume in the bow wave is increased compared to the film thickness, resulting in increased vertical flows. At the same time, the film builds up a fluid reservoir, with a smaller vertical velocity compared to that of the bow wave. This leads to a slower decrease of the Exit-function. However, it must be stated that the absolute mean residence time in falling film evaporators differs from the mean residence time in WFE, so that the dimensional RTD is vastly different for otherwise identical peripheral loads.

Figure 5.4 a) presents the dependence of the mean residence time on the peripheral load and equivalent film thickness of a falling film evaporator without evaporation. The mean residence time can be described using a hyperbolic function, which is equivalent to $\overline{\tau} \propto \Gamma^{-1}$. The mean residence time in the investigated set of experiments ranges in 8 s $\leq \overline{\tau} \leq$ 30 s for peripheral loads above 20 L/(m·h).

To further evaluate the results of this study, Table 5.2 compares the numerical values of this work with previously published residence time measurements for different fluids and wiper systems. Despite differences in wiper types and apparatus dimensions, the mean residence times in this study are similar to other measured data. Note that Fonseca *et al.* and Zeboudj *et al.* conducted measurements under very low peripheral loads, explaining their relatively high mean residence times considering their small apparatuses [77, 130]. In addition, all the residence time measurements stated were carried out at room temperature, except for the measurements by Jasch *et al.* which also considered elevated temperatures [22]. Nevertheless, the impact of evaporation on the residence time distribution was not examined in the mentioned studies, despite Widmer and Giger state that evaporation will significantly affect the residence time distribution [32]. This effect is therefore discussed in more detail in paragraph 5.1.3.3.1.

Table 5.2.: Overview of reported residence time measurements for different solvents and wiper types compared to this work.

wiper type	**test fluids**	d_0/mm	L/mm	A/m^2	**reference**
roller	diethylene glycol	80	256	0.064	*this work*
roller & comb	ethylene glycol	80	256	0.064	Jasch *et al.* [22]
comb	tributyl citrate (78wt%) & butan-1-ol (22wt%)	50.8	200	0.032*	Fonseca *et al.* [130]
blade	glycerol-water	55	250	0.043	Zeboudj *et al.* [77]
structured roll	tri- and tetraethylene glycol	150	600	0.282 *	Cvengroš *et al.* [51]
comb	tri- and tetraethylene glycol	150	600	0.283*	Cvengroš *et al.* [50]
blade	glycerol, oppanol, silicone oil	150	350	0.165*	Schweizer and Widmer [6]
blade	water	-	-	16	Widmer and Giger [32]
fixed & hinged blade	water	50	624*	0.098	Bressler [123]

$\Gamma/(\mathrm{L}\cdot\mathrm{m}^{-1}\cdot\mathrm{h}^{-1})$	η/(mPa · s)	w/ (m · s^{-1})	$\overline{\tau}$/s	**reference**
10 to 120	0.7 to 2.15	0.2 to 2.1	8 to 80	*this work*
29 to 58.8	7 to 21	0.84 to 2.3	14 to 25	Jasch *et al.* [22]
9.4*	-	0.16	20 to 120	Fonseca *et al.* [130]
0.2*	10 to 12	1.8 to 5.3	16 to 20	Zeboudj *et al.* [77]
	50	0.64 to 1.63	15.6 to 34.3	Cvengroš *et al.* [51]
40 to 127*	50	0.64 to 2.68	13.9 to 41.7	Cvengroš *et al.* [50]
110 to 2300	80 to 10 000		1 to 22	Schweizer and Widmer [6]
250 to 4000	1	-	10 to 20	Widmer and Giger [32]
65 to 200*	1	1.8 to 5.5	3 to 14	Bressler [123]

*: calculated value; -: not specified

5.1.3.2. Fluid Properties

The fluid properties, namely the surface tension, viscosity, and density, influence the fluid dynamics in WFE, as a gravity-driven, falling film occurs. In evaporating systems, temperature changes with operating pressure as well as the component under investigation, resulting in a variation of the thermophysical properties.

The results of diethylene glycol, isopropyl alcohol, and decan-1-ol at each pressure level are presented in Figure 5.4 a). Details about the related thermophysical properties for these components can be derived from Appelhaus *et al.* [23]. Table 5.3 summarizes the values of the test fluids used for isothermal conditions without evaporation, as well as their experimental uncertainties. The associated film Reynolds numbers are within the range of 1.5 to 30 while the Weber numbers are within the range of 0.003 to 0.3. Detailed numerical values of the shown data points are provided in Supplementary File S3, available online. The definition of dimensionless numbers are summarized in the nomenclature.

The proportionality $\overline{\tau} \propto \Gamma^{-1}$ holds for all experimental systems, although the specific range varies. For otherwise identical process conditions, diethylene glycol showed the lowest mean residence times of all fluids tested, while isopropyl alcohol showed the highest residence times. This goes along with diethylene glycol having the highest values for liquid density, viscosity, and surface tension, while isopropyl alcohol showed the lowest values for all properties. However, without evaporation, a film

Table 5.3.: Density ρ, viscosity η and surface tension γ of diethylene glycol, decan-1-ol, isopropyl alcohol at evaporation temperatures for the investigated process pressure p.

	p	ρ	η	γ	(η/ρ)
unit	bar	(g/cm^3)	(mPa·s)	(mN/m)	(s/cm^2)
diethylene glycol	8.0 ± 0.2	1.106 ± 0.001	2.15 ± 0.10	28.2 ± 1.2	194.4 ± 9.0
decan-1-ol	15.0 ± 0.5	0.820 ± 0.001	1.10 ± 0.08	14.9 ± 0.3	134.1 ± 9.8
isopropyl alcohol	1000 ± 20	0.780 ± 0.001	0.72 ± 0.05	12.8 ± 0.4	92.3 ± 6.4

rupture was not observable for the different fluids, so it was concluded that the difference in surface tension may not explain the differences in residence time. The density of decan-1-ol and isopropyl alcohol is 74% and 70% of diethylene glycol while the viscosity is 51% resp. 33% of diethylene glycol. To understand the differences in mean residence time, we need to consider the effect of the fluid properties on the fluid dynamics, whereby a higher density accelerates the gravity driven fluid flow while a higher viscosity decreases the fluid velocity. This becomes obvious when plotting the mean residence time over the equivalent film thickness in Figure 5.4 b), in which the different fluid systems become indistinguishable. Although the equivalent film thickness does not directly represent the real film thickness, it incorporates crucial fluid properties and their effect on fluid dynamics. Therefore, it seems to represent the overall changes in fluid volume in the investigated WFE well. The ratio $(\eta \cdot \Gamma)/(\rho)$ featured in Equation 5.3 appears to be the key indicator to compare various fluid systems under stable laminar flow conditions.

5.1.3.3. Residence Time Distribution during Evaporation

In WFE fluid dynamics, heat transfer and a change in liquid flow due to evaporation are highly interconnected. In general, wiper-induced turbulence improves heat transfer in WFE, while falling film evaporators are known to have superheated walls that lead to instabilities in the liquid film, which also affects the fluid dynamics [186]. Additionally, the rising vapor stream as well as a reduction in the peripheral load along the evaporator height influence the residence time distribution. The effect of increased heat fluxes and wiper speed is discussed in paragraph 5.1.3.3.1 and paragraph 5.1.3.3.2

5.1.3.3.1. Effect of Evaporation To investigate the effect of evaporation more closely, residence time distributions at different evaporation ratios and heat fluxes for diethylene glycol are shown in Figure 5.5 a) with dimensions and in Figure 5.5 b) normalized. Here, an increase in the temperature difference is equivalent to an increase in the heat flux and evaporation ratio. The heat fluxes vary in a range from 0 to 30 $\mathrm{kW/m^2}$, which corresponds to evaporation ratios of up to 0.6. An increase in the heat flux and thus higher evaporation ratios initially leads to a reduction of the sump peripheral load. The average residence times therefore shift towards higher values at higher heat flux, and the residence time distribution becomes broader. Interestingly, the RTD remains self-similar in the normalized representation but shows greater deviations between the individual experiments with evaporation than without evaporation. This indicates that the fundamental fluid dynamics is maintained but that the change in the liquid fractions in the film zone, bow wave, and gap zone as shown in Figure 5.1 affects the residence time distribution. To carry out a more detailed analysis of the influence of evaporation, the dependence of the mean residence time of the peripheral load

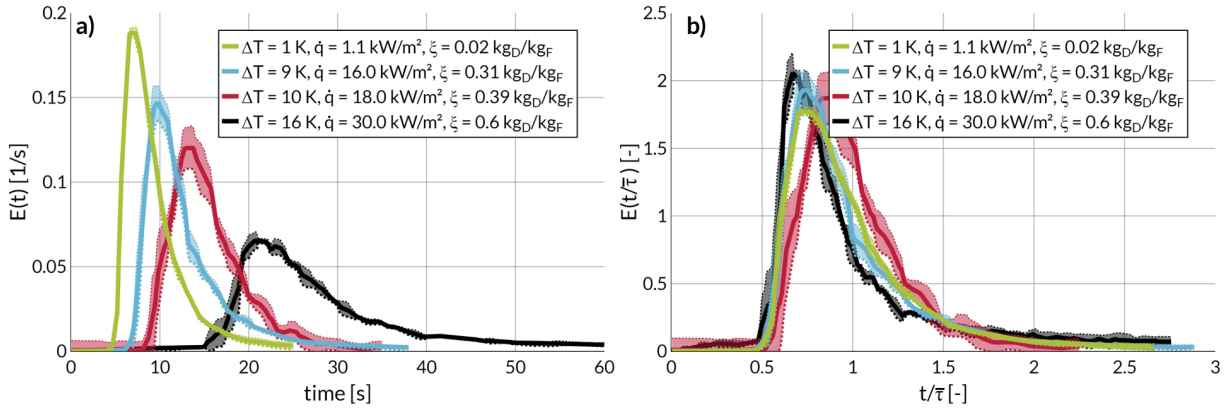

Figure 5.5.: Residence time distribution curves for different driving temperature differences in a) dimensional representation and b) normalized representation for diethylene glycol at 8 mbar and a wiper speed of 1.05 m/s.

is plotted in Figure 5.6 for different evaporation ratios. As discussed in subsubsection 5.1.3.2, the peripheral load is the main factor that influences the mean residence time. In order to distinguish the influence of evaporation and therefore the reduction of the peripheral load from the feed peripheral load, the mean residence times in Figure 5.6 are plotted against the sump peripheral load. Detailed numerical values of the underlying data points are given in Supplementary File S4, available online. As evaporation reduces liquid load, the mean residence time increases, as anticipated. However, the mean residence time with evaporation does not differ significantly from the general trend for experiments without evaporation when plotted against the sump peripheral load for evaporation ratios up to 0.5 as depicted in Figure 5.6. This seems counterintuitive at first, since the sump peripheral load only refers to the bottom of the evaporator, and therefore a higher axial velocity above this area is expected, resulting in a lower mean residence. Consequently, if the peripheral load were the only relevant parameter, the experimental points with evaporation in Figure 5.6 would lie below the data points without evaporation, which they do not. Therefore, additional influencing variables must affect the mean residence time and the fluid dynamics.

Furthermore, if the sump peripheral load becomes very low as the evaporation ratios increase, the mean residence time tends to rise more than it can be explained by the decrease of the local peripheral load, especially if one considers that the average peripheral load is higher than the sump peripheral load. An explanation for this could be found in the experimental setup and the associated hold-up volumes between the evaporator and the measurement cell, upstreaming gas flows decelerating the liquid flow, or a promoted film breakup. However, by modeling the experimental setup Appelhaus *et al.* showed that the experimental periphery influenced the result, but does not fully explain the increase in mean residence times. Furthermore, countercurrent vapor flows exhibit a negligible impact on liquid flow [26].

To further discuss the influence of possible film breakup and validate the assumption of a self-similar fluid dynamic behavior up to this point, optical images of a single segment of the evaporator for selected operating conditions are presented in Figure 5.7. In addition, full video recordings can be found in the Supplementary Files, available online. For different liquid loads and with low temperature

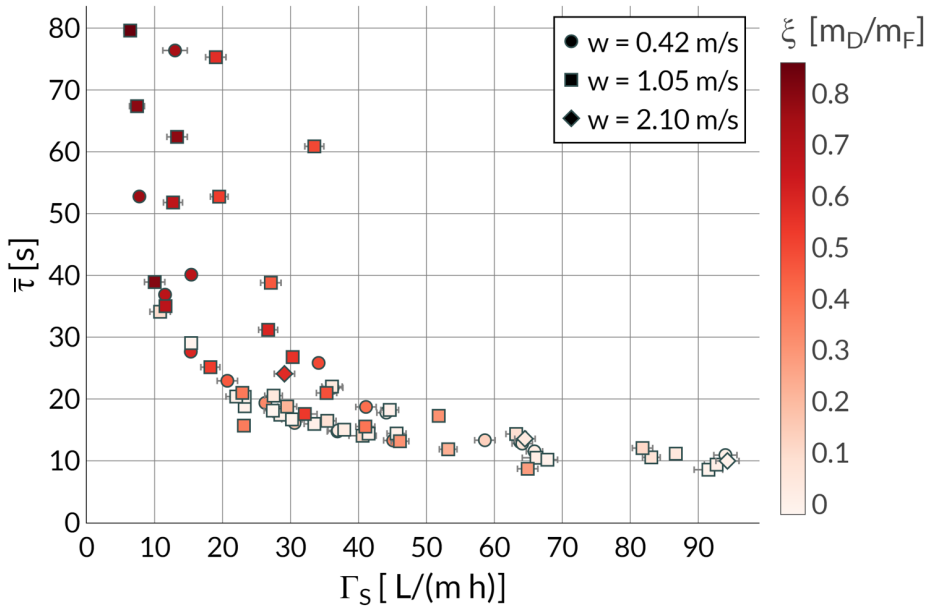

Figure 5.6.: Effect of sump peripheral load and evaporation ratio on the mean residence time for diethylene glycol at 8 mbar and different wiper speeds.

differences, the film remains constant, which is visible by the lack of bubbles and droplets on the evaporator surface. An increase in the liquid load leads to a more pronounced bow wave. The self-similarity therefore indicates a stable operation point with a fully wetted wall. However, for higher evaporation ratios, Figure 5.7 right side, the film starts to rupture and small droplets form very quickly. As these droplets adhere to the surface, the axial velocity decreases to zero m/s at that area. Thus, axial mass flow occurs mainly in the bow wave, which also tends to gradually diminish for very small peripheral loads but high evaporation ratios. This destabilization of liquid films are also reported for falling film evaporators [186]. Therefore, a large proportion of the disproportionate increase in the mean residence time is attributed to increasing dewetting. This should be taken into account when evaluating the thermal load, especially for very high evaporation ratios. This effect might be further amplified if mixtures comprising multiple - especially light-boiling - components are processed, as such compositions are recognized for their tendency to destabilize thin liquid films due to Marangoni effects [187]. To further investigate the impact of evaporation, it is essential to differentiate the potential rupture of the film from the reduction in peripheral load. This can be achieved through a segmental approach that models the residence time distribution, considering the reduction in liquid caused by evaporation in comparison to experimental results.

5.1.3.3.2. Wiper Speed The effect of the wiper speed on the mean residence time is illustrated in Figure 5.8. Detailed numerical values of the underlying data points are given in Supplementary File S5, available online. With evaporation ratios close to zero, the wiper speed does not significantly affect the mean residence time, which is consistent with the results of other studies for plain roller wipers [22]. It is important to note that the local force equilibrium at the wiper element is crucial, as the impacts of gap reduction and increased deceleration from the wiper element appear to compensate each other. In contrast, for wipers featuring structured surfaces, Cvengroš *et al.* 2000 and Cvengroš

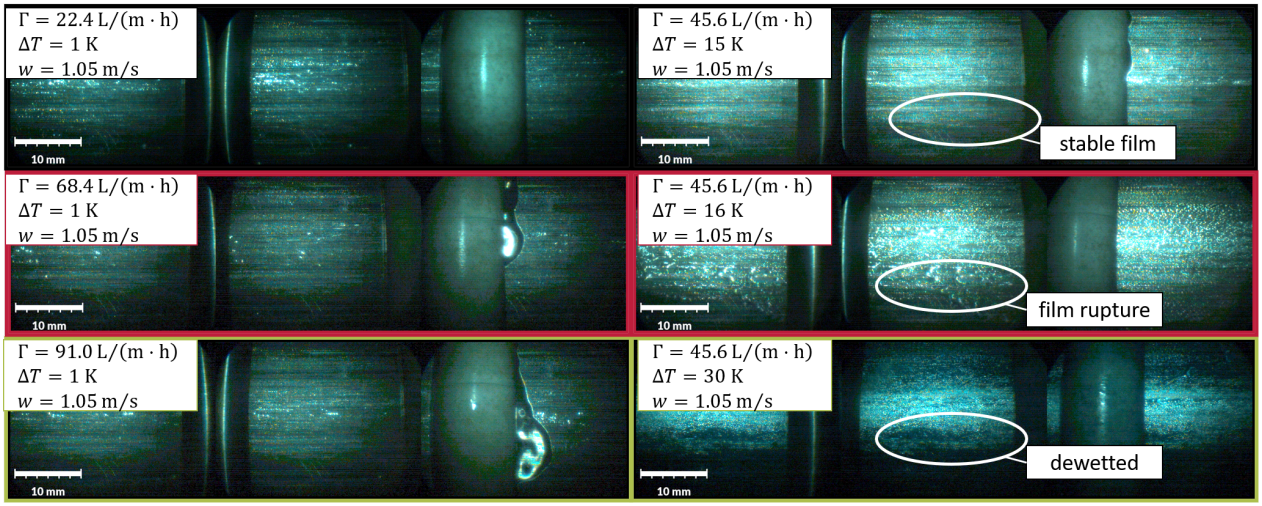

Figure 5.7.: Optical investigations of the inner surface of the evaporator for diethylene glycol. While the film remains stable for different peripheral loads without evaporation, a film rupture is observable for higher heat fluxes ultimately resulting in a dewetted surface.

et al. 2001 found that the mean residence time clearly depends on the speed of the wiper, directly influenced by the direction of the impulse from the wiper [50, 51]. The significance of the force equilibrium at the wiper element is evident, as research by Widmer and Giger and Schweizer and Widmer shows that for wipers with unstructured surfaces but a fixed gap, the mean residence time may vary with speed based on the fluid's thermophysical properties [6, 32].

Under evaporation conditions, the mean residence time increases, which has already been discussed in paragraph 5.1.3.3.1. However, it can also be seen that if evaporation occurs, the influence of the wiper speed becomes relevant for the mean residence time, as it increases up to a wiper speed of 1 m/s. The evaporation ratio and therefore the transferred heat flux also increase simultaneously. The increased turbulence due to the higher wiper speed leads to an increase in the product-side heat transfer coefficient, an effect that has also been described in the literature [63, 123]. As long as the product-side heat transfer coefficient limits the integral heat transfer coefficient, this will increase the heat flow and evaporation ratio, ultimately increasing the mean residence time. However, once the thermal resistance on the product side does not limit the heat transfer, a further increase in wiper speed does not affect the mean residence time. Thus, this effect will be mainly limited to appliances with low thermal resistances on the heating side and the wall side.

In terms of film stability, through wiping, the destabilizing effect due to increased heat transfer and the stabilizing effect due to faster renewal of the liquid film must be considered simultaneously. However, although a stabilizing effect of the wiping can be relevant for kinetically hindered film ruptures, our optical investigations during the evaporation indicate that the wiping speed does not significantly influence film stability and that the increase in heat transfer and the associated lower peripheral loads dominate fluid dynamics. The effect of the wiper speed is therefore primarily an increase of the mean residence time due to increased evaporation ratios and reduced liquid loads, whereas possible dewetting processes are significantly faster than the renewal by the wiper.

The behavior could be different if there are wave instabilities, as often observed in falling film

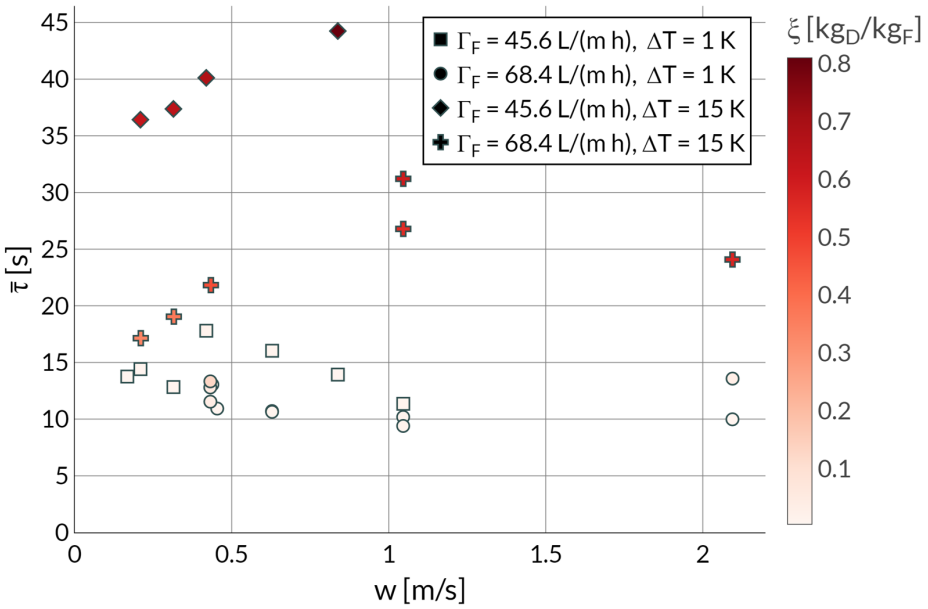

Figure 5.8.: Influence of the wiper speed on the mean residence time for different evaporation ratios without evaporation and with evaporation.

evaporators. Wave peaks can be two to six times larger than the mean thickness of the film [47]. The peaks are distributed by the wiper system. This stabilizes the film and leads to an increase in the average residence time as a result of the wiping process, particularly at higher film Reynolds numbers above 400 [32].

5.1.4. Conclusion

Consistent with the existing literature on fixed wiper geometries, comprehensive experimental investigations reveal that the peripheral liquid is a major factor affecting the residence time distribution in wiped film evaporators. Furthermore, the residence time distributions showed self-similarity, leading to a minimal residence time of approximately 1/3 $\overline{\tau}$ and a maximum of the Exit-function at 2/3 $\overline{\tau}$. Surface tension had no effect while a closed liquid film occurred, but may be important for systems with an actual film breakup. However, the mean residence time increases for roller wipers as the liquid density and viscosity decrease, with viscosity having the most significant impact.

Evaporation alters the residence time distribution mainly because the reduced mean peripheral load decreases axial velocities. However, this effect is superimposed at high heat fluxes, where increased evaporation tends to destabilize the film, accelerating its rupture. The latter may not be fully compensated for by a higher wiper speed, as redistribution is significantly slower than film rupture due to low liquid load in combination with elevated heat fluxes. As a result, the mean axial velocity of the liquid flow is reduced.

Another aspect during operation is the influence of the wiper speed. Although for non-evaporation conditions, the wiper frequency does not significantly affect the residence time distribution, it can increase the mean residence time during operation, as the wiper speed increases the product-side heat transfer coefficient and the evaporation ratio.

To further explore the operating behavior of WFE, the experimental parameters could be expanded to different wiper systems and binary mixtures. The heat transfer coefficient may vary between different wiper systems, influencing the residence time distribution. For inclined wiper elements, the bow wave may experience acceleration or deceleration. In the case of binary mixtures, it is anticipated that the film can become destabilized because of the enhanced surface forces resulting from Marangoni effects.

Acknowledgments

We gratefully acknowledge that this project was supported by Federal Ministry for Economic Affairs and Climate Action on the basis of a decision of the German Bundestag. This research was carried out as part of a project of the Industrielle Gemeinschaftsforschung (IGF) with project number 01IF22220N.

Abbreviations

Abbreviation	Meaning
FFE	Falling Film Evaporator
RTD	Residence Time Distribution
WFE	Wiped Film Evaporator

Nomenclature

Roman symbols

Symbol	Explanation	Unit
A	Antoine parameter	-
A	heat transfer area	m^2
B	Antoine parameter	K
C	Antoine parameter	K
c	concentration	mol m^{-3}
D	inner diameter of evaporator	m
E	Exit function	s^{-1}
h	heat transfer coeffient	W m^{-2} K^{-1}
h	heat of evaporation	J kg^{-1}
k	proportionality factor	-
p	pressure	Pa
$\dot{Q}$	heat flow	W
$\dot{q}$	heat flux	W m^{-2}
T	temperature	K
T_p	temperature product side	K
T_s	temperature utility side	K
t	time	s
U	voltage	V
$\dot{V}$	volume flow	m^3 s^{-1}
w	wiper speed	m s^{-1}

Greek symbols

Symbol	Explanation	Unit
Γ	mean peripheral load	m^3 m^{-1} s^{-1}
Γ_F	feed peripheral load	m^3 m^{-1} s^{-1}
Γ_S	sump peripheral load	m^3 m^{-1} s^{-1}
γ	surface tension	N m^{-1}
ΔT	temperature difference	K
ΔU	voltage drop	V
δ_{film}	equivalent film thickness	m

Symbol	Explanation	Unit
η	viscosity	Pa s
ρ	density	kg m^{-3}
$\overline{\tau}$	mean residence time	s
ξ	evaporation ratio	$\mathrm{kg_D\ kg_F^{-1}}$

Dimensionless Numbers

Number	Explanation	Definition
Fr	Froude number	$\Gamma^2 \cdot \delta_{\text{film}}^{-3} \cdot g^{-1}$
Ka	Kapitza number	$g \cdot \eta^4 \cdot \gamma^{-3} \cdot \rho^{-1}$
$\mathrm{Re}_{\text{film}}$	film Reynolds number	$\Gamma \cdot \eta^{-1}$
$\mathrm{We}_{\text{film}}$	film Weber number	$\rho \cdot \Gamma^2 \cdot \delta_{\text{film}}^{-1} \cdot \gamma^{-1}$

Declaration of generative AI and AI-assisted technologies in the writing process

During the preparation of this work the authors used DeepL Translate and Writefull in order to improve language and readibility. After using these services, the authors reviewed and edited the content as needed and take full responsibility for the content of the publication.

5.2. Product-side Heat Transfer Measurements under Evaporation Conditions

To contextualize and interpret the residence time measurements, the effect of peripheral load, wiper speed, and fluid properties on the heat transfer coefficient of the product side was investigated. Experimental data and equations from subsection 3.1.3 were used to calculate the heat transfer coefficients.

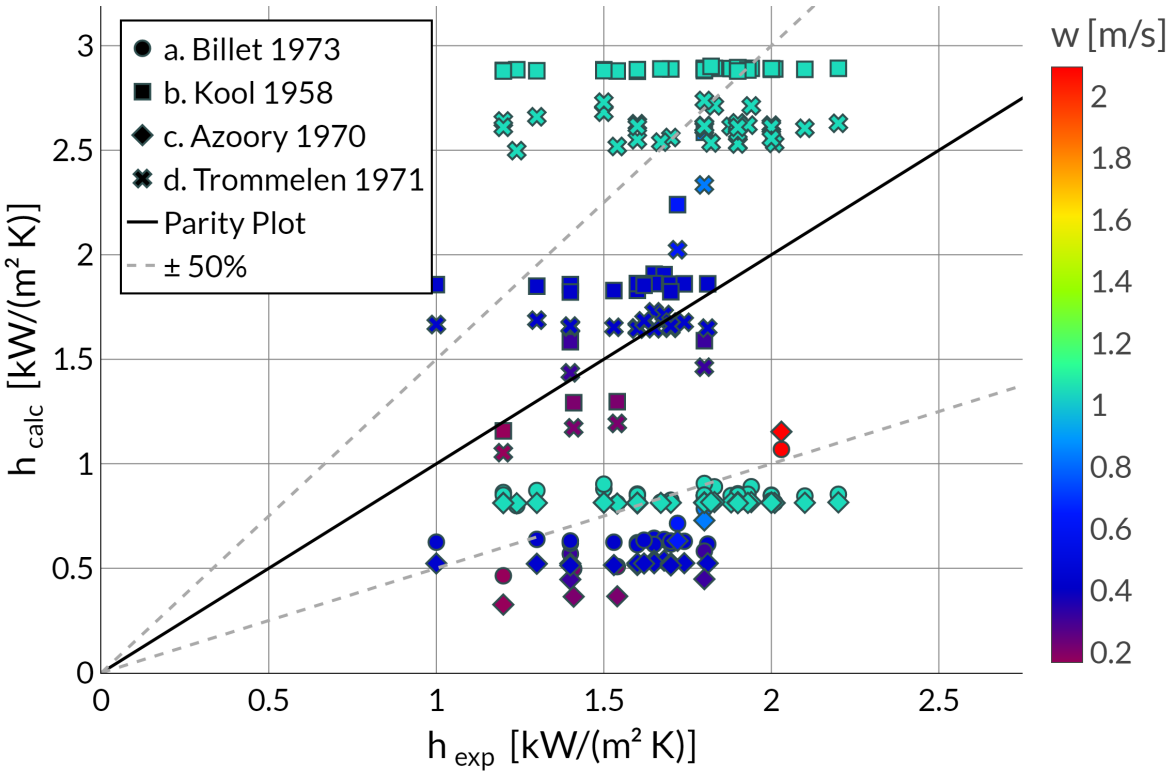

Figure 5.9.: Comparison of experimentally determined product-side heat transfer coefficients h_{exp} for diethylene glycol for different wiper speeds w with theoretical predictions h_{calc} using (a) Equation 2.8 [94], and (b) Equation 2.13 [63] without correction and with correction factors according to (c) Equation 2.16 [20] and (d) Equation 2.17 [98].

Figure 5.9 presents a parity plot that compares experimental product side heat transfer coefficients determined according to subsection 3.1.3 with predictions from selected literature correlations introduced in subsection 2.2.2. The experimental values range from 1 to 2 kW/(m^2·K) and do not include data from regimes with significantly reduced heat transfer due to dewetting. The operating range in which Jahnke *et al.* observed such a reduction is characterized by mass flows so low that residence time measurements were no longer feasible [65]. Consequently, this regime was not considered in the present study.

The experimentally determined heat transfer coefficients are higher than the typical overall values reported for systems involving organic components (see Figure 2.5). This is expected as the overall thermal resistance is the sum of the individual thermal resistances of the product side, the heating side, and the wall. Consequently, the observed range of the experimental data is physically plausible.

The uncertainties associated with the presented experimental results are provided in the Appendix (see Figure A.8). They are relatively high, mainly because of uncertainties in the measured mass flows of the sump and distillate streams, and the sensitivity of the heat transfer calculation to these measurements, as detailed in subsection 3.1.3.

The equations examined in Figure 5.9 include Equation 2.8 from Billet, which assumes steady-state heat transfer through a liquid film with K_1 set to 500 [94]. Furthermore, the penetration theory by Kool was considered (Equation 2.13) [63]. For case b, this equation was used without correction, while in cases c and d, correction factors by Azoory and Bott (Equation 2.16) [20] and Trommelen *et al.* (Equation 2.17) [98] were applied.

The experimental data were primarily recorded at wiper speeds of approximately 0.5 m/s and 1.0 m/s. None of the evaluated models were able to fully reproduce the variability observed in the experimental heat transfer coefficients, likely because of measurement uncertainties and variations of the process conditions. At both wiper speeds, the film model from Billet (a) and the corrected penetration theory by Azoory and Bott (c) systematically underestimated the product-side heat transfer coefficient [20, 94]. Compared to typical integral values for organic systems (see Figure 2.5), these predictions are too low. This discrepancy is plausible because both models were originally developed for large-scale equipment handling highly viscous media and are based on assumptions that do not apply to the current laboratory-scale configuration with low-viscosity fluids.

At the lower wiper speed of 0.5 m/s, of the penetration theory of Kool (b) yields a value range consistent with experimental observations, particularly when combined with the correction factor proposed by Trommelen *et al.* (d), which slightly improves agreement [63, 98]. However, at a higher wiper speed of approximately 1.0 m/s, both the original model by Kool (b) and the corrected version (d) significantly overestimate the experimentally determined heat transfer coefficients [63].

Although the results presented in subsubsection 5.1.3.3 reveal that increasing the wiper speed enhances heat transfer, this effect is overestimated by both the stationary film model and the penetration theory.

The approach of Kool assumes a fully scraped surface and likely overstates the influence of increased wiping frequency. Conversely, the correlation proposed by Billet does not account for the number of wiper blades in the WFE. This assumption appears to be disadvantageous for transferability, as the frequency of wiping directly influences the dynamics of film renewal and the film thickness, and thus also the heat transfer.

Among the examined equations, Equation 2.13 (b) in combination with Equation 2.17 (d) best matched the experimental data. The correction factor by Trommelen *et al.* effectively captures the influence of Prandtl number, even at low viscosities [98]. In contrast, the approach by Azoory and Bott significantly underpredicts heat transfer due to its overly conservative constant correction factor of 3.5 [20].

Equation 2.13 (b), based on transient conduction into a semi-infinite liquid layer, tends to overestimate heat transfer and thus provides an upper bound value. In contrast, Equation 2.8 (a), which assumes steady-state conduction and neglects turbulence or mechanical mixing effects, systematically underestimates heat transfer and therefore represents a lower bound value for the conditions encountered in WFE. In combination, these two models can be used to approximate a plausible range for the heat transfer coefficient.

5.3. Detailed Analysis of the Film along the Height during Evaporation

To investigate the influence of the varied parameters on the liquid film during evaporation, additional optical images were taken along the evaporator height. These images were captured for different feed loads, wiper speeds, and evaporation ratios, complementing those shown in section 5.1.
For this purpose, videos were recorded along the 25.6 cm long wiped evaporator surface after 9 cm, 16 cm, and 24 cm. The effect of superheat variation on the flow profile along the height was first examined, as shown in Figure 5.10. The left subfigure shows a moderate superheat of 10 K with an evaporation ratio of 0.67, while the right subfigure represents a higher superheat of 16 K with an evaporation ratio of 0.92, so that the liquid evaporates almost completely.
The images reveal that at the lower superheat, the flow profile remains largely unchanged along the height, characterized by a continuous liquid film and a distinct bow wave at all positions. At the higher superheat, no film break-up can be detected at the two higher measuring points either, whereas rapid liquid film break-up with extensive dry spots occurred in the lower region of the evaporator. For this operating point, the average residence time increased significantly to approximately 120 s, whereby the average residence time distribution was subject to substantially higher measurement deviations than at $\Delta T = 10\ K$. These observations support the hypothesis that at high evaporation ratios, the liquid film increasingly ruptures and is not renewed fast enough by the wiping process.
To further examine the effects of wiper speed and superheat, the wiper speed was varied for a peripheral load of $\Gamma = 68.6\ \mathrm{L/(m \cdot h)}$ and a superheat of 20 K, as shown in Figure 5.11. In the left image, the wiper speed was set to 1.05 m/s, while in the right image it was reduced to 0.42 m/s. In general, heat transfer improves with higher wiper speed, achieving an increase in evaporation ratio from 0.6 to 0.74. Consequently, the reduction in the volume of the bow wave is reduced at lower wiper speeds, whereas the bow wave gradually disappears at higher wiper speeds in the lower area of the evaporator. It can be observed that the film break-up is more noticeable in the experiment with the increased wiper speed, as a result of the reduced liquid peripheral load. At the same time, the mean residence time increases with a higher wiper speed, as discussed in section 5.1.

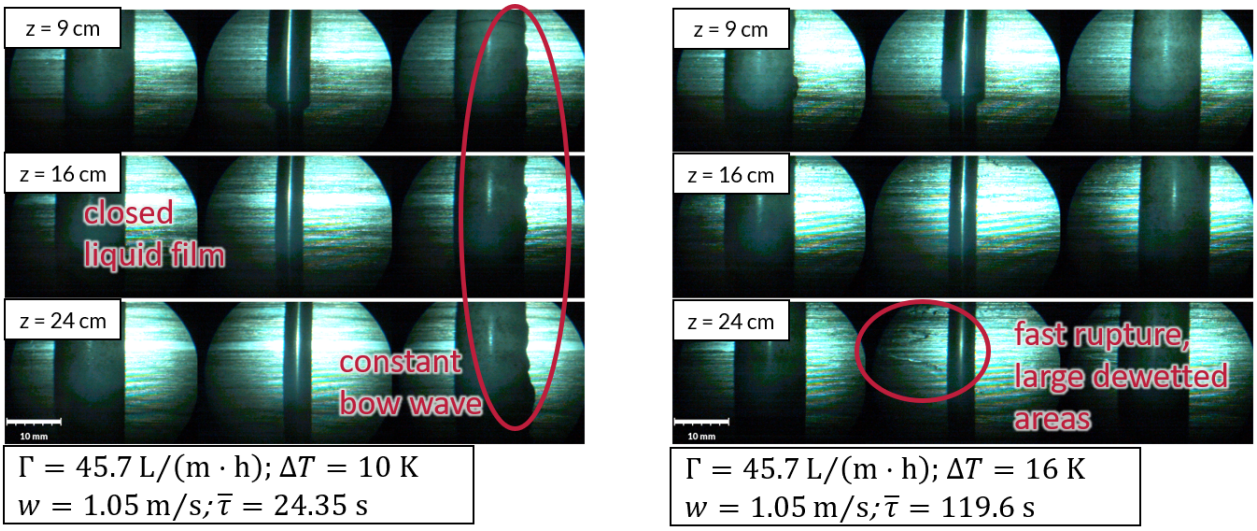

Figure 5.10.: Height series for a peripheral load of $\Gamma = 45.7\ \mathrm{L/(m \cdot h)}$ and a wiper speed of $w = 1.05$ m/s. **Left:** with a superheat of 10 K. **Right:** with a superheat of 16 K.

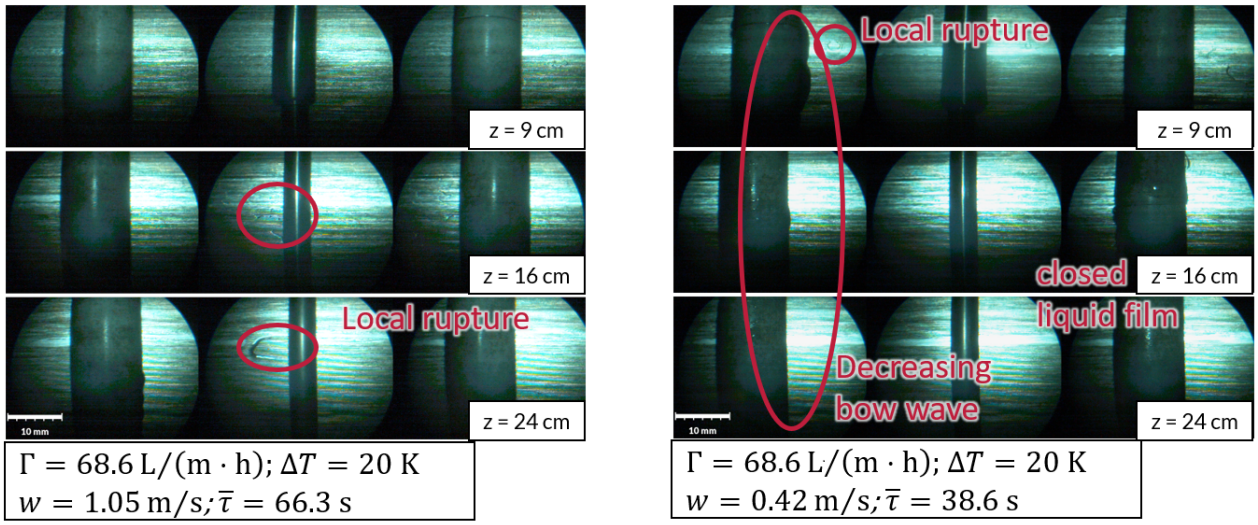

Figure 5.11.: Height series for a peripheral load of $\Gamma = 68.6\ \mathrm{L/(m \cdot h)}$ and a superheat of $\Delta T = 20\ \mathrm{K}$. **Left:** wiper speed of 1.05 m/s. **Right:** wiper speed of 0.42 m/s.

Figure 5.11 shows that film rupture is more pronounced at higher wiper speeds due to the enhanced heat transfer and therefore reduced peripheral load near the outlet of the evaporator. Conversely, at the lower wiper speed, local film ruptures were observed in the upper evaporator region. However, these remained relatively small and were quickly re-wetted by the wiper system. Although these local ruptures did not affect RTD or heat transfer in a significant way, they highlight the importance of dynamic effects for film stability in WFE. It can be concluded that local film ruptures do not notably influence process variables unless they occur in a larger area and persist over relevant time scales. However, rapid rupturing can result in a longer mean residence time, although it may initially leave the heat transfer unchanged, provided that the entire internal surface is periodically dewetted. This can result in a higher thermal load and eventually increased product degradation, despite seemingly consistent evaporation performance, potentially reducing overall process efficiency.

6. Modeling of Fluid Dynamics in Wiped Film Evaporators

To better understand the influence of process variables on fluid dynamics, a mechanistic model was developed in Modelica and validated against experimental data. In this chapter, the main assumptions underlying the model are outlined and their respective validity ranges are assessed. The structure of the model, including the physical equations, is presented and contextualized with experimental results from prior studies. The results are evaluated with respect to their transferability and the potential to extend the model to include heat transfer, which is further addressed in chapter 7.

6.1. Structure of the Developed Model

As demonstrated by the experimental results presented in chapter 5 and previous theoretical studies discussed in section 2.3, integral methods for modeling WFEs often result into large uncertainties due to significant variations in superheat, fluid properties, and peripheral load along the evaporator height. In contrast, CFD simulations, while detailed, are highly application-specific and challenging to generalize because of complex free surface dynamics at the gas-liquid interface and the variability of wiper geometries.

Thus, an intermediate modeling approach was developed in this work, considering the WFE in a segmental approach along the evaporator height. This approach avoids the level of detail and computational complexity of CFD models while, at the same time, it provides greater generalizability and applicability to different systems than integral equations.

For heat transfer, several segmental models have already been proposed, which demonstrated good agreement with experimental data on heat transfer, separation performance, and rectification effects [31, 40, 105]. In fluid dynamics, segmental models, such as those for stirred tank cascades, have been fitted to experimental RTD [77]. While these models accurately reproduce the measured residence times, they fall short in terms of predictability and extrapolation capability.

As part of this work, a fluid dynamic model was therefore initially developed that can reproduce the operating behavior of a WFE without evaporation. By closely coupling the model with physical boundary conditions, transferability was ensured. In addition to the actual residence time distribution, which is already known from the experimental measurements, the model also provides insights into liquid distribution and flow velocities within the apparatus.

Modeling was performed using the object-oriented language Modelica [188]. Modelica is an equation-based language designed to solve hybrid algebraic-differential equation systems. The system of equations, balanced in terms of unknowns and equations, is solved for each time step, with initial conditions defined for each simulation. In this approach, the individual regions of the WFE, such as the bow wave, film zone, and gap zone, are represented by algebraic and differential equations, which can be assembled into more complex fluid dynamic models by instantiating and connecting submodels. Because Modelica supports polymorphism and inheritance, it can be used for the development of a versatile global model. Concepts and equations can be easily adjusted or expanded to incorporate

different wiper designs or heat transfer equations at top level. The submodels are linked by connectors, enabling the transfer of state variables (e.g., pressure) and flow variables (e.g., mass flow rate associated with concentrations and specific enthalpies).

For the initial configuration of the model, geometric and operational parameters from subsection 2.1.2 were considered. The thermophysical fluid properties were calculated using TILMedia. Apparatus-related influencing factors included the evaporator diameter (d_r), number of wiper elements (N_B), wiper diameter (b), wiper type, and evaporator height (l_{WFE}). Operational parameters considered were rotational frequency (n) and feed mass flow rate ($\dot{m}_F$), alongside pressure and temperature, which indirectly influence residence time behavior through changes in density and viscosity.

When the model is extended to include the heat transfer in chapter 7, the superheat (ΔT) must also be considered, which is determined from the boiling temperatures at the given operating pressures in each segment. Therefore separate fluid class models are developed to incorporate the thermophysical properties of the model fluids characterized in chapter 4.

While all model variables are dynamically calculated at each time step during the simulations, the evaluation of model performance was focused on a set of physically meaningful process variables relevant to operational performance. Therefore, the velocity profile in the apparatus, the calculated film thicknesses as well as the total liquid hold-up and RTD were compared with the findings from experiments.

6.1.1. Force and Momentum Balance

While most of the model structure and equations are covered in subsection 6.2.2, the equations for force and momentum balance are detailed below.

For roller wipers, both the gap width and the rotational speed of the wiper roller around its own axis v_k (see Figure 6.3) are crucial for the resulting velocity profile within the wiper gap and thus for the formation of the film zone. The turbulence within the gap and the energy required for the wiping are strongly coupled to the friction between the fluid and the wiper, which depends on the rotational speed of the motor as well as the rotational speed of the roller wiper element around its own center. The latter can be determined theoretically based on a combined force and momentum balance, assuming that both the force equilibrium (Equation 6.1) and the moment equilibrium (Equation 6.2) are satisfied in steady-state operation.

$$\sum_{i=1}^{n} F_i = 0 \tag{6.1}$$

$$\sum_{i=1}^{n} F_{x,i} \cdot y_{s,i} + \sum_{j=1}^{m} F_{y,j} \cdot x_{s,j} = 0 \tag{6.2}$$

The forces and distances considered are illustrated in Figure 6.1. The main forces taken into account are the pressure force F_p, the frictional force F_R, the centrifugal force of the wiper element F_n and the frictional force F_{fric} attacking at the bearing axis along the height of an element Δz.

The centrifugal force is calculated based on the mass of the wiper element and the rotational speed n

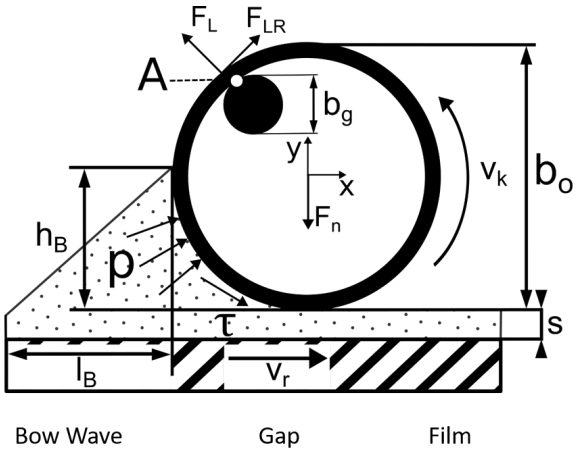

Figure 6.1.: Representation of force and momentum balance [25].

of the roller according to Equation 6.3.

$$\frac{F_n}{\Delta z} = m_{W,\Delta z} \cdot \frac{w^2}{0.5 \cdot d_r} = 2\pi^2 \cdot m_W \cdot n^2 \cdot d_r \tag{6.3}$$

The pressure force F_p is derived by integrating the static pressure distribution of the bow wave along the height of the bow wave h_B:

$$\frac{F_p}{\Delta z} = \int_s^{h_B} p(y)\, dy \tag{6.4}$$

Similarly, the frictional force F_R is determined by integrating the shear stress $\tau_R(y)$ along the wetted area, assuming constant shear stress:

$$\frac{F_R}{\Delta z} = \int_s^{h_B} \tau_R(y)\, dy \tag{6.5}$$

The points of application of the forces are crucial for analyzing the momentum balance. While the centrifugal force acts at the center of the wiper element, the centroids of the pressure and frictional forces are calculated according to Equation 6.6 and Equation 6.7.

$$y_s = \frac{\int_s^{h_B} F_x(y) \cdot y\, dy}{\int_s^{h_B} F_x(y)\, dy} \tag{6.6}$$

$$x_s = \frac{\int_s^{h_B} F_y(y) \cdot x(y)\, dy}{\int_s^{h_B} F_y(y)\, dy} \tag{6.7}$$

The integrations were performed numerically, resolving the force components into their x and y contributions. The shear stress τ_R was initially unknown. To estimate its value, it was assumed that the energy dissipated by friction at the bearing point during steady-state operation is only dependent on the friction force at the roller speed v_k. This leads to Equation 6.8 for the dissipated power $\dot{W}_{\text{Diss}}$ as a function of v_k.

$$\frac{\dot{W}_{\text{Diss}}}{\Delta z} = \frac{F_L}{\Delta z} \cdot \eta_R \cdot v_k \cdot \frac{b_i}{b} \tag{6.8}$$

In steady-state, the dissipated energy must be balanced by the energy supplied through the shear stress τ_R over the wetted surface of the wiper element. The shear stress is assumed to be constant along the wetted circumference, whereby no wetting was assumed after the nearest distance between the wiper element and the wall. This yields:

$$\frac{\dot{W}_{\text{Diss}}}{\Delta z} = \tau_R \cdot v_k \cdot \frac{b}{2} \cdot \arccos\left(\frac{0.5 \cdot b - h_B}{0.5 \cdot b}\right) \tag{6.9}$$

Within the simulations, the mass and energy balances were ensured for all flow variables. Specifically, mass flows of the feed, sump and distillate streams, as well as energy balances involving the latent heat of vaporization and specific enthalpies of the considered fluids, were accounted for. The system was treated as adiabatic, neglecting heat losses to the environment. For parameterization of the model, the experimentally determined mean values of the heating steam pressure, wiper speed, feed mass flow, and operating pressure were incorporated into the model, along with the geometric boundary conditions.
The model structure and results of the fluid dynamic modeling without heat transfer are presented in the following section 6.2.

6.2. Modeling and Simulation of the Fluid Dynamics without Evaporation

The following section represents an updated version of the following publication: D. Appelhaus, K. Jasch, S. Jahnke, H. Hassani Khab Bin, W. Tegethoff, J. Köhler, and S. Scholl. “A New Approach to Simulate the Fluid Dynamics in a Wiped Film Evaporator Using Modelica”. In: *Chem. Eng. Res. Des.* 161 (2020), pp. 115–124.
While updating only editorial changes were made.
A corrigendum to the publication was published, which is printed in section 6.3.

Abstract

Wiped film evaporators (WFE) or agitated thin film evaporators are efficient equipment for separating highly thermosensitive and viscous mixtures. There are different approaches to tailor residence time distribution (RTD) for specific applications and to maximize heat and mass transfer by equipment design or process parameter adjustment, like liquid load or wiper speed. However, the fundamental principles of fluid dynamics are only known to a limited extent. Although flow patterns and mass and heat transfer are highly interdependent, the effects of different wipers on liquid flow and, finally, on residence time behavior are poorly understood. In this work, a new model describing fluid dynamics and its impact on RTD is presented. The model is implemented in the equation-based modeling language Modelica. Several system variables – e.g. film thickness, hold-up or velocity profiles within

the liquid film – can be estimated. The effect of varying process parameters, like liquid load and fluid temperature, can also be evaluated. The model has been calibrated with results from RTD experiments in a WFE using a roller wiper. It is capable of describing the residence time behavior of the roller wiper system with good accuracy. Mean residence times can be reproduced within approx. $\pm$20%. Further results, such as film thickness or hold-up, provide additional insight into the fluid dynamics of characteristic regions – like bow wave, wiping and thin film zone – and the effects of several process parameters.

Abbreviations

CFD, computational fluid dynamics; CSTR, continuous stirred tank reactor; RTD, residence time distribution; WFE, wiped film evaporator

Keywords

Wiped Film Evaporator, Wiped Film Model, Modelica, Fluid Dynamics, Residence Time Distribution, Roller Wiper

Nomenclature

Latin symbols

Symbol	Explanation	Unit
A	pressure drop across the gap zone	$\mathrm{Pa \cdot m^{-1}}$
$a_1, a_2, a_3, a_4, a_5, a_6$	empirical constants	-
B_1	film parameter	m
B_2	film parameter	$\mathrm{m^{-1}}$
B_3	film parameter	m
b_g	diameter of guide rod	m
b_o	outer diameter of the roller wiper	m
b_i	inner diameter of the roller wiper	m
C_1	integration constant	$\mathrm{s^{-1}}$
C_2	integration constant	$\mathrm{m^2 \cdot s^{-1}}$
c	constant	-
d_r	diameter of apparatus	m
F_L	force normal to the rod	N
F_{LR}	force tangential to the rod	N
F_n	centrifugal force	N
Fr_R	rotational Froude number; $\mathrm{Fr}_R = \frac{d_r \cdot \omega^2 \cdot n^2}{g}$	-
g	standard acceleration of gravity	$\mathrm{m \cdot s^{-2}}$
h_B	height of bow wave	m
k_y	elements in y-direction in the film	-
l_B	length of bow wave	m

Symbol	Explanation	Unit
l_z	wiped length of the WFE	m
m_B	mass of the bow wave	kg
$\dot{m}_F$	feed mass flow	$\mathrm{kg \cdot s^{-1}}$
$\dot{m}_{ax}$	axial mass flow	$\mathrm{kg \cdot s^{-1}}$
$\dot{m}_{dead}$	dead volume mass flow	$\mathrm{kg \cdot s^{-1}}$
$\dot{m}_t$	tangential mass flow	$\mathrm{kg \cdot s^{-1}}$
N	number of CSTR	-
N_B	number of wiper elements	-
N_{Film}	number of tangential film elements	-
N_y	number of radial elements	-
N_z	number of vertical elements	-
n	wiper frequency	$\mathrm{s^{-1}}$
p	pressure	Pa
$\dot{p}$	tangential momentum flow	$\mathrm{kg \cdot m \cdot s^{-2}}$
R	radius	m
Re_F	rilm Reynolds number; $\mathrm{Re}_F = \frac{\dot{m}_F}{d_r \cdot \rho \cdot \nu}$	-
Re_R	rotational Reynolds number; $\mathrm{Re}_R = \frac{g \cdot d_r^2 \cdot n}{\nu}$	-
r	radius coordinate	m
s	gap width	m
$V_{\mathrm{CSTR},i}$	volume of main CSTR i	$\mathrm{m^3}$
$V_{\mathrm{dead},i}$	volume of dead CSTR i	$\mathrm{m^3}$
V_i	volume of element i	$\mathrm{m^3}$
V_H	liquid hold-up volume	$\mathrm{m^3}$
v	liquid velocity	$\mathrm{m \cdot s^{-1}}$
v_{ax}	axial velocity component	$\mathrm{m \cdot s^{-1}}$
$\overline{v}_{ax}$	mean axial velocity	$\mathrm{m \cdot s^{-1}}$
v_k	peripheral velocity of the roll	$\mathrm{m \cdot s^{-1}}$
v_r	peripheral velocity	$\mathrm{m \cdot s^{-1}}$
x, y, z	coordinates	m

Greek symbols

Symbol	Explanation	Unit
Γ	liquid peripheral load	$\mathrm{m^3 \cdot m^{-1} \cdot s^{-1}}$
β	dead volume factor	-
δ	film thickness	m
ζ	correction term	-
η	dynamic viscosity	$\mathrm{Pa \cdot s}$
ϑ	temperature	°C
ρ	density	$\mathrm{kg \cdot m^{-3}}$
σ	standard deviation	%
τ	shear stress	Pa

Symbol	Explanation	Unit
τ_u	shear stress at the wall	Pa
$\overline{\tau}$	mean residence time	s
Φ	angular coordinate	rad
ω	peripheral velocity	s^{-1}

6.2.1. Introduction

Increasing product quality in food, pharmaceuticals or fine chemicals production requires modern methods that minimize mechanical and thermal damage to valuable products. Wiped film evaporation allows for the efficient thermal separation of products at reduced process temperature and residence time [8]. Contrary to standard falling film evaporators, wiped film evaporators (WFE) distribute the liquid film on the inner wall of a heated cylinder using a rotating wiping system. This leads to higher heat and mass transfer rates, as well as an increased evaporation mass flow, compared to unwiped falling film [39, 43]. With respect to wiping elements, different WFE designs exist [17, 18, 51]. To characterize WFE, a good understanding about underlying mechanistic principles is utterly important. Therefore, several authors have used basic physical descriptions or empirical equations to describe fluid dynamics in WFE [45, 61, 81]. Others have employed computational fluid dynamics (CFD) to simulate mass flow within a WFE and to identify the flow profile in the liquid film [45, 61]. However, WFE modeling in these studies has been limited to fixed geometries of the wiping system. To the best of the authors' knowledge, a theoretical approach for more complex wiper systems such as roller wipers has not yet been presented in the open literature. Furthermore, experimental results for different wiper types are mostly limited to single wiper types or to comparing different wipers with each other. Differences between wipers are often explained by possible effects occurring during evaporation but cannot be sufficiently explained mechanistically. Residence time distributions (RTD) for more complex WFE have been modeled describing the WFE by a reduced substitute system. Although these models can reproduce the RTD accurately, there are only weak links between the process parameters and the presented models [77, 81]. To fill this gap, a more mechanistic approach was developed, simultaneously calculating the flow profile and the resulting RTD. Taking various wiper types into account, the model was created modularly using the object-oriented modeling language Modelica. A fluid dynamic model was set up for a roller wiping system and parametrized based on experiments [189]. The presented approach connects the RTD with internal variables, like geometry, process parameters and resulting fluid dynamics within the liquid film. It builds on existing models, extending their approaches into a more universal one.

6.2.2. Modeling

RTD are often used to characterize the fluid dynamic behavior of WFE [16, 50, 51]. However, theoretical knowledge of fluid dynamics and its influence on RTD for WFE is scarce. CFD simulations are well suited for accurate dynamic simulation of WFE, with a defined and constant distance between the wiping system and the apparatus wall. Nevertheless, it can become very complex and time-consuming to simulate wiping systems with movable elements. In these cases, the actual position

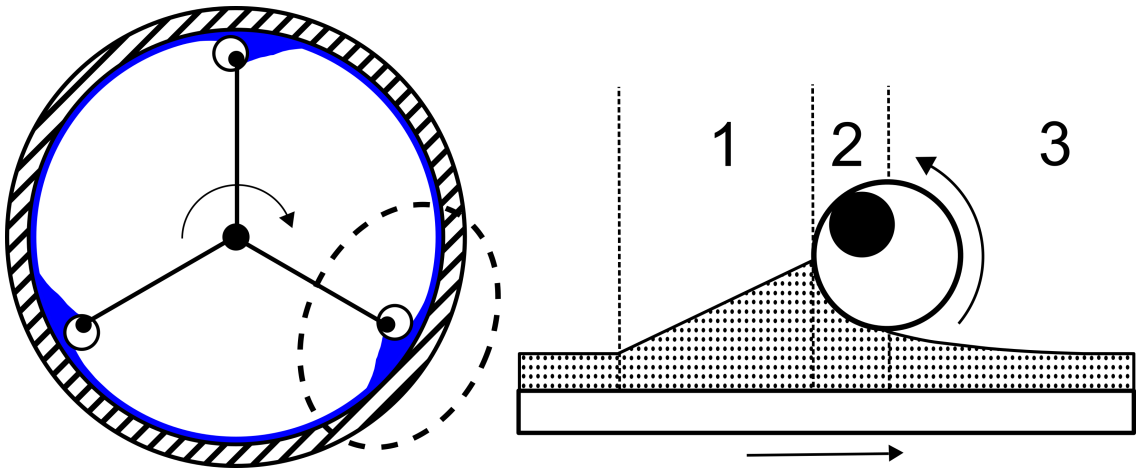

Figure 6.2.: Illustration of the wiper model with bow wave zone (1), gap or wiping zone (2) and thin film (3).

of the wiping elements and the shape of the thin film result from a complex interaction of fluid properties, wiper design and operational parameters. Therefore, a new model was developed, based on existing models, which were modified to account for the specific features of a roller wiper. This apparatus is characterized by a variable gap between wiping element and evaporator wall. To simplify the system, the following assumptions were made:

1. The viscosity of the fluid is constant and shows Newtonian behavior.
2. The distance between wipers is identical.
3. No evaporation occurs within the liquid film.
4. The process is isothermal and isobar.
5. The effect of surface tension is negligible.
6. The film surface was assumed to be flat because its height is small compared to the diameter of the apparatus.
7. The flow profiles in the gap and the film are considered laminar as the dimensions are small
8. The flow profile is independent of the height of the apparatus and stationary.

The assumptions 1 - 8, with the exception of assumption 6, are identical with the assumptions made by Schweizer for the theoretical consideration of WFE [16]. In some cases, additional assumptions were made for the individual areas, which are explained in more detail in subsubsection 6.2.2.1 at the relevant points. To model the RTD of a roller wiper, a two-step approach was used. Firstly, a fluid dynamic model of a WFE with a roller wiper was formulated. Secondly, a compartment model for the RTD as a system of continuous stirred tank reactors (CSTR) was developed.

6.2.2.1. Fluid Dynamic Model for the Film Created by a Roller Wiper

For the model, the height of the evaporator l_z was discretized into N_z height elements, each with a height of l_z/N_z . Furthermore, only one segment of the wiper was modeled. For this segment,

periodical boundary conditions were assumed. Using coordinate transformation, the wiping element was considered as stagnant, while the wall of the equipment moved with the speed of the wiper. The remaining element was divided into three zones, which were modeled individually. The WFE and the different fluid film zones are illustrated in Figure 6.2. This modular structure allows a later adjustment and extension of the entire system. The calculated results of each zone define the boundary conditions of the adjacent zones. The bow wave region has a highly complex and turbulent flow regime and cannot be modeled considering all parameters and the full complexity of the flow. Therefore, the model of the bow wave zone builds on the work of Schweizer, who used an empirical term to describe the height of the bow wave h_B as a function of dimensionless numbers [16]:

$$\frac{h_B}{d_r} = a_1 \cdot \mathrm{Re}_F^{a_2} \cdot \mathrm{Re}_R^{a_3} \cdot \mathrm{Fr}_R^{a_4} \cdot N_B^{a_5} \cdot \left(\frac{s}{b}\right)^{a_6} \tag{6.10}$$

The bow wave itself was considered as a triangle. The length of the bow wave region l_B was fitted with the overall mass balance. The fit parameters a_1 - a_6 of Equation 6.10 were determined experimentally by Schweizer for low and medium viscous liquids in a WFE with blade wipers. d_r represents the diameter of the rotor; Re_F and Re_R are the film and the rotational Reynolds number, respectively, while Fr_R represents the rotational Froude number. The term N_B represents the number of wiper elements while s stands for the gap width between the wiping element and the wall. b_0 is the thickness of the blade [16]. The empirical Equation 6.10 found by Schweizer was modified, as Schweizer´s model was suitable only for rigid wiper systems. Since the diameter of the rotor is unknown and assuming that the gap width is small compared to the diameter of the apparatus d_r was considered the inner diameter of the WFE. For the calculation of Re_F the feed mass flow $\dot{m}_F$ was divided by the number of wiper element while for b_0 the diameter of the roll was used, see Figure 6.3. For parameters a_2, a_3, a_4 and a_6, the values found by Schweizer for a medium viscosity fluid were adopted [16]. Since only one wiper element was considered in the model, the dependence on the number of rolls was not considered and a_5 was set to zero. Therefore, a_1 was modified taking into account the adjusted film Reynolds number. The values of a_2 and a_5 found by Schweizer were -0.388 and -0.333, respectively, while the number of wiper elements at the WFE in this work was 3. This means that a_1 would have to be multiplied by 0.453. However, this value resulted in unreasonably high bow waves and consequently very short bow wave lengths to close the mass balance. Therefore, a_1 was multiplied by 0.05 instead, since this value gave reasonable values for bow wave heights and lengths. Nevertheless, this is a somewhat arbitrary choice and further experiments are needed investigating the exact height and geometry of the bow wave for roller wipers. Alternatively, a_1 could be extracted from fitting model calculations to experimental results; this will be examined in future work. It is expected that smaller bow waves will occur using a roller wiper, as the moving elements should reduce the flow resistance. For fluid dynamics within the wiping zone, the velocity profile in the gap is important. The flow profile results from a pressure and a stress field. As an analytical solution for the turbulent flow is still missing and the dimensions within the gap are small, laminar flow was assumed to calculate the velocity profile. Effects of the in- and outlet were neglected. However, turbulent flow as well as boundary effects are likely to occur but are difficult to implement within a non-CFD-model. The effect of turbulent flow needs further investigation to include the necessary level of complexity within simpler models. Nevertheless, considering the made assumptions within

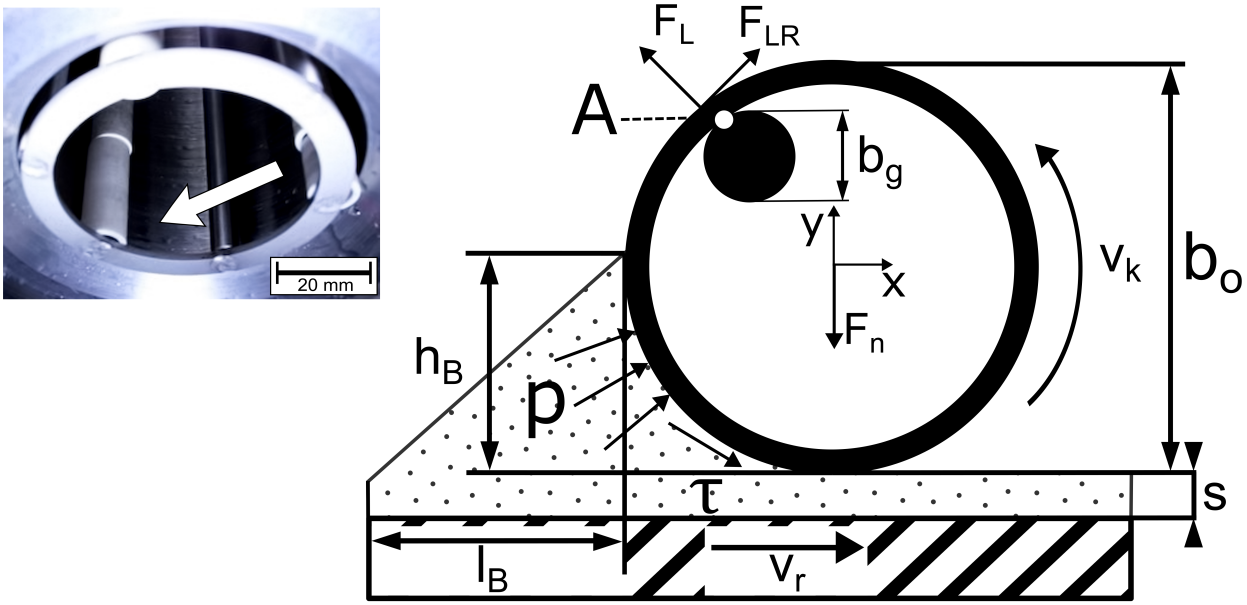

Figure 6.3.: Left: Bottom view of an installed roller wiper with the flow direction of the processed liquid. Right: Illustration of the derived model system of a roller wiper with attacking forces.

cylindrical coordinates, the velocity profile follows Equation 6.11.

$$0 = -\frac{1}{r}\frac{dp}{d\Phi} + \eta\left[\frac{\partial}{\partial r}\left(\frac{1}{r}\frac{\partial(rv)}{\partial r}\right)\right] \tag{6.11}$$

Using the bow wave height, the pressure in front of the gap was calculated. Assuming the pressure difference is nearly constant along the gap, it may be approximated by a constant A. As $dp/d\Phi$ is in cylindrical coordinates and it was assumed that the gap zone ends at half the diameter of the wiping roll diameter, A can be calculated by:

$$A = \frac{dp}{d\Phi} \approx \frac{\Delta p}{\Delta\Phi} \tag{6.12}$$

As Schweizer shows, the pressure in front of the gap primarily results from the pressure caused by centrifugal forces [16]. Assuming the diameter of the roll is large compared to the bow wave height, the pressure in the gap was calculated with the equations used for flat wipers [16]. Therefore, the pressure upfront the gap follows from:

$$\Delta p = \frac{\rho v^2 h_B^2}{2} \cdot (d_r - h_B) \tag{6.13}$$

As $\Delta\Phi$ is in cylindrical coordinates and the gap width ends at the nearest point of the roll to the wall it can be rewritten to:

$$\Delta\Phi = \frac{2 \cdot \left(\frac{b_0}{2}\right)}{d_r} = \frac{b_0}{d_r} \tag{6.14}$$

A from Equation 6.12 can therefore be rewritten to:

$$A \approx \frac{\Delta p}{\Delta \Phi} = \frac{\rho \omega^2 h_B d_r}{2 b_0} \cdot (d_r - h_B) \tag{6.15}$$

Integrating Equation 6.11, the velocity profile within the gap results to:

$$v(r) = \frac{A}{2\eta}\left(\log(r-s) + \frac{1}{2}\right) + \frac{C_1 r}{2} + \frac{C_2}{r} \tag{6.16}$$

The integration constants $C1$ and $C2$, can be calculated with the boundary conditions ($v(R) = v_r, v(R-s) = v_k$).

$$C_1 = \frac{v_k - v_r \cdot \frac{R}{R-s} + \frac{A \cdot R^2}{2\eta(R-s)}\left(\log(R) - \frac{1}{2}\right) - \frac{A \cdot \log(R-s)}{2\eta}\left(\log(R) - \frac{1}{2}\right)}{\frac{R-s}{2} - \frac{R^2}{2 \cdot (R-s)}} \tag{6.17}$$

$$C_2 = v_r \cdot R - \frac{C_1 \cdot R^2}{2} - \frac{A \cdot R^2}{2\eta}\left(\log(R) - \frac{1}{2}\right) \tag{6.18}$$

The rotational speed v_k of a single wiping element rolling over the film surface was calculated using force and torque equilibrium, which is illustrated in Figure 6.3. Additionally, the dissipated energy at the rod is equal to the energy transmitted by fluid friction, neglecting air friction and surface tension effects. The derivative of the velocity profile results in a term for the shear stress. Considering the possibility that the flow profile could be turbulent, a correction term ζ was added, which should exceed unity if the flow was turbulent. It was assumed that the shear stress is nearly constant along the wetted area of the roller wiper while the rotational speed of the roll is constant, so the dissipated energy must be equivalent to the energy the fluid transmitted.

$$\tau_R = \eta \cdot \zeta \cdot \left.\frac{dv}{dr}\right|_{r=R-s} = \eta \cdot \zeta \cdot \left(\frac{A}{2\eta}\left(\log(R-s) + 0.5\right) + \frac{C_1}{2} - \frac{C_2}{(R-s)^2}\right) \tag{6.19}$$

The calculated velocity profile was then passed to the model of the thin film. The velocity profile within the gap gives information about the mass flow $\dot{m}_t$ traveling tangentially to the cylinder wall.

$$\dot{m}_z = \rho \cdot \Delta z \int_0^s v(y) dy \tag{6.20}$$

The thin film zone starts directly behind the wiping zone. Although the film just behind the wiper was shown to be turbulent, this was neglected in a first approach [16, 64]. There are parallels between the free surface flow within a WFE and the liquid flow during surface coating processes with doctor blades [190]. Based on the results of CFD simulations for those processes, the film thickness changes considerably directly behind the gap, while it moves toward a fixed value in a large distance to the gap as seen in Figure 6.4. Therefore, the film thickness was fitted as an exponential function of the distance x to the gap.

$$\delta(x) = B_1 \cdot e^{B_2 \cdot x} + B_3 \tag{6.21}$$

The constants B_1,B_2 and B_3 for the exponential fit were computed using the boundary conditions

$\Delta(0\ \mathrm{m}) = s, v(y,0) = v(r)$ and $\delta(x)_{x\to\infty} = \frac{\dot{m}_t}{\rho\cdot\Delta z\cdot v_r}$. .
The value of B_1 can be calculated directly using Equation 6.22.

$$B_1 = s - B_3 \tag{6.22}$$

B_2 is a quantity for the energy dissipation in the film. It follows from the derivative of Equation 6.21 using discrete elements of the thin film.

$$B_2 = \frac{1}{B_1}\cdot\left.\frac{d\delta(x)}{dx}\right|_{x=0} \approx \frac{1}{B_1}\cdot\frac{\Delta\delta}{\Delta x} = \frac{1}{B_1}\cdot\frac{\delta_1-\delta_2}{x_1-x_2} \tag{6.23}$$

With the boundaries for the velocity, the tangential mass flow and momentum flow can be calculated as:

$$\dot{m}_t = \rho\cdot\Delta z\int_0^{\delta_1} v(y,x_1)dy = \rho\cdot\Delta z\int_0^{\delta_2} v(y,x_2)dy \tag{6.24}$$

$$\dot{p}_t = \int_0^{\delta_1} v^2(y,x_1)dy = \int_0^{\delta_2} v^2(y,x_2)dy + \tau_u\cdot\Delta x \tag{6.25}$$

The integrals were discretized along the height in k_y elements. It was assumed that the velocity profile $v_i(y)$ at point x_1 is similar to the velocity profile $v_j(y)$ at point x_2. Thus, $v_j(y)$ can be replaced by $\gamma\cdot v_i(y)$, whereby Δ_2 is obtained from the following equation:

$$\delta_2 = \frac{\sum_{i=1}^{k_y} v_i^2\cdot\delta_1^2}{\left(\sum_{i=1}^{k_y} v_i^2\cdot\frac{\delta_1}{k_y} - \tau_u\cdot\Delta x\right)\cdot k_y} \tag{6.26}$$

The shear stress τ_u depends on the velocity profile and the fluid viscosity. Assuming the fluid shows Newtonian behavior τ_u can be calculated using Equation 6.27.

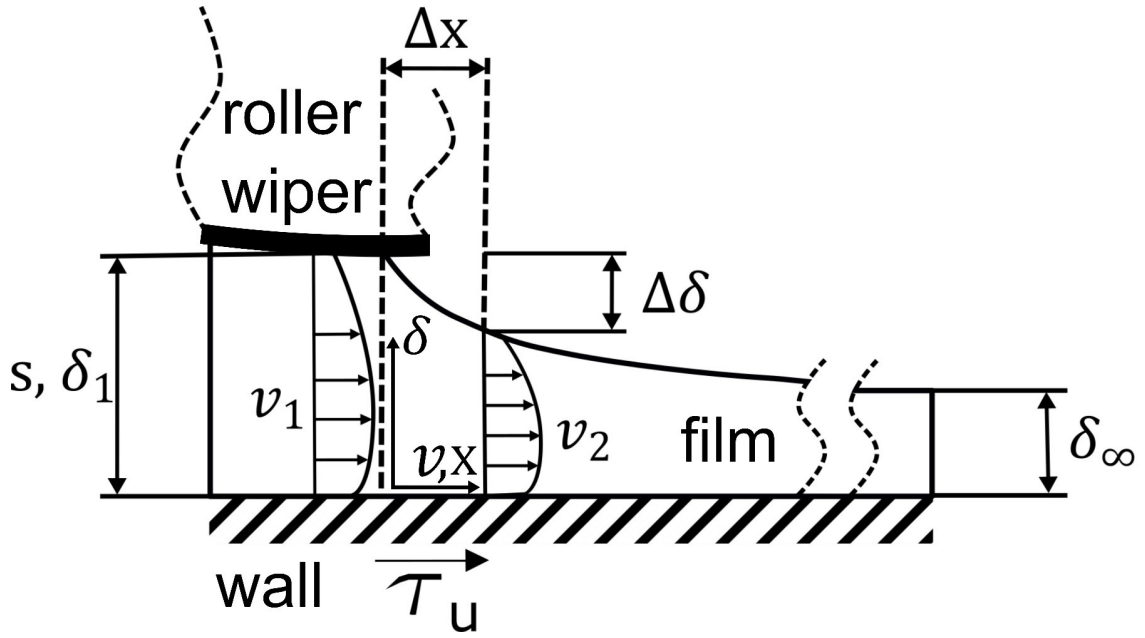

Figure 6.4.: Illustration of the used thin film model.

$$\tau_u = \eta \left. \frac{dv}{dr} \right|_{r=R} \tag{6.27}$$

However, it has to be stated that in WFE often non-Newtonian fluids with high viscosity and a complex shear stress behavior are treated. For example, polymeric solutions can have significant elastic behavior and relaxation times within the wiping frequency [16].
For the value of B_3, it was assumed that the radial film velocity at a large distance from the gap is identical to the wall velocity with transformed coordinates, according to Figure 6.4. Because $B_2 < 0$ m^{-1}, the factor B_3 can be expressed as:

$$B_3 = \frac{\dot{m}_t}{\rho \cdot \Delta z \cdot v_r} \tag{6.28}$$

Considering Equation 6.24 and Equation 6.28, while the velocity of the wiper and the pressure term are always positive the minimum thickness of the thin film is half the gap width. The tangential mass flow is therefore determined by the wiping zone and the velocity profile within it. In contrast, the vertical mass flow is defined by the gravitational force and the no-slip condition at the wall. This can be calculated by solving the force equilibrium for the laminar flow profile in steady state:

$$\frac{dv}{dy} = \frac{\rho \cdot g}{\eta} \cdot (\delta - y) \tag{6.29}$$

Integrating Equation 6.29 over the height s of the thin film, the mean axial velocity, which was used to calculate the vertical mass flow, is

$$\overline{v}_{\mathrm{ax}} = -\frac{1}{c} \cdot \frac{(g \cdot \rho \cdot \delta^2)}{\eta} \tag{6.30}$$

The constant c depends on the boundary conditions. Its value can be calculated to $c = 3$ for the film zone and $c = 12$ for the gap zone. Especially directly behind the wiper, the film starts to run transiently [16]. Because of that, the assumption of steady state is not justified here. However, due to the short time required for the transient start, the error due to this assumption is acceptable in this first approach, although this could be considered in future work in combination with further experimental work. As mentioned before, the bow wave zone is highly turbulent. The geometrical shape and the boundary conditions of the bow wave are not exactly known. For the calculation it was assumed that the shape of the bow wave is nearly triangular. Schweizer quantified the vertical mass flow of a triangular bow wave with film adhering to a vertical wiper blade using Equation 6.30, which describes the vertical flow in a square channel [16, 191, 192].

$$\overline{v}_{\mathrm{ax}} = \frac{g \cdot \rho \cdot l_B^2}{12 \cdot \eta} \left[1 - \frac{192 \cdot l_B}{\pi^5 \cdot h_B} \sum_{m=1,3,5,\ldots}^{\infty} \frac{1}{m^5} \cdot \tanh\left(\frac{\pi \cdot m \cdot h_B}{2 \cdot l_B} \right) \right] \tag{6.31}$$

Originally, this equation applies to laminar flow in the shape of an equilateral triangle, which usually not applies to the bow wave. However, as a first approximation, this equation was also used for the present roller wiper model, whereby the first five terms of the series were considered. Taking into account changed boundary conditions and geometries for different wiper types, Equation 6.31 could

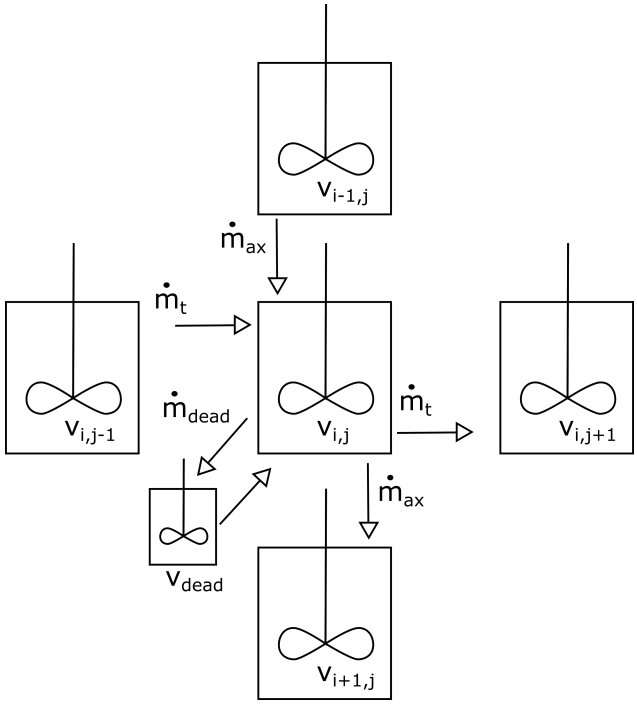

Figure 6.5.: Illustration of the used residence time model.

be adapted to reflect the actual system more accurately. Knowing the length of the wiping zone, the lengths of the bow wave l_B and the thin film were fitted with the feed mass flow, using the overall mass balance and the perimeter of the cylinder considering Equation 6.30 and Equation 6.31.

$$\dot{m}_F = \dot{m}_{\mathrm{v,bow\,wave}} + \dot{m}_{\mathrm{v,thin\,film}} + \dot{m}_{\mathrm{v,wiping\,zone}} \tag{6.32}$$

For a comparison of different evaporator sizes, as well as a quantitative measure of the surface wetting in the film flow equipment, the feed flow per unit wetted inner circumference Γ is used:

$$\Gamma = \frac{\dot{m}_F}{\pi \cdot d_r} \tag{6.33}$$

6.2.2.2. Compartment Model for Residence Time Distribution

Understanding the flow profile in one height element and assuming that this flow was similar in each height element, the flow in the equipment was described. To calculate the RTD, the internal flow morphology was represented by a system of CSTR. The mass flows, calculated by the zone models, were used for the mass flows in the CSTR model. The residence time model was built on a model from Zeboudj *et al.* who proposed several models to describe WFE [77]. This particular model has proven to reflect the RTD of a WFE within $\pm$5%. Unlike Cvengroš *et al.* Zeboudj *et al.* did not assume perfect mixing behind every height element [77, 81]. The system used in this research is schematically presented in Figure 6.5. The number of CSTR represents the degree of discretization. Therefore, the WFE was divided into N_z height elements and N_{Film} elements for the free thin film. The bow wave and the wiping zone were modeled as one CSTR each, so one height element consisted of (N_{Film}+2) CSTR. Tailing of the RTD was observed in most WFE experiments [51, 81]. Therefore, dead zones and

a dead volume factor β were introduced. The factor β quantified the mass flow, which connected the dead zone volume CSTR with every CSTR. In this work, β was also used to quantify the dead volume fraction of each CSTR, although it is most likely that the dead volume fraction and the mass flow were not necessarily identical, thus limiting the physical interpretability. However, this assumption was made to keep the number of fitting parameters at a minimum and to ensure that, for $\beta \to 0$, the dead zone was vanishing [77]. The volume of one element was calculated using the data of the WFE model. One element was made up of the volume of the main reactor V_{CSTR} plus its associated dead volume:

$$V_i = V_{\mathrm{CSTR},i} + V_{\mathrm{dead},i} \tag{25}$$

This can be rewritten with the factor β to:

$$V_{\mathrm{CSTR},i} + V_{\mathrm{dead},i} = (1-\beta)V_i + \beta V_i \tag{6.34}$$

The mass flow, which connects the main CSTR with the dead volume CSTR, was also set by the dead volume factor and correlated to the axial mass flow $\dot{m}_{\mathrm{dead}}$, as it was assumed that an increasing vertical mass flow would enhance the mass transfer between the dead zone and the main CSTR. This results in:

$$\dot{m}_{\mathrm{dead}} = \beta \cdot \dot{m}_{\mathrm{ax}} \tag{6.35}$$

Contrary to the model introduced by Zeboudj *et al.* the mass flow of the CSTR was determined by a mechanistic model [77]. Thus, the number of free parameters could be reduced. Furthermore, the results of the modeling can be used to characterize a WFE based on the gap width or liquid hold-up in the film. The latter may be determined independently, thus allowing for a plausibility check of the simulated value.

6.2.2.3. Model Implementation

The various models were connected to each other so that the overall WFE model was modular. Figure 6.6 depicts the implementation in Modelica. Module (1) represents the bow wave zone; module (2) the gap or wiping zone and module (3) symbolizes the modeled thin film zone. From this, a great variety of different wiper systems can be realized. As these various wiper systems are connected and share information about boundary conditions, only two free parameters are left: the gap width and the dead volume factor. The factor ζ (see Equation 6.19) describing the difference between the laminar and the turbulent flow profile, was another free parameter, although it was considered proportional to the rotor frequency. The models were implemented using the object-oriented modeling language Modelica. This allows for direct implementation of the equations describing the wiping system. In addition to the standard Modelica library v.3.4 [188], the TILMedia library of TLK-Thermo GmbH was used, which allows for accurate calculation of the physical properties of working fluids, depending on pressure and temperature. This calculation is based on experimental data and polynomial fitting functions.

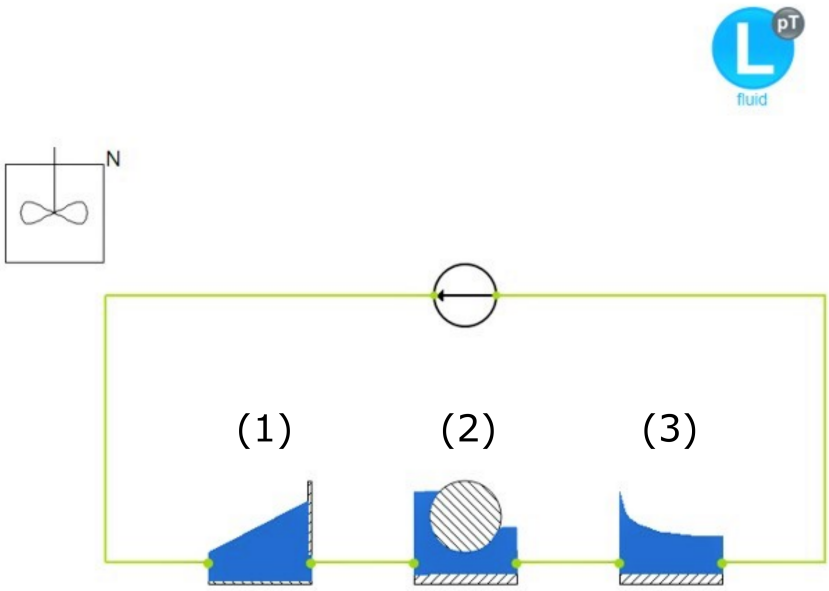

Figure 6.6.: Illustration of the connections between the used models in Modelica.

6.2.3. Results and Discussion

The model introduced in this research work was experimentally adapted. To parameterize the WFE model, the authors used the results of residence time measurements by Uhlendorf *et al.* from a roller wiper system with monoethylene glycol as test fluid at varying temperatures and viscosities. The parameters β and s were manually fitted with the experimental data to optimally represent the measured RTD [189]. For this purpose, the gap width s and the dead volume factor β were adjusted. Since an increase of β shifts the residence time distribution to later times, while a decreasing gap width s leads to a narrower but shorter residence time distribution, a suitable result is obtained. Especially as this model must be examined with regard to experimental results, this procedure was considered sufficient. If more parameters are varied or if a certain target value is to be unambiguously represented, the parameters must be optimized by means of a statistical procedure such as least squares. However, for the results considered here the difference between the applied methods and statistical procedures should be small. The model parameters and the parameters of the used experimental equipment are summarized in Table 6.2.

Table 6.2.: Parameters for the used model to fit the experimental data

Experimental parameters		**Model parameters**	
b_o [mm]	12	a_1 [-]	0.032
d_r [mm]	80	a_2 [-]	-0.388
N_B [-]	3	a_3 [-]	0.232
l_z [mm]	256	a_4 [-]	0.100
p [mbar]	1000	a_5 [-]	0.000
ϑ [°C]	20, 30, 50	a_6 [-]	-0.070
b_i [mm]	9	N_x [-]	20
b_g [mm]	5	N_{film} [-]	20
n [min^{-1}]	200, 550	N_z [-]	40

Figure 6.7 compares the experimental and calculated RTD for two sets of experimental runs: on the top, a variation of the liquid load Γ at constant temperature and, therefore, constant viscosity; on the bottom, a variation of temperature ϑ at constant liquid load. The values of viscosity at different temperatures are also given in Figure 6.7. The results show that the model could reproduce the experimental distributions within experimental scatter. The values of the regression coefficient were greater than 0.95 for all experiments considered. The RTD peak and the tailing effect, in particularly, could be simulated within the accuracy of the experiments. Further, the model properly captured the influence of operating and material parameters. However, the factor ζ was found to be larger than unity, which indicated that the calculated laminar velocity profile within the gap did not reflect the actual velocity profile. By definition, the factor ζ increases the calculated shear stress of the model compared to a laminar model. Therefore, ζ must increase as the film becomes turbulent. As the film turbulence increases with the Reynolds number, it was assumed that $\zeta \propto n$. In a first assumption, the parameter ζ was set to $0.6 \cdot n$ for the simulations of 20 °C and 30 °C and was doubled to $1.2 \cdot n$ for 50 °C, as the model did not consider a decreasing viscosity and, therefore, an increasing Reynolds number. For n, the value in seconds was used. As this work aimed to show the basic feasibility of predicting RTD based on physical relations, the exact value of ζ was less important. However, this indicated that the flow profile within the gap was turbulent and could not be fitted by a laminar flow profile without a correction term. Future work will address this aspect in more detail.

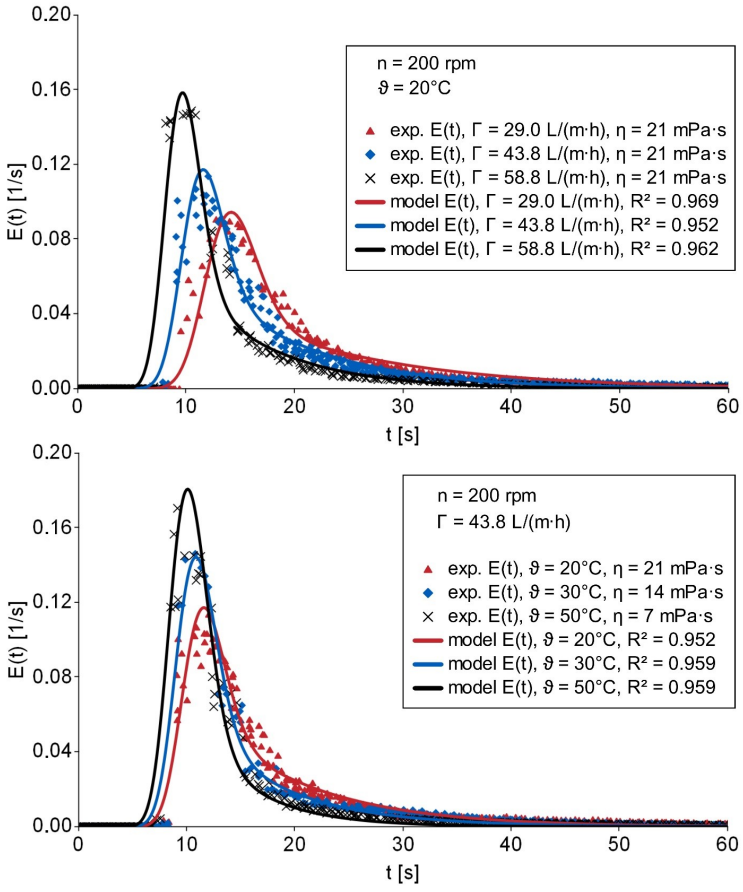

Figure 6.7.: Modeled RTD compared to experimental data. Top: Variation of liquid load Γ at constant temperature ϑ. Bottom: Variation of temperature ϑ at constant liquid load Γ.

To compare the simulated and experimental results, the characteristic values of mean residence time and standard deviation are presented in Figure 6.8. For all parameter changes, the model qualitatively follows the same trend as the experimental results. The absolute values of the mean residence time fall quite well within experimental uncertainty. The influence of the liquid load is captured qualitatively particularly well, as can be seen in the left part of Figure 6.8. Nevertheless, the mean residence time is slightly underestimated, especially for higher temperatures, as can be seen in the right part of Figure 6.8. For all temperatures and liquid loads the standard deviation of the model is significantly and systematically lower than the experimental values. There are several reasons for the differences between experiment and model. Firstly, the model was adapted in such a way that the RTD was optimally represented and R^2 is minimized. Secondly, the underestimation of the mean residence time stems from the relatively strong tailing (Figure 6.7), which is not completely captured for all experimental setups by the model. In addition, the experiments show a slightly broader RTD than in the simulations. In combination with experimental uncertainties, this also explains the lower standard deviation for the modeled data. Furthermore, this hints at shortcomings in the underlying fluid dynamic model – neglecting, for example, dispersion, turbulent effects and instabilities in the liquid flow. Most of these effects, which are not considered, result in an extended residence time, which is why it should be examined how great the relevance of these effects for WFE actually is. Nevertheless, the overall trend appears promising.

The presented RTD model builds on a comprehensive model of the characteristic liquid flow morphology in a WFE. By fitting the simulated RTD to experimental findings, the gap width and the dead volume factor were extracted (Figure 6.9). For a higher liquid load, the gap width increases, while the dead volume factor decreases. For higher temperatures, both values decrease. As outlined in Figure 6.3, the gap width of a real WFE sets itself due to the force equilibrium of fluid mechanic and centrifugal forces at the wiping element, depending on fluid properties, as well as operational and process parameters. The gap width influences the flow morphology of wipers with a variable gap width. This is an important factor, which has, as yet, been given only limited attention in the open literature. A detailed investigation of the influence the operational parameters have on the experimental results will follow in the future. However, the model presented here allows to link the experimental results with the modeled system parameters to deepen the understanding of WFE system behavior.

The extracted parameter values are in the anticipated order of magnitude and showed the expected dependencies. Due to the numerous assumptions and a still missing experimental validation of the adjusted parameters, however, no quantitative analysis, but only a qualitative analysis of the results and their physical significance is to be performed at this point.

With increasing temperature and, thus, decreasing viscosity, the gap width decreases, while an increased liquid load increases the gap width. The gap width is in the range of 0.7 mm to 1.2 mm and is, therefore, comparable to fixed blades of similar dimensions [16, 60]. Furthermore, the presented model shows that, although the absolute change of the values is small, it significantly impacts system behavior. For example, the mass flow within each zone was calculated according to Equation 6.32, while the hold-up volume within each zone was calculated using the dimensions of the liquid film in each zone. The results show that for n = 550 rpm and Γ = 43.8 L/(m·h) about 90% of the vertical mass flow is contained within the bow wave and the wiping zone, while 80% of the liquid hold-up is

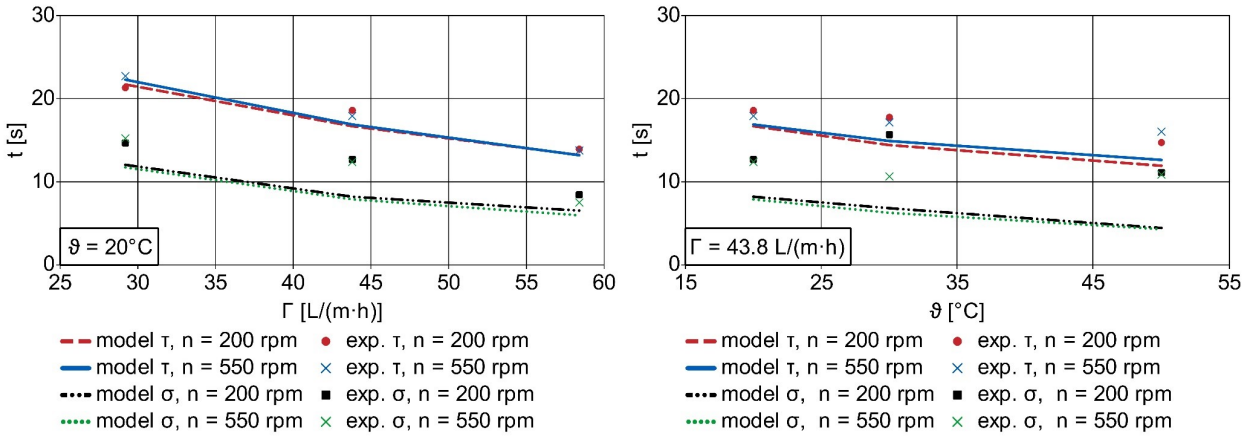

Figure 6.8.: Comparison of measured and simulated mean residence times and standard deviations. Left: Variation of liquid load Γ at constant temperature ϑ. Right: Variation of temperature ϑ at constant liquid load Γ.

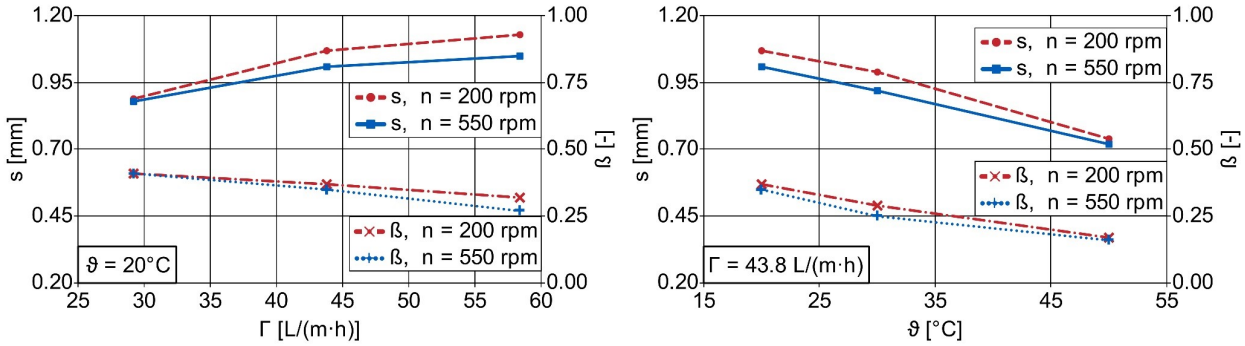

Figure 6.9.: Gap width and dead volume factor for the modeled parameters. Left: Variation of liquid load Γ at constant temperature ϑ. Right: Variation of temperature ϑ at constant liquid load Γ.

within the thin film zone. This is due to the proportionality of the vertical mass flow to the absolute height of the bow wave and the gap which is $\dot{m}_{\mathrm{ax}} \propto \delta^2$, while for the liquid hold-up the proportionality is $V_H \propto \delta$. Therefore, a smaller gap width does not necessarily result in higher mean residence time, as seen in Figure 6.8 and Figure 6.9. However, it decreases the liquid hold-up significantly. These findings are consistent with Schweizer's results [16]. In view of this, the exact geometries in a wiper system with dynamically mounted wipers are likely to have a significant impact on RTD and hold-up volume.

The dead volume factor can be interpreted as the not perfectly mixed part of the film. It describes the liquid near the wall experiencing only little turbulence. This results in the tailing effect, as seen in Figure 6.7 [81]. A pronounced tailing effect counteracts short residence times, since a certain amount of the liquid remains in the system for a relatively long time. This effect must be minimized for heat sensitive components. Furthermore, for efficient mixing and heat transfer turbulence in the film should be promoted. To accomplish short residence times the unmixed area should minimized, which correlates with a low value of β. As can be seen in Figure 6.9, the dead volume factor decreases with increasing liquid loading. Considering only slightly increasing gap widths, this indicates that the proportion of dead zones decreases. This can also be seen in Figure 6.7 as narrower residence time distributions correlate with larger liquid loads. For roller wipers the product of gap width and dead

volume factor also remains approximately constant at one temperature, which could be an indication of a laminar sublayer of constant thickness. In contrast, a lower viscosity leads to a decreasing gap width as well as to a lower dead volume factor. Thus, in addition to the proportion of poorly mixed areas, the hold-up volume also decreases significantly, which is reflected in a much narrower residence time distribution (see Figure 6.7). Particularly with highly viscous media, such as those frequently processed in WFE, a poorly mixed layer close to the wall must therefore be taken into account, which can significantly reduce heat transfer. In this case, an increase in the film Reynolds number should be aimed for. This can be achieved by changing the temperature or using wiper elements with a higher shear effect, e.g. blade wipers, although the associated possible dewetting effects and the higher energy requirement due to increasing dissipative effects should be considered. It can therefore be concluded that by calculating suitable parameters WFE can be better understood and tailored to specific processes. For an improved physical understanding of the fluid dynamic processes, a suitable model with sufficient variation possibilities is the basis. A thorough understanding of the complex relationship between the various process, plant and operational parameters can be achieved with the model presented in this thesis. However, further improvement and experimental validation of the model is necessary in order to be able to evaluate the determined quantities with regard to their accuracy.

As the presented model is much simpler than common CFD-based models and further physical equations can be implemented, it should be possible to describe occurring evaporation in an improved model. Therefore, the effects of evaporation must be considered within the model, which may lead to a completely different RTD. As WFEs are practically operated under evaporation conditions, the RTD within this regime is utterly important but not fully understood. Experimental and theoretical results are still missing, especially since the experimental setup as well as an implementation in CFD-simulations are challenging. A simpler model may be more useful as it can be adjusted easier. However, the current model is not applicable for evaporation, as it does not account for several effects of evaporation. To adjust the model, the bubbly regime must be considered. The area of heat transfer is biggest within the film zone resulting. Emerging bubbles will decrease the mean density while the film thickness may increase. Furthermore, the flow resistance can increase as bubbles block the flow of the liquid, while overall turbulence increases as well. Increased turbulence within the gap zone and the bow wave may significantly increase heat transfer, which might result in a different bubble regime within these areas. For wiper systems with a variable gap width, evaporation can influence the attacking forces at the wiper, resulting in completely different gap widths. Taking the established model for the residence time into account, the bubbles which occur primarily at the wall probably have a significant influence on the mixing rate resulting in tighter residence time distributions with less pronounced tailing. For mixtures, concentration of the lower boiling components can change viscosity and temperature along the height of the apparatus, resulting into an even more complex flow profile.

6.2.4. Conclusions and Outlook

This work presents a new, semi-empirical, fluid dynamic model for WFE, extending the work of Schweizer. Building on basic equations for describing the zones in the model, the approach was, for

the first time, adapted to a roller wiper system with a variable gap width between the wiper and the evaporator wall. A modular system was implemented using the Modelica modeling language. Due to the general approach and the modular structure, new blade geometries could readily be implemented and compared. The developed model was evaluated and fitted with experimental data. The measured mean residence times were reproduced by the new model with an accuracy of about 20%. The simulation results suggest a strong influence of the wiper type on RTD. The rolling movement in the roller wiper system likely results in a thicker film and less friction forces compared to other wiper types. Fixed wipers, like block or blade wipers, should result in higher film turbulence, enhancing mixing effects while reducing tailing. Material, angles, mass, or the diameter of the roller wipers clearly influence the flow profile and should always be considered when comparing the results of different systems. The model further suggests that the film is highly turbulent, which must be considered in an improved model. Currently, the gap width and the dead volume factor are free system parameters. Using the force and torque equilibrium as well as another model for the axial dispersion within the film, those parameters could be calculated directly, improving the model. For that purpose, a turbulent flow profile must be considered, and the model must be adapted. In the best case, there would be no need to adapt to experimental values, and the system could calculate the residence time distribution on the basis of the existing operating variables directly.
Because it neglected turbulent effects, the model presented here is still relatively simple and, therefore, requires further improvement. A next step could be calculating the proportion of the dead volume and mass transfer to the dead zone with a model that considers flow profile, convection, and axial dispersion. Such a model could be based on the axial dispersion model in tubes and may improve insight into WFE.
However, the model presented here may be suitable for comparing different WFE with one another. It offers a universal platform for physically based model equations, while its modular structure supports easy adaptation of the sub-models to alternative geometries. The internal variables calculated by the model, e.g. liquid hold-up, which are otherwise difficult to measure, can contribute to understanding and improving WFE. Finally, it is possible that this model could support the scale-up of WFE, accounting for different wiper types. In a next step, evaporation could also be considered. While CFD simulations examine model geometry and velocity profiles more accurately than the presented model, they also require great efforts in implementation work for varying the models. Modelica could turn out to be a powerful tool for simulating fluid dynamical systems, which are too complex for common CFD simulations. This has been shown by other authors, who simulated fluid dynamical systems with Modelica [193]. Although Modelica does not allow for complex CFD simulation, it can be used to represent a more complex system or a system as part of a whole plant [193, 194]. The present simulation also showed short calculation times of 7.9 s $\pm$ 0.09 s for integrating a model consisting of around 500 evaluation points in a time period of 60 s. Thus, this approach offers the possibility of real-time calculations and the optimization of experimental setups.

Acknowledgements

The free provision of the TILMedia library and the support from TLK-Thermo GmbH is gratefully acknowledged.

6.3. Corrigendum

A subsequent re-evaluation of the original study revealed an implementation error in one of the equations. Specifically, the segment height was not correctly accounted for in the calculation of the axial velocity in the liquid film. As a result, the axial velocity was underestimated and the volume of the film overestimated. To correct this error and to publish the updated figures and numerical values, the following corrigendum has been issued.

6.3.1. Corrigendum to "A new approach to simulate the fluid dynamics in a wiped film evaporator using Modelica" [Chem. Eng. Res. Des. 161 (2020) 115–124]

The authors regret that after publication, we identified an error in the implementation of our model: the length of the film height was missing from the equations of the model. However, the equations reported in the paper are correct. This affected the results for the film thickness and therefore the liquid hold-up in the film, leading to changes in residence time distribution. In addition, the model was extended to consider the hold-up volume between the injection point and the apparatus and between the apparatus and the exit measuring point during the experiments. This was also implemented in the simulation. As a result of these changes, the simulated residence time distributions as well as the mean residence times and the variance of the residence time distribution change. Figure 6.10, Figure 6.11, and Figure 6.12 present the updated results with the corrected model.

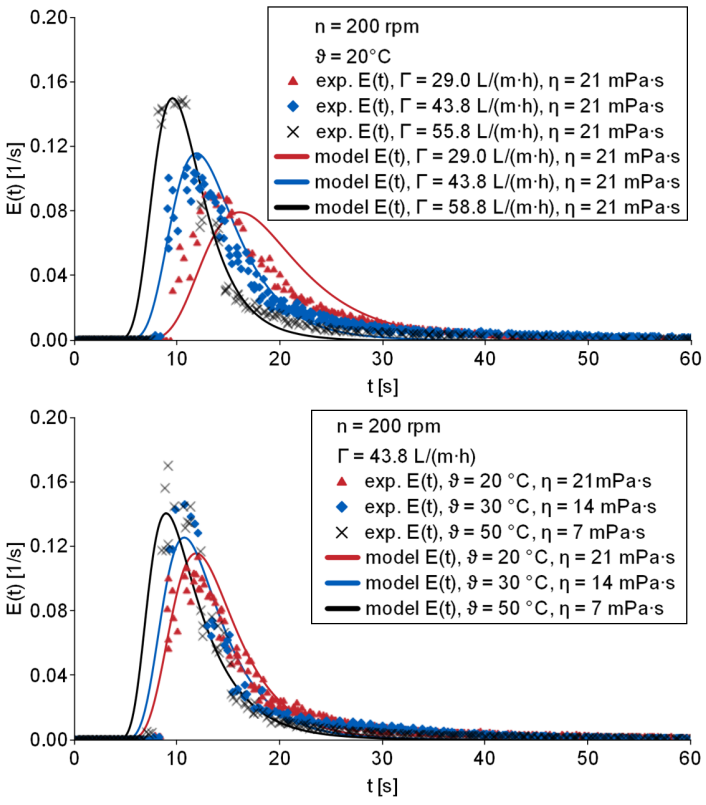

Figure 6.10.: Modeled RTD compared to experimental data. Top: Variation of the liquid load Γ at constant temperature ϑ. Bottom: Variation of temperature ϑ at constant liquid load Γ.

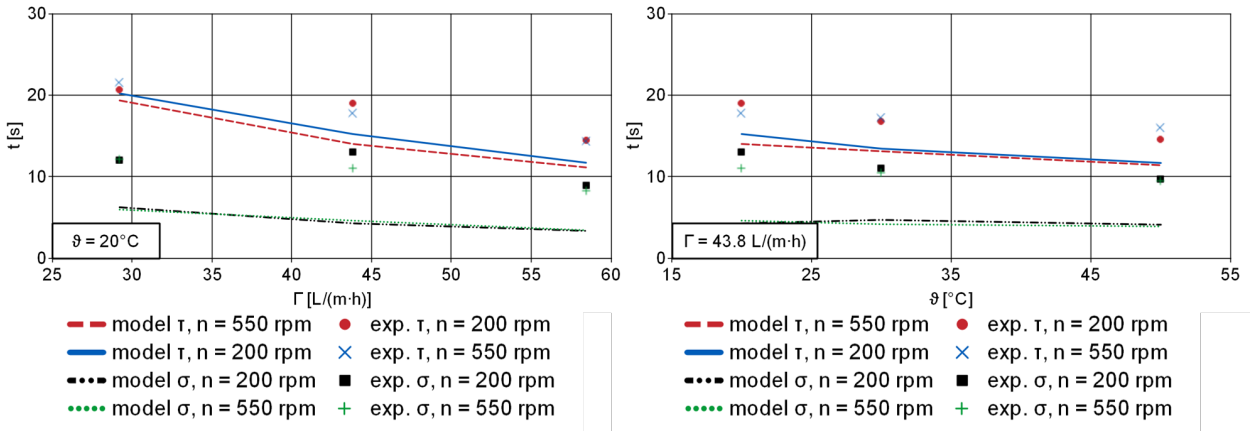

Figure 6.11.: Comparison of measured and simulated mean residence times and standard deviations. Left: Variation of liquid load at constant temperature. Right: Variation of temperature at constant liquid load.

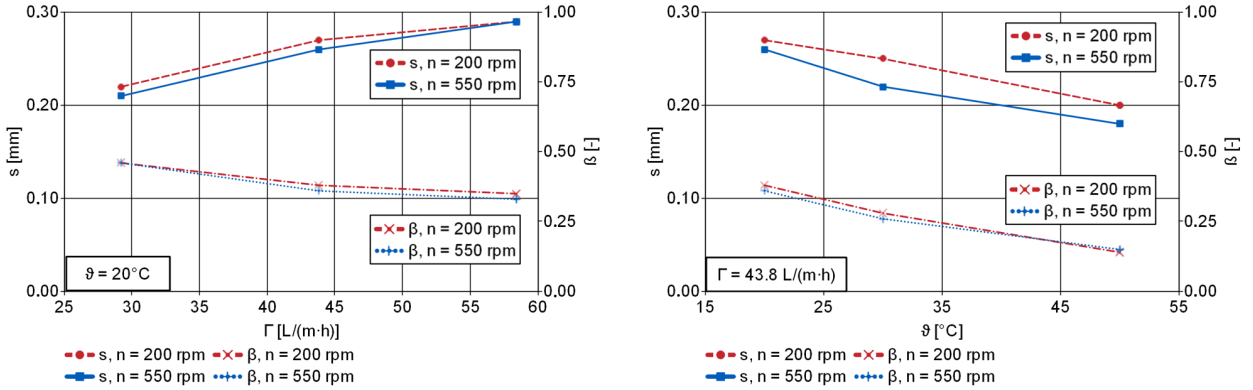

Figure 6.12.: Gap width and dead volume factor for the modeled parameters. Left: Variation of liquid load at constant temperature. Right: Variation of temperature at constant liquid load.

As can be seen, the model performs slightly worse with a narrower residence time distribution. This can also be seen in the updated Figure 6.11. The reported gap widths are reduced to about one third compared to the previous, incorrect version. However, the overall interpretation of our results remains unchanged. The updated results indicate that the deceleration by the wiper element might be more relevant for the overall fluid dynamics than originally assumed, which could be taken into account in further model improvements. Nevertheless, the general trend in the data remains, so the previous discussion of the results is still valid. The authors would like to apologize for any inconvenience caused by this oversight and appreciate the readers' attention to detail.

6.4. Findings of Fluid Dynamic Simulation and Limits of Modeling without Heat Transfer

The fluid dynamic model developed provides an initial insight into the interactions between the wiper system, operational parameters, and the resulting fluid dynamics. Within the fluid dynamics model, the width of the bow wave is adjusted by closing the mass balance. The gap width remains as a fitting parameter that can be adjusted to the experimentally measured residence time distribution. Calculating the gap width using force equilibrium at a roller wiper element was infeasible due to the sensitivity of the model to gap width changes and its coupling with bow wave height and mass balance. However, adjusting the gap width to the experimental data provides an initial impression of how variations in geometry influence RTD and how specific parameters affect the distribution of liquid volumes.

Implementing the differential equations for the CSTR-cascade allows for the calculation of not only an average residence time, as demonstrated by Schweizer, but also a full RTD for the simulated WFE [16]. Unlike earlier approaches to simulate RTDs, such as those of Zeboudj *et al.* this is based on a set of physical equations [77]. The model demonstrated good agreement between simulated and experimental residence time distributions and captured qualitative trends in film thicknesses consistent with visual observations under non-evaporation conditions. However, a direct validation of the simulated film thicknesses was not feasible due to limitations such as the curvature of the apparatus wall, the reflective surface, and uneven illumination in the experimental setup. Although non-contact measurement techniques like laser reflection methods, confocal-chromatic sensors or even LED-based methods could potentially be used [195, 196], their integration into a system with rotating wipers is challenging. Furthermore, many such techniques are not readily applicable under evaporation conditions [195]. Therefore, the ability of the model to be calibrated using comparatively simple and practical residence time distribution measurements, while providing insights into fluid dynamics, represents a valuable complement to the experimental data. Further calibration of the model using direct numerical simulations could enhance its predictive accuracy, though this was beyond the scope of this study.

However, the fluid dynamic model presented so far exhibits some limitations that should be addressed to improve its practical applicability. Its predictive capabilities depend on experimental RTDs for parameterization, which limits its generalizability. Furthermore, heat transfer, which is essential for the actual operation of a WFE, has been neglected, although it is a crucial parameter to capture the effects of decreasing liquid flow, film stability, and separation performance during operation. Therefore, the model discussed in this chapter was expanded to include heat transfer and to enhance its predictive capabilities. This extension establishes a comprehensive simulation framework for the entire apparatus during operation. The extended model, which includes heat transfer, is described and evaluated in the following chapter 7.

7. Modeling of Fluid Dynamics and Heat Transfer in Wiped Film Evaporators during Evaporation

The previous chapter introduced a modular model of fluid dynamics for a WFE, considering it under adiabatic conditions, meaning heat transfer and phase change are disregarded. To improve the applicability of the model, heat transfer and evaporation have been incorporated, while modifications were made to enhance predictive capabilities.

The commercial software Dymola 2024x was used as a working environment [197] for Modelica (version 3.6) [198]. For simulations, the native Python interface of Dymola was employed, allowing efficient management and automation of simulation scenarios. This approach guaranteed that the operational parameters of the simulations aligned with those of the respective experiments, ensuring a better comparison of the experimental and numerical results.

The evaporator was segmented into n_z discrete height elements, forming a segmental model of the entire apparatus. Following the approach in Jahnke, the reduction of the peripheral liquid load along the height was considered and a basis for modeling separation performance was established [40].

Within each height element submodels for fluid dynamics, heat transfer and residence time distribution were instantiated. For a potential extension to multicomponent systems, temperature- and concentration-dependent fluid classes were implemented, which can be used to calculate relevant fluid properties, such as density and viscosity, within each segment and are based on the model fluids characterized in chapter 4. Designing fluid dynamics and heat transfer submodels as interchangeable classes allows seamless integration of alternative modeling approaches, improving flexibility and adaptability of the simulation framework. This ultimately results in a strongly coupled and modular model, the basic structure of which is shown in Figure 7.2.

The models for the fluid dynamics and the RTD of each height element were designed analogously to the models presented in chapter 6. The bow wave model was simplified by assuming an isosceles triangular profile with equal height and length, and the axial velocity within the bow wave was estimated using the simplified relation Equation 2.4 [15]. The dead volume factor β in the CSTR submodel was set to 0.1, as the influence of this factor turned out to be negligible for the fluids under consideration. These simplifications reduced the number of unknowns in the model and allowed for direct predictions of RTDs and heat transfer characteristics.

Each segment includes a heat transfer model that calculates the vaporized liquid proportion using an enthalpy balance. The overall heat transfer coefficient was determined from the sum of the thermal resistances, incorporating contributions from the product, wall, and utility side. This allows for the determination of liquid and vapor phase fractions along the height, enabling an evaluation of evaporation and heat transfer impacts on fluid dynamics.

Different model equations for the product-side heat transfer, detailed in section 7.1, were implemented in the heat transfer model, with empirical equations and penetration theory from subsection 2.2.2 used to calculate the product side heat transfer coefficient. The modular design allows for selective replacement of individual heat transfer submodels, such as the product-side model, at the top level. The model-predicted heat transfer was compared to experimental data, and the influence of deviations

in the heat transfer prediction on the RTD and fluid dynamics was subsequently evaluated.

In addition to the WFE itself, the experimental periphery was modeled. This included the pipe section from the injection point to the evaporator and between the outlet of the WFE and the sensor.

The inlet was modeled as a laminar flow pipe based on the experimental geometry. The region between the outlet and the sensor system, which includes a T-fitting and a subsequent pipe section, was represented by a CSTR in series with a laminar flow pipe. The volume of the CSTR was determined from the dynamic filling level in the T-fitting, calculated using Torricelli's law under the assumption of negligible pressure losses. The pipe section between the T-fitting and the sensor was modeled as a laminar flow pipe, approximated by multiple CSTR cascades connected in parallel. The volumes and flow rates of the CSTRs were calculated from the geometric dimensions of the experimental setup.

7.1. Modeling of Fluid Dynamics in Wiped Film Evaporators during Evaporation

The following section represents an updated version of the following publication: D. Appelhaus, K. Jasch, M. Groth, and S. Scholl. "Modeling of Fluid Dynamics in Wiped Film Evaporators During Evaporation". In: *Sep. Purif. Technol.* 371 (2025), p. 132840.

While updating only editorial changes were made.

Abstract

This study aims to model and predict the operating behavior of wiped film evaporators with roller wipers. A modular model has been formulated in the modeling language Modelica. The established model considers heat transfer, evaporation, fluid dynamics, and residence time behavior. It is parametrized only on the basis of operational and geometrical parameters, which makes it fully predictive. The apparatus is discretized into a series of height elements with local calculation of fluid properties, heat transfer and fluid volumes. Different heat transfer models were considered for the product side, resulting in a deviation of approximately $\pm$25% for the simulated heat flow. The mean residence time can be predicted with $\pm$40% compared to experimental results for medium to high flow rates and moderate evaporation ratios. The shape of the simulated residence time distributions generally matches well with the experimental data. Greater deviations at higher evaporation ratios were attributed to possible de-wetting of the heated surface. The model can be used to predict the influence of the main operational parameters and provides a good basis for the design and re-evaluation of wiped film evaporators. Furthermore, it allows valuable insights into the underlying physics of wiped film evaporators. The model may also be adapted to other wiper geometries by modifying some of the included empirical equations.

7.1.1. Introduction

In wiped film evaporators (WFE), a mechanical wiper system distributes the liquid to be evaporated on the heated inner wall of a heat exchanger. They are suitable for separating highly viscous mixtures, gently evaporating temperature sensitive products [8] and can also be used in reactive distillation processes [13]. Compared to falling film evaporators, the wiping process increases heat transfer, shortens residence time, and tightens its distribution [81]. Nevertheless, the apparatus is among the most costly evaporators, and the numerous interrelationships of design parameters, operational conditions, and thermophysical properties complicate the development of a reliable model to describe the operational behavior of WFEs, thus limiting their applicability. A comprehensive model requires understanding the interactions between wiping, evaporation, and potential de-wetting phenomena. Fluid dynamics was first investigated by Schweizer and Widmer as well as Widmer and Giger [6, 32]. Schweizer and Widmer were able to predict the mean residence time in the unheated apparatus well for higher viscosity fluids. A numerical simulation for the laminar case was carried out by Komori *et al.* [60]. More recently, these have been complemented by CFD simulations for rigid wiper elements [45]. For moving wiper elements, substitute models based on stirred tank cascades were successfully applied [50], which were supplemented by experimental investigations [22] and numerical simulations [25]. Separately, heat transfer in WFE was modeled by various authors. There are both empirical equations based on dimensionless parameters [43, 91, 199] and mechanistic models based on penetration theory with and without a correction factor [20, 98, 99], which are discussed in more detail in subsubsection 7.1.2.3. The integral heat transfer [31, 61] and the simultaneous mass transport could be modeled using the segmented approach [19, 39].

In WFE, thin films improve heat transfer by providing a large surface area and reduced thermal resistance, thus reducing temperature gradients. At the same time, film stability must be considered. The formation and behavior of liquid films on heated walls is well-researched and has advanced recently with new measurement methods. For detailed reviews in this field, see Oron *et al.* and Craster and Matar [67, 106].

A liquid film flowing down a vertical wall can form ridges, and even small perturbations can lead to film flow instabilities [113, 114]. Therefore, the growth rate of instabilities depend on the surface tension and the angle of inclination for lower film Reynolds numbers [200]. For a non-heated falling film, the minimum thickness of the film can be estimated using the equations of El-Genk and Saber [112, 201].

Heat transfer towards a thin liquid film leads to the emergence of additional destabilizing mechanisms due to thermocapillary stress (Marangoni effect) [115, 116, 117, 118]. Destabilization is favored by low surface tension, low dynamic viscosity, and low thermal conductivities [110]. In addition, high temperature differences promote the instabilities of the liquid film [119, 120]. Instabilities can ultimately lead to film breakup and thus to the formation of dry spots [121]. It should be noted that film break-up is a dynamic process. Not only does the morphology of the observed dewetted areas differ significantly depending on the thermophysical properties of the fluid and the process conditions, but also the time period for the formation of the dry spots can differ by several orders of magnitude [125, 126, 127, 128].

The film stability of a liquid film to be evaporated in falling film evaporators thus depends on the

respective process parameters. Using a wiped film evaporator, a fluid can be evaporated even with otherwise unfeasible parameters [31].
Although the thermodynamic stability of the liquid film is crucial in coating applications and falling film evaporators, the kinetics of instabilities and the formation of dry spots are particularly relevant in wiped film evaporators. To prevent film breakdown, liquid redistribution must be faster than film rupture. Current WFE models cannot predict film breakdown or its impact on heat transfer due to variable film thickness under changing conditions, especially with flexible wiper elements, e.g. roller wipers. The interactions of fluid dynamics and heat transfer under evaporation conditions have hardly been considered. A comprehensive WFE model integrating fluid dynamics and heat transfer is needed, potentially extendable to include film stability. In this study, a modular model was developed to simultaneously simulate the fluid dynamics and heat transfer of WFE with roller wipers. The model assesses critical fluid dynamic parameters such as film thickness, residence time distributions, and heat transfer to evaluate thermal stress on processed fluids. Both, the model, which is parameterized on the basis of well-defined measurements, and simulation results on fluid dynamics and heat transfer are presented.

7.1.2. Model Equations and Structure

The fluid dynamic model based on the work of Appelhaus *et al.* was extended to include heat transfer and evaporation [25]. The underlying equations have been simplified to enhance versatility, allowing the model to be used for predictive modeling of operational behavior. The apparatus was divided into n_z equidistant height elements by discretization, whereby each height element was modeled separately as shown in Figure 7.1. This segmental approach has proven to be suitable for the calculation of heat transfer, fluid dynamic and mass transfer [31, 58, 61, 202], but has not yet been implemented as an overall model considering fluid dynamics and heat transfer simultaneously.

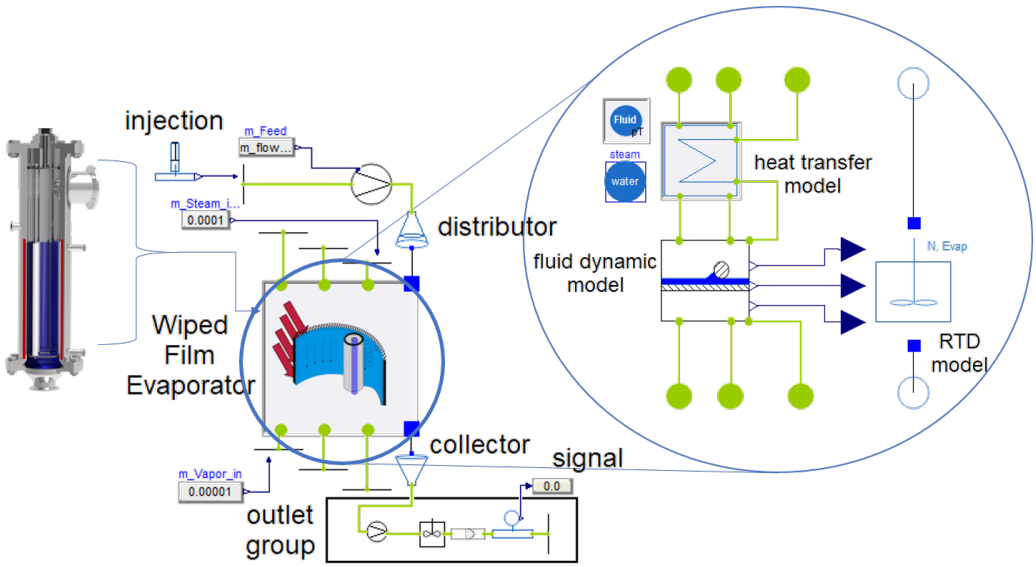

Figure 7.1.: Representation of the selected model structure with the WFE, which is discretized over the height into height elements, in which each height element consists of a heat transfer model, a fluid dynamic model and a stirred tank cascade.

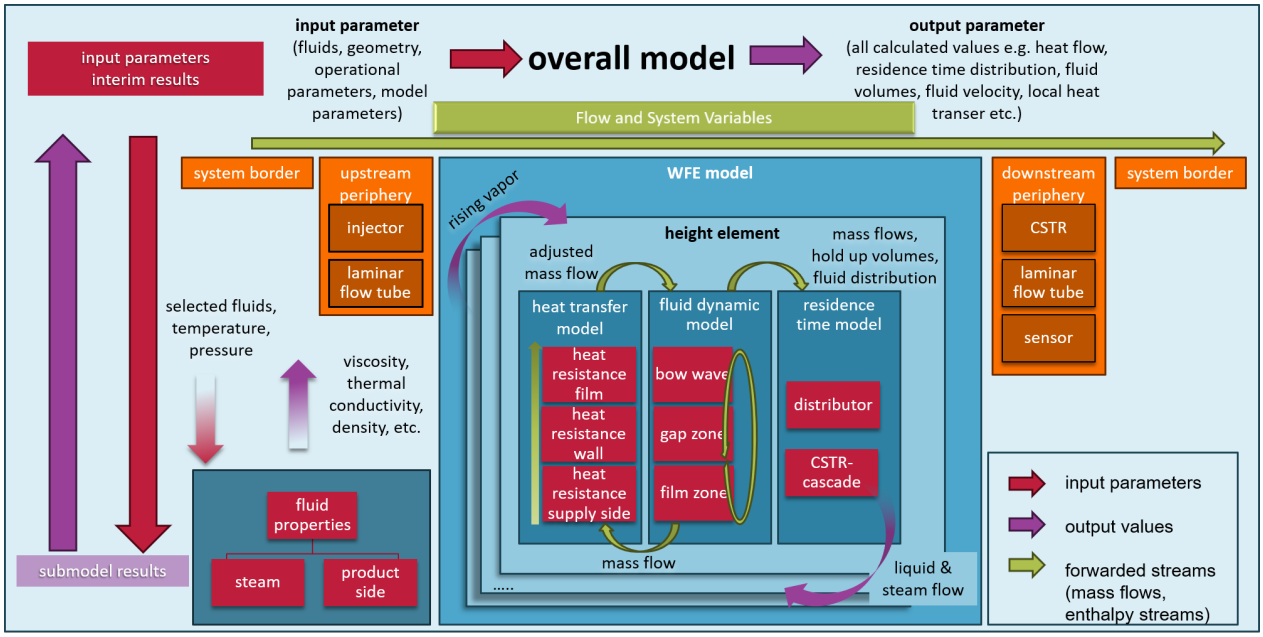

Figure 7.2.: Presentation of the overall model structure with the respective submodels and the information flow between the submodels.

7.1.2.1. Submodel Interconnection

Heat transfer, fluid dynamics, and residence time distribution submodels were modularly implemented using Modelica. The entire WFE is segmented along its height into n_z height elements and is incorporated into the overall model shown in Figure 7.1. The basic structure of the model with the interconnection of the individual submodels is presented in Figure 7.2. The submodels are instantiated as objects within the higher-level models. Key variables, such as liquid hold-up, input parameters, and calculated intermediate results, are exchanged between submodels via connectors. The algebraic system is solved for each time step using the Dymola DASSL solver for differential equations.
Based on temperature and composition, the fluid properties were calculated individually for each height element. In the respective submodel instances, heat transfer and fluid dynamics are independently modeled. The discretization number n_y of the film zone and the radial discretization of the velocity profile n_x are input parameters of the model. The volumes, fluid distribution, and mass flow rates derived from the fluid dynamic model are transmitted to the CSTR-based residence time model for each height segment through connectors linking the submodels. The source code for all models is available on request.

7.1.2.2. Parameterization

The geometric and operational parameters of the experimental investigations were used for the model parametrization. For this purpose, the mean values corresponding to the steady-state operation and the experimental geometry are used as input parameters. Laboratory-scale experiments were performed using a steam-heated WFE, with key parameters presented in Table 7.1.

Table 7.1.: Operational and geometrical parameters of the used WFE

wall material	**wiper type**	**height [m]**	**diameter [m]**
stainless steel	roller	0.256	0.08
area [m^2]	**Γ_{Feed} [L/(m·h)]**	**frequency [rpm]**	**medium**
0.06	20 ... 120	50 ... 500	diethylene glycol

Table 7.2.: Model parameters for the simulations

n_x	n_y	n_z
10	20	8
n_{CSTR}	β_{dead}	Source $a_1 \dots a_5$
5	0.1	(1) [199]

The specific peripheral load Γ and the wiper speed w were calculated considering the mass flow $\dot{m}$ and the wiper frequency n according to Equation 7.1 and Equation 7.2.

$$\Gamma = \frac{\dot{V}}{\pi \cdot d_r} \tag{7.1}$$

$$w = n \cdot \pi \cdot d_r \tag{7.2}$$

The additional model parameters were set according to Table 7.2. The parameters for the number of discretization elements were chosen sufficiently high so that a further increase would not change the simulation result. The dead volume factor β_{dead} introduced by Appelhaus *et al.* was found to have a negligible effect on the system considered in this document. This may be due to the low viscosity of the liquid diethylene glycol at its evaporation temperature of 117 °C at 8 mbar. However, it was set to a constant value of 0.1, as this resulted in a higher numerical stability of the simulation without significantly affecting the results.

7.1.2.3. Heat Transfer

The heat transfer submodel calculates local heat transfer coefficients and changes in vapor-liquid flow in a height element via the enthalpy balance. The total heat transfer coefficient U was calculated as the inverse of the heat transfer resistance $R = 1/UA$. The overall resistance to heat transfer can be determined by summing the heat transfer resistances from the product/film side, the apparatus wall, and the heat supply or steam side.:

$$R_{\mathrm{total}} = R_{\mathrm{product}} + R_{\mathrm{wall}} + R_{\mathrm{supply}} \tag{7.3}$$

The heat transfer resistance of the wall R_{wall} for a height element of the height dz results from the resistance to heat conduction through a tubular geometry:

$$R_{\mathrm{wall}} = \frac{\ln \frac{d_r+2s}{d_r}}{2 \cdot \pi \cdot \lambda_{\mathrm{wall}} \cdot dz} \tag{7.4}$$

Thereby is d_r the inner diameter of the apparatus and λ_{wall} the thermal conductivity of the wall.

For the heat transfer resistance on the supply side R_{supply}, in which steam is used as a heat source, the equations for the condensation of saturated vapors in a free falling film were applied (see [134]). It was postulated that the condensate of the heating steam is pure, stationary steam without the presence of non-condensable gases. The loss of pressure across the condensation surface was neglected. In this case, the local heat transfer coefficient is obtained by calculating the Nusselt number with the characteristic length of the film flow $\mathcal{L}$ according to Equation 7.5 with the kinematic viscosity of the liquid ν_F and the gravity of Earth $g = 9.81\ \text{m/s}^2$.

$$\mathcal{L} = \sqrt[3]{\frac{\nu_L^2}{g}} \tag{7.5}$$

The local Nusselt number for the laminar flow region can be calculated according to Equation 7.6 with the thermal conductivity of the liquid λ_L and the ratio of vapor to liquid density ρ_V/ρ_L.

$$\text{Nu}_{L,x,l} = \frac{h_{L,x,l}\mathcal{L}}{\lambda_L} = 0.693 \left(\frac{1 - \rho_V/\rho_L}{\text{Re}_{L,x}} \right)^{1/3} \tag{7.6}$$

The local Reynolds number is given by Equation 7.7 with the local periphery load Γ_x in relation to the dynamic viscosity of the liquid η_L.

$$\text{Re}_{\text{L},x} = \frac{\Gamma_x}{\eta_\text{L}} = \frac{\dot{m}_{\text{L},x}}{\pi \cdot d_o \cdot \eta_\text{L}} = \frac{\dot{m}_{\text{L},x}}{P_o \cdot \eta_\text{L}} \tag{7.7}$$

The waviness of the film flow was taken into account by the approach according to Kutateladze and Gogonin (see Equation 7.8) [203].

$$f_{\text{wavy}} = \frac{\text{Nu}_{\text{L},x,l,\text{wavy}}}{\text{Nu}_{\text{L},x,l}} = \begin{cases} 1 & \text{for } \text{Re}_{\text{L},x} < 1 \\ \text{Re}_{\text{L},x}^{0.04} & \text{for } \text{Re}_{\text{L},x} \geq 1 \end{cases} \tag{7.8}$$

The local Nusselt number for the turbulent flow region was calculated according to Equation 7.9 [204].

$$\text{Nu}_{L,x,t} = \frac{h_{L,x,t}\,\mathcal{L}}{\lambda_L} = \frac{0.0283\,\text{Re}_{L,x}^{7/24}\,\text{Pr}_L^{1/3}}{1 + 9.66\,\text{Re}_{L,x}^{-3/8}\,\text{Pr}_L^{-1/6}} \tag{7.9}$$

The local Nusselt number was then calculated by quadratic superposition of the laminar and turbulent Nusselt numbers based on Equation 7.10 [204].

$$\text{Nu}_{\text{L},x} = \sqrt[2]{(f_{\text{wavy}}\,\text{Nu}_{\text{L},x,l})^2 + \text{Nu}_{\text{L},x,t}^2} \cdot f_\eta \tag{7.10}$$

The influence of the temperature-dependent thermophysical properties can be taken into account by the factor f_η, which can be calculated according to Equation 7.11 with the liquid viscosity of the fluid adherent to the wall $\eta_{L,W}$ and at the surface of the film $\eta_{L,S}$. f_η was assumed to be 1 in these investigations.

$$f_\eta = \left(\frac{\eta_{L,S}}{\eta_{L,W}} \right)^{1/4} \tag{7.11}$$

In order to model the heat transfer resistance on the product side, different approaches were considered and evaluated as part of this work, which will be presented in more detail.

One of the most physically sound theories is penetration theory, which was originally formulated for mass transfer and can be modified and applied to heat transfer. It is based on the assumption that heat transfer on the product side occurs in the form of transient heat conduction in the film, which is then periodically mixed with the bow wave by the wiper. From this, Kool and Latinen derived the following equation for the film heat transfer coefficient h_P of WFE with the wiping time $t_{Sc} = \frac{1}{n \cdot N_B}$ [63, 97].

$$h_P = \frac{2}{\sqrt{\pi}} \sqrt{\frac{\lambda \cdot \rho \cdot c_P}{t_{Sc}}} \tag{7.12}$$

However, several authors measured heat transfer rates lower than expected from penetration theory [98, 99]. Therefore, penetration theory was extended to include a corrective term for turbulent flow and incomplete mixing of bulk and film. In this study, the empirical approach of Azoory and Bott was considered, in which a correction factor f was introduced as a function of the Prandtl number[20]:

$$h_P = \frac{2}{\sqrt{\pi}} \sqrt{\frac{\lambda_P \cdot \rho_P \cdot c_P}{t_{Sc}}} \cdot \frac{1}{f} \tag{7.13}$$

$$f = 3.5 + \frac{\mathrm{Pr}}{500} \tag{7.14}$$

Fully empirical approaches are based on Nusselt number correlations. These are usually a function of the Reynolds number in the film $\mathrm{Re}_F = \Gamma/\eta$, the rotational Reynolds number $\mathrm{Re}_R = (d^2 \cdot n \cdot \rho)/\eta$, the Prandtl number $\mathrm{Pr} = \eta \cdot c_P/\lambda$, the ratio of diameter to length of the WFE (d_E/h_{WFE}) and the number of wiper elements N_B. This results in Equation 7.15.

$$\mathrm{Nu} = \frac{h_P \cdot d_E}{\lambda} = a_1 \cdot \mathrm{Re}_F^{a_2} \cdot \mathrm{Re}_R^{a_3} \cdot \mathrm{Pr}^{a_4} \cdot (\frac{d_E}{L})^{a_5} \cdot N_B^{a_6} \tag{7.15}$$

Various authors have determined different coefficients of Equation 7.15 based on experiments. Table 7.3 lists coefficients from three different studies, frequently used in modeling WFE and utilized here as examples. While Skelland and Bott and Romero chose the diameter of the apparatus d_r as the characteristic length, Bott and Romero pointed out that due to the thin film, half the bow wave width should be chosen as the equivalent diameter d_E instead [43, 91, 199], resulting in different numerical values of the coefficients.

Table 7.3.: Parameters of Equation 7.15 for heat transfer by Skelland (1), Bott and Romero (2) and Bott and Romero (3)

Source	a_1	a_2	a_3	a_4	a_5	a_6
(1)	4.9	0.57	0.17	0.47	0.37	0
(2)	0.018	0.46	0.6	0.87	0.48	0.24
(3)	0.0023	0.5173	0.5749	0.9942	-0.4414	0.613

In the present work, the heat flow was determined based on the overall heat transfer coefficient, the heat transfer area, and the temperature difference between the supply and the product side. An enthalpy balance was used to model the evaporating proportion of the fluid. The experimental data were recorded for isothermal experiments, in which the temperature difference ΔT corresponds to the difference between the boiling point of the product and the condensation point of the steam.

$$\Delta T = T_{\mathrm{cond,steam}} - T_{\mathrm{boil,product}} \tag{7.16}$$

The fluid properties of the product side were calculated using the fluid properties published by Appelhaus *et al.* for diethylene glycol [23]. The equations according to IAPWS97 were used for the fluid properties of water and steam [133].
To evaluate which of the models presented is best suited for product-side heat transfer, the results of the different approaches are compared with experimental results in subsubsection 7.1.3.1.

7.1.2.4. Fluid Dynamics

For the modeling of the liquid distribution and the hold-up volumes, the fluid dynamic model of Appelhaus *et al.* was further refined and coupled to the heat transfer model [25]. The model relies on the premise that a wiper segment can be described through a coordination transformation involving a mobile wall and a stationary wiper element [58]. Separate fluid dynamic models were developed for the bow wave (1), the gap (2), and the film (3), which were connected to each other as shown in Figure 7.3. Since the aim of this study was to develop a model of the entire apparatus that is as predictive as possible, a number of assumptions were made regarding the fluid dynamic model:

1. Each height element fulfills the assumptions for the overall process of Appelhaus *et al.* (Newtonian fluid, no evaporation in fluid dynamic model, isothermal, isobar) [25]
2. The flow profile in each zone can be modeled as a laminar flow
3. The vertical flow is purely gravity driven
4. Film and bow wave are continuously mixed
5. Slip between liquid and wall is negligible
6. Dry-out and de-wetting of the surface do not occur

Laminar flow is widely assumed for falling films to allow for an analytical solution of the Navier-Stokes equations [6, 60]. However, CFD simulations as well as experimental laser Doppler-Anemometry measurements suggest that the liquid flow is turbulent, especially in the bow wave [6, 45]. In addition, dry out and de-wetting of the surface can be expected at the lower load limit [31].
The fluid dynamic submodel was modified to represent a height element, with calculated variables directly transferred to linked models, like the CSTR model, via connectors.
The model for calculating the characteristic dimensions of the bow wave has also been modified. A major limitation of the model of Appelhaus *et al.* was that the mass balance was closed by adjusting the length of the bow wave, whereby the gap width was used as a fitting parameter to the experimental

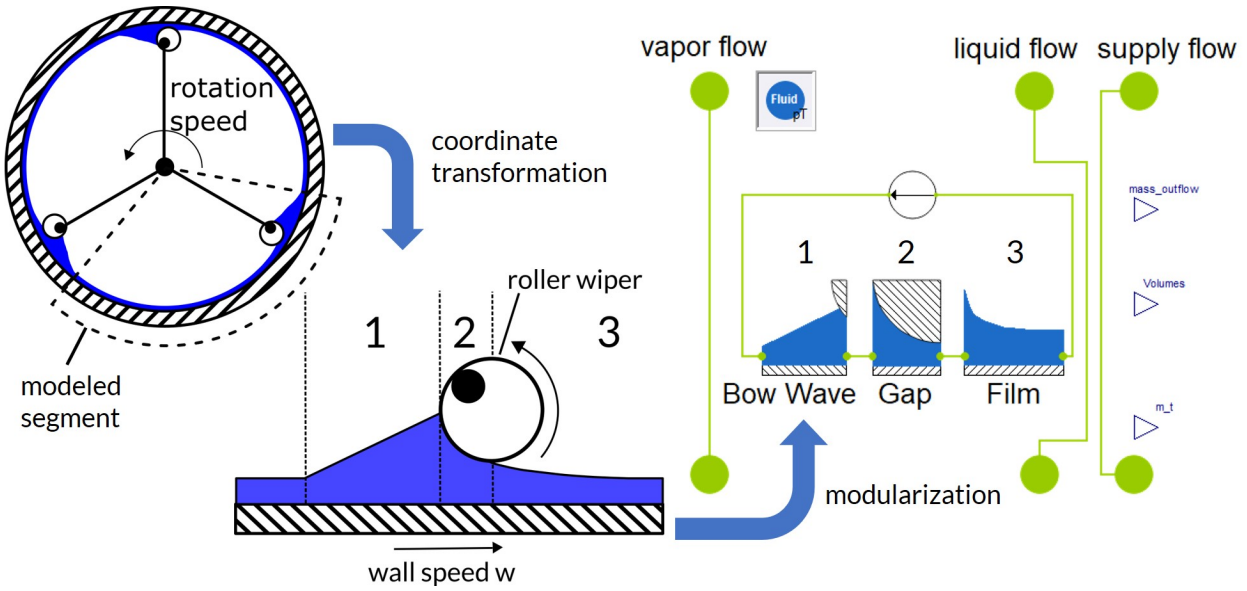

Figure 7.3.: Model structure to model the fluid dynamics. A single wiping segment was modeled using coordinate transformation and submodels of the zones' bow wave (1), gap (2) and film (3) were interconnected.

residence time measurements. However, to obtain a fully predictive model, it is necessary to reduce the number of degrees of freedom in the fluid dynamic submodel by one, which was achieved by assuming that the height of the bow wave is identical to the length of the bow wave. In this case, the width of the gap can be determined by the mass balance. Despite this, the bow wave's height or length must still be determined. This can be done using numerical methods like the volume of fluid method or through empirical correlations. For this model, the bow wave height correlation adapted by Appelhaus *et al.* (see Equation 7.17) was used [25]. Refer to the nomenclature section for definitions of dimensionless numbers.

$$\mathrm{Eu} = \frac{h_B}{d_r} = a_1 \cdot \mathrm{Re}_R^{a_2} \cdot \mathrm{Re}_F^{a_3} \cdot \mathrm{Fr}_R^{a_4} \cdot (s/b)^{a_5} \tag{7.17}$$

The parameters for Equation 7.17 were empirically derived for fixed wipers. Using mechanistic or system-specific equations could enhance model accuracy and stability. Furthermore, the calculation of the axial velocity v_{ax} was simplified using Equation 7.18 instead of the Taylor series employed by Appelhaus *et al.* as it produced similar results.

$$v_{ax} = \frac{K_1 \rho g}{\eta}(h_B + s)^2 \tag{7.18}$$

Equation 7.18 was adapted experimentally to the speed distribution in blade wipers, whereby the factor K_1 for an equilateral triangle was determined to be 0.0703 [15]. The factor K_1 also offers the potential to be adapted to different wiper systems in future model refinement. To take into account the rising vapor flow, the mean axial velocity of the film zone $\overline{v}_{ax}$ was adjusted by the tangential shear stress τ_δ according to Nusselt's assumptions for a liquid film with a gas counterflow, so that the axial

velocity for a film element was determined according to Equation 7.19 [111]:

$$\overline{v}_{ax} = \frac{1}{3} \cdot g \cdot \rho \cdot \frac{d_r^2}{\eta} - \frac{\tau_\delta \cdot d_r}{2\eta} \tag{7.19}$$

The shear stress τ_δ at the liquid-gas interface was obtained through Equation 7.20 to Equation 7.24 [111]:

$$C_d^2 = 8 \cdot \frac{\tau_\delta}{\overline{v}_V^2 \cdot \rho_V} \tag{7.20}$$

$$C_d^2 = \frac{64}{\mathrm{Re}_V \cdot k} \tag{7.21}$$

$$\mathrm{Re}_V = \frac{\rho_V \cdot \overline{v}_V \cdot 2 \cdot r_\delta}{\eta_V} \tag{7.22}$$

$$k = 1 - 2 \cdot \frac{\eta_V}{\eta_L} \cdot \frac{1/\tau_\delta^* - 2}{\left[\frac{r}{\delta_0} \cdot \left(1 - \frac{3}{2} \cdot \tau_\delta^*\right)^{1/3} - 1\right]} \tag{7.23}$$

$$\tau_\delta^* = \frac{\tau_\delta}{g \cdot \rho_L \cdot \delta} \tag{7.24}$$

The discharge coefficient C_d depends on the Reynolds number of the gas phase and the correction factor k. The value of k is determined using the ratio of the viscosity of the vapor to the viscosity of the liquid, η_V/η_L, along with the dimensionless shear stress τ_δ^*, which is determined by Equation 7.24, as well as the proportion of the inner radius to the local film thickness r/δ_0. For the calculation of the residence time distribution, a stirred tank cascade was assumed as used by Zeboudj *et al.* [77] and Appelhaus *et al.* [25]. The results of the fluid dynamic model were used to parameterize the stirred tank model. In order to correspond more closely to the falling film characteristic, a further discretization of the stirred tank cascade was carried out. For a height element n_{CSTR}, the vertically aligned stirred tank cascades were interconnected, matching the total volume of the fluid dynamic submodel's individual zones (see Figure 7.1 and Figure 7.3).
In addition, the system periphery of the validation experiments was considered by modeling the section between the tracer injection point and WFE as a laminar flow tube and the section between the sump and the tracer sensor as a combination of a CSTR and a laminar flow tube.

7.1.3. Results and Discussion

Simulation results were compared with the experimental data from WFE. The deviations of the simulated heat transfer and residence time distribution are discussed, and the influence of operating parameters such as the mean peripheral load and the wiper speed on the calculated residence time are shown.

7.1.3.1. Heat Transfer

The simulated integral heat flow for the different heat transfer models (see subsubsection 7.1.2.3) was compared with the corresponding experimental results and is shown for different temperature differences in a parity plot in Figure 7.4. Data from the Nusselt correlation (see Equation 7.15) are

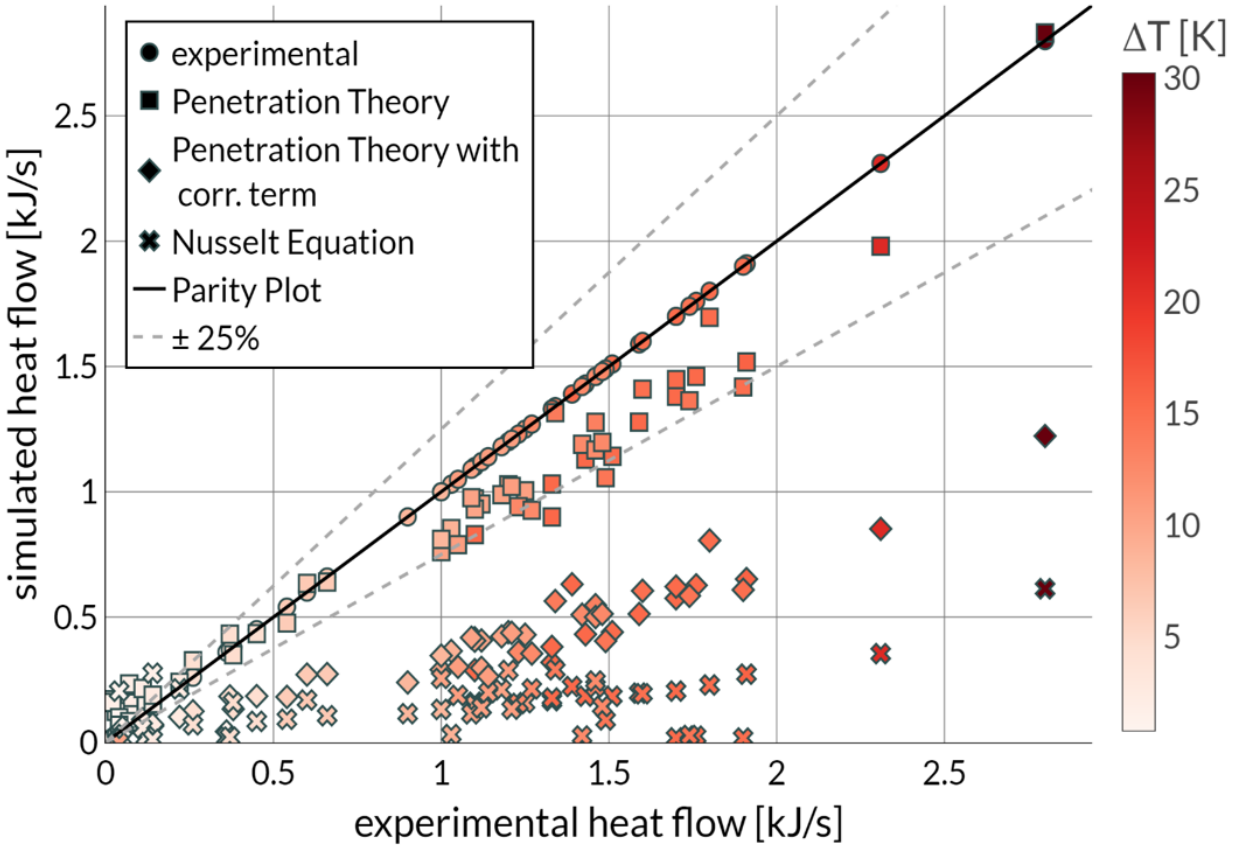

Figure 7.4.: Parity plot of heat transfer for different heat transfer models and different temperature differences.

derived using parameters from Bott and Romero. The alternative parameter sets in Table 7.3 yielded comparable results. The penetration theory without a correction factor most accurately predicts the experimental heat flow compared to all investigated models. The deviations from the experimental results are within 25%, which is within the range of established empirical correlations [91]. Although penetration theory tends to underestimate heat transfer systematically, it is not advisable to include a correction factor. This is because the experiment might have an increased effective heat transfer area resulting from extra heat conduction above and below the wiped region, a factor that is not currently considered in the simulation. Accounting for the effective heat transfer area could reduce the discrepancy without correction terms.

The application of penetration theory with a correction factor as well as the used Nusselt correlation led to significantly larger deviations. The results of the Nusselt correlation were obtained using the parameters of Skelland but were similar for the other parameter sets in Table 7.3 [199]. The heat transfer resistance on the heating side resulting from steam condensation is minimal, while the heat transfer resistance in the apparatus wall is comparable to the calculated product-side heat transfer resistance. The model used to calculate the product-side heat transfer is therefore essential for predicting the residence time distribution of an apparatus. The correction factor used will probably only become relevant at higher liquid viscosities, where the mixing between the bow wave and the film is expected to be less effective. For the fluid used with low viscosities down to 2.1 mPas and roller

wipers, the poor applicability of the correction factor arises mainly from the constant offset of 3.5 in the correction term calculation. Determined from experimental results, this limits the applicability of the corrected equation to significantly different fluid properties.
The inferior performance of the Nusselt correlation examined can be linked to the limited applicability of the incorporated dimensionless numbers. Although adapting Equation 7.15's parameters could yield better outcomes than penetration theory, the Nusselt correlations reported probably lack transferability in their current form. As already stated by Bott and Romero, the dependence on the inner diameter limits the transferability [91]. However, despite their introduction of the equivalent characteristic length d_E, the Nusselt equation continues to incorporate factors, such as the number of blades, that should not influence the heat transfer of an individual wiper segment. For a meaningful application of the Nusselt equation, the dimensionless numbers used should therefore depend only on parameters that actually have a direct influence on the heat transfer. Since both the penetration theory model with correction factor and the Nusselt correlation deviate too much from the experimental heat transfer, they are not considered further in subsubsection 7.1.3.2. Instead, the focus is on the difference between a simulation using the penetration theory and the direct use of experimentally determined heat flows.

7.1.3.2. Fluid Dynamics and Residence Time Distribution

To evaluate the quality of the fluid dynamic model, experimental residence time distributions were compared with the model predictions. The residence time distributions for selected experiments with and without evaporation are shown in Figure 7.5. The general shape of the residence time distributions with a rapid increase and a prolonged tailing can be reproduced well. Without evaporation, the mean residence time is well predicted for mean peripheral loads above 40 L/(m h), while the residence time distribution shifts to higher mean residence times for low liquid loads. Nevertheless, the discrepancies between experimental results and simulations are probably acceptable for many use cases in industrial contexts or when incorporating a model into a process simulation. For the experiments with evaporation, the residence time distributions for low temperature differences are well predicted, whereas the mean residence time is underestimated for higher temperature differences.
In order to further investigate the deviations of the model compared to the experimental results, the experimental mean residence times are compared with the simulated results in a parity plot in Figure 7.6. The shape of the simulated residence time distributions was considered by evaluating the second moment of the distributions. To investigate the effect of the heat flow the results based on the penetration theory are compared with the experimental heat flow as a given parameter for the simulation.
For mean residence times below 25 s coupled with higher mean peripheral loads, the model could predict the mean residence time experimentally determined with a deviation of $\pm 40\%$. This presents a reasonable performance of the overall model considering that the model is fully predictive with a computation time of less than 2 seconds. Therefore, it can be a good alternative to experimental investigations in many industrial applications. It should also be mentioned that the equation for the determination of the bow wave height was fitted empirically for blade wipers and can be further adapted by a suitable data set of experimental or CFD data. Likewise, the bow wave height may

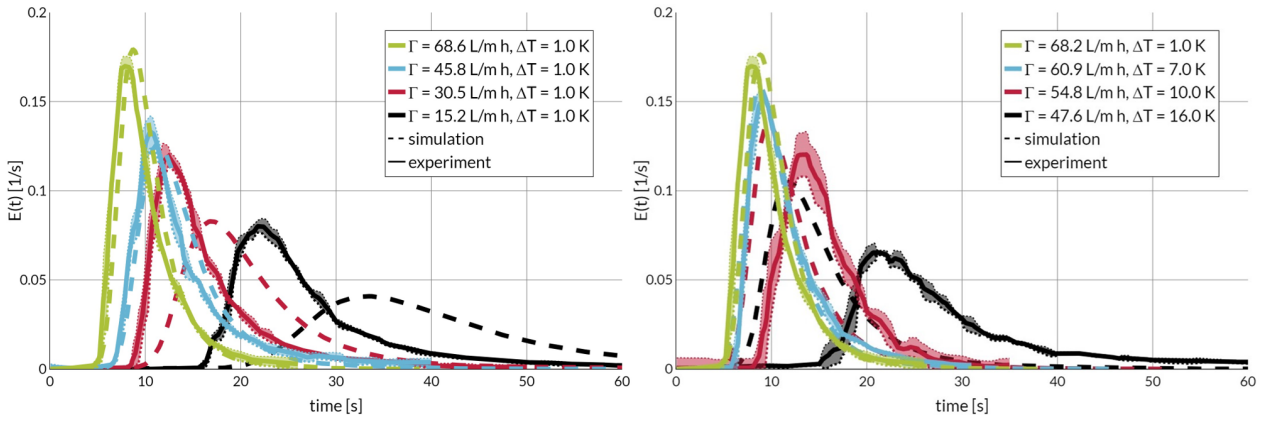

Figure 7.5.: Experimental and simulated residence time distributions for different mean peripheral loads without evaporation (left) and with evaporation (right).

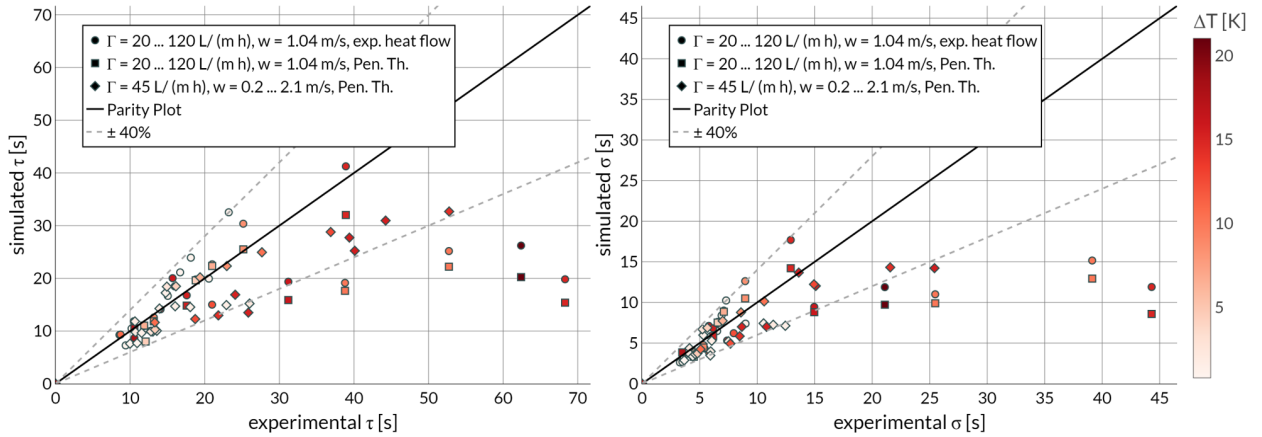

Figure 7.6.: Parity plots of mean residence time (left) and 2nd moment of residence time distribution (right) for different heat flows.

be adjusted iteratively within the physical boundary conditions of the model to further reduce the deviation between experimental and simulated residence time distributions.
Research indicates that CSTR surrogate models can effectively reproduce residence time distributions across different wiper systems [6, 77]. A segmented approach, suitable for the entire apparatus, was consistently used to calculate separation performance. Until now, the methods discussed have addressed only heat transfer [61] or have been restricted to examining the residence time distribution without evaporation [6, 25, 77]. Moreover, none of the predictive models accounted for the interaction between geometric and operating parameters along with the fluid's thermophysical properties. Instead, efforts have been directed towards the reproduction of existing experimental distributions of residence times. The proposed model has the ability to emulate both fluid dynamics and heat transfer in the context of different plant setups. Additionally, the modular design allows for the expansion of the comprehensive model or the substitution of submodels, such as incorporating different wiper models. However, it is also noticeable in the parity plots that there is a systematic deviation at high residence times. Without evaporation, the mean residence time tends to be overestimated, whereas it is underestimated under evaporation conditions, especially for higher superheat. This is probably due

to the fact that the assumptions of the underlying model are no longer fulfilled in these operating ranges. At low mean peripheral loads, the impact of volume flow alterations resulting from tracer injection is no longer negligible. The tracer volume of 0.5 mL is injected within 500 ms. At a volume flow of 6.5 L/h, this results in a temporary change of approximately 27%, which could be taken into account in the model if this range is of further interest.

This is different in the range with very high evaporation. Injection only changes the flow of the feed but has only a little effect on the peripheral sump load. The large deviation between the experiment and the simulations must therefore have a different reason. The discrepancy cannot be fully attributed to the underestimation caused by the heat transfer model, as is also apparent when the experimentally determined heat flows are directly considered. Furthermore, the effect of an uprising vapor flow is already accounted for within the model as well as the effect of the experimental periphery. Therefore, the effect can most probably be attributed to a periodic de-wetting of the apparatus wall in this region, a factor neglected during model development. Opposed to the closed fluid film hypothesis used in the fluid dynamics model, the axial fluid velocity decreases to 0 m/s, potentially leading to a notable rise in the mean residence time in this case. Experimental observations at low liquid loads revealed an uneven liquid distribution, significantly increasing the mean residence time depending on the wiper speed and the liquid load [51]. For roller wipers, the heat transfer coefficient also decreases at low sump loads, probably due to dewetting [31]. Additional destabilization mechanisms due to wall overheating, as discussed in subsection 7.1.1, suggest that de-wetting is likely at higher superheat and low liquid loads, potentially explaining the observed higher experimental mean residence times in this operational range. Since this range is a lower operating limit, extending the model to recognize de-wetting is useful. This effect could be incorporated into the model by including an additional de-wetting factor in the region of low sump peripheral loads. One potential approach to this is the one proposed by Jahnke *et al.* [31]. However, accurately predicting actual residence time distribution in this range is less crucial, since real processes are unlikely to operate here. Therefore, subsequent experimental or numerical research should concentrate on exploring the de-wetting dynamics for validation purposes.

An analogous evaluation results for the width of the residence time distribution represented by the second moment of the residence time distribution. Here too, greater deviations between experiment and simulation occur primarily at higher evaporation rates, which can probably also be explained to a large extent by the onset of de-wetting.

To further analyze the dependence of the model results on operational parameters and to illustrate possible use cases, the dependence of the simulated mean residence time and the simulated mean gap width was plotted for different wiper speeds and temperature differences in Figure 7.7 and Figure 7.8. As shown in Figure 7.7, the mean residence time decreases hyperbolically with the peripheral load. A notable increase in the mean residence time was observed at a mean peripheral load of approximately 20 L/m h or below, indicating that below this threshold the WFE no longer works properly. It is evident that the individual simulation results for the experiments without a temperature difference follow the general trend more closely than those of the data points with a higher temperature difference. Thus, it can be concluded that the effect of evaporation on residence time deserves closer consideration in the case of high evaporation rates.

Furthermore, the mean peripheral load has an impact on the mean gap width, which represents the

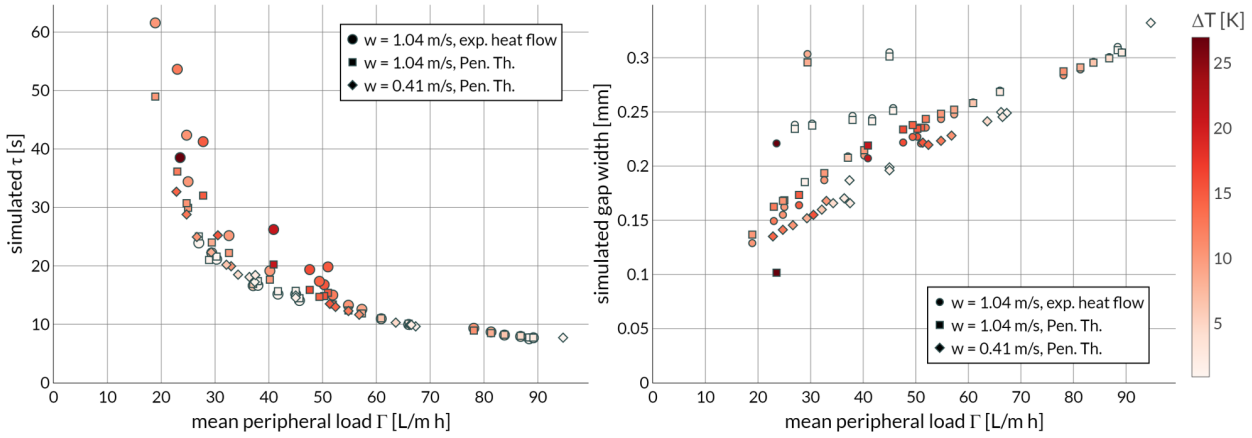

Figure 7.7.: Simulated mean residence time (left) and mean gap width (right) in dependence of the mean peripheral loads for different temperature differences ΔT and wiper speed w.

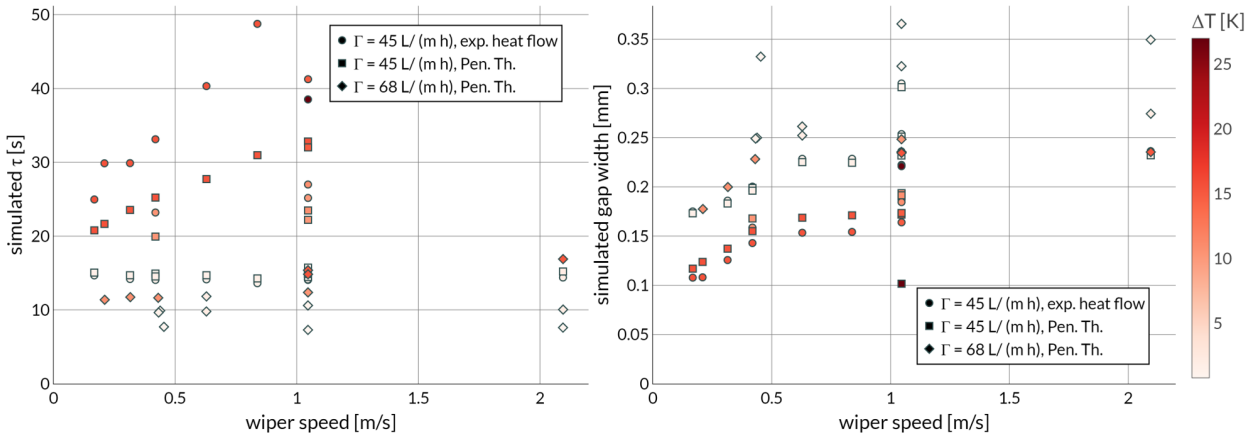

Figure 7.8.: Simulated mean residence time (left) and mean gap width (right) in dependence of the wiper speed for different temperature differences and mean peripheral loads Γ.

distance between the wiper element and the wall of the apparatus, averaged for all elements of height. In general, the simulated gap widths were in the range of 100 to 300 µm, which is lower than observed for blade wipers, but seems plausible given the reduced viscosity due to the higher temperatures [6]. The gap width decreases with a lower mean peripheral load and increased evaporation. Although this phenomenon can be attributed to evaporation, it remains unclear whether the observed de-wetting is a consequence of the reduction in film thickness or the increasing film instabilities resulting from evaporation. The latter is reinforced by the finding that, although the gap width is reduced with increasing wiper speed, this has a negligible impact on the mean residence time without a high temperature difference. In contrast, the stated gap widths are a mean value over the height of the apparatus, and the actual film thicknesses may be lower if the evaporation rate is high.

The influence of the wiper speed on the mean residence time and the width of the gap is illustrated in Figure 7.8. It can be seen that the wiper speed w does not have a significant influence on the mean residence time without evaporation, while the gap width increases with increasing wiper speed. This seems inconsistent at first, as the centrifugal force should increase with increasing wiper speed.

However, the increase in flow resistance before the wiper overcompensates for this effect, reducing the height of the bow wave as the width of the gap increases. This phenomenon is seen in the model only up to a wiper speed of 0.5 m/s, with minimal gap width change at higher speeds. However, this effect does not significantly impact the mean residence time. In contrast, the simulation indicates that the mean residence time during evaporation increases with wiper speed, primarily due to improved product-side heat transfer, which significantly decreases the peripheral load along the height.
Based on assumptions and model validation results, several refinements can enhance model quality and applicability. Additional process data should be taken into account during validation, whereby it should be noted that the data available in the literature often do not sufficiently provide a detailed description of relevant geometric data, in particular for the wiper system used. To enhance the utility of the model, it is advisable to employ industrial-scale equipment for validation purposes. It is recommended to incorporate insights derived from thin film break-up models, with particular emphasis on kinetics, which require the inclusion of contact angle data. Moreover, refining the calculations of heat transfer resistance by incorporating the effects of turbulence, non-condensable gases and gas flow may improve the accuracy of the models.

7.1.4. Conclusion

A comprehensive and mechanistic model for residence time and liquid hold-up in wiped film evaporators was presented, which extends the model of Appelhaus *et al.* by heat transfer and also allows predictive simulations of WFE [25]. The established model can describe heat transfer with a deviation of $\pm$25% and the mean residence time with $\pm$40% compared to experimental findings. Integration of fluid dynamics with a heat transfer and residence-time model offers a comprehensive representation of the operational behavior of a wiped film evaporator. This framework also allows the evaluation of additional variables such as liquid distribution and film thickness along the height of WFE. The accuracy of the model may be enhanced through the refinement of the underlying equations, particularly the empirical equation for the bow wave height. To enhance the heat transfer model, calculations can be extended to include areas above and below the wiped surface while integrating film thickness from the fluid dynamic model to improve calculation precision. In applications with evaporating fluids containing dissolved gases, expanding the heat transfer model to account for non-condensable gases can be advantageous. Additionally, the potential impact of operational phenomena, such as de-wetting, and the effective heat transfer surface should be considered. It is particularly important to critically examine the assumptions regarding a continuous liquid film and the neglect of surface effects. The physical processes underlying this model could be resolved more finely with the aid of CFD simulations. A more detailed experimental investigation focusing on film stability, including the comparison of high-speed images of the liquid film during operation with literature stability criteria, could significantly improve the model by integrating de-wetting dynamics into model validation. Either a qualitative evaluation or the incorporation of a correction factor at the onset can address de-wetting issues. Expanding the validation data to include various apparatus geometries on an industrial level and fluids with higher viscosity would also be highly beneficial. Beyond integrating de-wetting phenomena, the model could be expanded to include (binary) mixtures and mass transport, enabling the simulation of separation processes as well.

The notable benefits of the model we present include its ability to fully predict heat transfer and fluid dynamics specifically for short-cut calculations, as well as its modular design, which significantly enhances the versatility of the model framework. Generally, the model is applicable for designing and evaluating WFEs due to its quick computation speeds, straightforward parameterization, and accurate depiction of operating variables. It is also feasible to incorporate it into more complex flow simulations or heat exchanger designs.

7.1.5. Acknowledgements

We gratefully acknowledge that this project was supported by the Federal Ministry for Economic Affairs and Climate Action on the basis of a decision of the German Bundestag. This research was carried out as part of a project of Industrielle Gemeinschaftsforschung (IGF) with project number 01IF22220N.

Nomenclature

Roman symbols

symbol	explanation	unit
A	heat transfer surface	m^2
$a_1 \dots a_6$	coefficient of Nusselt equation	-
b	roller diameter	m
C_d	discharge coefficient	-
c_P	isobaric heat capacity	J kg^{-1} K^{-1}
d_E	equivalent length	m
d_r	inner diameter of apparatus	m
dz	length of a height element	m
f	correction factor	-
f_{wavy}	correction factor for waviness	-
f_η	correction factor for influence of viscosity	-
g	standard gravity	m s^{-2}
h_P	heat transfer coefficient of product side	W m^{-2} K^{-1}
h_L	local heat transfer coefficient of supply side	W m^{-2} K^{-1}
h_B	height of bow wave	m
K_1	coefficient for axial velocity	-
$\mathcal{L}$	characteristic length of free film (supply side)	m
N_B	number of wiper elements	-
n	wiper frequency	s^{-1}
n_{CSTR}	number of CSTR layers within one height element	-
n_x	number of segments in radial direction	-
n_y	number of segments in the film	-
n_z	number of segments along the height	-
P	outer perimeter of apparatus	m
R	heat transfer resistance	K W^{-1}
r_δ	free inner radius	K W^{-1}
s	gap width	m
T	temperature	K
t_{sc}	time between wiping occurrences	s
U	overall heat transfer coefficient	W m^{-2} K^{-1}
v_{ax}	axial flow velocity	m s^{-1}
v_S	axial flow velocity	m s^{-1}
w	wiper speed	m s^{-1}

Greek symbols

symbol	explanation	unit
β_{dead}	dead volume factor	-

symbol	explanation	unit
Γ	mean peripheral load	L m^{-1} s -1
Γ_{Feed}	feed peripheral load	L m^{-1} s -1
Γ_x	local peripheral load	L m^{-1} s -1
ΔT	temperature difference	K
δ	film thickness	m
δ_0	film thickness	m
δ^*	dimensionless film thickness	-
η	viscosity	Pa s
η_L	viscosity of liquid	Pa s
η_V	viscosity	Pa s
λ	thermal conductivity	kg m s^{-3} K^{-1}
λ_L	thermal conductivity of liquid	kg m s^{-3} K^{-1}
ν	kinematic viscosity	
ρ	density	kg m^{-3}
ρ_L	density of liquid	kg m^{-3}
ρ_V	density of vapor	kg m^{-3}
τ	mean residence time	s
τ_δ^*	dimensionless shear stress	-
τ_r	shear stress	N m^{-2}

Dimensionless Numbers

number	explanation	definition
Nu	Nusselt number	$h_P \cdot d \cdot \lambda^{-1}$
$\mathrm{Nu}_{\mathrm{L},x,l}$	local laminar Nusselt number	$h_{\mathrm{L},x,l} \cdot \mathcal{L} \cdot \lambda_L^{-1}$
$\mathrm{Nu}_{\mathrm{L},x,t}$	local turbulent Nusselt number	$h_{\mathrm{L},x,t} \cdot \mathcal{L} \cdot \lambda_L^{-1}$
$\mathrm{Nu}_{F,x}$	local Nusselt number	$h_{\mathrm{L},x} \cdot \mathcal{L} \cdot \lambda_L^{-1}$
Pr	Prandtl number	$\eta \cdot c_P \cdot \lambda^{-1}$
Re_F	film Reynolds number	$\Gamma \cdot \eta^{-1}$
$\mathrm{Re}_{\mathrm{L},x}$	local film Reynolds number	$\Gamma_x \cdot \eta^{-1}$
Re_V	vapor Reynolds number	$\overline{w}_G \cdot 2 \cdot r_\delta \cdot v_G^{-1}$
Re_R	rotational Reynolds number	$d^2 \cdot n \cdot \rho \cdot \eta^{-1}$

Declaration of generative AI and AI-assisted technologies in the writing process

During the preparation of this work, the authors used DeepL Translate/Write in order to improve language and readability. After using these services, the authors reviewed and edited the content as needed and take full responsibility for the content of the publication.

7.2. Assessment of the Model and Comparison to Experimental Results

The overall model was parameterized based on operational and geometric data from the experiments, as illustrated in Figure 7.9. Thermophysical properties were calculated from the fluid composition, pressure, and temperature. Fluid dynamic results, including axial velocity profiles and shear rates, served as the basis for parameterizing the CSTR cascade submodel, which was employed to calculate the RTD using appropriate differential equations. This modeling approach is fully predictive, relying solely on data available prior to experimental testing.

As shown in section 7.1, the model achieved good agreement within $\pm 40\%$ of the experimental RTD data, particularly in the technically relevant range of sump peripheral loads exceeding 20 L/(m·h). This performance is comparable to, or better than, previously reported predictive model equations for WFEs without evaporation [6, 16]. Moreover, the model allows for the estimation of not only RTD, but also local film thickness and hold-up volumes. It also provides velocity profiles and covers the technically relevant case of operation during evaporation.

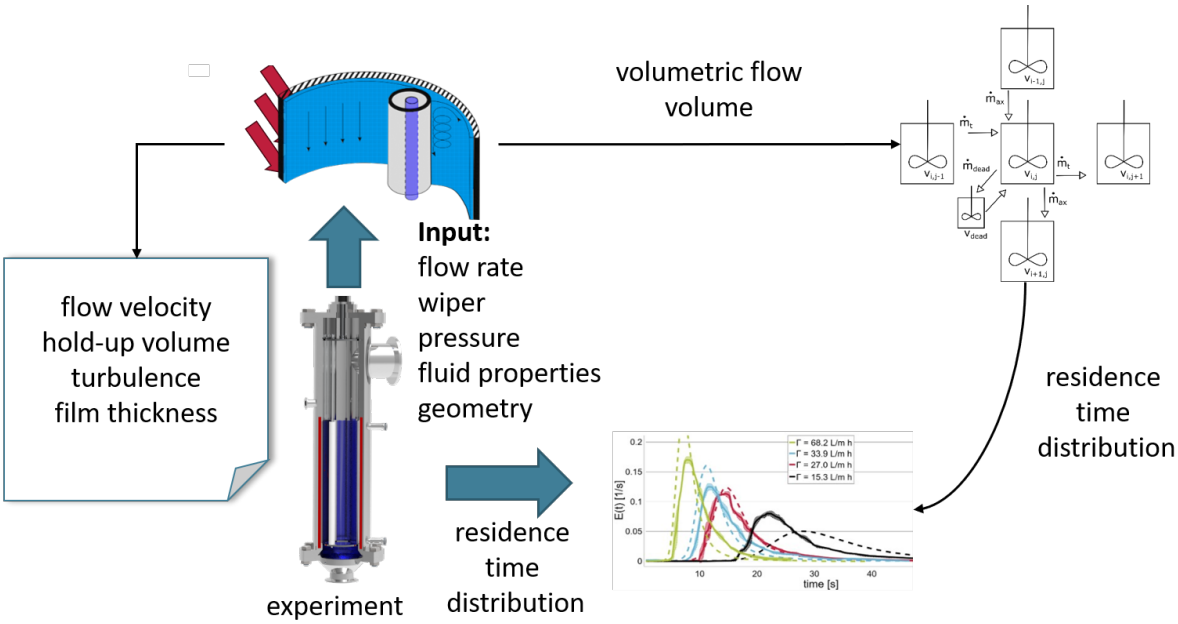

Figure 7.9.: Parameterization of the overall model based on experimental data and workflow to validate the resulting simulated residence time distribution with the corresponding experimental data.

As for the transferred heat flow, the simulated values were consistently underestimated for all evaluated models, as shown in Figure 7.4. This was expected for the corrected penetration theory by Azoory and Bott [20], in agreement with the experimental findings discussed in section 5.2.

In contrast, when simulating the unmodified penetration theory by Kool [63] the transferred heat flow is also underestimated, which contradicts the previously noted tendency in section 5.2 to overestimate product-side heat transfer coefficients (see Figure 5.9).

This discrepancy likely originates from differences in the calculation methods used for heat transfer on the utility side. In the evaluation of the experimental data, the heat transfer coefficients were obtained by inverse calculation based on the average Nusselt numbers derived from the measured condensate mass flows, as described in subsection 3.1.3. The developed model computes the condensed mass

flow rate directly based on locally calculated Nusselt numbers for each individual segment, neglecting possible heat losses.

Additionally, substantial uncertainties in the experimental values should be recognized, primarily due to the high sensitivity of the calculated heat transfer coefficients to small deviations in measured mass flows. However, these uncertainties could be reduced through improved thermal insulation of the heating section and extended measurement durations to minimize standard deviations if needed.

Besides the data available from experiments, the model allows a more in-depth analysis of fluid dynamics. For example, the simulated velocity profiles enable estimation of local Reynolds numbers and velocity gradients, providing insight into the potential for transitional or turbulent flow behavior and process boundaries. A comparison of the experimental data with the model predictions illustrates how the simulation results can be used to assess potential limitations of the experimental setup. Specifically, at low liquid loads, the injected tracer volume tends to shorten the experimentally determined mean residence time compared to simulations without evaporation. However, this effect is not observed in experiments with evaporation, likely due to higher feed flow rates and a lower relative impact of the tracer injection.

Instead, for higher superheat and low bottom peripheral loads, the simulations considerably underestimated the mean experimental residence time. A direct comparison of simulated and experimental RTDs with evaporation shows that for those simulations with higher mean residence times of the corresponding experiments, the simulations tend to significantly underestimate the occurring tailing behavior of the RTD. These discrepancies were particularly pronounced in cases where the experimental mean residence time significantly exceeded the experimentally observed general proportionality $\overline{\tau} \propto \Gamma_{\mathrm{sump}}^{-1}$. This observation supports the hypothesis that elevated superheat promotes film rupture, leading to destabilization of the liquid film and increased tailing. Film rupture is indicated in RTD-measurements by a shift in dimensionless residence time distribution and a notable increase in mean residence time.

Analysis of high-speed images across varying evaporation ratios confirmed that the deviating data points correlated with increased film rupture and reduced mean axial velocities. This destabilization is likely driven by thermal instabilities, such as temperature gradients and local overheating of the liquid film. The observations indicate that high superheat at low peripheral loads substantially compromises film stability, leading to prolonged residence times and deviations from the expected flow behavior of a closed film.

In binary mixtures, Marangoni effects, arising from surface tension gradients due to temperature and concentration differences, can further destabilize the film and accelerate rupture in heated regions even more, which could be subject to subsequent investigations.

While the influence of film rupture on heat transfer has been previously described by Jahnke, the present data show that the residence time distribution is affected earlier than the heat transfer performance [40]. This observation can be explained by the fact that film breakdown immediately reduces the axial velocity, while the heat transfer may still be ensured because of the periodic wetting of the entire heat-transferring surface. A significant drop in heat transfer occurs only when the liquid load is low enough to cause persistent dry-out of large areas of the inner surface.

Therefore, local hot spots can form even if the inner surface is periodically rewetted. Consequently, residence time increases and the thermal stress on the fluid intensifies. This creates a considerable risk

for temperature-sensitive fluids, where thermal degradation can potentially occur without a detectable decrease in the overall heat transfer rate. Against this background, further investigations using higher viscosity fluids are recommended. It is hypothesized that an increase in inertial forces in such systems may stabilize the film kinetically by delaying the onset of rupture. A deeper understanding of the rupture kinetics would allow improvements in the design of the evaporator and wiper, as well as an expansion of the process window in which stable operation can be ensured.

7.3. Recommendations for Model Improvement and Future Work

The findings of this work, in particular the deviations observed between the simulations and the experimental results, highlight several areas for future research and model refinement.
Although at first glance modeling film rupture might seem essential, it should be noted that such conditions represent operational limits that should be avoided in practice. Therefore, identifying the onset of film rupture is more relevant for process safety and optimization than accurately simulating this regime.
However, the model offers several promising prospects for improvement, including tighter coupling of fluid dynamics with heat- and mass-transfer processes. A stronger integration of the characteristic dimension of the film thickness into the model equation set is expected to improve its transferability and applicability. Additionally, a systematic incorporation of turbulence effects would improve the physical accuracy of the model, particularly in capturing the forces acting on the wiper and in representing heat and mass transfer more realistically.
To further develop and validate the model equations, the current experimental methodology could be enhanced and supplemented by high-resolution techniques for film thickness measurements such as laser-based or confocal sensors. These approaches could offer in-depth understanding of local film thicknesses, flow patterns, and temperature distributions but must be selected with care to function reliably during evaporation.
At the same time, CFD simulations can be applied to calculate liquid distribution, film geometry, and velocity profiles. The detailed insights gained into local flow behavior and the onset of turbulence enable a more comprehensive validation of the assumptions underlying the model developed in this work and support its refinement. While parameterizing a CFD model is complex and its generalizability to different systems is limited, the modular model presented here would complement the finding of a potential CFD model with its higher flexibility. Adapted submodels, including different wiper systems, heat transfer correlations, or film dynamics, can be independently replaced, allowing for a high transferability to different WFE-designs and an integration into other simulation frameworks.
CFD simulations could also improve dynamic analysis of the liquid film, for example, by examining the gas-liquid-interface and local instabilities. Insights from these simulations could be used to improve the understanding of the film behavior and its prediction. Alternatively, equations describing the thermodynamical stability of liquid films could be incorporated in the model and subsequently refined by empirical correction factors to account for potential surface effects and turbulence.
Beyond improvements in model accuracy, the reliability and transferability of the model can be enhanced by further experimental validation. In particular, reducing uncertainties related to dead volumes upstream and downstream of the evaporator would improve the comparability between

simulation and measurement. The modularity of the proposed model also offers the option of developing more submodels or even a full model library including several wiper designs, heat transfer correlations, and interchangeable film models at the top level. This would expand the usability of the model framework for industrial applications. For the purpose of validating this expanded model library, it is highly recommended to conduct scale-up experiments similar to those performed by Jahnke [40]. These experiments should validate the model within industrial scale to assess its robustness.

8. Summary and Outlook

Within this work, the fluid dynamics in a wiped film evaporator equipped with a roller wiper was systematically investigated under evaporation conditions. To achieve this, reference systems were characterized, and residence time experiments were carried out in a miniplant. Additionally, a predictive model was established and evaluated for the WFE system under consideration. This was done with the aim of better understanding the coupling between heat transfer and fluid dynamics, as well as identifying operational limits. This chapter summarizes the results and ultimately proposes possible options for future research and model refinements.

8.1. Summary

The study focused on the fluid dynamics of a WFE with a roller wiper system. To assess the influence of thermophysical properties, four reference fluid systems (diethylene glycol, isopropyl alcohol, decan-1-ol, glycerol) and binary mixtures of diethylene glycol with isopropyl alcohol, decan-1-ol, and glycerol were proposed. The density, viscosity, and surface tension were measured experimentally for these systems at elevated temperatures up to 130 °C. Correlation equations with defined validity ranges and error margins were derived, providing a set of model fluids for evaporator investigations. Subsequently, diethylene glycol, isopropyl alcohol, and decan-1-ol were selected as pure substances for further experiments, based on their representative thermophysical properties for WFE.
Experimental investigations of the residence time were conducted under both non-evaporation and evaporation conditions. The effects of various process parameters, including wiper frequency, superheat, and peripheral load, were analyzed. Additionally, the effect of varying fluid properties were investigated by employing previously selected pure components.
For diethylene glycol, the mean residence time was shown to be inversely proportional to the sump peripheral load, $\overline{\tau} \propto \Gamma^{-1}$. The mean residence time varied significantly between the investigated fluid systems, primarily due to differences in density and viscosity. In contrast, surface tension did not exhibit a measurable influence on residence time under closed-film conditions, where the liquid forms a continuous film on the heated surface.
The dependence of the mean residence time on density and viscosity was found to be governed by physical mechanisms similar to those observed in falling film evaporators, namely the interplay of gravity-driven flow and viscous drag. As a result, the mean residence time is only depending on the equivalent film thickness $\delta_{\mathrm{film}} = \left(\frac{3 \cdot \eta \cdot \Gamma}{\rho \cdot g}\right)^{1/3}$, such that $\overline{\tau} = f(\delta_{\mathrm{film}})$.
The experimentally determined residence time distributions exhibited self-similarity across a wide range of operating conditions. Thereby characteristic values of the dimensionless residence time distribution were observed. The minimum residence time was approximately $1/3 \cdot \overline{\tau}$. The maximum of the residence time density function was reached at $2/3 \cdot \overline{\tau}$, which corresponds to both the minimum residence time and the maximum of the residence time distribution of a falling film evaporator. After approximately $(2 \text{ to } 3) \cdot \overline{\tau}$, the residence time density function is back to zero, indicating that all tracer molecules had exited the evaporator by this point. Despite the similar shape of the normalized

residence time distributions, the absolute values of the mean residence time in the wiped film evaporator generally differ from those observed in a falling film evaporator under otherwise identical parameters. This results from the inherent differences in fluid dynamic, particularly the mechanical agitation of the liquid film.

At very low peripheral loads in the sump, a disproportionate increase in the mean residence time was observed, deviating from the behavior described above. This effect was especially pronounced under conditions of high evaporation ratios and heat flows. To analyze the underlying causes of these deviations, high-speed optical imaging with a built-in borescope was used under evaporation conditions. Evaluation of the recordings revealed an increase in film rupture at the inner wall of the evaporator in this regime, which was intensified by elevated wall superheat. The dewetting process was highly dynamic and transient, suggesting a strong dependence on fluid properties, particularly viscosity, and the associated inertia-driven forces that determine the kinetic stability of the film.

Although wall dewetting has been discussed in previous studies and its potential impact on heat transfer has been postulated [40], this work demonstrates that dewetting affects the residence time distribution significantly earlier than it affects heat transfer. This was due to the fact that heat transfer is maintained as long as the entire heat transfer surface is periodically rewetted by the fluid. Consequently, the apparent overall heat transfer coefficient on the product side only decreases when regions of the inner surface remain permanently dry.

In contrast, the residence time increases immediately when film rupture occurs after the wiper and discrete droplets form, leading to a reduction in axial fluid velocity. The optical images clearly captured this droplet formation, particularly in the lower section of the evaporator and at high wall superheat. It was shown that the wiper system can stabilize the liquid film kinetically. However, it was observed that during evaporation, mechanical agitation also enhanced heat transfer at increased wiper speeds. As a result, the peripheral load in the sump was reduced under evaporation conditions, which tended to increase the mean residence time because of enhanced film rupturing.

To gain a deeper understanding of the interaction between mechanical effects, heat transfer, and fluid dynamics, a wiped film evaporator model was developed in a modular framework in the equation-based modeling language Modelica. In a first step, a fluid dynamic model without evaporation was implemented, calculating velocity profiles and liquid hold-up based on force and momentum balances (including gravitational, viscous, and inertial forces) and by solving the Navier–Stokes equations under laminar flow conditions. The relevant fluid dynamic regions bow wave, gap, and film were implemented as individual submodels, which were subsequently combined into an integrated system model from which mean velocities and hold-up volumes were derived.

To enable comparison with experimental data, a complementary residence time model was developed based on a cascade of continuously stirred tank reactors (CSTRs), each based on the differential mass balance equations valid for a CSTR. For calibration, the wiper gap width and an additional dead volume factor representing incomplete mixing near the wall were fitted to experimental data. By adjusting these parameters, the model was in good agreement with the experimentally determined residence time distributions without evaporation at temperatures ranging from 20 °C to 50 °C. However, the tailing of the residence time distributions was consistently underestimated, indicating a potential limitation in capturing slow-flowing film regions or stagnant zones near the wall.

The fluid dynamic model was extended to account for evaporation and to enable a predictive calculation

of the residence time distribution based solely on known geometrical and operating parameters such as wiper design, fluid properties, temperature, and flow rates. A segmental approach was chosen, in which each vertical segment (height element) of the evaporator was considered as an individual submodel. Therefore, the existing fluid dynamic model was coupled with a heat transfer model that calculates the evaporated fraction of the fluid and adapts the volume flows in each segment. The overall apparatus was then composed as a series of height elements. In order to improve the accuracy of the model, the experimental periphery, in particular the pipe sections between the tracer injection and the evaporator as well as between the evaporator and the residence time sensor, were included in the system model. To ensure predictive capability without calibration experiments, all fitting parameters were fixed. The dead volume factor was set to $\beta = 0.1$, and the unknown length of the bow wave was assumed to be equal to its height, based on geometrical considerations.

Subsequently, the previously conducted experiments were simulated using the extended model and the results were compared with experimental data. The implemented heat transfer model captured the experimental data with reasonable accuracy, typically within 25%. However, a systematic underestimation of the heat transfer was observed, likely due to heat conduction in non-wiped regions not being accounted for in the model.

The mean residence time showed reasonable agreement between simulation and experiment within $\pm$40%, provided that the peripheral sump load exceeded 20 L/(m·h). At lower peripheral loads, systematic deviations occurred. Under non-evaporation conditions, the model overestimated the mean residence time, which was attributed to the pronounced influence of the tracer injection for low feed volume flows. In contrast, under evaporation conditions for high evaporation ratios associated with low peripheral loads, the residence time was vastly underestimated. This discrepancy coincided with visual observation of film rupture, which led to an increased experimental mean residence time – a scenario that was not included within the model assumptions.

It can be concluded that in cases of (partial) film ruptures, the residence time increases much more than would be expected based solely on simulations or measurements for the stable film. This finding is particularly relevant for temperature-sensitive fluids, such as certain pharmaceutical products.

Overall, the results of the simulation study demonstrated the interdependence of wiper dynamics, heat transfer, and fluid flow using a mechanistic, modular modeling approach. The developed model enables quantitative prediction of process characteristics such as heat transfer and residence time distribution and serves as a valuable tool to analyze system behavior under varying operating conditions.

To calculate the residence time distribution in a WFE with low evaporation ratios, it can be assumed that the RTD is self-similar and that the mean residence time can be estimated as a function of the equivalent film thickness δ_{film} for different thermophysical properties and peripheral loads. Changing peripheral loads and thermophysical properties in a WFE under higher evaporation ratios lead to increasing uncertainties with this simplified approach. Here, segment-based modeling is recommended, as was successfully demonstrated in this work with the Modelica model presented.

By refining the modeling assumptions and further developing the experimental methodology, the current study also laid the groundwork for an extended and more broadly applicable model. The next section outlines specific directions for future research and model refinement.

8.2. Outlook

This work has improved the understanding of the coupled interactions between film agitation, heat transfer, and fluid flow in wiped film evaporators. At the same time, it has highlighted several unresolved challenges in the design, operation, and performance evaluation of such systems. These challenges can be addressed by further experimental investigations and adaptation of the presented mechanistic model.

From an experimental perspective, efforts should focus not only on reducing measurement uncertainties but also on assessing the transferability of the results. This includes conducting experiments with high-viscosity fluids, e.g. polymer solutions, sugar solutions or silicone oils, as well as investigating wiped film evaporators with modified geometries and different wiper designs. Investigating wiper systems such as fixed blade wipers, which are commonly used for high-viscosity fluids, could provide valuable data for further model development.

In addition, reference experiments on pilot-scale equipment can substantially enhance the understanding of scaling behavior and improve the generalizability of the simulations. Experimental uncertainties may be further minimized by reducing the hold-up volumes upstream and downstream of the evaporator.

Automatic, computer-aided image analysis of the high-speed recordings can provide quantitative data on film rupture, despite the challenges posed by nonuniform lighting and the highly reflective inner surface. Furthermore, the interpretation of experimental results can be further enhanced by incorporating complementary CFD simulations, including turbulence models (e.g., k-ε or k-ω models). The resulting flow behavior and velocity profiles can be used to refine the governing equations in the Modelica-based model, especially for the bow wave and gap zones, where turbulent flow profiles are expected. A possible approach involves estimating the thickness of a laminar sublayer and assuming a laminar profile only within this sublayer. The results of the CFD simulations could also be used to validate the model predictions for film thickness and velocity profiles.

Model development should continue with a focus on expanding the validity of the model, improving predictive accuracy, and expanding its operational limits. To broaden its applicability, the model should be adapted for different wiper geometries and validated against evaporators with those wiper designs. A promising beginning would involve implementing geometries that are well-defined, like fixed or movable blade wipers.

Beyond the pure fluids studied here, the model could be extended to binary mixtures with property gradients along the evaporator height. The segmental approach used in the current model is generally well suited for this purpose. Such enhancements would greatly increase the relevance of the model for complex industrial separation tasks.

The assumptions of the model should be re-evaluated with regard to the findings of this work. At low peripheral loads with high wall superheat, the assumption of a fully wetting liquid film proved invalid, as evidenced by experimental observations of partial film rupture. This could be addressed by modeling partial film ruptures or incorporating a correction factor within this regime.

Moreover, the slowdown of the fluid in the axial direction caused by the wiper has a more significant impact on fluid dynamics than initially expected, likely leading to thicker films than the current model calculates. Therefore, inertial forces and the associated transient acceleration of the flow should be

more accurately incorporated into the model, for example, by implementing unsteady Navier–Stokes equations or adding inertial terms to the force balance equations.
Overall, the presented methodology, based on experimental studies and segment-based modular modeling, provides valuable information and predictive capabilities for the assessment of wiped film evaporators. In addition, it offers substantial potential for further development, including design cases not yet addressed and optimization of industrial processes and equipment design.

References

[1] P. Gabrielli, L. Rosa, M. Gazzani, R. Meys, A. Bardow, M. Mazzotti, and G. Sansavini. “Net-Zero Emissions Chemical Industry in a World of Limited Resources”. In: *One Earth* 6.6 (2023), pp. 682–704.

[2] S. Mohan and R. Katakojwala. “The Circular Chemistry Conceptual Framework: A Way Forward to Sustainability in Industry 4.0”. In: *Curr. Opin. Green Sustain.* 28 (2021), p. 100434.

[3] B. Bruns, F. Herrmann, M. Polyakova, M. Grünewald, and J. Riese. “A Systematic Approach to Define Flexibility in Chemical Engineering”. In: *J. Adv. Manuf. Process.* 2.4 (2020), e10063.

[4] C. Acar, I. Dincer, and A. Mujumdar. “A Comprehensive Review of Recent Advances in Renewable-Based Drying Technologies for a Sustainable Future”. In: *Dry. Technol.* 40.6 (2022), pp. 1029–1050.

[5] S. Scholl. “Verfahrenstechnisches Design von Verdampfern. Process Engineering Design of Evaporators”. In: *Chem. Ing. Tech.* 82.12 (2010), pp. 2179–2187.

[6] P. Schweizer and F. Widmer. “Residence Time of Medium- and High-Viscosity Fluids in a Thin-Film Evaporator”. In: *Verfahrenstechnik* 15.1 (1981), pp. 29–33.

[7] B. Kaiser and M. Kranz. “Dünnschichtverdampfer in der thermischen Trenntechnik”. In: *Vak. Forsch. Prax.* 11.2 (1999), pp. 71–77.

[8] W. L. Hyde and W. B. Glover. “Evaporation of Difficult Products – Agitated Thin-Film Evaporation Overcomes Common Problems”. In: *Chem. Process.* 60.2 (1997), p. 59.

[9] W. Ahmad, A. Ostonen, K. Jakobsson, P. Uusi-Kyyny, V. Alopaeus, U. Hyväkkö, and A. W. King. “Feasibility of Thermal Separation in Recycling of the Distillable Ionic Liquid [DBNH][OAc] in Cellulose Fiber Production”. In: *Chem. Eng. Res. Des.* 114 (2016), pp. 287–298.

[10] V. Anand P., S. Mishra, J. Gnanasoundari, R. Rajeev, N. Desigan, P. Velavendan, K. Venkatesan, and K. Ananthasivan. “Wiped Film Evaporator With a Roller Wiper and an Internally Mounted Condenser for the Recovery of TBP and N-DD From Degraded PUREX Solvent”. In: *Chem. Eng. Res. Des.* 192 (2023), pp. 223–238.

[11] J. M. Spörl, F. Batti, M.-P. Vocht, R. Raab, A. Müller, F. Hermanutz, and M. R. Buchmeiser. “Ionic Liquid Approach Toward Manufacture and Full Recycling of All-Cellulose Composites”. In: *Macromol. Mater. Eng.* 303.1 (2018), p. 1700335.

[12] H. J. Saleem and A. R. Karim. “Re-Refining of Used Lubricating Oil by Vacuum Distillation/Thin Wiped Film Evaporation Technique”. In: *Petrol. Sci. Technol.* 38.4 (2020), pp. 323–330.

[13] X. Shao, W. Feng, Z. Guo, and W. Chen. “Continuous and Safe Alkylation of 1,3,5-Trihydroxy-2,4,6-trinitrobenzene using Wiped Film Evaporator/Distillation Coupled Technology”. In: *Org. Process Res. Dev.* 26.9 (2022), pp. 2665–2673.

[14] Adisa Azapagic, ETHOS Research, and European Solvent Recycler Group (ESRG). *Carbon Footprint of Recycled Solvents at the Sectoral Level Compared to Virgin Solvents*. Tech. rep. 2018.

[15] D. Kern and H. Karakas. “Mechanically Aided Heat Transfer”. In: *Heat Transfer* 2 (1959), p. 141.

[16] P. Schweizer. “Fluiddynamik des mechanisch beeinflussten Flüssigkeitsfilmes”. PhD Thesis. ETH Zurich, 1979.

[17] H. Abichandani, S. C. Sarma, and D. R. Heldman. “Hydrodynamics and Heat Transfer in Thin Film Scraped Surface Heat Exchangers - a Review”. In: *J. Food Process Eng* 9.2 (1986), pp. 143–172.

[18] S. Komori, K. Takata, R. Nagaosa, and Y. Murakami. “The Effects of Multiple Inclined Blades on Flow and Mixing Characteristics in an Agitated Thin-Film Evaporator”. In: *J. Chem. Eng. Jpn.* 23.5 (1990), pp. 550–555.

[19] K. Dieter. “Wärmeübergangsmessungen an Dünnschichtverdampfern”. In: *Chem. Ing. Tech.* 32.8 (1960), pp. 521–524.

[20] S. Azoory and T. R. Bott. “Local Heat Transfer Coefficients in a Model “Falling Film” Scraped Surface Exchanger”. In: *Can. J. Chem. Eng.* 48.4 (1970), pp. 373–377.

[21] R. Billet. “Performance of Thin-Film Distillation and Its Application”. In: *Separ. Technol.* 2.4 (1992), pp. 183–191.

[22] K. Jasch, T. Grützner, G. Rosenthal, and S. Scholl. “Experimental Investigation of the Residence Time Behavior of a Wiped Film Evaporator”. In: *Chem. Eng. Res. Des.* 165 (2021), pp. 162–171.

[23] D. Appelhaus, F. Claus, S. Knoblauch, K. Jasch, and S. Scholl. “Density, Viscosity, Refractive Index, and Surface Tension of Binary Mixtures of 3-oxa-1,5-Pentanediol with 2-Propanol, 1,2,3-Propanetriol, and 1-Decanol from 283.15 to 403.15 K as Reference Systems for Evaporation Experiments”. In: *J. Chem. Eng. Data* 69.9 (2024), pp. 2927–2948.

[24] D. Appelhaus, K. Jasch, H. Meyer, and S. Scholl. “Evaporation Effects on Residence Time in Wiped Film Evaporators with Roller Wipers”. In: *Chem. Eng. Res. Des.* 218 (2025), pp. 341–349.

[25] D. Appelhaus, K. Jasch, S. Jahnke, H. Hassani Khab Bin, W. Tegethoff, J. Köhler, and S. Scholl. “A New Approach to Simulate the Fluid Dynamics in a Wiped Film Evaporator Using Modelica”. In: *Chem. Eng. Res. Des.* 161 (2020), pp. 115–124.

[26] D. Appelhaus, K. Jasch, M. Groth, and S. Scholl. “Modeling of Fluid Dynamics in Wiped Film Evaporators During Evaporation”. In: *Sep. Purif. Technol.* 371 (2025), p. 132840.

[27] J. D. Ford and R. W. Missen. “On the Conditions for Stability of Falling Films Subject to Surface Tension Disturbances; The Condensation of Binary Vapors”. In: *Can. J. Chem. Eng.* 46.5 (1968), pp. 309–312.

[28] M. L. Madlen. “Apparatus for Film-Type Distillation”. US2500900A. 1950.

[29] G. G. Zahm. “Apparatus for Concentrating Liquids”. US2546381A. 1951.

[30] H. L. Freese and W. B. Glover. “Mechanically Agitated Thin-Film Evaporators”. In: *Chem. Eng. Prog.* 75 (1979), pp. 52–58.

[31] S. Jahnke, K. Jasch, and S. Scholl. “Wiped Film Evaporators: Segmental Assessment of Wetting Behavior and Heat Transfer Performance”. In: *Chem. Eng. Res. Des.* 163 (2020), pp. 67–75.

[32] F. Widmer and A. Giger. “Residence Time Control in Thin-Film Evaporators”. In: *Chem. Process Eng.* 51.11 (1970), p. 63.

[33] R. Schneider. “Ein neuer Dünnschichtverdampfer”. In: *Chem. Ing. Tech.* 27.5 (1955), pp. 257–261.

[34] D. Bethge. “Short Path and Molecular Distillation”. In: *Vacuum Technology in the Chemical Industry*. Ed. by W. Jorisch. 1st ed. Wiley, 2014, pp. 281–294.

[35] B. Babos and A. Uihidy. “Verfahren zur kontinuierlichen Diazotierung von Anilin im Dünnschichtreaktor”. In: *Chemie Technik* 13.11 (1961), pp. 662–665.

[36] A. Mützenberg and A. Giger. “Chemical Reactions in Thin-Film Equipment”. In: *Trans. Instn Chem. Engrs.* 46 (1968), pp. 187–189.

[37] L. Liu, Y. Zhang, S. Su, K. Yu, F. Nie, and Y. Li. “Reaction–Thin Film Evaporation Coupling Technology for Highly Efficient Synthesis of Higher Alkyl Methacrylate”. In: *Processes* 12.6 (2024), p. 1233.

[38] P. Dieter, S. Rudolf, S. Werner, and G. Emil. “Construction And Arrangement Of Wipers In Thin-Film Evaporators”. US3090732A. 1963.

[39] J. Lopez-Toledo. “Heat and Mass Transfer Characteristics of a Wiped Film Evaporator”. PhD Thesis. The University of Texas at Austin, 2006.

[40] S. Jahnke. *Benetzung und Leistungscharakterisierung von Dünnschichtverdampfern*. 1st ed. ICTV-Schriftenreihe Series v.47. Göttingen: Cuvillier Verlag, 2024.

[41] A. A. Al-Hemiri, E. F. Mansour, and J. A. Al-Ani. “Simulation of Wiped Film Evaporator”. In: *Iraqi J. Chem. Pet. Eng.* 9.2 (2008), pp. 43–50.

[42] A. Skoczylas and J. Dziak. “Separation Efficiency of Thin-Layer Evaporators”. In: *Comput. Chem. Eng.* 14.9 (1990), pp. 1001–1007.

[43] T. R. Bott and J. J. B. Romero. “Heat Transfer Across a Scraped Surface”. In: *The Canadian Journal of Chemical Engineering* 41.5 (1963), pp. 213–219.

[44] D. Woschitz and F. Widmer. “Lokaler Stoffaustausch (Wärmeaustausch) zwischen Wand und Fluid in einem Dünnschichtverdampfer”. In: *Chem. Ing. Tech.* 55.3 (1983), pp. 230–231.

[45] S. B. Pawar, A. Mujumdar, and B. Thorat. “CFD Analysis of Flow Pattern in the Agitated Thin Film Evaporator”. In: *Chem. Eng. Res. Des.* 90.6 (2012), pp. 757–765.

[46] W. Hauschild. “Leistung von Dünnschichtverdampfern mit zwangsläufig ausgebildeten Filmen”. In: *Chem. Ing. Tech.* 25.10 (1953), pp. 573–574.

[47] H. Brauer. “Strömung und Wärmeübergang bei Rieselfilmen”. In: *VDI-Forschungsheft* 22.457 (1956), pp. 2–39.

[48] R. Bressler. “Versuche über die Verdampfung von dünnen Flüssigkeitsfilmen”. In: *VDI-Zeitung* 100.15 (1958), pp. 630–638.

[49] R. Van Der Piepen. “Aufbau und Einsatz von Dünnschichtverdampfern”. In: *Verfahrenstechnik* 2.1 (1968), pp. 28–32.

[50] J. Cvengroš, Š. Pollák, and J. Lutišan. “Characteristics of a Comb Wiper for the Film Evaporator”. In: *Chem. Eng. Technol.* 23.1 (2000), pp. 55–60.

[51] J. Cvengroš, Š. Pollák, M. Micov, and J. Lutišan. “Film Wiping in the Molecular Evaporator”. In: *Chem. Eng. J.* 81.1-3 (2001), pp. 9–14.

[52] F. Widmer and P. Schweizer. “Fluiddynamik des mechanisch beeinflussten Flüssigkeitsfilmes”. In: *Swiss Chem* 1.6 (1979), pp. 91–96.

[53] A. R. Gudheim and J. Donovan. “Heat Transfer in Thin Film Centrifugal Processing Units”. In: *Chem. Engng Prog. Symp. Ser*. Vol. 29. 1957, p. 137.

[54] B. Babos and A. Ujhidy. “Über die Möglichkeiten der Weiterentwicklung von Dünnschichtreaktoren”. In: *Chem. Techn.* 15.11 (1963), pp. 649–652.

[55] L. AG. “Dünnschichtverdampfer mit einer zweiteiligen Wärmebehandlungskammer”. 19252199. 1969.

[56] D. Bethge. “Dünnschichtverdampfer”. EP 3 103 538 A1. 2016.

[57] J. A. Biesenberger. *Principles of Polymerization Engineering*. Ed. by D. H. Sebastian. New York u.a.: Wiley, 1983.

[58] T. F. L. McKenna and T. F. L. McKenna. “Design Model of a Wiped Film Evaporator. Applications to the Devolatilisation of Polymer Melts”. In: *Chem. Eng. Sci.* (1995).

[59] W. Qin, H. Li, M. Luo, and S. Cong. “Research on the Influence of Fluid Viscosity on the Inlet Flow Parameters of Wiped Film Molecular Distillation”. In: *E3S Web of Conferences* 522 (2024). Ed. by F. Yan, M. Li, X. Hou, and Y. Long, p. 01033.

[60] S. Komori, K. Takata, and Y. Murakami. “Flow and Mixing Characteristics in an Agitated Thin-Film Evaporator with Vertically Aligned Blades”. In: *J. Chem. Eng. Jpn.* 22.4 (1989), pp. 346–351.

[61] F. Rossi, M. Corbetta, D. Geraci, C. Pirola, and F. Manenti. “First-Principles Non-Equilibrium Dynamic Modelling of Agitated Thin-Film Evaporators”. In: *Chem. Eng. Trans.* 43 (2015), pp. 1429–1434.

[62] E. Kirschbaum and K. Dieter. “Wärmeübergang und Teildestillation in Dünnschichtverdampfern”. In: *Chem. Ing. Tech.* 30.11 (1958), pp. 715–720.

[63] J. Kool. “Heat Transfer in Scraped Vessels and Pipes Handing Viscous Materials”. In: *Trans. Inst. Chem. Engrs.* 36 (1958), p. 259.

[64] S. B. Pawar, A. Mujumdar, and B. Thorat. “Flow Pattern and Heat Transfer in Agitated Thin Film Dryer”. In: *Chem. Eng. Process. Process Intensif.* 50.7 (2011), pp. 687–693.

[65] S. Jahnke, D. Appelhaus, K. Jasch, and S. Scholl. “Wetting Situations and Heat Transfer Performance of Wiped Film Evaporators at Different Scales”. In: *73. Starch Convention, Online, 28.03. – 30.03.2022*. 2022.

[66] K. Wang, Y. Zhang, S. Gong, B. Bai, and W. Ma. “Dynamics of a Thin Liquid Film Under Shearing Force and Thermal Influences”. In: *Exp. Therm. Fluid Sci.* 85 (2017), pp. 279–286.

[67] R. V. Craster and O. K. Matar. “Dynamics and Stability of Thin Liquid Films”. In: *Rev. Mod. Phys.* 81.3 (2009), pp. 1131–1198.

[68] W. Schicketanz. “Mittlere treibende Temperaturdifferenz bei der Rückstandseindampfung im Dünnschichtverdampfer”. In: *Chem. Ing. Tech.* 57.4 (1985), pp. 335–342.

[69] K. Dieter and W. Hübner. “Leistungsverhalten von Dünnschichtverdampfern I”. In: *Chem. Z* 94 (1970), p. 445.

[70] W. B. Glover. “Scaleup of Agitated Thin-Film Evaporators: Process-Design, Mechanical-Design and Physical-Property Parameters Must All Be Taken into Account”. In: *Chem. Eng-new. York.* 111.4 (2004). Section: 55, pp. 55+.

[71] H.-J. Godau. “Strömungsvorgänge in Dünnschichtverdampfern”. In: *VEB Chemiefaserwerk* (1974).

[72] A. Mutzenburg. “Agitated Thin-Film Evaporators. Part 1. Thin-Film Technology”. In: *Chem Eng (New York)* 72.19 (1965), pp. 175–178.

[73] S. Komori, S. Komori, K. Takata, K. Takata, Y. Murakámi, and Y. Murakami. “Flow Structure and Mixing Mechanism in an Agitated Thin-Film Evaporator”. In: *J. Chem. Eng. Jpn.* (1988).

[74] H.-J. Godau. “Flow Processes in Thin-Film Evaporators”. In: *Int. Chem. Eng.* 15.3 (1975), pp. 445–449.

[75] M. Yataghene, M. Yataghene, F. Fayolle, F. Francine, J. Legrand, and L. Jack. “Flow Patterns Analysis Using Experimental Piv Technique Inside Scraped Surface Heat Exchanger in Continuous Flow Condition”. In: *Appl. Therm. Eng.* (2011).

[76] P. Błasiak and S. Pietrowicz. “Towards a Better Understanding of 2D Thermal-Flow Processes in a Scraped Surface Heat Exchanger”. In: *Int. J. Heat Mass Transfer* 98 (2016), pp. 240–256.

[77] S. Zeboudj, N. Belhaneche-Bensemra, R. Belabbes, and P. Bourseau. “Modelling Of Flow In A Wiped Film Evaporator”. In: *Chem. Eng. Sci.* 61.4 (2006), pp. 1293–1299.

[78] A. Xiang, A. Xiang, and S. Xu. “Comparison of Two Turbulent Models in Simulating Evaporating Liquid Film in a Wiped Molecular Distillator”. In: *Sci. China. Chem.* (2005).

[79] J. M. McKelvey and G. V. Sharps. “Fluid Transport In Thin Film Polymer Processors”. In: *Polym. Eng. Sci.* 19.9 (1979), pp. 651–659.

[80] D. B. Clemons. “Axial Mixing of a Low-Viscosity Liquid in a Wiped-Film Evaporator”. In: *Ind. Eng. Chem. Fundam.* 8.2 (1969), pp. 279–281.

[81] J. Cvengroš, V. Badin, and Š. Pollák. “Residence Time Distribution in a Wiped Liquid Film”. In: *Chem Eng Biochem Eng J* 59.3 (1995), pp. 259–263.

[82] A. S. Xiang, X. M. Wang, and S. L. Xu. “Feed Rate on Velocity Field of Liquid Film in a Wiped Film Molecular Distillatory”. In: *Adv. Mater. Res-switz.* 560 (2012), pp. 46–51.

[83] S.-S. Zheng, S.-S. Zheng, Y. Hu, Y. Huang, K. Zou, K. Zou, Y. Peng, and Y.-T. Peng. “Numerical Simulation of Flow Pattern for Non-Newtonian Flow in Agitated Thin Film Evaporator”. In: *Chinese Phys.* (2022).

[84] C.-J. Ri, Y.-C. Kim, S.-W. Kim, and J. H. Chloe. “A Simulation of Evaporation Dissolution Process for a Lyocell Solution in a Vertical Wiped Film Evaporator (1: Simulation of Flow Process for Solution)”. In: *Cellul. Chem. Technol* 57 (2023), pp. 741–748.

[85] H. A. Leniger and J. Veldstra. “Wärmedurchgang in einem Dünnschichtverdampfer”. In: *Chem. Ing. Tech.* 31.8 (1959), pp. 493–497.

[86] H. Benkhelifa, A. Haddad Amamou, G. Alvarez, and D. Flick. “Modelling Fluid Flow, Heat Transfer And Crystallization In A Scraped Surface Heat Exchanger”. In: *Acta Hortic.* 802 (2008), pp. 163–170.

[87] J. Dziak. “Mass and Heat Transfer During Thin-Film Evaporation of Liquid Solutions”. In: *Advanced Topics in Mass Transfer*. Ed. by M. El-Amin. InTech, 2011.

[88] R. Billet. *Verdampfung und ihre technischen Anwendungen*. Verlag Chemie, 1981.

[89] R. Billet. “Evaporation”. In: *Ullmann’s Encyclopedia of Industrial Chemistry*. Ed. by Wiley-VCH. 1st ed. Wiley, 2000.

[90] T. R. Bott, S. Azoory, and K. E. Porter. “Scraped-Surface Heat Exchangers Part II—The Effects of Axial Dispersion on Heat Transfer”. In: *Trans IChemE* 46 (1968), pp. 37–42.

[91] T. R. Bott and J. J. B. Romero. “The Characteristic Dimension in Scraped Surface Heat Transfer”. In: *Can. J. Chem. Eng.* 44.4 (1966), pp. 226–230.

[92] K. Stankiewicz and M. A. Rao. “Heat Transfer in Thin-Film Wiped-Surface Evaporation of Model Liquid Foods”. In: *J. Food Process Eng.* 10.2 (1988), pp. 113–131.

[93] E. L. Lustenader, R. Richter, and F. J. Neugebauer. “The Use of Thin Films for Increasing Evaporation and Condensation Rates in Process Equipment”. In: *J. Heat Transf.* 81.4 (1959), pp. 297–306.

[94] R. Billet. *Industrielle Destillation*. Verlag Chemie, 1973.

[95] P. Danckwerts. “Continuous Flow Systems”. In: *Chem. Eng. Sci.* 2.1 (1953), pp. 1–13.

[96] P. Harriott. “Heat Transfer in Scraped-Surface Heat Exchangers”. In: *Chem. Eng. Prog. Symp. Ser.* 55 (1959), p. 137.

[97] G. Latinen. “Correlation of Scraped Film Heat Transfer in the Votator-Discussion”. In: *Chem. Eng. Sci.* 9.4 (1959), pp. 263–266.

[98] A. M. Trommelen, W. J. Beek, and H. C. Van De Westelaken. “A Mechanism for Heat Transfer in a Votator-Type Scraped-Surface Heat Exchanger”. In: *Chem. Eng. Sci.* 26.12 (1971), pp. 1987–2001.

[99] R. De Goede and E. De Jong. “Heat Transfer Properties of a Scraped-Surface Heat Exchanger in the Turbulent Flow Regime”. In: *Chem. Eng. Sci.* 48.8 (1993), pp. 1393–1404.

[100] A. Skelland, D. Oliver, and S. Tooke. “Heat Transfer in Water-Cooled Scraped-Surface Heat Exchanger”. In: *Brit. Chem. Eng. Pr. Tec.* 7.n 5 (1962), p 346–353.

[101] K. Dieter. “Leistungsverhalten von Dünnschichtverdampfern, II. - Stoffaustauschzahlen beim Destillieren”. In: *Chem. Ztg* 94.12 (1970), pp. 445–451.

[102] H. Miyashita and T. W. Hoffman. “Local Heat Transfer Coefficients In Scraped-Film Heat Exchanger”. In: *J. Chem. Eng. Jpn.* 11.6 (1978), pp. 444–450.

[103] H. Miyashita, M. Yoshida, T. Yamane, and T. Nishimura. “Heat Transfer Correlation in High Prandtl (High Schmidt) Number Fluid in Votator Type Scraped Surface Heat Exchanger”. In: *J. Chem. Eng. Jpn.* 30.3 (1997), pp. 545–549.

[104] R. Higbie. “The Rate of Absorption of Pure Gas Into a Still Liquid During Short Periods of Exposure”. In: *Trans. Am. Inst. Chem. Engrs.* 31 (1935), pp. 365–389.

[105] F. Schaal, K. Schilling, and H. Hasse. “Separation Efficiency of Thin-Film Evaporators: Experiments With Water–Ethylene Glycol and Methanol–Water and Stage-Based Modeling”. In: *Chem. Eng. Process. Process Intensif.* 47.2 (2008), pp. 209–214.

[106] A. Oron, S. H. Davis, and S. G. Bankoff. “Long-Scale Evolution Of Thin Liquid Films”. In: *Rev. Mod. Phys.* 69.3 (1997), pp. 931–980.

[107] D. Hartley and W. Murgatroyd. “Criteria for the Break-Up of Thin Liquid Layers Flowing Isothermally Over Solid Surfaces”. In: *Int. J. Heat Mass Tran.* 7.9 (1964), pp. 1003–1015.

[108] K. Morison, Q. Worth, and N. O’dea. “Minimum Wetting and Distribution Rates in Falling Film Evaporators”. In: *Food Bioprod. Process.* 84.4 (2006), pp. 302–310.

[109] T. Young. “III. An Essay on the Cohesion of Fluids”. In: *Philos. Trans. Roy. Soc. London* 95 (1805), pp. 65–87.

[110] S. P. Lin. “Stability Of Liquid Flow Down A Heated Inclined Plane”. In: *Lett. Heat Mass Trans.* 2.5 (1975), pp. 361–369.

[111] W. Nusselt. “Die Oberflächenkondensation des Wasserdampfes”. In: *Z.VDI* 60 (1916), pp. 541–546.

[112] M. S. El-Genk and H. H. Saber. “Minimum Thickness of a Flowing Down Liquid Film on a Vertical Surface”. In: *Int. J. Heat Mass Transf.* 44.15 (2001), pp. 2809–2825.

[113] F. Weise and S. Scholl. “Evaporation of Pure Liquids With Increased Viscosity in a Falling Film Evaporator”. In: *Heat Mass Transfer* 45.7 (2009), pp. 1037–1046.

[114] D. J. Benney. “Long Waves on Liquid Films”. In: *J. Math. Phys. Camb.* 45.1-4 (1966), pp. 150–155.

[115] V. Hallett. “Surface Phenomena Causing Breakdown of Falling Liquid Films During Heat Transfer”. In: *Int. J. Heat Mass Tran.* 9.4 (1966), pp. 283–294.

[116] L. A. Davalos-Orozco. “Stability of Thin Liquid Films Falling Down Isothermal and Nonisothermal Walls”. In: *Interfacial Phenomena and Heat Transfer* 1.2 (2013), pp. 93–138.

[117] N. Mascarenhas and I. Mudawar. “Study of the Influence of Interfacial Waves on Heat Transfer in Turbulent Falling Films”. In: *Int. J. Heat Mass Tran.* 67 (2013), pp. 1106–1121.

[118] S. Chattopadhyay, A. Mukhopadhyay, A. K. Barua, and A. K. Gaonkar. “Thermocapillary Instability On A Film Falling Down A Non-Uniformly Heated Slippery Incline”. In: *Int. J. Non Linear Mech.* 133 (2021), p. 103718.

[119] Y. Akkuş, H. I. Tarman, B. Çetin, and Z. Dursunkaya. “Two-Dimensional Computational Modeling of Thin Film Evaporation”. In: *Int. J. Therm. Sci.* 121 (2017), pp. 237–248.

[120] K. Sinha, K. Schweikert, A. Sielaff, and P. Stephan. “On the Nature of Microlayer Formation With Ethanol-Water Mixtures”. In: *Int. J. Therm. Sci.* 203 (2024), p. 109135.

[121] O. E. Shklyaev and E. Fried. “Stability of an Evaporating Thin Liquid Film”. In: *J. Fluid Mech.* 584 (2007), pp. 157–183.

[122] W. H. Reay. “Recent Advances in Thin Film Evaporation”. In: *Ind. Chem.* 39 (1963), pp. 293–297.

[123] R. Bressler. *Untersuchung des Wärmeüberganges in einem Dünnschichtverdampfer*. Wiesbaden: VS Verlag für Sozialwissenschaften, 1960.

[124] K. Guo, M. Yuan, and S.-L. Xu. “Study on Flow Regime in Wiped Film Molecular Distillation”. In: *Gao Xiao Hua Xue Gong Cheng Xue Bao/Journal of Chemical Engineering of Chinese Universities* 23.2 (2009), pp. 187–192.

[125] J. Becker, G. Grün, R. Seemann, H. Mantz, K. Jacobs, K. R. Mecke, and R. Blossey. “Complex Dewetting Scenarios Captured By Thin-Film Models”. In: *Nature Mater* 2.1 (2003), pp. 59–63.

[126] S. Gong, W. Ma, and T.-N. Dinh. “An Experimental Study of Rupture Dynamics of Evaporating Liquid Films on Different Heater Surfaces”. In: *Int. J. Heat Mass Tran.* 54.7-8 (2011), pp. 1538–1547.

[127] Y. V. Lyulin, S. E. Spesivtsev, I. V. Marchuk, and O. A. Kabov. “Study of Dynamics of Thin Liquid Layer Breakdown Under Conditions of Spot Heating and Formation of a Droplet Cluster”. In: *Thermophys. Aeromech.* 24.6 (2017), pp. 949–952.

[128] D. Zaitsev, D. Kochkin, and O. Kabov. “Dynamics of Liquid Film Rupture Under Local Heating”. In: *Int. J. Heat Mass Tran.* 184 (2022), p. 122376.

[129] N. Parker. “Agitated Thin-Film Evaporators, Part. 2: Equipment’s and Economics”. In: *Chem. Eng* 72.19 (1965), pp. 179–185.

[130] J. D. Fonseca, A. Suaza, R. F. Cortes, I. D. Gil, G. Rodríguez, and A. Orjuela. “Rapid Feasibility Assessment for the Use of Wiped-Film Evaporation in the Purification of Thermally Labile Products”. In: *Chem. Eng. Res. Des.* 146 (2019), pp. 141–153.

[131] T. Fujita and T. Ueda. “Heat Transfer to Falling Liquid Films and Film Breakdown - I”. In: *Int. J. Heat Mass Transf.* 21.2 (1978), pp. 97–108.

[132] F. Claus. “Entwicklung und Charakterisierung einer photometerischen Methode zur Verweilzeitmessung in Dünnschichtverdampfern”. Student thesis. 2022.

[133] W. Wagner *et al.* “The IAPWS Industrial Formulation 1997 for the Thermodynamic Properties of Water and Steam”. In: *J. Eng. Gas Turbines Power* 122.1 (2000), pp. 150–184.

[134] R. Numrich and J. Müller. “J1 Filmwise Condensation of Pure Vapors”. In: *VDI Heat Atlas*. Ed. by VDI e. V. Berlin, Heidelberg: Springer Berlin Heidelberg, 2010, pp. 903–918.

[135] E. O. Lebigot. *Uncertainties: A Python Package For Calculations With Uncertainties*.

[136] F. Widmer. “Behavior of Viscous Polymers during Solvent Stripping or Reaction in an Agitated Thin Film”. In: *Polymerization Kinetics and Technology*. Ed. by N. A. J. Platzer. Vol. 128. Advances in Chemistry. Washington, D. C.: American Chemical Society, 1973, pp. 51–67.

[137] A. EFCE Working Party on Distillation, Extraction, W. Arlt, U. Onken, and I. of Chemical Engineers (Great Britain). *Recommended Test Mixtures for Distillation Columns*. 2nd ed. London: Institution of Chemical Engineers London, 1990.

[138] A. Skoczylas and A. Urbański. “Residence Time of Liquid in a Thin Layer Evaporator Equipped with a Spiral Element”. In: *Chem. Eng. J. Biochem. Eng. J.* 56.2 (1995), pp. 51–58.

[139] C. Bradtmöller and S. Scholl. “Proposal for a Viscous Test Mixture—Densities, Viscosities, and Vapor–Liquid Equilibrium Data of the Binary Mixture 2-Methyl-2-butanol + 2-Methyl-1-propanol”. In: *J. Chem. Eng. Data* 61.1 (2016), pp. 272–285.

[140] Y. H. Mori, N. Tsui, and M. Kiyomiya. “Surface and Interfacial Tensions and Their Combined Properties in Seven Binary, Immiscible Liquid-Liquid-Vapor Systems”. In: *J. Chem. Eng. Data* 29.4 (1984), pp. 407–412.

[141] C.-W. Chang, T.-L. Hsiung, C.-P. Lui, and C.-H. Tu. “Densities, Surface Tensions, and Isobaric Vapor–Liquid Equilibria for the Mixtures of 2-Propanol, Water, and 1,2-Propanediol”. In: *Fluid Phase Equilibr.* 389 (2015), pp. 28–40.

[142] S. S. Katti and S. Pathak. “Surface Thermodynamic Properties of Alcohols and Related Compounds”. In: *J. Chem. Eng. Data* 14.1 (1969), pp. 73–76.

[143] W. H. Rinkenbach. “Properties of Diethylene Glycol”. In: *Ind. Eng. Chem.* 19.4 (1927), pp. 474–476.

[144] J. Ortega. “Densities and Refractive Indices of Pure Alcohols As a Function of Temperature”. In: *J. Chem. Eng. Data* 27.3 (1982), pp. 312–317.

[145] E. Calvo, A. Penas, M. Pintos, R. Bravo, and A. Amigo. “Refractive Indices and Surface Tensions of Binary Mixtures of 1,4-Dioxane + 1-Alkanols at 298.15 K”. In: *J. Chem. Eng. Data* 46.3 (2001), pp. 692–695.

[146] M. L. Kijevčanin, E. M. Živković, B. D. Djordjević, I. R. Radović, J. Jovanović, and S. P. Šerbanović. “Experimental Determination and Modeling of Excess Molar Volumes, Viscosities and Refractive Indices of the Binary Systems (pyridine+1-Propanol, +1,2-Propanediol, +1,3-Propanediol, and +glycerol). New UNIFAC-VISCO Parameters Determination”. In: *J. Chem. Thermodyn.* 56 (2013), pp. 49–56.

[147] D. Sagdeev, M. Fomina, G. Mukhamedzyanov, and I. Abdulagatov. “Experimental Study of the Density and Viscosity of Polyethylene Glycols and Their Mixtures at Temperatures from 293K to 473K and at Atmospheric Pressure”. In: *J. Chem. Thermodyn.* 43.12 (2011), pp. 1824–1843.

[148] C. Yang, H. Lai, Z. Liu, and P. Ma. “Densities and Viscosities of Diethyl Carbonate + Toluene, + Methanol, and + 2-Propanol from (293.15 to 363.15) K”. In: *J. Chem. Eng. Data* 51.2 (2006), pp. 584–589.

[149] U. Domańska and M. Królikowska. “Density and Viscosity of Binary Mixtures of 1-Butyl-3-methylimidazolium Thiocyanate + 1-Heptanol, 1-Octanol, 1-Nonanol, or 1-Decanol”. In: *J. Chem. Eng. Data* 55.9 (2010), pp. 2994–3004.

[150] M. Almasi. “Densities and Viscosities of Binary Mixtures Containing Diethylene Glycol and 2-Alkanol”. In: *J. Chem. Eng. Data* 57.11 (2012), pp. 2992–2998.

[151] E. D. Nikitin, P. A. Pavlov, and A. P. Popov. “(Gas+ liquid) Critical Temperatures and Pressures of Polyethene Glycols from HOCH2CH2OH to H (OCH2CH2) $\nu \approx$ 13.2 OH”. In: *J. Chem. Therm.* 27.1 (1995), pp. 43–51.

[152] Thermodynamics Research Center, NIST Boulder Laboratories, Chris Muzny director. “Thermodynamics Source Database”. In: *NIST Chemistry WebBook, NIST Standard Reference Database Number 69*. Ed. by P. Linstrom and W. Mallard. Gaithersburg MD, 20899: National Institute of Standards and Technology, 1997.

[153] E. Nikitin, P. Pavlov, and P. Skripov. “Measurement of the Critical Properties of Thermally Unstable Substances and Mixtures by the Pulse-Heating Method”. In: *J. Chem. Therm.* 25.7 (1993), pp. 869–880.

[154] S. K. Begum, R. J. Clarke, M. S. Ahmed, S. Begum, and M. A. Saleh. “Densities, Viscosities, and Surface Tensions of the System Water + Diethylene Glycol”. In: *J. Chem. Eng. Data* 56.2 (2011), pp. 303–306.

[155] P. Virtanen *et al.* “SciPy 1.0: Fundamental Algorithms for Scientific Computing in Python”. In: *Nat. Methods* 17 (2020), pp. 261–272.

[156] M. A. Iglesias-Otero, J. Troncoso, E. Carballo, and L. Romaní. “Density and Refractive Index in Mixtures of Ionic Liquids and Organic Solvents: Correlations and Predictions”. In: *J. Chem. Thermodyn.* 40.6 (2008), pp. 949–956.

[157] M. Kleiber and R. Joh. “D1 Berechnungsmethoden für Stoffeigenschaften”. In: *VDI-Wärmeatlas*. Berlin, Heidelberg: Springer Berlin Heidelberg, 2013, pp. 137–174.

[158] S. Sugden. “CXLII.—A Relation between Surface Tension, Density, and Chemical Composition”. In: *J. Chem. Soc. Trans.* 125.0 (1924), pp. 1177–1189.

[159] O. Redlich and A. T. Kister. “Algebraic Representation of Thermodynamic Properties and the Classification of Solutions”. In: *Ind. Eng. Chem.* 40.2 (1948), pp. 345–348.

[160] W. Niemeier and D. Tengen. “Stochastic Properties of Confidence Ellipsoids after Least Squares Adjustment, Derived from GUM Analysis and Monte Carlo Simulations”. In: *Mathematics* 8.8 (2020), p. 1318.

[161] J. A. Riddick, W. B. Bunger, T. Sakano, and A. Weissberger. *Organic Solvents: Physical Properties and Methods of Purification*. 4th ed. Techniques of chemistry v. 2. New York: Wiley, 1986.

[162] J. Gary, J. Crichton Jr., and R. Feild Jr. “Equilibria Data for Two Viscous Ternary Liquid Systems.” In: *Ind. Eng. Chem. Chem. Eng. Data Series* 3.1 (1958), pp. 111–112.

[163] T. Sun and A. S. Teja. “Density, Viscosity, and Thermal Conductivity of Aqueous Ethylene, Diethylene, and Triethylene Glycol Mixtures between 290 K and 450 K”. In: *J. Chem. Eng. Data* 48.1 (2003), pp. 198–202.

[164] W. V. Steele, R. D. Chirico, A. B. Cowell, S. E. Knipmeyer, and A. Nguyen. “Thermodynamic Properties and Ideal-Gas Enthalpies of Formation for Methyl Benzoate, Ethyl Benzoate, (*R*)-(+)-Limonene, *tert* -Amyl Methyl Ether, *trans* -Crotonaldehyde, and Diethylene Glycol”. In: *J. Chem. Eng. Data* 47.4 (2002), pp. 667–688.

[165] M. Diaz Peña and G. Tardajos. “Isothermal Compressibilities of N-1-Alcohols from Methanol to 1-Dodecanol at 298.15, 308.15, 318.15, and 333.15 K”. In: *J. Chem. Thermodyn.* 11.5 (1979), pp. 441–445.

[166] M. Al-Hayan. “Densities, Excess Molar Volumes, and Refractive Indices of 1,1,2,2-Tetrachloroethane and 1-Alkanols Binary Mixtures”. In: *The Journal of Chemical Thermodynamics* 38.4 (2006), pp. 427–433.

[167] G. H. Findenegg. “Dichte und Ausdehnungskoeffizienten einiger flüssiger Alkanole und Carbonssäuren”. In: *Monatsh. Chem.* 104.4 (1973), pp. 998–1007.

[168] A. A. Mohammad, K. H. Alkhaldi, M. S. AlTuwaim, and A. S. Al-Jimaz. “Effect Of Temperature And Chain Length On The Viscosity And Surface Tension Of Binary Systems Of N,N-Dimethylformamide With 1-Octanol, 1-Nonanol And 1-Decanol”. In: *J. Chem. Thermodyn.* 74 (2014), pp. 7–15.

[169] S. Matsuo and T. Makita. “Viscosities of Six 1-Alkanols at Temperatures in the Range 298-348 K and Pressures up to 200 MPa”. In: *Int. J. Thermophys.* 10.4 (1989), pp. 833–843.

[170] M. Hasan, D. F. Shirude, A. P. Hiray, U. B. Kadam, and A. B. Sawant. “Densities, Viscosities, and Speed of Sound Studies of Binary Mixtures of Methylbenzene with Heptan-1-ol, Octan-1-ol, and Decan-1-ol at (303.15 and 313.15) K”. In: *J. Chem. Eng. Data* 51.5 (2006), pp. 1922–1926.

[171] A. Rodríguez, J. Canosa, A. Domínguez, and J. Tojo. “Dynamic Viscosities of Diethyl Carbonate with Linear and Secondary Alcohols at Several Temperatures”. In: *J. Chem. Eng. Data* 49.1 (2004), pp. 157–162.

[172] F.-M. Pang, C.-E. Seng, T.-T. Teng, and M. Ibrahim. “Densities and Viscosities of Aqueous Solutions of 1-Propanol and 2-Propanol at Temperatures from 293.15 K to 333.15 K”. In: *J. Mol. Liq.* 136.1-2 (2007), pp. 71–78.

[173] C.-T. Yeh and C.-H. Tu. “Densities, Viscosities, Refractive Indexes, and Surface Tensions for Binary Mixtures of 2-Propanol + Benzyl Alcohol, + 2-Phenylethanol and Benzyl Alcohol + 2-Phenylethanol at T = (298.15, 308.15, and 318.15) K”. In: *J. Chem. Eng. Data* 52.5 (2007), pp. 1760–1767.

[174] J. Hales and J. Ellender. “Liquid Densities from 293 to 490 K of Nine Aliphatic Alcohols”. In: *J. Chem. Thermodyn.* 8.12 (1976), pp. 1177–1184.

[175] L. F. Hoyt. “New Table of the Refractive Index of Pure Glycerol at 20°C”. In: *Ind. Eng. Chem.* 26.3 (1934), pp. 329–332.

[176] J. B. Segur and H. E. Oberstar. “Viscosity of Glycerol and Its Aqueous Solutions”. In: *Ind. Eng. Chem.* 43.9 (1951), pp. 2117–2120.

[177] F. Bandarkar, I. S. Khattab, F. Martinez, M. Khoubnasabjafari, S. Vahdati, and A. Jouyban. “Viscosity and Surface Tension of Glycerol + *N* -Methyl-2-Pyrrolidone Mixtures from 293 to 323 K”. In: *Phys. Chem. Liq.* 53.1 (2015), pp. 104–116.

[178] G. I. Egorov, D. M. Makarov, and A. M. Kolker. “Volume Properties of Liquid Mixture of Water+Glycerol over the Temperature Range from 278.15 to 348.15 K at Atmospheric Pressure”. In: *Thermochim. Acta* 570 (2013), pp. 16–26.

[179] K. Takamura, H. Fischer, and N. R. Morrow. “Physical Properties of Aqueous Glycerol Solutions”. In: *J. Petrol. Sci. Eng.* 98-99 (2012), pp. 50–60.

[180] M.-L. Ge, J.-L. Ma, and B. Chu. “Densities and Viscosities of Propane-1,2,3-triol + Ethane-1,2-diol at T = (298.15 to 338.15) K”. In: *J. Chem. Eng. Data* 55.7 (2010), pp. 2649–2651.

[181] M. J. Iqbal, M. A. Rauf, and N. Ijaz. “Surface Tension Measurements of Glycerol with Organic Cosolvents”. In: *J. Chem. Eng. Data* 37.1 (1992), pp. 45–47.

[182] N. Al Azri, H. Mantripragada, R. Patel, C. Kowall, G. Cormack, N. Proust, R. Enick, and G. Veser. “Process Intensification for Production of Dispersants via Integration of Reaction and Separation in a Horizontal Thin Film Evaporator”. In: *Chem. Eng. J.* 489 (2024), p. 151541.

[183] D. P. Biddiscombe, R. R. Collerson, R. Handley, E. F. G. Herington, J. F. Martin, and C. H. S. Sprake. “364. Thermodynamic Properties of Organic Oxygen Compounds. Part VIII. Purification and Vapour Pressures of the Propyl and Butyl Alcohols”. In: *J. Chem. Soc.* (1963), p. 1954.

[184] D. Ambrose and R. Townsend. “681. Thermodynamic Properties of Organic Oxygen Compounds. Part IX. The Critical Properties and Vapour Pressures, Above Five Atmospheres, of Six Aliphatic Alcohols”. In: *J. Chem. Soc.* (1963), p. 3614.

[185] O. A. Asbjørnsen. “G2. The Distribution of Residence Times in a Falling Water Film”. In: *Chem. Eng. Sci.* 14.1 (1961), pp. 211–226.

[186] S. G. Bankoff. “Stability of Liquid Flow down a Heated Inclined Plane”. In: *Int. J. Heat Mass Tran.* 14.3 (1971), pp. 377–385.

[187] E. Sultan, A. Boudaoud, and M. B. Amar. “Evaporation of a Thin Film: Diffusion of the Vapour and Marangoni Instabilities”. In: *J. Fluid Mech.* 543.-1 (2005), p. 183.

[188] Modelica Association. *Modelica - A Unified Object-Oriented Language for Systems Modeling Version 3.4*. 2017.

[189] A. Uhlendorf, T. Grützner, G. Rosenthal, and S. Scholl. “Experimental Investigation of the Residence Time Behavior of a Wiped Film Evaporator”. unpublished. 2018.

[190] M. Schmidt, U. Schloßer, and E. Schollmeyer. “Computational Fluid Dynamics Investigation of the Static Pressure at the Blade in a Blade Coating Process”. In: *Text. Res. J.* 79.7 (2009), pp. 579–584.

[191] R. J. Cornish and E. A. Milne. “Flow In A Pipe Of Rectangular Cross-Section”. In: *Proc. R. Soc. London A.* 120.786 (1928), pp. 691–700.

[192] W. M. Owen. “Laminar to Turbulent Flow in a Wide Open Channel”. In: *Trans. Am. Soc. Civil Eng.* 119.1 (1954), pp. 1157–1164.

[193] A. de La Calle, L. J. Yebra, and S. Dormido. “Modeling of a Falling Film Evaporator”. In: *Proceedings of the 9th International MODELICA Conference; September 3-5; 2012; Munich; Germany*. 76. Linköping University Electronic Press; Linköpings universitet, 2012, pp. 941–948.

[194] T. Bäuml and H. Kühnelt. “Simulation of 2-Dimensional Flows in Modelica With the Cascaded Digital Lattice Boltzmann Method”. In: *Proceedings of the 10th International Modelica Conference*. 96. Linköping University Electronic Press; Linköpings universitet, 2014, pp. 1221–1226.

[195] A. Kossolapov, B. Phillips, and M. Bucci. “Can LED Lights Replace Lasers For Detailed Investigations Of Boiling Phenomena?” In: *Int. J. Multiphas. Flow* 135 (2021), p. 103522.

[196] L. Villafañe, A. Aliseda, S. Ceccio, P. Di Marco, N. Machicoane, and T. J. Heindel. “50 Years of International Journal of Multiphase Flow: Experimental methods for dispersed multiphase flows”. In: *Int. J. Multiphas. Flow* 189 (2025), p. 105239.

[197] Dassault Systémes AB. *Dymola - Dynamik Modeling Laboratory Release Notes*. 2023.

[198] Modelica Association. *Modelica - A Unified Object-Oriented Language for Systems Modelling, Language Specification, Version 3.6*. 2023.

[199] A. Skelland. “Correlation Of Scraped-Film Heat Transfer In The Votator”. In: *Chem. Eng. Sci.* 7.3 (1958), pp. 166–175.

[200] J. M. Floryan, S. H. Davis, and R. E. Kelly. “Instabilities of a Liquid Film Flowing Down a Slightly Inclined Plane”. In: *Phys. Fluids* 30.4 (1987), pp. 983–989.

[201] Y. Lu, F. Stehmann, S. Yuan, and S. Scholl. “Falling Film on a Vertical Flat Plate – Influence of Liquid Distribution and Fluid Properties on Wetting Behavior”. In: *Appl. Therm. Eng.* 123 (2017), pp. 1386–1395.

[202] B. W. Lee, K. Yin, K. Splaine, and B. Roesch. “Thin-Film Evaporator Model for Continuous Active Pharmaceutical Ingredient Manufacturing”. In: *Ind. Eng. Chem. Res.* 59.7 (2020), pp. 3252–3260.

[203] S. Kutateladze and I. Gogonin. “Heat Transfer in Film Condensation of Slowly Moving Vapour”. In: *Int. J. Heat Mass Tran.* 22.12 (1979), pp. 1593–1599.

[204] J. Müller. “Heat Transfer During Film Condensation—Uniform Description Of Heat And Mass Transfer Of Film Flows And Related Processes”. In: *Chem. Eng. Process. Process Intensif.* (1994).

A. Appendix

A.1. Additional Information on Residence Time Measurement

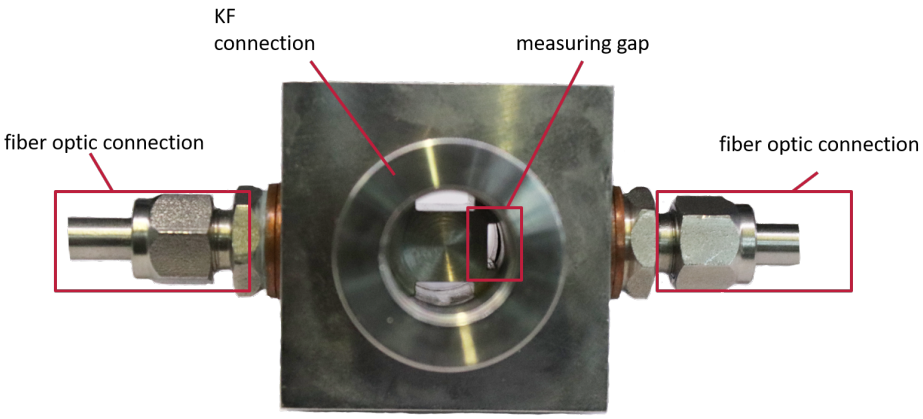

Figure A.1.: Image of the measuring point used for the residence time measurements with labels.

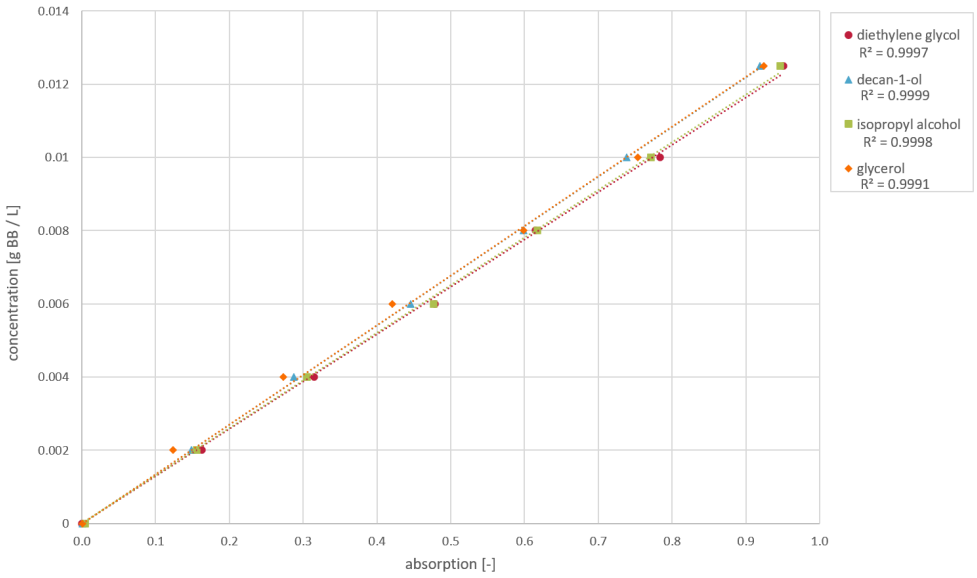

Figure A.2.: Concentration set as a function of the measured absorption for the tested substance systems diethylene glycol, decan-1-ol, isopropyl alcohol, and glycerol (Claus 2022) [132].

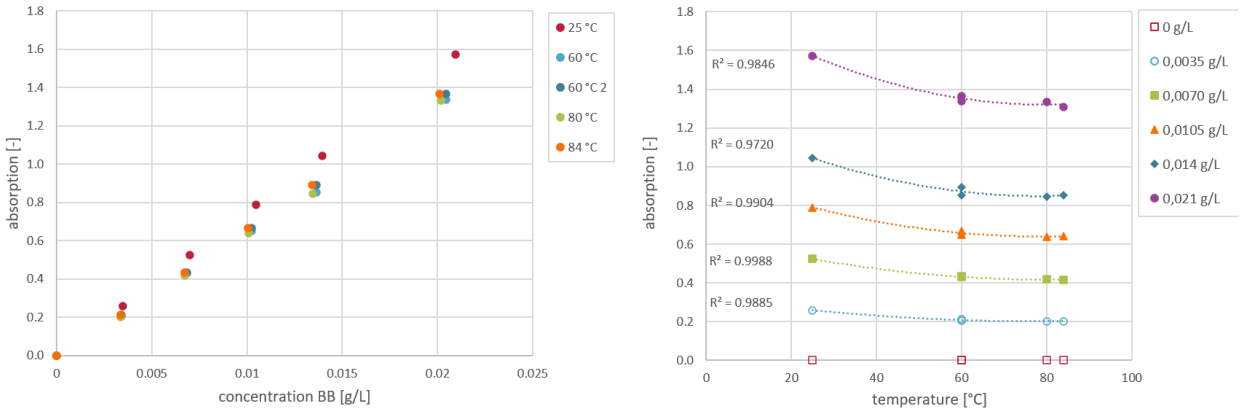

Figure A.3.: Dependence of the measured absorbance values on the concentration and temperature (Claus 2022)[132].

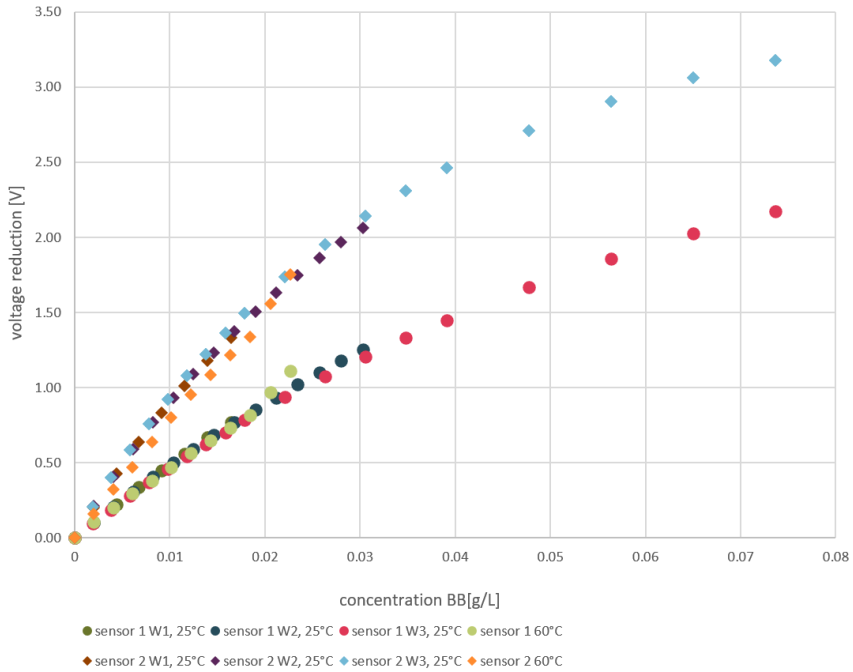

Figure A.4.: Dependence of the measured voltage losses of the sensors used on the concentration and temperature (with 3 replicate measurements for 25 °C) (Claus 2022)[132].

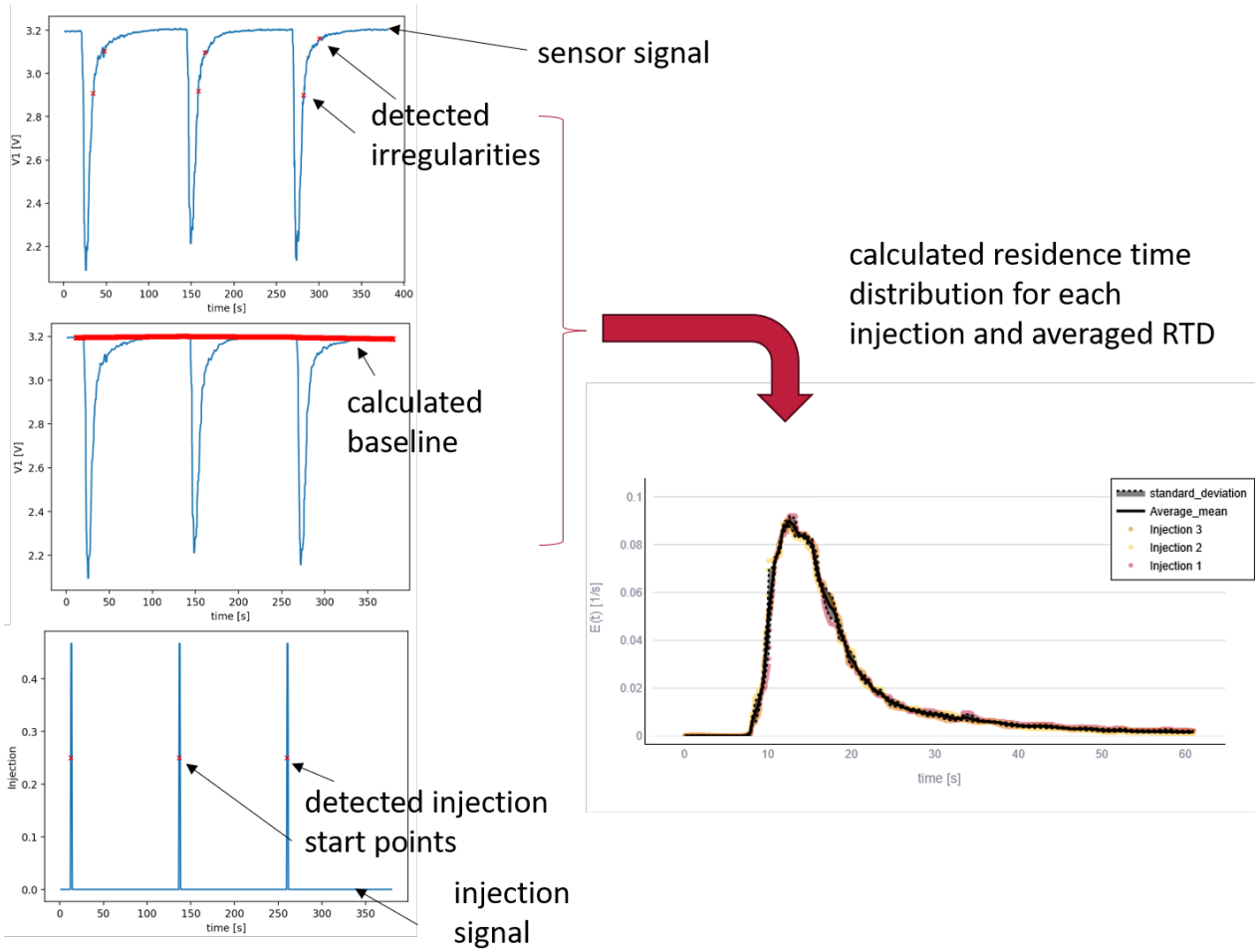

Figure A.5.: Procedure for calculating the residence time distribution with detection of irregularities within the sensor signal, calculation of the baseline, detection of the injection time and calculation of the averaged residence time distribution.

A.2. Characterization of the Mass and Energy Balance of the Miniplant Used

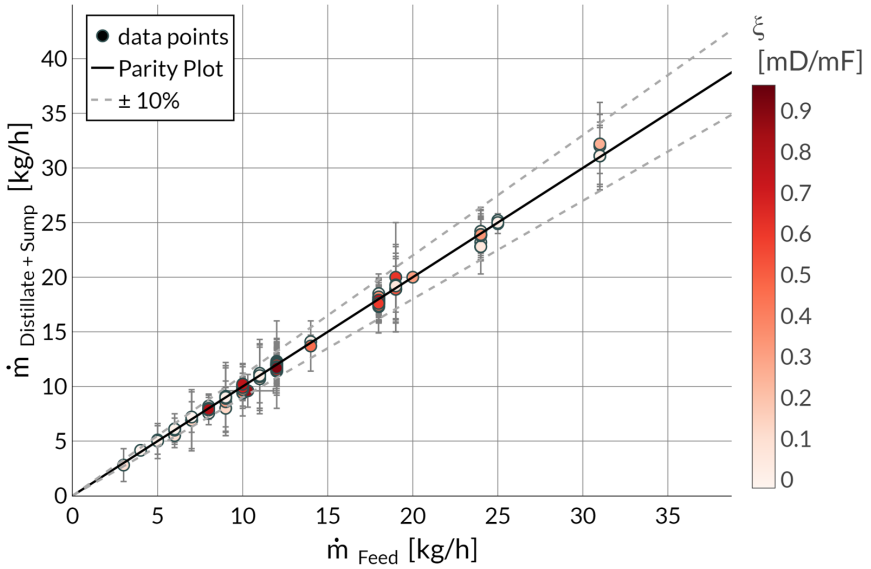

Figure A.6.: Experimental data on mass balance: Summed measured values mass flow distillate and sump over mass flow feed.

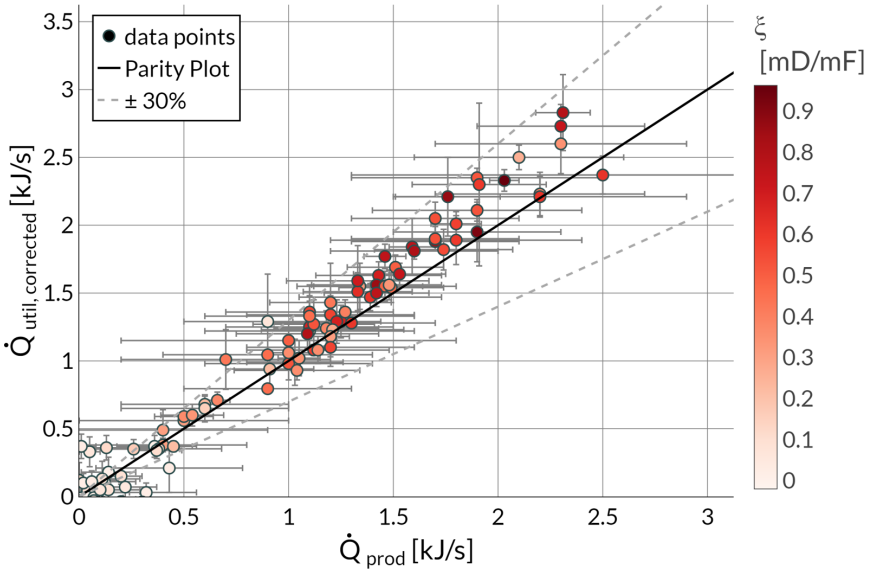

Figure A.7.: Experimental data on the heat balance: Corrected heat flow on the heating side (corrected with $\dot{Q}_{\mathrm{loss}} = 1.034$ kW) via heat flow on the product side.

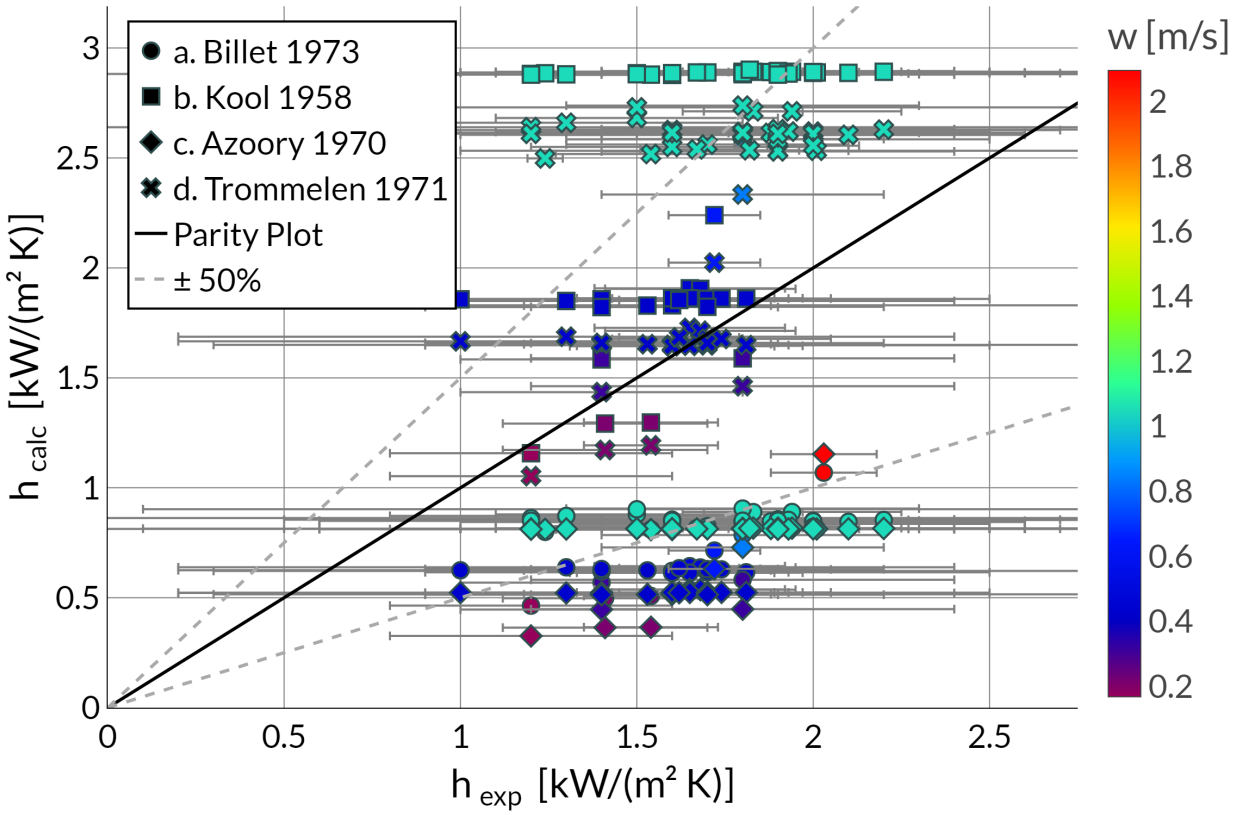

Figure A.8.: Comparison of experimentally determined product-side heat transfer coefficients with standard deviations for diethylene glycol with theoretical predictions using (a) Equation 2.8 [94], and (b–d) Equation 2.13 [63] without correction and with correction factors according to (c) Equation 2.16 [20] and (d) Equation 2.17 [98].

A.3. Supporting Information

Density, Viscosity, Refractive Index and Surface Tension of Binary Mixtures of 3-Oxa-1,5-Pentanediol with 2-Propanol, 1,2,3-Propanetriol and 1-Decanol from 283.15 to 403.15 K as Reference Systems for Evaporation Experiments

Table A.1 shows the calculated excess refractive index $n^E_{D,exp}$ and the estimated excess refractive index $n^E_{D,est}$.
Table A.2 shows the calculated excess volumes v^E_{exp} and the estimated excess refractive index v^E_{est}.
Table A.3 shows the calculated excess logarithmic viscosity $\ln(\eta)^E_{exp}$ and the estimated excess logarithmic viscosity $\ln(\eta)^E_{est}$.
Table A.4 shows the calculated excess parachor P^E_{exp} and the estimated excess parachor P^E_{est}.

Table A.1.: Excess refractive index $n^E_{D,exp}$ and estimated value of excess refractive index $n^E_{D,est}$ of all studied systems at T = 293.15 K and p = 101 kPa

T/K [a]	x_2 [b]	n^E_D		x_2 [b]	n^E_D	
		exp.	est.		exp.	est.
diethylene glycol (1) & decan-1-ol (2)						
293.15	0.0835	-0.001355	-0.001319	0.583	-0.002331	-0.002293
	0.1667	-0.002105	-0.002098	0.6667	-0.001992	-0.001976
	0.2499	-0.002493	-0.002513	0.7489	-0.001591	-0.001594
	0.3334	-0.002757	-0.002677	0.8328	-0.001140	-0.001133
	0.4164	-0.002438	-0.002666	0.9165	-0.000548	-0.000603
	0.5002	-0.002517	-0.002528			
diethylene glycol (1) & isopropyl alcohol (2)						
293.15	0.836	0.003757	0.003574	0.5834	0.011679	0.011682
	0.1667	0.006820	0.006641	0.6666	0.010559	0.010554
	0.2427	0.008888	0.008902	0.7500	0.008767	0.008776
	0.3335	0.010758	0.010839	0.8333	0.006571	0.006395
	0.4166	0.011868	0.011848	0.9166	0.003446	0.003456
	0.500000	0.011942	0.012125			
diethylene glycol (1) & glycerol (2)						
293.15	0.835	0.000021	-0.000024	0.5833	0.000035	0.000020
	0.1667	0.000010	-0.000030	0.6668	0.000032	0.000021
	0.2503	-0.000091	-0.000025	0.7513	0.000017	0.000017
	0.3335	-0.000034	-0.000013	0.8334	0.000034	0.000009
	0.4167	-0.000005	0.000000	0.9167	0.000001	0.000001
	0.5000	0.000025	0.000012			

[a]: Uncertainty of temperature measurement: 0.02 K
[b]: Uncertainty of mole fraction: 0.0013

Table A.2.: Excess volume v^E_{exp} and estimated value of excess volume v^E_{est} of all studied systems at p = 101 kpa

T/K [a]	x_2 [b]	v^E		x_2 [b]	v^E	
		exp.	est.		exp.	est.
diethylene glycol (1) & decan-1-ol (2)						
293.15	0.083500	0.175202	0.173986	0.583000	0.536482	0.537525
	0.166700	0.326582	0.304095	0.666700	0.487668	0.512151
	0.249900	0.378681	0.400081	0.748900	0.469478	0.456206
	0.333400	0.445478	0.468726	0.832800	0.321964	0.359176
	0.416400	0.520025	0.513589	0.916500	0.169945	0.211410
	0.499800	0.533818	0.536869			
298.15	0.083500	0.178713	0.173297	0.583000	0.541854	0.537971
	0.166700	0.328229	0.304489	0.666700	0.490298	0.509820
	0.249900	0.381944	0.402079	0.748900	0.475627	0.451215
	0.333400	0.451280	0.471945	0.832800	0.324194	0.352637
	0.416400	0.524325	0.517060	0.916500	0.160420	0.205946
	0.499800	0.536009	0.539384			
303.15	0.083500	0.180226	0.172551	0.583000	0.542996	0.538031
	0.166700	0.331112	0.304704	0.666700	0.494390	0.507232
	0.249900	0.386476	0.403764	0.748900	0.483355	0.446116
	0.333400	0.458414	0.474743	0.832800	0.321061	0.346123
	0.416400	0.539677	0.520055	0.916500	0.174438	0.200567
	0.499800	0.544817	0.541436			
308.15	0.083500	0.179665	0.171748	0.583000	0.545441	0.537705
	0.166700	0.335210	0.304739	0.666700	0.499877	0.504386
	0.249900	0.392249	0.405135	0.748900	0.479444	0.440908
	0.333400	0.457887	0.477119	0.832800	0.333307	0.339634
	0.416400	0.536914	0.522576	0.916500	0.175331	0.195271
	0.499800	0.549702	0.543025			
313.15	0.083500	0.180251	0.170888	0.583000	0.549124	0.536992
	0.166700	0.336801	0.304594	0.666700	0.500489	0.501283
	0.249900	0.391032	0.406191	0.748900	0.476748	0.435591
	0.333400	0.462993	0.479074	0.832800	0.318855	0.333170
	0.416400	0.545111	0.524621	0.916500	0.162635	0.190059
	0.499800	0.550484	0.544150			
318.15	0.083500	0.178644	0.169970	0.583000	0.548155	0.535894
	0.166700	0.335782	0.304270	0.666700	0.495994	0.497923
	0.249900	0.390870	0.406934	0.748900	0.475176	0.430166
	0.333400	0.464699	0.480607	0.832800	0.319595	0.326730
	0.416400	0.539609	0.526192	0.916500	0.166072	0.184931
	0.499800	0.552364	0.544813			
323.15	0.083500	0.181453	0.168995	0.583000	0.536451	0.534410
	0.166700	0.335796	0.303766	0.666700	0.498754	0.494305
	0.249900	0.395884	0.407363	0.748900	0.467894	0.424632
	0.333400	0.462850	0.481719	0.832800	0.314252	0.320315
	0.416400	0.535018	0.527286	0.916500	0.163062	0.179887
	0.499800	0.544406	0.545013			
328.15	0.083500	0.178616	0.167963	0.583000	0.537288	0.532539
	0.166700	0.336812	0.303083	0.666700	0.489768	0.490430
	0.249900	0.393548	0.407477	0.748900	0.468213	0.418990
	0.333400	0.466520	0.482409	0.832800	0.302528	0.313926
	0.416400	0.541357	0.527906	0.916500	0.153287	0.174927
	0.499800	0.542705	0.544749			
333.15	0.083500	0.176758	0.166873	0.583000	0.532977	0.530283
	0.166700	0.338794	0.302220	0.666700	0.481425	0.486297
	0.249900	0.392072	0.407278	0.748900	0.455634	0.413239
	0.333400	0.461800	0.482677	0.832800	0.306002	0.307561

[a]: Uncertainty of temperature measurement: 0.02 K

[b]: Uncertainty of mole fraction: 0.0013

Table A.2.: Excess volume v^E_{exp} and estimated value of excess volume v^E_{est} of all studied systems at p = 101 kpa (continued)

T/K [a]	x_2 [b]	v^E		x_2 [b]	v^E	
		exp.	est.		exp.	est.
	0.416400	0.538458	0.528051	0.916500	0.144157	0.170050
	0.499800	0.541784	0.544022			
338.15	0.083500	0.175855	0.165726	0.583000	0.523266	0.527641
	0.166700	0.330197	0.301178	0.666700	0.473609	0.481907
	0.249900	0.391405	0.406764	0.748900	0.450409	0.407380
	0.333400	0.462472	0.482524	0.832800	0.295469	0.301221
	0.416400	0.526000	0.527720	0.916500	0.143339	0.165258
	0.499800	0.535989	0.542833			
343.15	0.083500	0.172437	0.164522	0.583000	0.526077	0.524612
	0.166700	0.333910	0.299956	0.666700	0.472709	0.477260
	0.249900	0.387201	0.405937	0.748900	0.445609	0.401412
	0.333400	0.459124	0.481950	0.832800	0.292675	0.294905
	0.416400	0.524314	0.526914	0.916500	0.135107	0.160549
	0.499800	0.536308	0.541180			
348.15	0.083500	0.166399	0.163261	0.583000	0.523255	0.521198
	0.166700	0.326784	0.298554	0.666700	0.459040	0.472355
	0.249900	0.383619	0.404795	0.748900	0.441085	0.395335
	0.333400	0.451566	0.480954	0.832800	0.282668	0.288615
	0.416400	0.517932	0.525633	0.916500	0.142950	0.155925
	0.499800	0.531454	0.539064			
353.15	0.083500	0.168113	0.161943	0.583000	0.514515	0.517397
	0.166700	0.328121	0.296973	0.666700	0.452002	0.467193
	0.249900	0.380592	0.403339	0.748900	0.436678	0.389150
	0.333400	0.449202	0.479536	0.832800	0.280195	0.282349
	0.416400	0.522381	0.523876	0.916500	0.118928	0.151384
	0.499800	0.521169	0.536484			
358.15	0.083500	0.167139	0.160567	0.583000	0.499553	0.513211
	0.166700	0.326184	0.295212	0.666700	0.451612	0.461773
	0.249900	0.378047	0.401570	0.748900	0.432214	0.382856
	0.333400	0.447216	0.477697	0.832800	0.270012	0.276109
	0.416400	0.511333	0.521645	0.916500	0.118693	0.146927
	0.499800	0.510937	0.533442			
363.15	0.083500	0.163360	0.159134	0.583000	0.496877	0.508639
	0.166700	0.320823	0.293272	0.666700	0.444377	0.456096
	0.249900	0.375903	0.399486	0.748900	0.420284	0.376454
	0.333400	0.440627	0.475436	0.832800	0.259405	0.269893
	0.416400	0.505635	0.518938	0.916500	0.118156	0.142554
	0.499800	0.506426	0.529937			
373.15	0.083500	0.172098	0.156096	0.583000	0.513085	0.498336
	0.166700	0.340489	0.288853	0.666700	0.471844	0.443970
	0.249900	0.405791	0.394377	0.748900	0.451158	0.363323
	0.333400	0.481745	0.469650	0.832800	0.293330	0.257535
	0.416400	0.535879	0.512099	0.916500	-0.864445	0.134060
	0.499800	0.528183	0.521536			
383.15	0.083500	0.160808	0.152829	0.583000	0.490026	0.486488
	0.166700	0.327263	0.283716	0.666700	0.453531	0.430814
	0.249900	0.385097	0.388011	0.748900	0.429763	0.349759
	0.333400	0.473093	0.462178	0.832800	0.270467	0.245277
	0.416400	0.513217	0.503359	0.916500	0.101218	0.125901
	0.499800	0.507688	0.511283			
393.15	0.083500	0.145072	0.149333	0.583000	0.463679	0.473097
	0.166700	0.313495	0.277861	0.666700	0.433615	0.416628
	0.249900	0.369909	0.380390	0.748900	0.390900	0.335760

[a]: Uncertainty of temperature measurement: 0.02 K

[b]: Uncertainty of mole fraction: 0.0013

Table A.2.: Excess volume v^E_{exp} and estimated value of excess volume v^E_{est} of all studied systems at p = 101 kpa (continued)

T/K [a]	x_2 [b]	v^E		x_2 [b]	v^E	
		exp.	est.		exp.	est.
	0.333400	0.455674	0.453019	0.832800	0.246599	0.233119
	0.416400	0.496610	0.492718	0.916500	0.126253	0.118078
	0.499800	0.483463	0.499178			
403.15	0.083500	0.135016	0.145608	0.583000	0.436804	0.458162
	0.166700	0.294505	0.271287	0.666700	0.394728	0.401413
	0.249900	0.348586	0.371512	0.748900	0.384495	0.321326
	0.333400	0.426737	0.442175	0.832800	0.231873	0.221060
	0.416400	0.466608	0.480176	0.916500	0.106947	0.110591
	0.499800	0.463072	0.485220			
diethylene glycol (1) & isopropyl alcohol (2)						
283.15	0.083600	-0.125061	-0.037241	0.583400	-0.354211	-0.384693
	0.166700	-0.203815	-0.134198	0.666600	-0.274825	-0.299689
	0.242700	-0.282227	-0.239140	0.750000	-0.215174	-0.186400
	0.333500	-0.353833	-0.349246	0.833300	-0.117730	-0.072355
	0.416600	-0.371214	-0.411768	0.916600	0.024139	0.005478
	0.500000	-0.358161	-0.424573			
288.15	0.083600	-0.124419	-0.041628	0.583400	-0.369521	-0.399516
	0.166700	-0.206332	-0.141708	0.666600	-0.298157	-0.314572
	0.242700	-0.291314	-0.248783	0.750000	-0.232561	-0.200367
	0.333500	-0.366007	-0.360857	0.833300	-0.127668	-0.083960
	0.416600	-0.385080	-0.424799	0.916600	0.014106	-0.001717
	0.500000	-0.377355	-0.438707			
293.15	0.083600	-0.125767	-0.046882	0.583400	-0.393867	-0.418435
	0.166700	-0.215567	-0.150880	0.666600	-0.317634	-0.333488
	0.242700	-0.303311	-0.260753	0.750000	-0.246215	-0.218001
	0.333500	-0.381576	-0.375489	0.833300	-0.143205	-0.098491
	0.416600	-0.402762	-0.441371	0.916600	0.007634	-0.010646
	0.500000	-0.400838	-0.456754			
298.15	0.083600	-0.129210	-0.053003	0.583400	-0.418829	-0.441447
	0.166700	-0.227459	-0.161715	0.666600	-0.342522	-0.356435
	0.242700	-0.318416	-0.275048	0.750000	-0.265578	-0.239299
	0.333500	-0.400791	-0.393144	0.833300	-0.164874	-0.115948
	0.416600	-0.424560	-0.461484	0.916600	-0.005167	-0.021310
	0.500000	-0.424547	-0.478715			
303.15	0.083600	-0.134857	-0.059991	0.583400	-0.444741	-0.468554
	0.166700	-0.233515	-0.174212	0.666600	-0.364186	-0.383415
	0.242700	-0.332502	-0.291670	0.750000	-0.291196	-0.264264
	0.333500	-0.423930	-0.413822	0.833300	-0.183806	-0.136331
	0.416600	-0.450807	-0.485138	0.916600	-0.015249	-0.033707
	0.500000	-0.448766	-0.504590			
308.15	0.083600	-0.142830	-0.067846	0.583400	-0.476524	-0.499755
	0.166700	-0.251182	-0.188371	0.666600	-0.401366	-0.414426
	0.242700	-0.350096	-0.310618	0.750000	-0.323685	-0.292894
	0.333500	-0.446901	-0.437521	0.833300	-0.200401	-0.159640
	0.416600	-0.477437	-0.512334	0.916600	-0.032840	-0.047839
	0.500000	-0.478308	-0.534377			
313.15	0.083600	-0.153261	-0.076568	0.583400	-0.510163	-0.535050
	0.166700	-0.263282	-0.204193	0.666600	-0.431704	-0.449470
	0.242700	-0.371467	-0.331892	0.750000	-0.354287	-0.325189
	0.333500	-0.474392	-0.464242	0.833300	-0.234454	-0.185874
	0.416600	-0.509243	-0.543070	0.916600	-0.048865	-0.063705
	0.500000	-0.509144	-0.568078			
318.15	0.083600	-0.157486	-0.086157	0.583400	-0.550794	-0.574439

[a]: Uncertainty of temperature measurement: 0.02 K

[b]: Uncertainty of mole fraction: 0.0013

Table A.2.: Excess volume v^E_{exp} and estimated value of excess volume v^E_{est} of all studied systems at p = 101 kpa (continued)

T/K [a]	x_2 [b]	v^E		x_2 [b]	v^E	
		exp.	est.		exp.	est.
	0.166700	-0.278703	-0.221677	0.666600	-0.469609	-0.488545
	0.242700	-0.392479	-0.355492	0.750000	-0.383531	-0.361150
	0.333500	-0.502328	-0.493986	0.833300	-0.257860	-0.215035
	0.416600	-0.542191	-0.577347	0.916600	-0.063953	-0.081305
	0.500000	-0.550833	-0.605693			
323.15	0.083600	-0.168790	-0.096613	0.583400	-0.589840	-0.617923
	0.166700	-0.297702	-0.240823	0.666600	-0.511173	-0.531653
	0.242700	-0.417852	-0.381418	0.750000	-0.421696	-0.400777
	0.333500	-0.535558	-0.526752	0.833300	-0.290738	-0.247122
	0.416600	-0.581263	-0.615165	0.916600	-0.083920	-0.100639
	0.500000	-0.590342	-0.647221			
328.15	0.083600	-0.182977	-0.107936	0.583400	-0.637290	-0.665501
	0.166700	-0.320567	-0.261632	0.666600	-0.557214	-0.578793
	0.242700	-0.443472	-0.409671	0.750000	-0.469835	-0.444069
	0.333500	-0.570058	-0.562540	0.833300	-0.324284	-0.282134
	0.416600	-0.622500	-0.656525	0.916600	-0.104732	-0.121707
	0.500000	-0.632809	-0.692662			
333.15	0.083600	-0.191253	-0.120126	0.583400	-0.689385	-0.717173
	0.166700	-0.338596	-0.284103	0.666600	-0.603882	-0.629964
	0.242700	-0.474228	-0.440249	0.750000	-0.509509	-0.491027
	0.333500	-0.610888	-0.601351	0.833300	-0.359530	-0.320073
	0.416600	-0.666517	-0.701425	0.916600	-0.127505	-0.144509
	0.500000	-0.683642	-0.742017			
338.15	0.083600	-0.202713	-0.133183	0.583400	-0.747152	-0.772939
	0.166700	-0.370175	-0.308237	0.666600	-0.666810	-0.685168
	0.242700	-0.510644	-0.473154	0.750000	-0.561444	-0.541651
	0.333500	-0.654133	-0.643183	0.833300	-0.407926	-0.360937
	0.416600	-0.718703	-0.749866	0.916600	-0.153603	-0.169046
	0.500000	-0.743839	-0.795285			
343.15	0.083600	-0.222177	-0.147107	0.583400	-0.811829	-0.832799
	0.166700	-0.388451	-0.334033	0.666600	-0.734580	-0.744404
	0.242700	-0.544121	-0.508385	0.750000	-0.627368	-0.595940
	0.333500	-0.700503	-0.688038	0.833300	-0.450771	-0.404728
	0.416600	-0.770672	-0.801849	0.916600	-0.179400	-0.195317
	0.500000	-0.800328	-0.852466			
diethylene glycol (1) & glycerol (2)						
293.15	0.083500	-0.067648	-0.071007	0.583300	-0.208136	-0.209427
	0.166700	-0.123624	-0.125089	0.666800	-0.191385	-0.194073
	0.250300	-0.164537	-0.165054	0.751300	-0.152530	-0.166709
	0.333500	-0.189471	-0.192338	0.833400	-0.113486	-0.127298
	0.416700	-0.208809	-0.208437	0.916700	-0.066430	-0.072414
	0.500000	-0.212732	-0.214079			
298.15	0.083500	-0.069082	-0.068226	0.583300	-0.211142	-0.206706
	0.166700	-0.117961	-0.121346	0.666800	-0.191480	-0.190897
	0.250300	-0.159780	-0.161373	0.751300	-0.155970	-0.163053
	0.333500	-0.185321	-0.189138	0.833400	-0.119877	-0.123586
	0.416700	-0.202572	-0.205702	0.916700	-0.063147	-0.069659
	0.500000	-0.211394	-0.211534			
303.15	0.083500	-0.063786	-0.065745	0.583300	-0.208705	-0.204222
	0.166700	-0.116535	-0.117969	0.666800	-0.193015	-0.188072
	0.250300	-0.153911	-0.158007	0.751300	-0.154360	-0.159868
	0.333500	-0.182669	-0.186168	0.833400	-0.121433	-0.120393
	0.416700	-0.197782	-0.203137	0.916700	-0.067235	-0.067309

[a]: Uncertainty of temperature measurement: 0.02 K

[b]: Uncertainty of mole fraction: 0.0013

Table A.2.: Excess volume v^E_{exp} and estimated value of excess volume v^E_{est} of all studied systems at p = 101 kpa (continued)

T/K [a]	x_2 [b]	v^E		x_2 [b]	v^E	
		exp.	est.		exp.	est.
	0.500000	-0.211536	-0.209158			
308.15	0.083500	-0.068507	-0.063564	0.583300	-0.207755	-0.201974
	0.166700	-0.111278	-0.114958	0.666800	-0.189298	-0.185599
	0.250300	-0.154871	-0.154955	0.751300	-0.154191	-0.157155
	0.333500	-0.181577	-0.183426	0.833400	-0.118123	-0.117721
	0.416700	-0.196986	-0.200742	0.916700	-0.066668	-0.065362
	0.500000	-0.206005	-0.206951			
313.15	0.083500	-0.066510	-0.061682	0.583300	-0.201334	-0.199962
	0.166700	-0.115862	-0.112315	0.666800	-0.187077	-0.183477
	0.250300	-0.149521	-0.152218	0.751300	-0.155531	-0.154912
	0.333500	-0.174370	-0.180913	0.833400	-0.122604	-0.115568
	0.416700	-0.192795	-0.198516	0.916700	-0.067548	-0.063820
	0.500000	-0.201997	-0.204915			
318.15	0.083500	-0.066229	-0.060099	0.583300	-0.203520	-0.198188
	0.166700	-0.113945	-0.110038	0.666800	-0.186424	-0.181708
	0.250300	-0.145806	-0.149795	0.751300	-0.151851	-0.153141
	0.333500	-0.176541	-0.178630	0.833400	-0.122296	-0.113934
	0.416700	-0.192730	-0.196460	0.916700	-0.069949	-0.062682
	0.500000	-0.206884	-0.203048			
323.15	0.083500	-0.059136	-0.058816	0.583300	-0.200297	-0.196649
	0.166700	-0.113771	-0.108127	0.666800	-0.187414	-0.180290
	0.250300	-0.149182	-0.147686	0.751300	-0.149757	-0.151842
	0.333500	-0.172637	-0.176575	0.833400	-0.117173	-0.112821
	0.416700	-0.194376	-0.194573	0.916700	-0.067763	-0.061949
	0.500000	-0.206177	-0.201350			
328.15	0.083500	-0.062424	-0.057832	0.583300	-0.198767	-0.195348
	0.166700	-0.107018	-0.106583	0.666800	-0.183215	-0.179225
	0.250300	-0.143553	-0.145892	0.751300	-0.149330	-0.151013
	0.333500	-0.170467	-0.174749	0.833400	-0.120112	-0.112227
	0.416700	-0.190174	-0.192856	0.916700	-0.067198	-0.061619
	0.500000	-0.199819	-0.199823			
333.15	0.083500	-0.058922	-0.057147	0.583300	-0.199012	-0.194282
	0.166700	-0.110482	-0.105406	0.666800	-0.187696	-0.178511
	0.250300	-0.145159	-0.144412	0.751300	-0.150656	-0.150656
	0.333500	-0.170107	-0.173152	0.833400	-0.118338	-0.112153
	0.416700	-0.192866	-0.191309	0.916700	-0.068346	-0.061694
	0.500000	-0.202629	-0.198465			
338.15	0.083500	-0.063136	-0.056762	0.583300	-0.201119	-0.193454
	0.166700	-0.107403	-0.104596	0.666800	-0.187082	-0.178149
	0.250300	-0.148689	-0.143247	0.751300	-0.147075	-0.150770
	0.333500	-0.171635	-0.171785	0.833400	-0.118358	-0.112598
	0.416700	-0.194896	-0.189931	0.916700	-0.065011	-0.062173
	0.500000	-0.199863	-0.197276			
343.15	0.083500	-0.063493	-0.056677	0.583300	-0.197900	-0.192862
	0.166700	-0.106246	-0.104152	0.666800	-0.181343	-0.178138
	0.250300	-0.145930	-0.142396	0.751300	-0.152153	-0.151355
	0.333500	-0.175136	-0.170646	0.833400	-0.113714	-0.113564
	0.416700	-0.188524	-0.188723	0.916700	-0.063520	-0.063057
	0.500000	-0.199001	-0.196257			
348.15	0.083500	-0.059953	-0.056890	0.583300	-0.196645	-0.192506
	0.166700	-0.107094	-0.104074	0.666800	-0.184612	-0.178480
	0.250300	-0.145152	-0.141860	0.751300	-0.152448	-0.152411
	0.333500	-0.172609	-0.169736	0.833400	-0.117596	-0.115049

[a]: Uncertainty of temperature measurement: 0.02 K

[b]: Uncertainty of mole fraction: 0.0013

Table A.2.: Excess volume v^E_{exp} and estimated value of excess volume v^E_{est} of all studied systems at p = 101 kpa (continued)

T/K [a]	x_2 [b]	v^E		x_2 [b]	v^E	
		exp.	est.		exp.	est.
	0.416700	-0.191914	-0.187684	0.916700	-0.063984	-0.064344
	0.500000	-0.200137	-0.195408			
353.15	0.083500	-0.064401	-0.057403	0.583300	-0.197459	-0.192387
	0.166700	-0.110030	-0.104364	0.666800	-0.182880	-0.179173
	0.250300	-0.146444	-0.141638	0.751300	-0.147951	-0.153939
	0.333500	-0.172132	-0.169055	0.833400	-0.116962	-0.117054
	0.416700	-0.189550	-0.186815	0.916700	-0.066522	-0.066036
	0.500000	-0.203371	-0.194729			
358.15	0.083500	-0.062031	-0.058216	0.583300	-0.200452	-0.192505
	0.166700	-0.106409	-0.105020	0.666800	-0.183300	-0.180218
	0.250300	-0.141435	-0.141730	0.751300	-0.152492	-0.155938
	0.333500	-0.168335	-0.168603	0.833400	-0.118496	-0.119578
	0.416700	-0.189314	-0.186116	0.916700	-0.064828	-0.068132
	0.500000	-0.201138	-0.194219			
363.15	0.083500	-0.061815	-0.059328	0.583300	-0.198277	-0.192859
	0.166700	-0.104938	-0.106042	0.666800	-0.185995	-0.181615
	0.250300	-0.138571	-0.142137	0.751300	-0.152406	-0.158408
	0.333500	-0.169467	-0.168380	0.833400	-0.115616	-0.122622
	0.416700	-0.191314	-0.185586	0.916700	-0.065403	-0.070632
	0.500000	-0.201126	-0.193879			
373.15	0.083500	-0.031697	-0.062450	0.583300	-0.179365	-0.194277
	0.166700	-0.086533	-0.109187	0.666800	-0.163686	-0.185464
	0.250300	-0.121256	-0.143893	0.751300	-0.119131	-0.164762
	0.333500	-0.147568	-0.168621	0.833400	-0.128216	-0.130270
	0.416700	-0.179284	-0.185035	0.916700	-0.058249	-0.076845
	0.500000	-0.171192	-0.193708			
383.15	0.083500	-0.037985	-0.066769	0.583300	-0.191306	-0.196641
	0.166700	-0.093613	-0.113799	0.666800	-0.179198	-0.190721
	0.250300	-0.130263	-0.146908	0.751300	-0.133493	-0.173001
	0.333500	-0.157409	-0.169778	0.833400	-0.142929	-0.139996
	0.416700	-0.191289	-0.185162	0.916700	-0.077474	-0.084675
	0.500000	-0.182734	-0.194215			
393.15	0.083500	-0.048294	-0.072286	0.583300	-0.207501	-0.199952
	0.166700	-0.108826	-0.119877	0.666800	-0.200516	-0.197385
	0.250300	-0.140046	-0.151179	0.751300	-0.152359	-0.183125
	0.333500	-0.169735	-0.171851	0.833400	-0.163081	-0.151801
	0.416700	-0.204944	-0.185968	0.916700	-0.092167	-0.094122
	0.500000	-0.198320	-0.195401			
403.15	0.083500	-0.054947	-0.079001	0.583300	-0.230796	-0.204208
	0.166700	-0.114164	-0.127421	0.666800	-0.229835	-0.205456
	0.250300	-0.160652	-0.156709	0.751300	-0.179170	-0.195133
	0.333500	-0.190972	-0.174839	0.833400	-0.193589	-0.165686
	0.416700	-0.224869	-0.187453	0.916700	-0.121349	-0.105186
	0.500000	-0.220200	-0.197265			

[a]: Uncertainty of temperature measurement: 0.02 K

[b]: Uncertainty of mole fraction: 0.0013

Table A.3.: Excess logarithmic viscosity $\ln(\eta)^E_{exp}$ and estimated value of excess logarithmic viscosity $\ln(\eta)^E_{est}$ of all studied systems at p = 101 kpa

T/K [a]	x_2 [b]	$\ln(\eta/\text{mPa}\cdot\text{s})^E$		x_2 [b]	$\ln(\eta/\text{mPa}\cdot\text{s})^E$	
		exp.	est.		exp.	est.
diethylene glycol (1) & decan-1-ol (2)						
293.15	0.083500	-0.052897	-0.029581	0.583000	-0.148461	-0.135306
	0.166700	-0.062678	-0.056777	0.666700	-0.138786	-0.131923
	0.249900	-0.077437	-0.081236	0.748900	-0.123591	-0.118950
	0.333400	-0.103247	-0.102359	0.832800	-0.096637	-0.093946
	0.416400	-0.120751	-0.119086	0.916500	-0.050856	-0.055039
	0.499800	-0.140176	-0.130528			
303.15	0.083500	-0.043615	-0.025282	0.583000	-0.117273	-0.113812
	0.166700	-0.049869	-0.048470	0.666700	-0.110497	-0.110530
	0.249900	-0.062034	-0.069217	0.748900	-0.097166	-0.099265
	0.333400	-0.081976	-0.086989	0.832800	-0.073243	-0.078077
	0.416400	-0.097419	-0.100893	0.916500	-0.037700	-0.045554
	0.499800	-0.111643	-0.110205			
313.15	0.083500	-0.035935	-0.021604	0.583000	-0.094649	-0.095073
	0.166700	-0.040070	-0.041348	0.666700	-0.089392	-0.091815
	0.249900	-0.049737	-0.058881	0.748900	-0.077685	-0.081988
	0.333400	-0.066065	-0.073728	0.832800	-0.056972	-0.064106
	0.416400	-0.079227	-0.085144	0.916500	-0.028807	-0.037180
	0.499800	-0.090513	-0.092548			
323.15	0.083500	-0.029874	-0.018547	0.583000	-0.078030	-0.079089
	0.166700	-0.033165	-0.035408	0.666700	-0.073504	-0.075778
	0.249900	-0.040830	-0.050228	0.748900	-0.063332	-0.067121
	0.333400	-0.054518	-0.062578	0.832800	-0.045533	-0.052034
	0.416400	-0.065538	-0.071837	0.916500	-0.021942	-0.029916
	0.499800	-0.074858	-0.077557			
333.15	0.083500	-0.025890	-0.016111	0.583000	-0.066286	-0.065860
	0.166700	-0.029072	-0.030653	0.666700	-0.062156	-0.062419
	0.249900	-0.035145	-0.043259	0.748900	-0.053117	-0.054662
	0.333400	-0.046856	-0.053537	0.832800	-0.037726	-0.041861
	0.416400	-0.056024	-0.060973	0.916500	-0.016740	-0.023763
	0.499800	-0.063898	-0.065234			
343.15	0.083500	-0.024143	-0.014296	0.583000	-0.058283	-0.055386
	0.166700	-0.027699	-0.027082	0.666700	-0.054206	-0.051738
	0.249900	-0.032356	-0.037974	0.748900	-0.045814	-0.044612
	0.333400	-0.042574	-0.046605	0.832800	-0.032589	-0.033586
	0.416400	-0.049822	-0.052552	0.916500	-0.012506	-0.018720
	0.499800	-0.056496	-0.055577			
353.15	0.083500	-0.023893	-0.013102	0.583000	-0.052965	-0.047666
	0.166700	-0.028255	-0.024694	0.666700	-0.048754	-0.043735
	0.249900	-0.031810	-0.034372	0.748900	-0.040510	-0.036971
	0.333400	-0.040544	-0.041784	0.832800	-0.028532	-0.027209
	0.416400	-0.046251	-0.046574	0.916500	-0.008551	-0.014788
	0.499800	-0.051939	-0.048587			
363.15	0.083500	-0.024435	-0.012530	0.583000	-0.049525	-0.042701
	0.166700	-0.029555	-0.023491	0.666700	-0.044792	-0.038410
	0.249900	-0.032544	-0.032453	0.748900	-0.036781	-0.031739
	0.333400	-0.040218	-0.039071	0.832800	-0.025199	-0.022732
	0.416400	-0.044427	-0.043039	0.916500	-0.004086	-0.011966
	0.499800	-0.049123	-0.044264			
373.15	0.083500	-0.024395	-0.012578	0.583000	-0.047328	-0.040491
	0.166700	-0.031076	-0.023471	0.666700	-0.042198	-0.035763
	0.249900	-0.033665	-0.032218	0.748900	-0.034133	-0.028915
	0.333400	-0.040975	-0.038469	0.832800	-0.022558	-0.020153

[a]: Standard uncertainty of temperature measurement: $u(T) = 0.03$ K

[b]: Standard uncertainty of mole fraction: $u(x) = 0.0013$

Table A.3.: Excess logarithmic viscosity $\ln(\eta)^E_{exp}$ and estimated value of excess logarithmic viscosity $\ln(\eta)^E_{est}$ of all studied systems at p = 101 kpa (continued)

T/K [a]	x_2 [b]	$\ln(\eta/\text{mPa}\cdot\text{s})^E$		x_2 [b]	$\ln(\eta/\text{mPa}\cdot\text{s})^E$	
		exp.	est.		exp.	est.
	0.416400	-0.043404	-0.041947	0.916500	0.000258	-0.010255
	0.499800	-0.047440	-0.042607			
383.15	0.083500	-0.023642	-0.013247	0.583000	-0.046097	-0.041035
	0.166700	-0.031953	-0.024635	0.666700	-0.040778	-0.035794
	0.249900	-0.034502	-0.033666	0.748900	-0.032641	-0.028501
	0.333400	-0.041483	-0.039976	0.832800	-0.020960	-0.019472
	0.416400	-0.042708	-0.043297	0.916500	0.004539	-0.009654
	0.499800	-0.046531	-0.043617			
393.15	0.083500	-0.021389	-0.014538	0.583000	-0.046032	-0.044335
	0.166700	-0.031555	-0.026983	0.666700	-0.040629	-0.038503
	0.249900	-0.034578	-0.036798	0.748900	-0.032987	-0.030495
	0.333400	-0.041776	-0.043593	0.832800	-0.021133	-0.020691
	0.416400	-0.041486	-0.047091	0.916500	0.010664	-0.010164
	0.499800	-0.046413	-0.047294			
403.15	0.083500	-0.016944	-0.016449	0.583000	-0.048003	-0.050389
	0.166700	-0.029607	-0.030515	0.666700	-0.043317	-0.043891
	0.249900	-0.033825	-0.041613	0.748900	-0.036024	-0.034898
	0.333400	-0.042028	-0.049320	0.832800	-0.025222	-0.023808
	0.416400	-0.041140	-0.053327	0.916500	0.011002	-0.011784
	0.499800	-0.047511	-0.053638			
diethylene glycol (1) & isopropyl alcohol (2)						
283.15	0.083600	0.046170	0.040347	0.583400	0.091815	0.069252
	0.166700	0.072749	0.066086	0.666600	0.071996	0.057720
	0.242700	0.069204	0.079570	0.750000	0.054799	0.044762
	0.333500	0.101169	0.085902	0.833300	0.036692	0.030848
	0.416600	0.103577	0.084679	0.916600	0.025590	0.016031
	0.500000	0.100065	0.078630			
293.15	0.083600	0.038718	0.042064	0.583400	0.102034	0.113965
	0.166700	0.067122	0.072453	0.666600	0.085615	0.105652
	0.242700	0.069774	0.092153	0.750000	0.065476	0.091418
	0.333500	0.103995	0.107462	0.833300	0.041183	0.070206
	0.416600	0.109732	0.114948	0.916600	0.015324	0.040433
	0.500000	0.108752	0.117021			
303.15	0.083600	0.040338	0.043319	0.583400	0.132654	0.145239
	0.166700	0.073208	0.077341	0.666600	0.120008	0.138361
	0.242700	0.082758	0.101774	0.750000	0.099318	0.122480
	0.333500	0.121112	0.123639	0.833300	0.072575	0.095776
	0.416600	0.132036	0.137168	0.916600	0.035777	0.055907
	0.500000	0.135849	0.144541			
313.15	0.083600	0.045555	0.044111	0.583400	0.165904	0.163075
	0.166700	0.083044	0.080750	0.666600	0.156348	0.155847
	0.242700	0.098664	0.108432	0.750000	0.135700	0.137948
	0.333500	0.141415	0.134433	0.833300	0.104647	0.107557
	0.416600	0.157346	0.151339	0.916600	0.061703	0.062454
	0.500000	0.165589	0.161189			
323.15	0.083600	0.049532	0.044441	0.583400	0.185835	0.167473
	0.166700	0.089996	0.082679	0.666600	0.177241	0.158110
	0.242700	0.109501	0.112128	0.750000	0.155243	0.137820
	0.333500	0.154418	0.139845	0.833300	0.120653	0.105550
	0.416600	0.173187	0.157460	0.916600	0.069796	0.060073
	0.500000	0.183917	0.166965			
333.15	0.083600	0.049086	0.044309	0.583400	0.178426	0.158433
	0.166700	0.088745	0.083129	0.666600	0.167319	0.145149

[a]: Standard uncertainty of temperature measurement: $u(T) = 0.03$ K

[b]: Standard uncertainty of mole fraction: $u(x) = 0.0013$

Table A.3.: Excess logarithmic viscosity $\ln(\eta)^E_{exp}$ and estimated value of excess logarithmic viscosity $\ln(\eta)^E_{est}$ of all studied systems at p = 101 kpa (continued)

T/K [a]	x_2 [b]	$\ln(\eta/\text{mPa}\cdot\text{s})^E$		x_2 [b]	$\ln(\eta/\text{mPa}\cdot\text{s})^E$	
		exp.	est.		exp.	est.
	0.242700	0.108447	0.112861	0.750000	0.140806	0.122099
	0.333500	0.151605	0.139874	0.833300	0.099591	0.089755
	0.416600	0.169301	0.155532	0.916600	0.039649	0.048766
	0.500000	0.178570	0.161870			
343.15	0.083600	0.041825	0.043714	0.583400	0.131724	0.135955
	0.166700	0.075367	0.082100	0.666600	0.113246	0.116965
	0.242700	0.090190	0.110632	0.750000	0.077298	0.090782
	0.333500	0.125621	0.134521	0.833300	0.023330	0.060172
	0.416600	0.136849	0.145555	0.916600	-0.062652	0.028531
	0.500000	0.139026	0.145902			
diethylene glycol (1) & glycerol (2)						
293.15	0.083500	-0.085293	-0.081717	0.583300	-0.259953	-0.252284
	0.166700	-0.151486	-0.148794	0.666800	-0.220210	-0.226906
	0.250300	-0.195889	-0.201002	0.751300	-0.192637	-0.187038
	0.333500	-0.240882	-0.237357	0.833400	-0.128334	-0.135797
	0.416700	-0.257000	-0.257937	0.916700	-0.073154	-0.072653
	0.500000	-0.256182	-0.262809			
303.15	0.083500	-0.078249	-0.075079	0.583300	-0.240777	-0.233387
	0.166700	-0.139594	-0.136663	0.666800	-0.207019	-0.210618
	0.250300	-0.182981	-0.184660	0.751300	-0.181024	-0.174339
	0.333500	-0.222952	-0.218240	0.833400	-0.121290	-0.127196
	0.416700	-0.236784	-0.237498	0.916700	-0.071190	-0.068453
	0.500000	-0.240565	-0.242475			
313.15	0.083500	-0.070122	-0.068808	0.583300	-0.222183	-0.215440
	0.166700	-0.126555	-0.125209	0.666800	-0.192750	-0.195092
	0.250300	-0.167589	-0.169234	0.751300	-0.169008	-0.162172
	0.333500	-0.204159	-0.200185	0.833400	-0.114686	-0.118898
	0.416700	-0.216582	-0.218174	0.916700	-0.068262	-0.064360
	0.500000	-0.222552	-0.223215			
323.15	0.083500	-0.062030	-0.062903	0.583300	-0.202990	-0.198444
	0.166700	-0.113617	-0.114434	0.666800	-0.177192	-0.180328
	0.250300	-0.151871	-0.154723	0.751300	-0.155864	-0.150536
	0.333500	-0.185214	-0.183193	0.833400	-0.106470	-0.110903
	0.416700	-0.196480	-0.199964	0.916700	-0.063767	-0.060376
	0.500000	-0.203211	-0.205029			
333.15	0.083500	-0.055244	-0.057364	0.583300	-0.184822	-0.182398
	0.166700	-0.102313	-0.104337	0.666800	-0.161726	-0.166327
	0.250300	-0.137693	-0.141128	0.751300	-0.142759	-0.139431
	0.333500	-0.167788	-0.167263	0.833400	-0.097817	-0.103211
	0.416700	-0.178057	-0.182869	0.916700	-0.058326	-0.056500
	0.500000	-0.184817	-0.187917			
343.15	0.083500	-0.050251	-0.052192	0.583300	-0.168629	-0.167304
	0.166700	-0.092841	-0.094918	0.666800	-0.147828	-0.153087
	0.250300	-0.125767	-0.128448	0.751300	-0.130784	-0.128859
	0.333500	-0.152754	-0.152395	0.833400	-0.089870	-0.095823
	0.416700	-0.162013	-0.166888	0.916700	-0.052822	-0.052731
	0.500000	-0.168415	-0.171879			
353.15	0.083500	-0.046747	-0.047386	0.583300	-0.154870	-0.153160
	0.166700	-0.085307	-0.086177	0.666800	-0.135830	-0.140609
	0.250300	-0.116639	-0.116683	0.751300	-0.120665	-0.118817
	0.333500	-0.139871	-0.138590	0.833400	-0.083517	-0.088737
	0.416700	-0.148208	-0.152022	0.916700	-0.048221	-0.049071
	0.500000	-0.154623	-0.156915			

[a]: Standard uncertainty of temperature measurement: $u(T) = 0.03$ K

[b]: Standard uncertainty of mole fraction: $u(x) = 0.0013$

Table A.3.: Excess logarithmic viscosity $\ln(\eta)^E_{exp}$ and estimated value of excess logarithmic viscosity $\ln(\eta)^E_{est}$ of all studied systems at p = 101 kpa (continued)

T/K [a]	x_2 [b]	$\ln(\eta/\text{mPa}\cdot\text{s})^E$		x_2 [b]	$\ln(\eta/\text{mPa}\cdot\text{s})^E$	
		exp.	est.		exp.	est.
363.15	0.083500	-0.044102	-0.042947	0.583300	-0.143257	-0.139967
	0.166700	-0.078965	-0.078114	0.666800	-0.125856	-0.128893
	0.250300	-0.108129	-0.105833	0.751300	-0.112781	-0.109308
	0.333500	-0.128868	-0.125847	0.833400	-0.079178	-0.081954
	0.416700	-0.136255	-0.138270	0.916700	-0.044811	-0.045519
	0.500000	-0.142848	-0.143025			
373.15	0.083500	-0.041321	-0.038874	0.583300	-0.132312	-0.127724
	0.166700	-0.073027	-0.070728	0.666800	-0.117214	-0.117940
	0.250300	-0.099505	-0.095898	0.751300	-0.105600	-0.100330
	0.333500	-0.118775	-0.114166	0.833400	-0.075381	-0.075474
	0.416700	-0.125750	-0.125633	0.916700	-0.042374	-0.042075
	0.500000	-0.131275	-0.130209			
383.15	0.083500	-0.037512	-0.035168	0.583300	-0.121168	-0.116432
	0.166700	-0.066323	-0.064021	0.666800	-0.108092	-0.107748
	0.250300	-0.090754	-0.086879	0.751300	-0.097536	-0.091883
	0.333500	-0.108441	-0.103548	0.833400	-0.070269	-0.069298
	0.416700	-0.115767	-0.114111	0.916700	-0.039324	-0.038739
	0.500000	-0.119779	-0.118467			
393.15	0.083500	-0.032028	-0.031828	0.583300	-0.109087	-0.106091
	0.166700	-0.058074	-0.057992	0.666800	-0.097310	-0.098318
	0.250300	-0.080740	-0.078775	0.751300	-0.088554	-0.083968
	0.333500	-0.097015	-0.093992	0.833400	-0.063814	-0.063424
	0.416700	-0.103671	-0.103703	0.916700	-0.035204	-0.035512
	0.500000	-0.107404	-0.107799			
403.15	0.083500	-0.023622	-0.028854	0.583300	-0.095417	-0.096701
	0.166700	-0.047328	-0.052640	0.666800	-0.084621	-0.089651
	0.250300	-0.068535	-0.071587	0.751300	-0.077162	-0.076585
	0.333500	-0.083465	-0.085498	0.833400	-0.054830	-0.057853
	0.416700	-0.089577	-0.094410	0.916700	-0.028739	-0.032392
	0.500000	-0.093002	-0.098205			

[a]: Standard uncertainty of temperature measurement: $u(T) = 0.03$ K

[b]: Standard uncertainty of mole fraction: $u(x) = 0.0013$

Table A.4.: Excess parachor P^E_{exp} and estimated value of excess parachor P^E_{est} of all studied systems at p = 101 kpa

T/K [a]	x_2 [b]	P^E		x_2 [b]	P^E	
		exp.	est.		exp.	est.
diethylene glycol (1) & decan-1-ol (2)						
293.15	0.083500	-19.704482	-13.299100	0.583000	-9.817805	-6.934402
	0.166700	-18.930230	-18.679184	0.666700	-6.989222	-5.663930
	0.249900	-17.504765	-18.969666	0.748900	-5.765109	-5.352028
	0.333400	-15.312155	-16.420298	0.832800	-5.507309	-5.232347
	0.416400	-12.350397	-12.822416	0.916500	-3.380208	-4.040195
	0.499800	-11.026758	-9.400249			
303.15	0.083500	-16.671165	-12.744143	0.583000	-4.927393	-5.666367
	0.166700	-15.040302	-17.834567	0.666700	-4.644915	-4.320049
	0.249900	-15.031371	-17.987142	0.748900	-2.527564	-3.999495
	0.333400	-12.151244	-15.368136	0.832800	-0.162709	-4.021520
	0.416400	-8.585098	-11.713771	0.916500	1.485019	-3.234167

[a]: Uncertainty of temperature measurement: 0.2 K

[b]: Uncertainty of mole fraction: 0.0013

Table A.4.: Excess parachor P^E_{exp} and estimated value of excess parachor P^E_{est} of all studied systems at p = 101 kpa (continued)

T/K [a]	x_2 [b]	P^E		x_2 [b]	P^E	
		exp.	est.		exp.	est.
	0.499800	-8.277036	-8.219589			
313.15	0.083500	-17.962329	-12.246761	0.583000	-6.425330	-4.697388
	0.166700	-16.376374	-17.068443	0.666700	-5.738600	-3.350879
	0.249900	-14.831195	-17.095427	0.748900	-4.599168	-3.068067
	0.333400	-13.471440	-14.429494	0.832800	-1.279615	-3.216060
	0.416400	-11.231765	-10.761493	0.916500	-0.608532	-2.710491
	0.499800	-8.300180	-7.259849			
323.15	0.083500	-18.274573	-11.806952	0.583000	-5.068843	-4.027465
	0.166700	-17.617613	-16.380810	0.666700	-4.356298	-2.756420
	0.249900	-16.196168	-16.294521	0.748900	-2.063178	-2.557742
	0.333400	-11.444326	-13.604372	0.832800	-3.152160	-2.815967
	0.416400	-8.908044	-9.965580	0.916500	-6.251987	-2.469168
	0.499800	-9.191821	-6.521029			
333.15	0.083500	-16.408131	-11.424718	0.583000	-5.879764	-3.656600
	0.166700	-15.965103	-15.771669	0.666700	-5.238595	-2.536672
	0.249900	-14.254214	-15.584423	0.748900	-2.685438	-2.468522
	0.333400	-11.668989	-12.892770	0.832800	-2.919227	-2.821241
	0.416400	-8.980074	-9.326033	0.916500	-3.746344	-2.510196
	0.499800	-7.833251	-6.003127			
343.15	0.083500	-15.709741	-11.100057	0.583000	-3.949511	-3.584790
	0.166700	-14.792575	-15.241021	0.666700	-4.515779	-2.691634
	0.249900	-12.117205	-14.965135	0.748900	-2.208711	-2.800406
	0.333400	-12.361531	-12.294688	0.832800	-1.937853	-3.231882
	0.416400	-9.613210	-8.842852	0.916500	1.970274	-2.833577
	0.499800	-7.256843	-5.706145			
353.15	0.083500	-12.676939	-10.832971	0.583000	-3.027705	-3.812038
	0.166700	-12.001052	-14.788864	0.666700	-0.666654	-3.221307
	0.249900	-10.484121	-14.436655	0.748900	1.528445	-3.553394
	0.333400	-8.531292	-11.810126	0.832800	-3.537940	-4.047891
	0.416400	-5.986691	-8.516037	0.916500	-0.827554	-3.439310
	0.499800	-5.464686	-5.630083			
363.15	0.083500	-14.603948	-10.623459	0.583000	-6.177238	-4.338342
	0.166700	-15.682648	-14.415200	0.666700	-7.101111	-4.125690
	0.249900	-12.981352	-13.998984	0.748900	-2.414272	-4.727486
	0.333400	-11.557765	-11.439084	0.832800	-7.599373	-5.269267
	0.416400	-9.925863	-8.345588	0.916500	-6.929642	-4.327395
	0.499800	-7.530239	-5.774940			
diethylene glycol (1) & isopropyl alcohol (2)						
283.15	0.083600	-4.647074	-4.502605	0.583400	-8.641957	-8.291909
	0.166700	-7.353707	-7.523063	0.666600	-6.722932	-6.830606
	0.242700	-8.790162	-9.211304	0.750000	-4.792113	-5.165848
	0.333500	-9.838078	-10.116938	0.833300	-3.593511	-3.414194
	0.416600	-9.551456	-10.090787	0.916600	-1.418096	-1.667402
	0.500000	-8.959872	-9.428503			
293.15	0.083600	-4.199534	-4.096925	0.583400	-7.499838	-7.770651
	0.166700	-7.037076	-6.883341	0.666600	-6.586742	-6.418772
	0.242700	-9.226524	-8.470200	0.750000	-4.558532	-4.860704
	0.333500	-9.247608	-9.356696	0.833300	-3.088834	-3.210171
	0.416600	-9.397065	-9.378779	0.916600	-1.210857	-1.562166
	0.500000	-9.798920	-8.802570			
303.15	0.083600	-3.323164	-3.710936	0.583400	-9.042430	-7.422897
	0.166700	-6.436611	-6.301414	0.666600	-6.352146	-6.156634
	0.242700	-8.284960	-7.826966	0.750000	-5.637411	-4.668029

[a]: Uncertainty of temperature measurement: 0.2 K

[b]: Uncertainty of mole fraction: 0.0013

Table A.4.: Excess parachor P^E_{exp} and estimated value of excess parachor P^E_{est} of all studied systems at p = 101 kpa (continued)

T/K [a]	x_2 [b]	P^E		x_2 [b]	P^E	
		exp.	est.		exp.	est.
	0.333500	-9.988124	-8.737658	0.833300	-3.908197	-3.074615
	0.416600	-9.662813	-8.835602	0.916600	-1.971736	-1.483885
	0.500000	-7.527776	-8.356875			
313.15	0.083600	-2.831351	-3.344638	0.583400	-6.239744	-7.248647
	0.166700	-5.103217	-5.777282	0.666600	-5.785553	-6.044193
	0.242700	-7.624466	-7.281600	0.750000	-3.786427	-4.587822
	0.333500	-8.411055	-8.259825	0.833300	-3.213107	-3.007523
	0.416600	-8.106066	-8.461258	0.916600	-1.495219	-1.432562
	0.500000	-6.935290	-8.091417			
323.15	0.083600	-3.095435	-2.998031	0.583400	-6.893792	-7.247900
	0.166700	-4.506980	-5.310944	0.666600	-5.579784	-6.081449
	0.242700	-6.739346	-6.834105	0.750000	-3.797052	-4.620083
	0.333500	-7.377106	-7.923197	0.833300	-2.744138	-3.008898
	0.416600	-7.895206	-8.255745	0.916600	-0.954752	-1.408194
	0.500000	-7.635700	-8.006198			
333.15	0.083600	-0.888010	-2.671115	0.583400	-8.009077	-7.420657
	0.166700	-6.032792	-4.902401	0.666600	-6.238331	-6.268402
	0.242700	-7.052733	-6.484478	0.750000	-5.859755	-4.764813
	0.333500	-7.628921	-7.727773	0.833300	-4.274432	-3.078737
	0.416600	-9.273298	-8.219064	0.916600	-0.753222	-1.410782
	0.500000	-8.015624	-8.101215			
343.15	0.083600	-1.147567	-2.363891	0.583400	-6.202925	-7.766918
	0.166700	-4.574857	-4.551652	0.666600	-5.372572	-6.605051
	0.242700	-6.273990	-6.232721	0.750000	-5.131004	-5.022012
	0.333500	-7.990158	-7.673553	0.833300	-4.148093	-3.217043
	0.416600	-10.069558	-8.351215	0.916600	-1.840069	-1.440326
	0.500000	-8.250015	-8.376471			
diethylene glycol (1) & glycerol (2)						
293.15	0.083500	0.922808	-0.352038	0.583300	-3.743853	-3.632932
	0.166700	-0.492347	-0.639467	0.666800	-3.379355	-4.241534
	0.250300	-0.605309	-0.994228	0.751300	-4.259034	-4.482223
	0.333500	-1.794219	-1.484407	0.833400	-3.218882	-4.085589
	0.416700	-2.399612	-2.125482	0.916700	-3.167929	-2.720407
	0.500000	-2.892680	-2.875367			
303.15	0.083500	1.123956	-0.296589	0.583300	-2.816945	-3.522468
	0.166700	-2.281436	-0.606312	0.666800	-3.728647	-4.012927
	0.250300	-0.449425	-1.007769	0.751300	-3.715223	-4.147600
	0.333500	-0.733280	-1.529967	0.833400	-4.696409	-3.709991
	0.416700	-2.193658	-2.164775	0.916700	-4.393459	-2.429616
	0.500000	-2.022024	-2.860834			
313.15	0.083500	-0.194606	-0.284387	0.583300	-4.059009	-3.461955
	0.166700	-1.101168	-0.626753	0.666800	-4.092486	-3.853921
	0.250300	-2.226175	-1.068920	0.751300	-3.497710	-3.901027
	0.333500	-2.942906	-1.613327	0.833400	-4.161490	-3.427675
	0.416700	-3.337767	-2.236664	0.916700	-2.241509	-2.209296
	0.500000	-4.142729	-2.882774			
323.15	0.083500	1.161621	-0.315434	0.583300	-2.759496	-3.451396
	0.166700	-1.065727	-0.700789	0.666800	-3.686672	-3.764516
	0.250300	-1.244204	-1.177680	0.751300	-3.936125	-3.742502
	0.333500	-2.252028	-1.734485	0.833400	-3.490162	-3.238640
	0.416700	-2.936010	-2.341146	0.916700	-3.194344	-2.059446
	0.500000	-3.065638	-2.941188			
333.15	0.083500	0.316138	-0.389729	0.583300	-3.620755	-3.490788

[a]: Uncertainty of temperature measurement: 0.2 K

[b]: Uncertainty of mole fraction: 0.0013

Table A.4.: Excess parachor P^E_{exp} and estimated value of excess parachor P^E_{est} of all studied systems at p = 101 kpa (continued)

T/K [a]	x_2 [b]	P^E		x_2 [b]	P^E	
		exp.	est.		exp.	est.
	0.166700	-1.071818	-0.828422	0.666800	-3.927477	-3.744712
	0.250300	-1.578262	-1.334049	0.751300	-2.983270	-3.672027
	0.333500	-1.902346	-1.893443	0.833400	-3.300665	-3.142886
	0.416700	-2.309520	-2.478223	0.916700	-1.391436	-1.980068
	0.500000	-3.150461	-3.036077			
343.15	0.083500	0.883752	-0.507273	0.583300	-1.989014	-3.580133
	0.166700	-0.448428	-1.009650	0.666800	-3.450867	-3.794510
	0.250300	-0.536917	-1.538027	0.751300	-2.725657	-3.689601
	0.333500	-1.379269	-2.090200	0.833400	-2.293375	-3.140415
	0.416700	-1.612130	-2.647895	0.916700	-2.014755	-1.971160
	0.500000	-1.931481	-3.167439			
353.15	0.083500	-1.215352	-0.668064	0.583300	-3.964065	-3.719431
	0.166700	-1.000148	-1.244475	0.666800	-4.622418	-3.913909
	0.250300	-2.098281	-1.789615	0.751300	-4.409101	-3.795223
	0.333500	-3.628651	-2.324756	0.833400	-3.655212	-3.231224
	0.416700	-2.686571	-2.850161	0.916700	-2.357871	-2.032723
	0.500000	-3.889882	-3.335275			
363.15	0.083500	-0.022153	-0.872105	0.583300	-3.816935	-3.908681
	0.166700	-1.998148	-1.532895	0.666800	-4.597506	-4.102910
	0.250300	-2.651369	-2.088813	0.751300	-3.993086	-3.988895
	0.333500	-3.187540	-2.597110	0.833400	-3.109598	-3.415316
	0.416700	-2.960154	-3.085021	0.916700	-2.535073	-2.164757
	0.500000	-3.142904	-3.539586			

[a]: Uncertainty of temperature measurement: 0.2 K

[b]: Uncertainty of mole fraction: 0.0013

A.4. Declaration of generative AI and AI-assisted technologies in the writing process

During the preparation of this dissertation, the author used the following AI-models and AI-assisted technologies:

1. DeepL Translate/Write to improve language and readability.
2. Writefull to improve language and readability
3. ChatGPT featuring the GPT-4o model to review text structure and clarity

After using these services, the authors reviewed and edited the content as needed and take full responsibility for the content of this work.

A.5. List of Publications

List of Peer Reviewed Papers

- D. Appelhaus, K. Jasch, S. Jahnke, H. Hassani Khab Bin, W. Tegethoff, J. Köhler, and S. Scholl. "A New Approach to Simulate the Fluid Dynamics in a Wiped Film Evaporator Using Modelica". In: *Chem. Eng. Res. Des.* 161 (2020), pp. 115–124
- D. Appelhaus, Y. Lu, R. Schenkendorf, S. Scholl, and K. Jasch. "Machine Learning Supports Robust Operation of Thermosiphon Reboilers". In: *Chem. Ing. Tech.* 93.12 (2021), pp. 1976–1986
- D. Appelhaus, F. Claus, S. Knoblauch, K. Jasch, and S. Scholl. "Density, Viscosity, Refractive Index, and Surface Tension of Binary Mixtures of 3-oxa-1,5-Pentanediol with 2-Propanol, 1,2,3-Propanetriol, and 1-Decanol from 283.15 to 403.15 K as Reference Systems for Evaporation Experiments". In: *J. Chem. Eng. Data* 69.9 (2024), pp. 2927–2948
- D. Appelhaus, K. Jasch, M. Groth, and S. Scholl. "Modeling of Fluid Dynamics in Wiped Film Evaporators During Evaporation". In: *Sep. Purif. Technol.* 371 (2025), p. 132840
- D. Appelhaus, K. Jasch, H. Meyer, and S. Scholl. "Evaporation Effects on Residence Time in Wiped Film Evaporators with Roller Wipers". In: *Chem. Eng. Res. Des.* 218 (2025), pp. 341–349

List of Presentations

- D. Appelhaus, H. H. K. Bin, K. Jasch, W. Tegethoff, J. Köhler, and S. Scholl. "Modelica in Process Engineering: Unit Operation Modeling with Robust Calculation Methods for Themophysical Properties." In: *13th Congress of Chemical Engineering and 6th European Congress of Applied Biotechnology. Online 20.03.2021 – 23.09.2021*. 2021
- D. Appelhaus, K. Jasch, and S. Scholl. "Understanding Fluid Dynamics in Wiped Film Evaporators – Modeling of Residence Time and Flow Behavior". In: *Annual Meeting on Reaction Engineering and ProcessNet Subject Division Heat and Mass Transfer, Würzburg*. 2022

- D. Appelhaus, H. H. K. Bin, L. Nielsen, K. Jasch, W. Tegethoff, J. Köhler, and S. Scholl. “Modellierung von Kläranlagen mit thermisch vernetzten Teilprozessen zur Steigerung der Energie- und Ressourceneffizienz”. In: *Jahrestreffen Prozess-, Apparate- und Anlagentechnik, DECHEMA, Frankfurt am Main, Germany, 21.11. – 22.11.2022*. 2022
- S. Jahnke, D. Appelhaus, K. Jasch, and S. Scholl. “Wetting Situations and Heat Transfer Performance of Wiped Film Evaporators at Different Scales”. In: *73. Starch Convention, Online, 28.03. – 30.03.2022*. 2022
- D. Appelhaus, F. Claus, K. Jasch, and S. Scholl. “Bestimmung des Verweilzeitverhaltens in Dünnschichtverdampfern unter Verdampfungsbedingungen”. In: *Jahrestreffen der DECHEMA-Fachgruppen Fluidverfahrenstechnik und Adsorption, Frankfurt am Main, Germany, 21.03. - 23.03.2023*. 2023
- D. Appelhaus, K. Jasch, and S. Scholl. “Modeling of Fluid Dynamics in Wiped Film Evaporators During Evaporation”. In: *27th International Congress of Chemical and Process Engineering, Prag, 26. – 29. August 2024*. 2024
- D. Appelhaus, M. Gebauer, K. Jasch, and S. Scholl. “Die Fluiddynamik von binären Gemischen in Dünnschichtverdampfern unter Verdampfungsbedingungen”. In: *Dechema/VDI Jahrestreffen Fluidverfahrenstechnik 2024, Bochum, 4. – 6. März 2024*. 2024
- D. Appelhaus, K. Jasch, and S. Scholl. “A Modular Model to Predict Fluid Dynamics and Residence Time Distribution in Wiped Film Evaporators During Evaporation”. In: *Jahrestreffen der Dechema/VDI Fachgruppe Wärme- und Stoffübertragung, Stuttgart 10.-12. März 2025*. 2025
- D. Appelhaus, K. Jasch, and S. Scholl. “GVT-Projekt des Jahres 2025 – Wertstoffrückgewinnung mittels Dünnschichtverdampfung”. In: *Mitgliederversammlung der Forschungs-Gesellschaft Verfahrens-Technik e.V. (GVT), April 2025*. 2025

List of Posters

- D. Appelhaus, K. Jasch, R. Schenkendorf, and S. Scholl. “Stabilitätsanalyse eines Naturumlaufverdampfers mittels datenbasierter Merkmal- und Mustererkennung”. In: *ProcessNet Fachgruppentreffen Fluidverfahrenstechnik, Berchtesgaden, Deutschland, 26.02.-28.02.2020*. Poster. 2020
- D. Appelhaus, K. Jasch, R. Schenkendorf, and S. Scholl. “Datenbasierte Stabilitätsanalyse eines Naturumlaufverdampfers mittels maschinellen Lernens”. In: *Jahrestreffen der ProcessNet-Fachgemeinschaft Prozess-, Apparate- und Anlagentechnik, Web-Konferenz, 09.11.-10.11.2020*. Poster. 2020
- D. Appelhaus, S. Jahnke, K. Jasch, and S. Scholl. “Towards a Better Understanding of Wiped Film Evaporators - Using a Modular Model for Fluid Dynamics and Heat Transfer”. In: *The 12th International Conference on Distillation & Absorption, Toulouse, France, 18.09. - 21.09.2022*. Poster. 2022

- D. Appelhaus, S. Scholl, and K. Jasch. “Find the Error - Machine Learning as a Tool for Identifying Unstable Operating Points in Thermosiphon Reboilers”. In: *The 12th International Conference on Distillation & Absorption, Toulouse, France, 18.09. - 21.09.2022*. Poster. 2022
- D. Appelhaus, H. Hupfeld, K. Jasch, and S. Scholl. “Datengestützte Modellierung und Bewertung von Naturumlaufverdampfern”. In: *Jahrestreffen der DECHEMA-Fachgruppen Computational Fluid Dynamics und Wärme- und Stoffübertragung, Frankfurt am Main, Germany, 06.03. - 08.03.2023*. Poster. 2023
- D. Appelhaus, K. Jasch, H. Meyer, and S. Scholl. “Effects of Evaporation on the Residence Time in Wiped Film Evaporators”. In: *Annual meeting of the DECHEMA/VDI Group Fluid Separations, Bochum 3. – 5. Februar 2025*. Poster. 2025

List of Supervised Seminar Papers and Theses

The following study-related works and final theses were prepared under the supervision of the author of this dissertation during his doctoral studies.

- P. Clasen, F. Lüdtke, P. Schult, and J.-E. Thode. “Die Stadt als Rohstoff – Wertstoffrückgewinnung für eine nachhaltige Landwirtschaft”. Project thesis. 2021
- S. M. Wicht. “Entwicklung eines Modells zur Phosphorfällung mit Modelica”. Research project. 2021
- T. Xiong. “Klassifizierung und Prädiktion des Instabilitätsverhaltens eines Naturumlaufverdampfers mittels Machine Learning”. Master thesis. TU Braunschweig, 2021
- L. Bierstedt, W. Hoffmann, C. Michaelis, and C. Moschner. “Dünnschichtverdampfer für die Destillation thermisch sensibler Stoffe”. Project thesis. 2022
- J. Boskamp. “Optische Erfassung und Charakterisierung der Flüssigkeitsverteilung in Dünnschichtverdampfern”. Student thesis. 2022
- F. Claus. “Entwicklung und Charakterisierung einer photometerischen Methode zur Verweilzeitmessung in Dünnschichtverdampfern”. Student thesis. 2022
- H. Hupfeld. “Datengestützte Modellierung des Betriebsverhaltens von Naturumlaufverdampern”. Master thesis. TU Braunschweig, 2022
- M. Luther. “Modellierung und Bilanzierung der Methanogenese in Faulbehältern”. Master thesis. TU Braunschweig, 2022
- S. M. Wicht. “Modellierung der Niedertemperaturtrocknung in der Zuckerindustrie zur Optimierung von Energiebedarf und Stromerzeugung”. Master thesis. TU Braunschweig, 2022
- M. Gebauer. “Charakterisierung der Trennleistung und Fluiddynamik eines Dünnschichtverdampfers für ein binäres Gemisch”. Student thesis. 2023

- D. Rakebrand. “Charakterisierung des Wäremübertragungs und der Verweilzeit von Diethylenglykol in einem Dünnschichtverdampfer”. Bachelor thesis. 2023
- Z. Wu. “Phasengleichgewicht und Trennleistung in Dünnschichtverdampfern für binäre Modellstoffsysteme”. Student thesis. 2024
- M. Anochin, J. Goeritz, M. Krajewski, H. Meyer, and J. Schwabauer. “Chemische Industrie im Wandel-Elektrosynthese als Basis einer nachhaltigen Prozessindustrie”. Project thesis. 2024
- M. Groth. “Modellierung der Fluiddynamik und Verweilzeitverteilung in einem Dünnschichtverdampfer unter Verdampfungsbedingungen”. Student thesis. 2024
- M. Mengen. “Charakterisierung der Flüssigkeitsverteilung in einem Dünnschichtverdampfer unter Verdampfungsbedingungen”. Student thesis. 2024
- H. Meyer. “Fluiddynamische Charakterisierung eines Dünnschichtverdampfers unter Verdampfungsbedingungen”. Bachelor thesis. 2024
- J. Schwabauer. “Experimentelle Bestimmung der Schaumfähigkeit von Wasser-Tensid-Systemen unter Siedebedingungen”. Bachelor thesis. 2024
- R. Herbst. “Charakterisierung des Wärmeübergangs und des Verweilzeitverhaltens eines Dünnschichtverdampfers bei der Verdampfung binärer Gemische”. Master thesis. TU Braunschweig, 2024

ISSN 1860-1316
ISBN 978-3-68952-373-2

Cuvillier Verlag Göttingen
Internationaler wissenschaftlicher Fachverlag